International Journal of Aerospace Engineering

New Developments in Fault-Tolerant Control and Fault-Tolerant Cooperative Control of Unmanned Aerial Systems

Lead Guest Editor: Ziquan Yu
Guest Editors: Youmin Zhang, Ban Wang, and Lingxia Mu

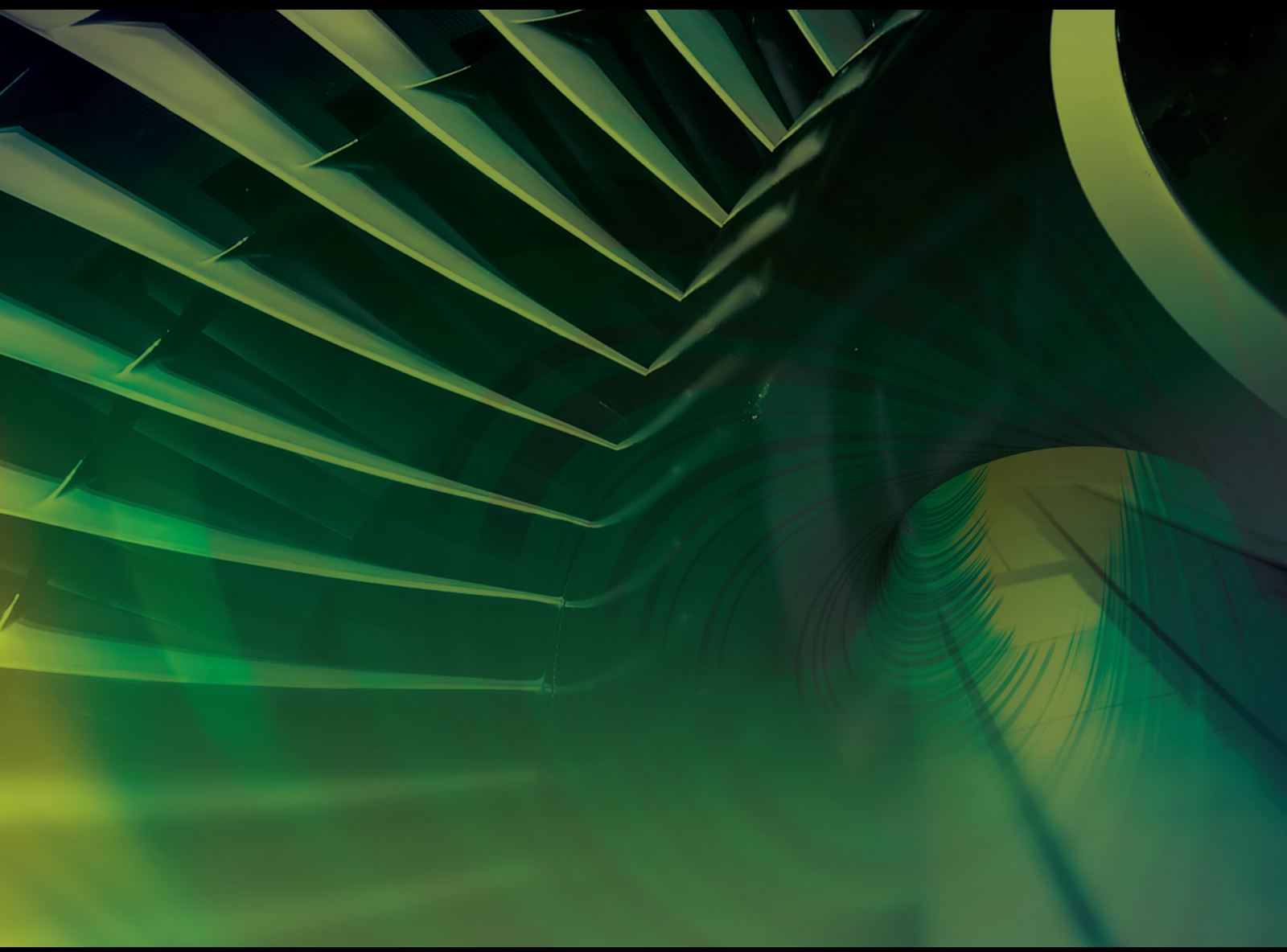

New Developments in Fault-Tolerant Control and Fault-Tolerant Cooperative Control of Unmanned Aerial Systems

International Journal of Aerospace Engineering

New Developments in Fault-Tolerant Control and Fault-Tolerant Cooperative Control of Unmanned Aerial Systems

Lead Guest Editor: Ziquan Yu
Guest Editors: Youmin Zhang, Ban Wang, and Lingxia Mu

Contents

Hindawi
International Journal of Aerospace Engineering
Volume 2023, Article ID 6413085, 19 pages
https://doi.org/10.1155/2023/6413085

Research Article

A Modified Robust Adaptive Fault Compensation Design for Spacecraft with Guaranteed Transient Performance

Xuelian Yao, Yi Yang, and Mingyu Wu

Jiangsu University of Technology, Changzhou, China

Correspondence should be addressed to Yi Yang; kkndext@126.com

Received 26 May 2022; Revised 26 August 2022; Accepted 3 February 2023; Published 7 March 2023

Academic Editor: Lingxia Mu

A modified, robust adaptive fault compensation design is proposed for rigid spacecraft systems with uncertain actuator failures and unknown disturbances. The feedback linearization method is first introduced to linearize the nonlinear dynamics, and a model-reference adaptive controller is designed to suppress the unknown external disturbances and stabilize the linearized system. Then, a composite adaptive controller is developed by integrating multiple controllers designed for the corresponding actuator failure conditions, which can handle the essentially multiple uncertainties (failure time, values, type, and failure pattern) of actuator failures simultaneously. To further improve the transient performance problem in the failure compensation control, an $H\infty$ compensator is introduced as an additional item in the basic controller to attenuate the adverse effects on tracking performance caused by parameter estimation errors. From the theoretical analysis and simulation results, it is obvious that the designed scheme can not only guarantee the stability of the closed-loop system is stable and asymptotical tracking properties for a given reference signal but also greatly improve the transient performance of the spacecraft system during the process of failure compensation.

1. Introduction

Component (actuator or sensor) failures and external disturbances are common in performance-critical systems, which can lead to loss of performance and even cause catastrophic accidents. Hence, to maintain an acceptable level of performance and guarantee system stability in the event of uncertain component failures, remarkable progresses have been made in the area of fault-tolerant control (FTC) and disturbance suppression [1–7].

Reaction wheels are commonly used in spacecraft as the actuators, which may fail in the course of system operation. Precise attitude control in the case of disturbances and uncertain actuator failures have widely studied in the existing literature. Excellent overviews were provided by the survey papers [8, 9] to make FTC designs for spacecraft control system. In [10], a fault tolerant control scheme was proposed for spacecraft attitude stabilization by integrating learning observer and backstepping control design. A novel adaptive event-triggered controller was designed to handle disturbances, model uncertainties, actuator failures, and limited communication, simultaneously [11]. In this paper, only loss of actuator effectiveness fault was considered in the control system design. Adaptive observer-based fault-tolerant tracking control schemes were widely used to deal with the attitude tracking problem for spacecraft experience disturbances and actuator failures [12, 13]. Fault detection and identification based FTC scheme was designed for spacecraft control system subject to multiple actuator faults, parameter uncertainties, and external disturbances [14]. Nonlinear model predictive control approach was used to control the coupled translational-rotational motion of a spacecraft in the presence of one actuator failure [15]. In [16], a new adaptive attitude tracking control scheme was developed for a flexible spacecraft system subject to external disturbances and uncertain failures. The sliding mode control (SMC) technology is insensitive to some disturbances and uncertainties very much [17]. Numerous works related to SMC-based spacecraft FTC design were reported in [18] and the references therein.

For the recently advanced space missions, the system performance either in the stable state and the instantaneous one are equally important. Bad transient performance may

exist although the steady performance can be obtained successfully finally, which are potentially dangerous to performance-critical systems. The problem of transient performance improvement has been widely researched based on several inspired control approaches, such as model reference adaptive control (MRAC) [19], H_∞ control [20], adaptive control [21, 22] and sliding mode control [23]. To improve the transient dynamics through modifying MRAC design, [24, 25] have used fuzzy logic and genetic algorithm, illustrated some simulations without analytical support to manifest the effectiveness of the designed scheme. Dynamic regressor extension and the technique of mixing parameter estimation were introduced by [26], which removed the assumption of some prior knowledge with high-frequency gain, whereas such a scheme may cause a complicated task for issues of practical interests. Considering that actuator saturation, together with the excessive tracking error of the closed-loop system's trajectory may also be led by large adaptive rates, with the exception of the plant's reference model, [27] introduced an auxiliary reference model with the characterization of the classical MRAC framework. However, the simulation results show that the larger values of the user-defined rate parameter will cause larger overshoots. Most of the aforementioned schemes deal only with system parameter uncertainties without considering the uncertainties of actuator failure.

Recently, more attention has been paid to the study of FTC designs with guaranteed transient performance [28]. Investigating the prescribe performance fault tolerance control for chaser spacecraft. The uncertainties of model, actuator failure, and external disturbances were summarized as lumped disturbances, which were estimated by a finite-time extended state observer. Based on the estimated information from the observer, an adaptive backstepping controller was designed to achieve the desired trajectory [29]. Addressed the problem of finite-time attitude-tracking control for a rigid spacecraft with inertial uncertainties, external disturbances, actuator saturations, and faults. A fast nonsingular terminal sliding mode manifold integrating with fuzzy approximation technique was constructed to develop an enhanced FTC scheme. It can guarantee the real finite-time stability instead of asymptotical stability. Similar to the study in [29, 30], we proposed a fault-tolerant nonsingular fixed-time control scheme based on neural networks for spacecraft maneuver mission, which can accelerate the convergence rate and improve control accuracy. A robust FTC algorithm was synthesized by employing a low-pass filter and an auxiliary dynamic system along with adaptive backstepping design, which achieved attitude tracking despite the presence of disturbances, actuator faults, and input saturation [31]. In [32], a fault-tolerant controller, based on dynamic surface design and nonlinear extended state observer, was developed for attitude tracking dynamics of the combined spacecraft in the presence of inertia uncertainty, actuator failure, and external disturbance. Such a scheme can drive the attitude tracking error to converge to one small neighborhood of zero. However, the uncertainties of both actuator failure and external disturbance were considered to be lumped disturbances by the previous literatures, and fuzzy logic system, neural networks, or observers were investigated to estimate the lumped disturbance. As [33] pointed out in most conditions, actuator failure and disturbance cannot be handled in the same way due to their different mechanisms.

As has been pointed out by [34], the parameter estimation error of the adaptive controller is one of the most significant factors that lead to the undesired transient. It is widely known that unanticipated actuator failures will bring about parametric uncertainties in the system. And the parameter estimation error is inevitable no matter which adaptive control scheme is adopted. Despite recent advances in transient performance improvement design for spacecraft fault-tolerant control system, it is still a challenging problem on how to guarantee transient performance for spacecraft system with uncertain actuator faults and external disturbances. Hence, it is an interesting and meaningful topic to investigate the problem of attitude tracking control with guaranteed transient and steady state performance for spacecraft subject to both actuator failures and external disturbances, which motivates the main results in this paper. The spacecraft attitude control problem under uncertain actuator failures and unknown disturbances is solved by proposed backstepping-based adaptive control scheme in literature [35]. On this basis, the problem of actuator failure compensation design for spacecraft attitude control system with guaranteed transient performance is further studied in this paper. The major contributions and excellence of our proposed methodology are as follows:

(i) Unlike the works which focus on the design of adaptive FTC for spacecraft systems with the weakness of a bad transient performance under the condition of unanticipated actuator failures, this paper further concerns the transient performance problem for the actuator failure compensation design. A performance index is adopted to assess the degree of the transient performance enhancement and characterize the weight of the designed H_∞ compensator in the modified MRAC system

(ii) Compared with the current MRAC based transient performance improvement schemes, this paper first couple the modified MRAC and direct adaptive FTC control techniques to increase the fault tolerance capability of the MRAC scheme

(iii) In contrast to the existing literatures regarding the uncertainties of both actuator failure and external disturbance as lumped disturbances, this paper solve the uncertain actuator failures and disturbances separately according to their different mechanisms

(iv) Detailed analysis of the performance of both transient and system steady state, and the valid proof according to the asymptotic output tracking as well

The remaining section is composed as follows. Section 2 formulates the control problems, describes some preliminaries on the feedback linearization theory, and presents two lemmas, which are important for the compensator design and performance analysis. Section 3 describes the modified

MRAC and the adaptive failure compensation design, as well as the closed-loop system performance analysis. Section 4 gives the simulation background and numerical simulation results.

2. Spacecraft Model and Problem Description

This chapter first introduces the rigid spacecraft system model and some basic concepts, then describes the actuator fault compensation of the spacecraft system.

2.1. Rigid Spacecraft Model. The mathematical model of a rigid spacecraft system is formulated by the following equations:

$$\begin{bmatrix} \dot{q}_0 \\ \dot{q} \end{bmatrix} = \frac{1}{2} \begin{bmatrix} -q^T \\ q_0 I + q^{\times} \end{bmatrix} \omega, \qquad J\dot{\omega} = -\omega^{\times} J\omega + Du(t) + d(t), \tag{1}$$

where q_0 and $q = [q_1, q_2, q_3]^T \in R^3$ denote the scalar and vector parts of the unit-quaternion, respectively. The quaternion also satisfies the constraint equation $q^T q + q_0^2 = 1$, $\omega \in R^3$ denotes the inertial angular velocity of the spacecraft expressed in the body frame, and the inertia matrix $J \in R^{(3\times 3)}$ is assumed to be known in this study. The notations $\zeta^{\times}$, $\forall \zeta = [\zeta_1, \zeta_2, \zeta_3]$, can be expressed as

$$\zeta^{\times} = \begin{bmatrix} 0 & -\zeta_3 & \zeta_2 \\ \zeta_3 & 0 & -\zeta_1 \\ -\zeta_2 & \zeta_1 & 0 \end{bmatrix}. \tag{2}$$

$u(t) \in R^4$ is the control input produced by reaction wheels. As the orientation matrix of the reaction wheel, $D \in R^{(3\times 4)}$ is available for a given spacecraft. In this research, we consider

$$D = \begin{bmatrix} -1 & 0 & 0 & \frac{1}{\sqrt{3}} \\ 0 & -1 & 0 & \frac{1}{\sqrt{3}} \\ 0 & 0 & -1 & \frac{1}{\sqrt{3}} \end{bmatrix}. \tag{3}$$

$d(t) = [d_1, d_2, d_3]^T \in R^3$ represents disturbance vector, which comes in many forms: gravity gradients, solar pressure, atmospheric drag, pressure forces, and so on. In practice, these forces are bounded. For the major topic of our interest, each component of $d(t)$ is modeled as

$$d_i(t) = c_i + \sum_{j=1}^{n_i} a_{ij} \sin \omega_{ij} t + \sum_{j=1}^{n_i} b_{ij} \cos \omega_{ij} t = \theta_{di}^{*T} \varpi_{di}(t), \tag{4}$$

where c_i, a_{ij}, and b_{ij} are unknown amplitudes, and ω_{ij} are known frequencies.

$$\theta_{di}^{*} = \left[c_{i0}, a_{i1}, \cdots, a_{in_i}, b_{i1}, \cdots, b_{in_i}\right]^T \in R^{2n_i+1}, \varpi_{di}(t) = \left[1, \sin \omega_{i_1} t, \cdots, \sin \omega_{i_{n_i}} t, \cos \omega_{i_1} t, \cdots, \cos \omega_{i_{n_i}} t\right]^T \in R^{2n_i+1}. \tag{5}$$

Define $x = [q^T, \omega^T]^T$ and $y = q$ as the state and output vector, the spacecraft attitude control system (1) is rewritten as

$$\dot{x} = f(x) + g(x)u_d(t) + g(x)d(t), \qquad y = h(x), \tag{6}$$

where

$$f(x) = \begin{bmatrix} 1/2\sqrt{1 - (\|q\|)^2}\omega - 1/2\omega^{\times} q \\ -J^{-1}\omega^{\times} J\omega \end{bmatrix}, \qquad g(x) = [g_1, g_2, g_3] = \begin{bmatrix} 0 \\ J^{-1} \end{bmatrix}, \tag{7}$$

and

$$u_d = Du. \tag{8}$$

2.2. Control Problem Statement. This research mainly focuses on the issue of the spacecraft attitude control involves uncertain actuator failures. The classical actuator failures is expressed as

$$\bar{u}_j(t) = \bar{u}_{j0} + \sum_{i=1}^{q_j} \bar{u}_{ji} f_{ji}(t), \; t \geq t_j, \tag{9}$$

where $j \in \{1, 2, 3, 4\}$, $t_j > 0$, $\bar{u}_{j0}$, and $\bar{u}_{ji}$ represent unknown failure parameters. $f_{ji}(t)$, $i = 1, 2, \cdots, q_j$ are known. The Equation (9) can also be rewritten into the below-parameterized expression

$$\bar{u}_j(t) = \theta_j^T \varpi_j(t), \tag{10}$$

where $\theta_j = [\bar{u}_{j0}, \bar{u}_{j1}, \cdots, \bar{u}_{jq_j}]^T \in R^{q_j+1}$, $\varpi_j(t) = [1, f_{j1}(t), \cdots, f_{jq_j}(t)]^T \in R^{q_j+1}$. As specifically pointed out, the failure model (9) can describe stuck-in-place, complete failure, and oscillatory failure which usually occur in the spacecraft system.

In the system, if there is any uncertain actuator fault, then the input $u(t)$ applying to the system is

$$u(t) = (I - \sigma(t))v(t) + \sigma(t)\bar{u}(t), \tag{11}$$

where $v(t)$ denotes the control input signal. $\bar{u}(t) = [\bar{u}_1, \bar{u}_2, \bar{u}_3, \bar{u}_4]^T$ and$\sigma(t) = \text{diag}\{\sigma_1, \sigma_2, \sigma_3, \sigma_4\}$ are defined fault pattern matrix, i.e, when the j-th actuator fails $\sigma_j(t) = 1$, if there is no failure $\sigma_j(t) = 0$. Substituting Equation

(11) into the second equation of (1), the system model is expressed as

$$J\dot{\omega} = -\omega^{\times} J\omega + D[(I - \sigma(t))v(t) + \sigma(t)\bar{u}(t)] + d(t). \quad (12)$$

For the output $y(t) = q$ to track a given command $y_m(t)$, at least three functional inputs at any time are needed, so that the independent control inputs are enough to make sure that the output can track the arbitrary given output signals. Therefore, no more than one actuator failure can be allowed in the system; the compensable failure cases and the corresponding failure patterns are listed as

(i) no failure case, $\sigma_{(1)} = \text{diag}\{0, 0, 0, 0\}$

(ii) u_1 failure case, $\sigma_{(2)} = \text{diag}\{1, 0, 0, 0\}$

(iii) u_4 failure case, $\sigma_{(3)} = \text{diag}\{0, 0, 0, 1\}$

(iv) u_3 failure case, $\sigma_{(4)} = \text{diag}\{0, 0, 1, 0\}$

(v) u_2 failure case, $\sigma_{(5)} = \text{diag}\{0, 1, 0, 0\}$

2.2.1. Control Objective. For system (1), which has one uncertain failure (9) at most, an adaptive controller $v(t)$ is designed to guarantee system stability and output tracking with guaranteed transient performance. To show the design process of failure compensation control accompanied by satisfactory transient performance, we design the adaptive scheme for the three failure patterns as following:

$$\begin{aligned} &\sigma_{(1)} = \text{diag}\{0, 0, 0, 0\}, \\ &\sigma_{(2)} = \text{diag}\{1, 0, 0, 0\}, \\ &\sigma_{(3)} = \text{diag}\{0, 0, 0, 1\}. \end{aligned} \quad (13)$$

Remark 1. The studied spacecraft of this paper are actuated by four reaction wheels. We can learn from the orientation matrix of reaction wheel given in (3) that three of them are mounted where their spin axes are parallel to the body frame, respectively, and the other one is mounted where its spin axis points to some fixed direction. According to the configuration of reaction wheels, the control design for the u_1 failure case can be expended to address the u_2 and u_3 failure cases, so in this paper, only the three failure cases (13) are taken into account to demonstrate the detail design process.

2.3. Feedback Linearization. For a kind of nonlinear systems with the input and output of $m$dimension

$$\dot{x} = f(x) + g(x)u, y = h(x). \quad (14)$$

Definition 2. The system (14) has a vector relative degree $\{\rho_1, \rho_2, \cdots, \rho_m\}$, $1 \le \rho_i \le n$, at a point x_0 for $\forall x$ in a neighborhood of if the below two conditions hold

(i) $L_{g_j} L_f^k h_i(x) = 0$, for all $1 \le j \le m, 1 \le i \le m, 0 < k < \rho_i - 1$ and $L_{g_j} L_f^{\rho_i - 1} h_i(x) \ne 0$, for some $j \in \{1, 2, \cdots, m\}$, and

(ii) the $m \times m$ matrix $G(x)$ is defined as

$$G(x) = \begin{bmatrix} L_{g_1} L_f^{\rho_1 - 1} h_1(x) & \cdots & L_{g_m} L_f^{\rho_1 - 1} h_1(x) \\ L_{g_1} L_f^{\rho_2 - 1} h_2(x) & \cdots & L_{g_m} L_f^{\rho_2 - 1} h_2(x) \\ \cdots & & \cdots \\ L_{g_1} L_f^{\rho_m - 1} h_m(x) & \cdots & L_{g_m} L_f^{\rho_m - 1} h_m(x) \end{bmatrix}. \quad (15)$$

Then the system (14) has the relative degree $\rho = \sum_{i=1}^{m} \rho_i$, with ρ_i being the subrelative degree of the i-th output $y_i = h_i(x)$. If the equilibrium point of system (1) is $x_0 = [0, 0, 0, 0, 0, 0]^T$, we can obtain that $\rho_1 = \rho_2 = \rho_3 = 2$ and the relative degree $\rho = n = 6$. By the twice differentiation to the system output y_i, the control input u_d in the differential equation is expressed in the form of a nonzero factor.

To be specific, the Equation (6) is denoted as

$$\begin{bmatrix} \ddot{y}_1 \\ \ddot{y}_2 \\ \ddot{y}_3 \end{bmatrix} = \begin{bmatrix} F_1(x) \\ F_2(x) \\ F_3(x) \end{bmatrix} + \begin{bmatrix} G_1(x) \\ G_2(x) \\ G_3(x) \end{bmatrix} [u_d + d(t)], \quad (16)$$

where

$$\begin{aligned} F_1(x) &= -\frac{1}{4} q_1 \left(\omega_1^2 + \omega_2^2 + \omega_3^2\right) + \frac{J_1 - J_2}{2J_3} q_2 \omega_1 \omega_2 \\ &\quad + \frac{J_1 - J_3}{2J_2} q_3 \omega_1 \omega_3 + \frac{J_2 - J_3}{2J_1} q_0 \omega_2 \omega_3, \\ F_2(x) &= -\frac{1}{4} q_2 \left(\omega_1^2 + \omega_2^2 + \omega_3^2\right) + \frac{J_2 - J_1}{2J_3} q_1 \omega_1 \omega_2 \\ &\quad + \frac{J_3 - J_1}{2J_2} q_0 \omega_1 \omega_3 + \frac{J_2 - J_3}{2J_1} q_3 \omega_2 \omega_3, \\ F_3(x) &= -\frac{1}{4} q_3 \left(\omega_1^2 + \omega_2^2 + \omega_3^2\right) + \frac{J_1 - J_2}{2J_3} q_0 \omega_1 \omega_2 \\ &\quad + \frac{J_3 - J_1}{2J_2} q_1 \omega_1 \omega_3 + \frac{J_3 - J_2}{2J_1} q_2 \omega_2 \omega_3, \\ G_1(x) &= \left[\frac{q_0}{2J_1}, -\frac{q_3}{2J_2}, \frac{q_2}{2J_3}\right], G_2(x) = \left[\frac{q_3}{2J_1}, \frac{q_0}{2J_2}, -\frac{q_1}{2J_3}\right], G_3(x) \\ &= \left[-\frac{q_2}{2J_1}, \frac{q_1}{2J_2}, \frac{q_0}{2J_3}\right]. \end{aligned} \quad (17)$$

The system (14) can be feedback linearized through differential homeomorphic mapping. Supposing there exists a differential homeomorphic mapping with the form $T(x) = \xi = [h_1(x), L_f h_1(x), h_2(x), L_f h_2(x), h_3(x), L_f h_3(x)]^T$.

Under the afore-mentioned coordinate transform, the system (6) can be transformed into three linear subsystems with the following normal form:

$$\begin{aligned}
\dot{\xi}_{11} &= \xi_{12},\\
\dot{\xi}_{12} &= F_1(x) + G_1(x)[u_d + d(t)],\\
\dot{\xi}_{21} &= \xi_{22},\\
\dot{\xi}_{22} &= F_2(x) + G_2(x)[u_d + d(t)],\\
\dot{\xi}_{31} &= \xi_{32},\\
\dot{\xi}_{32} &= F_3(x) + G_3(x)[u_d + d(t)],\\
y &= [\xi_{11}, \xi_{21}, \xi_{31}]^T,
\end{aligned} \tag{18}$$

with (11), the system (18) can be described as

$$\begin{aligned}
\dot{\xi}_{11} &= \xi_{12},\\
\dot{\xi}_{12} &= F_1(x) + G_{1\sigma}(x)v + \bar{G}_{1\sigma}(x)\bar{u}(t) + G_1(x)d(t),\\
\dot{\xi}_{21} &= \xi_{22},\\
\dot{\xi}_{22} &= F_2(x) + G_{2\sigma}(x)v + \bar{G}_{2\sigma}(x)\bar{u}(t) + G_2(x)d(t),\\
\dot{\xi}_{31} &= \xi_{32},\\
\dot{\xi}_{32} &= F_3(x) + G_{3\sigma}(x)v + \bar{G}_{3\sigma}(x)\bar{u}(t) + G_3(x)d(t),\\
y &= [\xi_{11}, \xi_{21}, \xi_{31}]^T,
\end{aligned} \tag{19}$$

where $G_{i\sigma}(x) = G_i(x)D(I - \sigma(t))\bar{G}_{i\sigma}(x) = G_i(x)D\sigma(t)$, and $i = 1, 2, 3$.

2.3.1. Nonlinear Feedback Control Law. The feedback linearization design can be applied to generate an ideal controller, on the condition that the system parameters and fault parameters of a nonlinear system (6) are accessible. From Equation (16), we can get the following equation:

$$\ddot{y}_i = F_i(x) + G_i(x)[u_d + d(t)], \quad i = 1, 2, 3. \tag{20}$$

Considering the uncertainty of external disturbance $d(t)$, we set the control signal as

$$G_i(x)u_d = W_{di} \triangleq -F_i(x) + u_{Li} - G_i(x)\hat{d}(t), \tag{21}$$

where W_{di} denotes the desired control signal generated from a chosen control that is designed for the closed-loop system, u_{Li} is the control law to be proposed, and $\hat{d}(t)$ is the estimator of $d(t)$. Then, the linearized system can be obtained

$$\ddot{y}_i = u_{Li} + G_i(x)\left[d(t) - \hat{d}(t)\right], \quad i = 1, 2, 3. \tag{22}$$

Lemma 3. (State-feedback H_∞ optimal control). *Consider a linear time-invariant system*

$$\begin{aligned}
\dot{x} &= Ax + B_1u_w + B_2u,\\
z &= C_1x,\\
y &= C_2x,
\end{aligned} \tag{23}$$

where $x \in R^{n_x}$ is the state, $u \in R^{n_u}$ is the control input, $u_w \in R^{n_w}$ is the disturbance, $z \in R^{n_z}$ is the regulated output to be controlled, and $y \in R^{n_y}$ is the measured output. A, B_1, B_2, C_1, and C_2 are matrices of appropriate dimensions and satisfying the assumptions.

Assumption 4. (A, B_1) is stabilizable; (A, C_2) is detectable; B_1 is column full rank, and C_2 is row full rank; $n_w \le n_y \le n_x$.

If there exists an $\varepsilon < 0$ such that the Riccati equation

$$A^TP + PA - \varepsilon^{-1}PB_2R^{-1}B_2^TP + \gamma^{-1}C_1^TC_1 + \varepsilon S = 0, \tag{24}$$

has a solution $P \ge 0$, where $R \in R^{n_u \times n_u}$ and $S \in R^{n_x \times n_x}$ are given positive-definite matrices.

A state feedback controller $u_s = -((1/2\varepsilon)R^{-1}B_2^TP)x$ can be designed to stabilize the system (23), and the transfer function $G_{wz}(s)$ between disturbance w and output z satisfy the following condition

$$\|G_{wz}(s)\|_\infty < \gamma, \tag{25}$$

for a prespecified constant $\gamma > 0$. It should be noted that γ can be arbitrarily close to the H_∞ optimum by choosing a sufficiently small ε.

Lemma 5. *Let $z = H(s)w$, where $H(s)$ have all their roots in* $\mathrm{Re}[s] \ge -\delta/2$, *for any $\delta \ge 0$ and $w \in L^2$, we have*

$$\|z_t\|_2^\delta \le \|H(s)\|_\infty^\delta \|w_t\|_2^\delta, \tag{26}$$

where $\|z_t\|_2^\delta$ is defined as $\|z_t\|_2^\delta = {}^\Delta \left(\int_0^t e^{-\delta(t-\tau)}[z^T(\tau)z(\tau)]d\tau\right)^{1/2}$ for $\forall z \in [0,\infty) \longrightarrow R^n$' and $\delta \ge 0$ and $t \ge 0$. If $H(s)$ is strict, then

$$|z(t)| \le \|H(s)\|_2^\delta \|w_t\|_2^\delta, \tag{27}$$

and if $H(s)$ is a stable n-order transfer function, then

$$\|z_t\|_\infty \le 2n\|H(s)\|_\infty \|w\|_\infty. \tag{28}$$

3. Actuator Failure Compensation Design

In this section, a direct adaptive control scheme is proposed to be combined with a basic control law derived from the modified MRAC design, which is not only adaptive to unknown disturbances but also able to handle uncertain patterns, values, and times of actuator failures. The simplified block diagram is shown in Figure 1.

To achieve the control objective, we will complete four design steps:

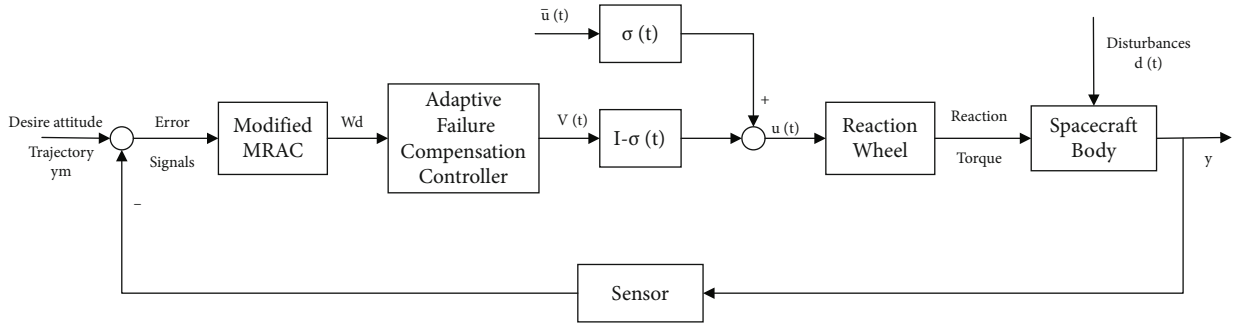

Figure 1: Block diagram of control system.

(1) Derive a desired control signal from modified MRAC technique for the closed-loop system to achieve the desired system performance

(2) Design a composite nominal controller to handle all possible failure patterns simultaneously, with the known parameters of actuator failures

(3) Develop an adaptive control scheme with the estimation of failure parameters updated based on system performance errors, and

(4) Analyze transient and steady-state performance for failure accommodation

In order to obtain an appropriate adaptive law $v(t)$, the error of the control signal equation which is led by the actuator uncertainties is examined. A desired control equation $G_i(x)u_d(t) = W_{di}$ (with $u_d(t) = Du(t)$) is defined to be satisfied by the nominal control signal $v^*(t)$ to be designed in the next section. In the light of (11), we define $u^*(t)$ as $u^*(t) \triangleq (I-\sigma)v^*(t) + \sigma\bar{u}(t)$ and obtain

$$G_i(x)u_d(t) = W_{di} + G_i(x)D(I-\sigma)[v(t) - v^*(t)]. \tag{29}$$

Substituting (21) into (29), we have

$$G_i(x)u_d(t) = -F_i(x) + u_{Li} - G_i(x)\hat{d}(t) + G_i(x)D(I-\sigma)[v(t) - v^*(t)], \tag{30}$$

and the linearized system $\ddot{y}_i = u_{Li}$ can be rewritten into

$$\ddot{y}_i = u_{Li} + G_i(x)D(I-\sigma)[v(t) - v^*(t)] + G_i(x)\left[d(t) - \hat{d}(t)\right]. \tag{31}$$

In this paper, we rewrite the linearized subsystem (31) into the transfer function form as

$$y_i = G_{pi}(s)u_{ri} = k_{pi}\frac{Z_{pi}(s)}{R_{pi}(s)}\left[u_{Li} + G_i(x)(I-\sigma)(v-v^*) + G_i(x)\left(d-\hat{d}\right)\right], \tag{32}$$

with $u_{ri} = u_{Li} + G_i(x)D(I-\sigma)(v-v^*) + G_i(d-\hat{d})$, and its reference model is

$$y_{mi} = W_{mi}(s)r_i = k_{mi}\frac{Z_{mi}(s)}{R_{mi}(s)}r_i, \tag{33}$$

where $Z_{pi}(s)$, $R_{pi}(s)$, $Z_{mi}(s)$, and $R_{mi}(s)$ are monic Hurwitz polynomials of degree m_{pi}, n_{pi}, , and p_{mi}, respectively, $\rho_i = n_{pi} - m_{pi} = p_{mi} - q_{mi} = 2$. The relative degree of $W_{mi}(s)$ is the same as that of $G_{pi}(s)$.

3.1. Modified MRAC Design. A model reference adaptive controller is constructed as follows

$$u_{Li} = \theta_i^T\omega_i + c_{0i}r_i + u_{ci}, \quad c_{0i} = \frac{k_{mi}}{k_{pi}}, \tag{34}$$

where $\omega_i = [\omega_{i1}^T, y_i]^T$, $\theta_i = [\theta_{i1}^T, \theta_{i2}]^T$, $\omega_{i1} = (\alpha_i(s)/\Lambda_i(s))y$, $\alpha_i(s) = [s^{n_{pi}-2}, s^{n_{pi}-3}, \cdots, s, 1]$, $\Lambda_i(s) = Z_{mi}\lambda_i(s)$, and $\lambda_i(s)$ are monic Hurwitz polynomials of degree $n_{pi} - q_{mi} - 1$; $\theta_i \in R^{2n_i-1}$ is the vector of controller parameters; u_{ci} is a proper H_∞ compensator to be designed later.

Remark 6. To derive the relation between the parameter estimation error of actuator failure and transient performance, we just talk about the uncertainties of actuator failure and disturbance assuming the system parameters are known. If all the system parameters are known, the nominal controller of MRAC can be $u_{Li} = \theta_i^{*T}\omega_i + c_{0i}r_i + u_{ci}$, with known $\theta_i^* = [\theta_{i1}^{*T}, \theta_{i2}^*]^T$.

For a given transform function $G_{pi}(s)$, there is a desired reference value vector $\theta_i^* = [\theta_{i1}^{*T}, \theta_{i2}^*]^T$ to make the following matching conditions valid

$$\frac{c_{0i}k_{pi}Z_{pi}}{R_{pi} - k_{pi}Z_{pi}\left(\left(\alpha_i^T(s)\theta_{i1}^*/\Lambda_i(s)\right) + \theta_{i2}^*\right)} = W_{mi}(s). \tag{35}$$

Multiplying both sides with y_i and using the equation

$R_{pi}(s)y_i = k_{pi}Z_{pi}(s)u_{ri}k_{pi}Z_{pi}$, we have

$$c_{oi}k_{pi}Z_{pi}y_i = W_{mi}(s)\left[k_{pi}Z_{pi}u_{ri} - k_{pi}\left(\frac{\theta_{i1}^{*T}\alpha_i(s)}{\Lambda_i(s)}y_i + \theta_{i2}^*\right)Z_{pi}y_i\right]. \tag{36}$$

Dividing both sides by $k_{pi}Z_{pi}$ we have

$$y_i = \frac{W_{mi}(s)}{c_{0i}}\left[u_{ri} - \frac{\theta_{i1}^{*T}\alpha_i(s)}{\Lambda_i(s)}y_i - \theta_{i2}^*y_i\right]. \tag{37}$$

The spacecraft system parameters are known; that is, in the MRAC law, θ_i is substituted by the desired value θ_i^*. To be more specific, the control u_{Li} is designed as

$$u_{Li} = \frac{\theta_{i1}^{*T}\alpha_i(s)}{\Lambda_i(s)}y_i + \theta_{i2}^*y_i + c_{0i}r_i + u_{ci} = -K_i\xi_i + c_{0i}r_i + u_{ci}, \tag{38}$$

where $K_i = [K_{i1}, K_{i2}]$ are the design controller parameters corresponding with θ_i^*, $\xi_i = [\xi_{i1}, \xi_{i2}]^T$. Substituting (38) into (30), we have

$$G_i(x)u_d(t) = -F_i(x) - G_i(x)\widehat{d}(t) + G_i(x)D(I-\sigma)[v(t) - v^*(t)] - K_i\xi_i + c_{0i}r_i + u_{ci}. \tag{39}$$

Furthermore, the linearized subsystem (18) is described as

$$\begin{aligned}\dot{\xi}_{i1} &= \xi_{i2},\\ \dot{\xi}_{i2} &= -K_i\xi_i + c_{0i}r_i + u_{ci} + G_i(x)D(I-\sigma)[v(t) - v^*(t)]\\ &\quad + G_i(x)\left[d(t) - \widehat{d}(t)\right].\end{aligned} \tag{40}$$

We then revise the above equation in the form of state space as follows:

$$\begin{aligned}\dot{\xi}_i &= (A_{ci} - B_{ci}K_i)\xi_i + B_{ci}[G_i(x)D(I-\sigma)(v - v^*)\\ &\quad + G_i(x)\left(d - \widehat{d}\right) + u_{ci} + c_{0i}r_i],\\ y_i &= C_{ci}\xi_i,\end{aligned} \tag{41}$$

where $A_{ci} \in R^{2\times 2}$, $B_{ci} \in R^{2\times 1}$, and $C_{ci} \in R^{1\times 2}$ are the standard form of integrator chains. We also revise the reference model (33) in the state space as follows:

$$\begin{aligned}\dot{\xi}_{mi} &= A_{mi}\xi_{mi} + B_{mi}r_i,\\ y_{mi} &= C_{mi}\xi_{mi},\end{aligned} \tag{42}$$

where A_{mi}, B_{mi}, and C_{mi} are the minimal realization of $W_{mi}(s)$, i.e.,

$$\begin{aligned}A_{mi} &= \begin{bmatrix}0 & 1\\ -a_{i1} & -a_{i2}\end{bmatrix} \in R^{2\times 2},\\ B_{mi} &= [0, 1]^T \in R^{2\times 1},\end{aligned} \tag{43}$$

and $C_{mi} = [1, 0] \in R^{1\times 2}$. Denoting $e_i = \xi_i - \xi_{mi}$, we can obtain

$$\begin{aligned}\dot{e}_i &= (A_{ci} - B_{ci}K_i)\xi_i + B_{ci}[G_i(x)D(I-\sigma)(v - v^*)\\ &\quad + G_i(x)\left(d - \widehat{d}\right) + u_{ci} + c_{0i}r_i] - A_{mi}\xi_{mi} - B_{mi}r_i.\end{aligned} \tag{44}$$

If the controller parameters K_i is set to satisfy $A_{ci} - B_{ci}K_i = A_{mi}$ and $B_{ci}c_{0i} = B_{mi}$, then

$$\begin{aligned}\dot{e}_i &= A_{mi}e_i + \frac{B_{mi}}{c_{0i}}\left[G_i(x)D(I-\sigma)(v - v^*) + G_i(x)\left(d - \widehat{d}\right) + u_{ci}\right],\\ e_{i1} &= C_{mi}e_i.\end{aligned} \tag{45}$$

With the system model (32), (33) and the controller (34), we obtain

$$y_i = \frac{W_{mi}(s)}{c_{0i}}\left[G_i(x)D(I-\sigma)(v - v^*) + G_i(x)\left(d - \widehat{d}\right) + c_{0i}r_i + u_{ci}\right]. \tag{46}$$

Remark 7. For the tracking error dynamics (45) and output dynamic (46), one may discover that the parameter estimation error items $d - \widehat{d}$ and the controller parameter errors $v - v^*$ can be regarded as the disturbance input and plays an important role in system tracking performance. Hence, the attenuation of the disturbance made by $G_i(x)D(I-\sigma)(v - v^*) + G_i(x)(d - \widehat{d})$ on the closed-loop system is designed by proposing the compensator u_{ci} as an H_∞ optimal controller.

Equation (45) is considered as a special form of (23). With (45) and Lemma 3, a transient performance compensator u_{ci} is designed for the system (45) by the following steps as shown next.

Step 1: initialize $\varepsilon_i > 0$ and $0 < \gamma_i < \|W_{mi}(s)/c_{0i}\|_\infty$, choose two positive-definite matrices $S_{ci} \in \mathfrak{R}^{2\times 2}$ and $R_{ci} \in \mathfrak{R}^{1\times 1}$, and solve the following Riccati equation

$$y_i = \frac{W_{mi}(s)}{c_{0i}}\left[G_i(x)D(I-\sigma)(v - v^*) + G_i(x)\left(d - \widehat{d}\right) + c_{0i}r_i + u_{ci}\right]. \tag{47}$$

and obtain the state feedback gain

$$y_i = \frac{W_{mi}(s)}{c_{0i}}\left[G_i(x)D(I-\sigma)(v - v^*) + G_i(x)\left(d - \widehat{d}\right) + c_{0i}r_i + u_{ci}\right]. \tag{48}$$

If there is no solution, decrease ε_i and repeat this step

again until getting an appropriate positive-definite solution $P_{ci} = P_{ci}^T > 0$ to ensure that the state feedback gain is obtained. The H_∞ compensator which is based on measurement feedback

$$u_{ci} = K_{ci} e_i, \tag{49}$$

is constructed by state feedback gain K_{ci}, which guarantees that the system (45) with $G_i(x)D(I-\sigma)(v-v^*) + G_i(x)(d - \widehat{d})$ disturbance attenuation γ_i is stable.

Step 2: Return to step 1 and reduce the transient performance index until getting a gratifying transient or the optimum γ_i

Remark 8. The standard algorithm can be used to confirm whether the positive-definite solution of a Riccati equation exists. According to the above processes, the optimal compensator of H_∞ can be obtained by selecting sufficiently small ε_i. However, it may cause the gain K_{ci} too large. For the whole control system, the large gain will reduce the stability margin and increase the influence of measurement noise. In practical application, a compromise is usually adopted in the H_∞ compensator design. It turns out that the suboptimum H_∞ compensator for a given $0 < \gamma_i < \|W_{mi}(s)/c_{0i}\|_\infty$ can also achieve a satisfactory transient performance through the following theoretical analysis and simulation.

3.2. Nominal Compensation Design. As mentioned previously, the spacecraft system is turned into three-linear subsystem (18) derived from the feedback linearization technique. To derive the failure compensation control law $u(t)$, we write the three subsystems together as

$$[\ddot{y}_1, \ddot{y}_2, \ddot{y}_3]^T = F(x) + G_D(x)[(I-\sigma)v + \sigma\bar{u}] + G(x)d(t), \tag{50}$$

where $G_D(x) = G(x)D \in R^{3\times 4}$ is regarded as control distribution matrix.

3.2.1. Design for no Failure Case. On this condition, $\sigma(t) = \sigma_{(1)} = \text{diag}\{0,0,0,0\}$, $u(t) = v(t)$, and $G_D(x)v(t) = W_d(t)$. The signal $v(t)$ is designed as

$$v(t) = v_{(1)}^*(t) = h_{21}(x)v_{0(1)}^*(t) \tag{51}$$

for a chosen $h_{21}(x) \in R^{4\times 4}$, and signal $v_{0(1)}^*(t)$ to be calculated from

$$G_D(x)h_{21}(x)v_{0(1)}^*(t) = W_d(t). \tag{52}$$

The solution $v_{0(1)}^*(t)$ may be derived as

$$v_{0(1)}^*(t) = K_{21}(x)W_d(t), \tag{53}$$

with matrix function $K_{21}(x) \in R^{4\times 3}$.

3.2.2. Design for the u_1 Failure Case. In this situation, $\sigma(t) = \sigma_{(2)} = \text{diag}\{1,0,0,0\}$, $u_1 = \bar{u}_1$, and $u_i = v_i$ for $i = 2,3,4$, with $G_D(x) = [G_{D1}, G_{D2}, G_{D3}, G_{D4}] = [G_{D1}, G_{D(2)}] \in R^{3\times 4}$ for $G_{D(2)} = [G_{D2}, G_{D3}, G_{D4}] \in R^{3\times 3}$, $v = [v_1, v_2, v_3, v_4]^T = [v_1, v_{a(2)}^T]^T \in R^4$ for $v_{a(2)} = [v_2, v_3, v_4]^T \in R^3$, equation $G_D(x)u(t) = W_d(t)$ becomes

$$G_{D1}\bar{u}_1(t) + G_{D(2)}v_{a(2)}(t) = W_d(t). \tag{54}$$

In this situation, the signal v_1 is set to be $v_1 = 0$. A nonsingular matrix function $h_{22}(x) \in R^{3\times 3}$ is chosen to set

$$\begin{aligned} v(t) &= \left[v_1(t), v_{a(2)}^T(t)\right]^T = v_{(2)}^*(t) = \left[0, v_{a(2)}^{*T}(t)\right]^T, \\ v_{a(2)}^*(t) &= h_{22}(x)v_{0(2)}^*(t), \end{aligned} \tag{55}$$

with $v_{0(2)}^*(t) \in R^3$ to be deduced from

$$G_{D1}\bar{u}_1(t) + G_{D(2)}h_{22}(x)v_{0(2)}^*(t) = W_d(t). \tag{56}$$

We can obtain

$$v_{0(2)}^*(t) = K_{22}(x)W_d(t) + K_{221}(x)\bar{u}_1(t), \tag{57}$$

with matrix function $K_{22}(x) \in R^{3\times 3}$ and vector $K_{221}(x) \in R^{3\times 1}$.

3.2.3. Design for the u_4 Failure Case. Similarly, $\sigma(t) = \sigma_{(3)} = \text{diag}\{0,0,0,1\}$, $u_4 = \bar{u}_4$, and $v_4(t)$ are chosen as $v_4(t) = 0$ and $v_i(t) = u_i(t)$ for $i = 1,2,3$. With $G_D(x) = [G_{D1}, G_{D2}, G_{D3}, G_{D4}] = [G_{D(1)}, G_{D4}] \in R^{3\times 4}$ for $G_{D(1)} = [G_{D1}, G_{D2}, G_{D3}] \in R^{3\times 3}$ and $v(t) = [v_{a(3)}^T(t), v_4(t)]^T$ for $v_{a(3)}(t) = [v_1(t), v_2(t), v_3(t)]^T \in R^3$, and $G_D(x)u(t) = W_d(t)$ becomes

$$G_{D(1)}v_{a(3)}(t) + G_{D4}\bar{u}_4(t) = W_d(t). \tag{58}$$

The signal $v(t)$ is proposed as

$$\begin{aligned} v(t) &= \left[v_{a(3)}^T(t), v_4(t)\right]^T = v_{(3)}^*(t) = \left[v_{a(3)}^{*T}(t), 0\right]^T, \\ v_{a(3)}^*(t) &= h_{23}v_{0(3)}^*(t), \end{aligned} \tag{59}$$

with a chosen matrix $h_{23} \in R^{3\times 3}$ and a deduced signal $v_{0(3)}^*(t) \in R^3$ from

$$G_{D(1)}h_{23}v_{0(3)}^*(t) + G_{D4}\bar{u}_4(t) = W_d(t). \tag{60}$$

Similarly, we have

$$v_{0(3)}^*(t) = K_{23}W_d(t) + K_{234}\bar{u}_4(t), \tag{61}$$

with matrix function $K_{23} \in R^{3\times 3}$ and vector $K_{234} \in R^{3\times 1}$.

3.2.4. Composite Control Law. Define three indicator functions χ_j^*, $j = 1,2,3$, which are corresponding to the considered three failure models $\sigma_{(j)}$ and $j = 1,2,3$, respectively.

That is, if $\sigma = \sigma_{(j)}$ and $\chi_j^* = 1$; otherwise, $\chi_j^* = 0$ and $j = 1, 2, 3$. Then, a synthetic control law is obtained by integrating the three individual controllers

$$v^*(t) = \sum_{j=1}^{3} \chi_j^*(t) v_{(j)}^*(t), \tag{62}$$

to handle the three failure cases.

For $v_{a(2)}^*(t) = h_{22} v_{0(2)}^*(t)$, with $v_{0(2)}^*(t)$ in (57), signal $v_{a(2)}^*(t)$ can be further expressed as

$$v_{a(2)}^*(t) = h_{22} K_{22} W_d(t) + h_{22} K_{221} \bar{u}_1(t) \in R^3. \tag{63}$$

For $\bar{u}_1(t)$ in (10), we express

$$\bar{u}_1(t) = \theta_1^{*T} \varpi_1(t) = \varpi_1^T(t) \theta_1^*, \tag{64}$$

where $\theta_1^* = [\bar{u}_{10}, \bar{u}_{11}, \cdots, \bar{u}_{1q_1}]^T \in R^{q_1+1}$, and $\varpi_1(t) = [1, f_{11}(t), \cdots, f_{1q_1}(t)]^T \in R^{q_1+1}$.

Therefore, we have

$$\begin{aligned} \chi_2^*(t) v_{a(2)}^*(t) = {} & \{\chi_{21}^*(t), \chi_{22}^*(t), \chi_{23}^*(t)\} h_{22} K_{22} W_d(t) \\ & + \left[\theta_{1(1)}^{*T}(t) \varpi_1(t) \phi_{2,1}, \theta_{1(2)}^{*T}(t) \varpi_1(t) \phi_{22}, \theta_{1(3)}^{*T}(t) \varpi_1(t) \phi_{23}\right]^T, \end{aligned} \tag{65}$$

where $\chi_{2i}^*(t) = \chi_2^*(t)$, $\theta_{1(i)}^*(t) = \chi_2^*(t) \theta_1^*$, $i = 1, 2, 3$, and $\phi_2 = h_{22} K_{221} = [\phi_{21}, \phi_{22}, \phi_{23}]^T$.

In the same way, to designate $v_{\chi_1(1)}^*(t)$ and $v_{\chi_3(3)}^*(t)$, we express

$$\chi_1^*(t) v_{(1)}^*(t) = \text{diag}\{\chi_{11}^*(t), \chi_{12}^*(t), \chi_{13}^*(t), \chi_{14}^*(t)\} h_{21} K_{21} W_d(t) \tag{66}$$

$$\begin{aligned} \chi_3^*(t) v_{a(3)}^*(t) = {} & \text{diag}\{\chi_{31}^*(t), \chi_{32}^*(t), \chi_{33}^*(t)\} h_{23} K_{23} W_d(t) \\ & + \left[\theta_{4(1)}^{*T}(t) \varpi_4(t) \phi_{31}, \theta_{4(2)}^{*T}(t) \varpi_4(t) \phi_{32}, \theta_{4(3)}^{*T}(t) \varpi_4(t) \phi_{33}\right]^T, \end{aligned} \tag{67}$$

where $\chi_{1i}^*(t) = \chi_1^*(t)$, $i = 1, 2, 3, 4$, $\chi_{3i}^*(t) = \chi_3^*(t)$, and $\theta_{4(i)}^*(t) = \chi_3^*(t) \theta_4^*$, $i = 1, 2, 3$.

3.3. Adaptive Fault Tolerant Control Design. The adaptive version of the nominal control law is as follows (62):

$$\begin{aligned} v(t) = \sum_{j=1}^{3} \chi_j(t) v_{(j)}(t) = \sum_{j=1}^{3} v_{\chi_j(j)}(t) = {} & v_{\chi_1(1)}(t) \\ & + \left[0, v_{\chi_2 a(2)}^T(t)\right]^T + \left[v_{\chi_3 a(3)}^T(t), 0\right]^T. \end{aligned} \tag{68}$$

In view of (65)–(67), we derive

$$v_{\chi_1(1)}(t) \triangleq \text{diag}\{\chi_{11}(t), \chi_{12}(t), \chi_{13}(t), \chi_{14}(t)\} h_{21} K_{21} W_d(t), \tag{69}$$

$$\begin{aligned} v_{\chi_2 a(2)}(t) \triangleq {} & \text{diag}\{\chi_{21}(t), \chi_{22}(t), \chi_{23}(t)\} h_{22} K_{22} W_d(t) \\ & + \left[\theta_{1(1)}^T(t) \varpi_1(t) \phi_{21}, \theta_{1(2)}^T(t) \varpi_1(t) \phi_{22}, \theta_{1(3)}^T(t) \varpi_1(t) \phi_{23}\right]^T, \end{aligned} \tag{70}$$

$$\begin{aligned} v_{\chi_3 a(3)}(t) \triangleq {} & \text{diag}\{\chi_{31}(t), \chi_{32}(t), \chi_{33}(t)\} h_{23} K_{23} W_d(t) \\ & + \left[\theta_{4(1)}^T(t) \varpi_4(t) \phi_{31}, \theta_{4(2)}^T(t) \varpi_4(t) \phi_{32}, \theta_{4(3)}^T(t) \varpi_4(t) \phi_{33}\right]^T, \end{aligned} \tag{71}$$

where $\chi_{ji}(t)$, $\theta_{1(i)}(t)$, and $\theta_{4(i)}(t)$ are the estimates of $\chi_{ji}^*(t)$, $\theta_{1(i)}^*(t)$, and $\theta_{4(i)}^*(t)$, respectively.

From (65)–(71), we obtain

$$v(t) - v^*(t) = \tilde{v}_{\chi_1(1)}(t) + \left[0, \tilde{v}_{\chi_2 a(2)}^T(t)\right]^T + \left[\tilde{v}_{\chi_3 a(3)}^T(t), 0\right]^T, \tag{72}$$

where

$$\begin{aligned} \tilde{v}_{\chi_1(1)}(t) = {} & \{\tilde{\chi}_{11}(t), \tilde{\chi}_{12}(t), \tilde{\chi}_{13}(t), \tilde{\chi}_{14}(t)\} h_{21} K_{21} W_d(t), \\ \tilde{v}_{\chi_2 a(2)}(t) = {} & \text{diag}\{\tilde{\chi}_{21}(t), \tilde{\chi}_{22}(t), \tilde{\chi}_{23}(t)\} h_{22} K_{22} W_d(t) \\ & + \left[\tilde{\theta}_{1(1)}^T(t) \varpi_1(t) \phi_{21}, \tilde{\theta}_{1(2)}^T(t) \varpi_1(t) \phi_{22}, \tilde{\theta}_{1(3)}^T(t) \varpi_1(t) \phi_{23}\right]^T, \tilde{v}_{\chi_3 a(3)}(t) \triangleq \text{diag}\{\tilde{\chi}_{31}(t), \tilde{\chi}_{32}(t), \tilde{\chi}_{33}(t)\} h_{23} K_{23} W_d(t) \\ & + \left[\tilde{\theta}_{4(1)}^T(t) \varpi_4(t) \phi_{31}, \tilde{\theta}_{4(2)}^T(t) \varpi_4(t) \phi_{32}, \tilde{\theta}_{4(3)}^T(t) \varpi_4(t) \phi_{33}\right]^T. \end{aligned} \tag{73}$$

3.3.1. State Error Equations. Introducing $e \in R^6 = [e_1^T, e_2^T, e_3^T]^T = [e_{11}, e_{12}, e_{21}, e_{22}, e_{31}, e_{32}]^T$, $e_{i1} = y_i - y_{mi} = \xi_{i1} - \xi_{mi1}$, $e_{i2} = \dot{\xi}_{i1} - \dot{\xi}_{mi1} = \dot{e}_{i1}$, and $i = 1, 2, 3$. With the three subsystems

$$\begin{aligned}\dot{e}_i = A_{mi}e_i + \frac{B_{mi}}{c_{0i}}&[G_i(x)D(I-\sigma)(v-v^*) \\ &- (1/2\varepsilon_i)R_{ci}^{-1}B_{ci}^T P_{ci}e_i + G_i(x)\left(d-\widehat{d}\right)\Big], \quad i = 1, 2, 3,\end{aligned} \tag{74}$$

we have

$$\begin{aligned}\begin{bmatrix}\ddot{e}_{11} + \alpha_{12}\dot{e}_{11} + \alpha_{11}e_{11} \\ \ddot{e}_{21} + \alpha_{22}\dot{e}_{21} + \alpha_{21}e_{21} \\ \ddot{e}_{31} + \alpha_{32}\dot{e}_{31} + \alpha_{31}e_{31}\end{bmatrix} &= \frac{1}{c_0}\left[G(x)D(I-\sigma)(v-v^*) + G(x)\left(d-\widehat{d}\right)\right] \\ &- \begin{bmatrix}(1/2\varepsilon_1 c_0)R_{c1}^{-1}B_{c1}^T P_{c1}e_1 \\ (1/2\varepsilon_2 c_0)R_{c2}^{-1}B_{c2}^T P_{c2}e_2 \\ (1/2\varepsilon_3 c_0)R_{c3}^{-1}B_{c3}^T P_{c3}e_3\end{bmatrix}.\end{aligned} \tag{75}$$

If $\sigma = \sigma_{(1)} = \text{diag}\{0, 0, 0, 0\}$, with (72) and (73), we rewrite (75) as

$$\begin{aligned}\begin{bmatrix}\ddot{e}_{11} + \alpha_{12}\dot{e}_{11} + \alpha_{11}e_{11} \\ \ddot{e}_{21} + \alpha_{22}\dot{e}_{21} + \alpha_{21}e_{21} \\ \ddot{e}_{31} + \alpha_{32}\dot{e}_{31} + \alpha_{31}e_{31}\end{bmatrix} &= \frac{1}{c_0}\left[\sum_{i=1}^{4} G_{Di}\tilde{\chi}_{1i}\nu_{1i} + \sum_{i=1}^{3} G_{D(i+1)}\tilde{\chi}_{2i}\nu_{2i}\right. \\ &\left. + \sum_{i=1}^{3} G_{Di}\tilde{\chi}_{3i}\nu_{3i} + \sum_{i=1}^{3} G_{D(i+1)}\widetilde{\theta}_{1(i)}^T\varpi_1\phi_{2i} + \sum_{i=1}^{3} G_{Di}\widetilde{\theta}_{4(i)}^T\varpi_4\phi_{3i}\right] \\ &+ \frac{1}{c_0}\begin{bmatrix}\sum_{j=1}^{3} G_{1j}\widetilde{\theta}_{dj}^T(t)\varpi_{dj} \\ \sum_{j=1}^{3} G_{2j}\widetilde{\theta}_{dj}^T(t)\varpi_{dj} \\ \sum_{j=1}^{3} G_{3j}\widetilde{\theta}_{dj}^T(t)\varpi_{dj}\end{bmatrix} - \begin{bmatrix}\left(\frac{1}{2\varepsilon_1 c_0}\right)R_{c1}^{-1}B_{c1}^T P_{c1}e_1 \\ \left(\frac{1}{2\varepsilon_2 c_0}\right)R_{c2}^{-1}B_{c2}^T P_{c2}e_2 \\ \left(\frac{1}{2\varepsilon_3 c_0}\right)R_{c3}^{-1}B_{c3}^T P_{c3}e_3\end{bmatrix} \triangleq \tilde{E}_1.\end{aligned} \tag{76}$$

If $\sigma = \sigma_{(2)} = \text{diag}\{1, 0, 0, 0\}$, with (72) and (73), we rewrite (75) as

$$\begin{aligned}\begin{bmatrix}\ddot{e}_{11} + \alpha_{12}\dot{e}_{11} + \alpha_{11}e_{11} \\ \ddot{e}_{21} + \alpha_{22}\dot{e}_{21} + \alpha_{21}e_{21} \\ \ddot{e}_{31} + \alpha_{32}\dot{e}_{31} + \alpha_{31}e_{31}\end{bmatrix} &= \frac{1}{c_0}\left[\sum_{i=2}^{4} G_{Di}\tilde{\chi}_{1i}\nu_{1i} + \sum_{i=1}^{3} G_{D(i+1)}\tilde{\chi}_{2i}\nu_{2i}\right. \\ &\left. + \sum_{i=2}^{3} G_{Di}\tilde{\chi}_{3i}\nu_{3i} + \sum_{i=1}^{3} G_{D(i+1)}\widetilde{\theta}_{1(i)}^T\varpi_1\phi_{2i} + \sum_{i=2}^{3} G_{Di}\widetilde{\theta}_{4(i)}^T\varpi_4\phi_{3i}\right] \\ &+ \frac{1}{c_0}\begin{bmatrix}\sum_{j=1}^{3} G_{1j}\widetilde{\theta}_{dj}^T(t)\varpi_{dj} \\ \sum_{j=1}^{3} G_{2j}\widetilde{\theta}_{dj}^T(t)\varpi_{dj} \\ \sum_{j=1}^{3} G_{3j}\widetilde{\theta}_{dj}^T(t)\varpi_{dj}\end{bmatrix} - \begin{bmatrix}\left(\frac{1}{2\varepsilon_1 c_0}\right)R_{c1}^{-1}B_{c1}^T P_{c1}e_1 \\ \left(\frac{1}{2\varepsilon_2 c_0}\right)R_{c2}^{-1}B_{c2}^T P_{c2}e_2 \\ \left(\frac{1}{2\varepsilon_3 c_0}\right)R_{c3}^{-1}B_{c3}^T P_{c3}e_3\end{bmatrix} \triangleq \tilde{E}_2\end{aligned} \tag{77}$$

If $\sigma = \sigma_{(3)} = \text{diag}\{0, 0, 0, 1\}$, with (72) and (73), we rewrite (75) as

$$\begin{aligned}\begin{bmatrix}\ddot{e}_{11} + \alpha_{12}\dot{e}_{11} + \alpha_{11}e_{11} \\ \ddot{e}_{21} + \alpha_{22}\dot{e}_{21} + \alpha_{21}e_{21} \\ \ddot{e}_{31} + \alpha_{32}\dot{e}_{31} + \alpha_{31}e_{31}\end{bmatrix} &= \frac{1}{c_0}\left[\sum_{i=1}^{3} G_{Di}\tilde{\chi}_{1i}\nu_{1i} + \sum_{i=1}^{2} G_{D(i+1)}\tilde{\chi}_{2i}\nu_{2i}\right. \\ &\left. + \sum_{i=1}^{3} G_{Di}\tilde{\chi}_{3i}\nu_{3i} + \sum_{i=1}^{2} G_{D(i+1)}\widetilde{\theta}_{1(i)}^T\varpi_1\phi_{2i} + \sum_{i=1}^{3} G_{Di}\widetilde{\theta}_{4(i)}^T\varpi_4\phi_{3i}\right] \\ &+ \frac{1}{c_0}\begin{bmatrix}\sum_{j=1}^{3} G_{1j}\widetilde{\theta}_{dj}^T(t)\varpi_{dj} \\ \sum_{j=1}^{3} G_{2j}\widetilde{\theta}_{dj}^T(t)\varpi_{dj} \\ \sum_{j=1}^{3} G_{3j}\widetilde{\theta}_{dj}^T(t)\varpi_{dj}\end{bmatrix} - \begin{bmatrix}\left(\frac{1}{2\varepsilon_1 c_0}\right)R_{c1}^{-1}B_{c1}^T P_{c1}e_1 \\ \left(\frac{1}{2\varepsilon_2 c_0}\right)R_{c2}^{-1}B_{c2}^T P_{c2}e_2 \\ \left(\frac{1}{2\varepsilon_3 c_0}\right)R_{c3}^{-1}B_{c3}^T P_{c3}e_3\end{bmatrix} \triangleq \tilde{E}_3\end{aligned} \tag{78}$$

where $G_D = [G_{D1}, G_{D2}, G_{D3}, G_{D4}]$, $\nu_1 = h_{21}K_{21}W_d = [\nu_{11}, \nu_{12}, \nu_{13}, \nu_{14}]^T$, $\nu_2 = h_{22}K_{22}W_d = [\nu_{21}, \nu_{22}, \nu_{23}]^T$, and $\nu_3 = h_{23}K_{23}W_d = [\nu_{31}, \nu_{32}, \nu_{33}]^T$, $\widetilde{\theta}_{dj} = \theta_{dj} - \widehat{\theta}_{dj}$.

From Equations (76)–(78), we can obtain the state error equation

$$\dot{e} = A_m e + B_m\tilde{E}_k = A_m e + B_{m\tilde{E}_k}, \tag{79}$$

where $A_m = \text{diag}\{A_{m1}, A_{m2}, A_{m3}\} \in R^{6\times 6}$ and E_{kj} is the j th component of $\tilde{E}_k$, $k = 1, 2, 3$, $B_{m\tilde{E}_k} =$

$[B_{m1}^T\tilde{E}_{k1}, B_{m2}^T\tilde{E}_{k2}, B_{m3}^T\tilde{E}_{k3}]^T \in R^6$, and $B_m = \text{diag}\{B_{m1}, B_{m2}, B_{m3}\} \in R^{6\times 3}$.

3.3.2. Adaptive Laws. According to the state error Equation (79), adaptive laws are chosen for the parameter $\widehat{\theta}_{di}$ and the parameters $\chi_{1i}(t)$, $\chi_{2i}(t)$, $\chi_{3i}(t)$, $\theta_{1(i)}(t)$, and $\theta_{2(i)}(t)$ of the failure compensator as

$$\dot{\widehat{\theta}}_{di} = \frac{1}{c_0}\sum_{j=1}^{3}\Gamma_{di}\varpi_{di}e_{Pj}G_{ji}, \tag{80}$$

$$\dot{\chi}_{1i}(t) = \begin{cases} -\dfrac{\gamma_{1i}}{c_0}\displaystyle\sum_{j=1}^{3}e_{Pj}G_{Di}\nu_{1i}\, i = 2, 3, \\ -\dfrac{\gamma_{1i}}{c_0}\displaystyle\sum_{j=1}^{3}e_{Pj}G_{Di}\nu_{1i} + f_{\chi_{1i}}\, i = 1, 4, \end{cases} \tag{81}$$

$$\dot{\chi}_{2i}(t) = \begin{cases} -\dfrac{\gamma_{2i}}{c_0}\displaystyle\sum_{j=1}^{3}e_{Pj}G_{D(i+1)}\nu_{2i} i = 1, 2\,, \\ \dfrac{\gamma_{2i}}{c_0}\displaystyle\sum_{j=1}^{3}e_{Pj}G_{D(i+1)}\nu_{2i} + f_{\chi_{2i}}\, i = 3\,, \end{cases} \tag{82}$$

$$\dot{\chi}_{3i}(t) = \begin{cases} -\dfrac{\gamma_{3i}}{c_0}\displaystyle\sum_{j=1}^{3}e_{Pj}G_{Di}\nu_{3i} i = 2, 3, \\ -\dfrac{\gamma_{3i}}{c_0}\displaystyle\sum_{j=1}^{3}e_{Pj}G_{Di}\nu_{3i} + f_{\chi_{3i}}\, i = 1, \end{cases} \tag{83}$$

$$\dot{\theta}_{1(t)}(t) = \begin{cases} -\dfrac{1}{c_0}\displaystyle\sum_{j=1}^{3}\Gamma_{1i}e_{Pj}G_{D(i+1)}\varpi_1\phi_{2i} i = 1, 2, \\ -\dfrac{1}{c_0}\displaystyle\sum_{j=1}^{3}\Gamma_{1i}e_{Pj}G_{D(i+1)}\varpi_1\phi_{2i} + f_{\theta_{1(i)}}\, i = 3, \end{cases} \tag{84}$$

$$\dot{\theta}_{4(t)}(t) = \begin{cases} -\dfrac{1}{c_0}\displaystyle\sum_{j=1}^{3}\Gamma_{4i}e_{Pj}G_{Di}\varpi_1\phi_{2i} i = 2, 3, \\ -\dfrac{1}{c_0}\displaystyle\sum_{j=1}^{3}\Gamma_{4i}e_{Pj}G_{Di}\varpi_1\phi_{2i} + f_{\theta_{4(i)}} i = 1, \end{cases} \tag{85}$$

where $\Gamma_{di} = \Gamma_{di}^T > 0$, $\Gamma_{1i} = \Gamma_{1i}^T > 0$, $\Gamma_{4i} = \Gamma_{4i}^T > 0$, $\gamma_{1i} > 0$, $\gamma_{2i} > 0$, and $\gamma_{3i} > 0$ are the adaptive gains, and $f_{\chi_{1i}}$ is the projection algorithm. Consequently, based on adaptive laws $\dot{\chi}_{11} = -(\gamma_{11}/c_0)\sum_{j=1}^{3}e_{Pj}G_{D1}\nu_{11} + f_{\chi_{11}}$, we can derive that $0 \le \chi_{11} \le 1$ and $(\chi_{11} - \chi_{11}^*)f_{\chi_{11}} \le 0$. $f_{\chi_{2i}}$, $f_{\chi_{3i}}$, $f_{\theta_{1(i)}}$, and $f_{\theta_{4(i)}}$ have the same characteristics with $f_{\chi_{1i}}$.

3.3.3. Stability Performance Analysis

(i) For period $t \in [T_0, \infty)$, $\sigma = \sigma_{(1)}$. Lyapunov function is defined as

$$V_0 = \frac{1}{2}e^TPe + \frac{1}{2}\sum_{i=1}^{3}\widetilde{\theta}_{di}^T\Gamma_{di}^{-1}\widetilde{\theta}_{di} + \frac{1}{2}\left[\sum_{i=1}^{4}\tilde{\chi}_{1i}^2\gamma_{1i}^{-1} + \sum_{i=1}^{3}\tilde{\chi}_{2i}^2\gamma_{2i}^{-1} + \sum_{i=1}^{3}\tilde{\chi}_{3i}^2\gamma_{3i}^{-1} + \sum_{i=1}^{3}\widetilde{\theta}_{1(i)}^T\Gamma_{1i}^{-1}\widetilde{\theta}_{1(i)} + \sum_{i=1}^{3}\widetilde{\theta}_{4(i)}^T\Gamma_{4i}^{-1}\widetilde{\theta}_{4(i)}\right]. \tag{86}$$

By differentiating V_0 in the interval $[T_0, \infty)$, we can obtain

$$\dot{V}_0 = \frac{1}{2}e^TA_m^TPe + \frac{1}{2}e^TPA_me + \frac{1}{c_0}\left[\sum_{j=1}^{3}\sum_{i=1}^{4}e_{Pj}G_{Di}\tilde{\chi}_{1i}\nu_{1i} + \sum_{j=1}^{3}\sum_{i=1}^{2}e_{Pj}G_{D(i+1)}\tilde{\chi}_{2i}\nu_{2i} + \sum_{i=1}^{4}\gamma_{1i}^{-1}\tilde{\chi}_{1i}\dot{\tilde{\chi}}_{1i} + \sum_{i=1}^{3}\gamma_{2i}^{-1}\tilde{\chi}_{2i}\dot{\tilde{\chi}}_{2i} + \sum_{i=1}^{3}\gamma_{3i}^{-1}\tilde{\chi}_{3i}\dot{\tilde{\chi}}_{3i} + \sum_{i=1}^{3}\widetilde{\theta}_{1(i)}^T\Gamma_{1i}^{-1}\dot{\widetilde{\theta}}_{1(i)} + \sum_{i=1}^{3}\widetilde{\theta}_{4(i)}^T\Gamma_{4i}^{-1}\dot{\widetilde{\theta}}_{4(i)}, \tag{87}$$

where $e_P = [e_{P1}, e_{P2}, e_{P3}] \in R^{1\times 3}$ and e_{Pi} are the $(i+1)$-th column components of $e^TP \in R^{1\times 6}$, $i = 1, 2, 3$, and $P = \text{diag}\{P_{c1}, P_{c2}, P_{c3}\}$.

Substituting Equations (80)–(85) into (87), one would have

$$\dot{V}_0 = \frac{1}{2}\sum_{i=1}^{3}e_i^T\left(A_{mi}^TP_{ci} + P_{ci}A_{mi} - \frac{1}{\varepsilon_i}P_{ci}B_{mi}R_{ci}^{-1}B_{mi}^TP_{ci}\right)e_i, \quad t \in [T_0, T_1). \tag{88}$$

Based on of Lemma 3, we can obtain

$$\dot{V}_0 = -\frac{1}{2}\sum_{i=1}^{3}e_i^T\left(\gamma_i^{-1}C_{mi}^TC_{mi} + \varepsilon_iS_i\right)e_i \le 0. \tag{89}$$

(ii) If actuator u_1 fails over the period (T_1, ∞), i.e., $\sigma = \sigma_{(2)}$, we define

$$V_1 = \frac{1}{2}e^TPe + \frac{1}{2}\sum_{i=1}^{3}\widetilde{\theta}_{di}^T\Gamma_{di}^{-1}\widetilde{\theta}_{di} + \frac{1}{2}\left[\sum_{i=2}^{4}\tilde{\chi}_{1i}^2\gamma_{1i}^{-1} + \sum_{i=1}^{3}\tilde{\chi}_{2i}^2\gamma_{2i}^{-1} + \sum_{i=2}^{3}\tilde{\chi}_{3i}^2\gamma_{3i}^{-1} + \sum_{i=1}^{3}\widetilde{\theta}_{1(i)}^T\Gamma_{1i}^{-1}\widetilde{\theta}_{1(i)} + \sum_{i=2}^{3}\widetilde{\theta}_{4(i)}^T\Gamma_{4i}^{-1}\widetilde{\theta}_{4(i)}\right]. \tag{90}$$

By differentiating V_1 in the interval (T_1, ∞) and

combining Equations (80)–(84), we can obtain

$$\dot{V}_1 = -\frac{1}{2}\sum_{i=1}^{3} e_i^T \left(\gamma_i^{-1} C_{mi}^T C_{mi} + \varepsilon_i S_i\right) e_i \le 0. \tag{91}$$

(iii) Assume that u_1 is normal, and only u_4 fails at T_1 and remains failed on the interval (T_1, ∞); that is, $\sigma = \sigma_{(3)}$. We define

$$V_2 = \frac{1}{2} e^T P e + \frac{1}{2}\sum_{i=1}^{3} \widetilde{\theta}_{di}^T \Gamma_{di}^{-1} \widetilde{\theta}_{di} + \frac{1}{2}\left[\sum_{i=1}^{3} \tilde{\chi}_{1i}^2 \gamma_{1i}^{-1} + \sum_{i=1}^{2} \tilde{\chi}_{2i}^2 \gamma_{2i}^{-1} + \sum_{i=1}^{3} \tilde{\chi}_{3i}^2 \gamma_{3i}^{-1} + \sum_{i=1}^{2} \widetilde{\theta}_{1(i)}^T \Gamma_{1i}^{-1} \widetilde{\theta}_{1(i)} + \sum_{i=1}^{3} \widetilde{\theta}_{4(i)}^T \Gamma_{4i}^{-1} \widetilde{\theta}_{4(i)}\right]. \tag{92}$$

The time derivative of V_2 is

$$\dot{V}_2 = -\frac{1}{2}\sum_{i=1}^{3} e_i^T \left(\gamma_i^{-1} C_{mi}^T C_{mi} + \varepsilon_{mi} S_i\right) e_i \le 0, \quad t \in [T_1, T_2). \tag{93}$$

With $\dot{V}_k, (k = 0, 1, 2) \le 0$ for three different failure scenarios and the adopted projection scheme of adaptive laws, we can conclude that all the signals in the close-loop system are bounded, and the output error gradually decreases to zero over time.

To sum up, the below theorem is obtained.

Theorem 9. *For the spacecraft system (1) with potential uncertain actuator faults (9) and unknown disturbances (4), controller (68) designed based on an H_∞ transient performance compensator (49), and its parameter adaptive laws (80)–(85) can ensure that the system is stable and perform the given maneuvers asymptotically, if for any failure pattern $\sigma(t)$ belongs to failure pattern set $\Sigma = \{\sigma_{(j)}, j = 1, 2, 3\}$. The following condition holds the following equivalent actuation matrix. $G_\sigma(x) = G(x)D(I - \sigma(t))$ is a full rank in the domain U (definition is $U \subset R^6 \longrightarrow V \subset R^3$).*

3.3.4. Transient Performance Analysis. Then, the transient performance is analyzed by the criteria of the bound of both L_∞ and mean square tracking error at any time.

With (45) and (49), we can get the following output tracking error dynamic equation

$$e_{i1} = \frac{W_{mi}(s)}{c_{0i}}\left[G_i(x)D(I - \sigma)(\nu - \nu^*) + G_i(x)\left(d - \widehat{d}\right)\right]. \tag{94}$$

Since the order of the stable reference model $W_{mi}(s)$ is p_{mi}, it can be derived from Lemma 5 that

$$\|e_{i1}(t)\|_\infty \le 2p_{mi}\|W_{mi}(s)\|_\infty \left\| G_i(x)D(I - \sigma)(\nu - \nu^*) + G_i(x)\left(d - \widehat{d}\right)\right\|. \tag{95}$$

From Theorem 9, we have $\widetilde{\theta}_{di} \in L_\infty$ and $(\nu - \nu^*) \in L_\infty$. With Lemma 3, one can prove that $W_{mi}(s)$ is stable and

$$\|W_{mi}(s)\|_\infty < \gamma_i, \tag{96}$$

and thereby, we have

$$\|e_{i1}(t)\|_\infty \triangleq \sup_{t \ge 0} |e_{i1}(t)| \le \gamma_i c_i, \tag{97}$$

where $c_i > 0$. Then, according to

$$\int_{t_1}^{t_2} |H(s)x|^2 dt \le \|H(s)\|_\infty^2 \int_{t_1}^{t_2} |x|^2 dt, \tag{98}$$

we have

$$\frac{1}{t}\int_{t_0}^{t_0+t} |e_{i1}|^2 d\tau \le \|W_{mi}(s)\|_\infty^2 \left(\frac{1}{t}\int_{t_0}^{t_0+t} |G_i(x)D(I - \sigma)(\nu - \nu^*) + G_i(x)\left(d - \widehat{d}\right)\right|^2 d\tau\Bigg) \le \gamma_i^2 c_i. \tag{99}$$

Theorem 10. *For the improved controller (34), the performance index of H_∞ compensator is γ_i, and the output tracking error $e_{i1} = y_i - y_{mi}$ and $i = 1, 2, 3$ of the system (32) satisfies the following inequality condition:*

$$\frac{1}{t}\int_{t_0}^{t_0+t} |e_{i1}|^2 d\tau \le \|W_{mi}(s)\|_\infty^2 \left(\frac{1}{t}\int_{t_0}^{t_0+t} |G_i(x)D(I - \sigma)(\nu - \nu^*) + G_i(x)\left(d - \widehat{d}\right)\right|^2 d\tau\Bigg) \le \gamma_i^2 c_i. \tag{100}$$

where constant $c_i > 0$.

According to Theorem 10, the transient characteristics rely on the performance level of the H_∞ compensator. Both Theorem 9 and Theorem 10 show that the control objective is reached by our proposed control scheme.

4. Simulations

MATLAB/SIMULINK software has been used to carry out numerical simulations to verify the effectiveness and performance of the proposed control scheme. The nominal moments of inertia parameters $J = \text{diag}\{40.45, 42.09, 42.36\}(kg \cdot m^2)$, orientation matrix of the reaction wheel, and the external disturbances $d(t) = [\sin(0.01t) + 1, 1.5\cos(0.01t) - 1, 2\sin(0.01t) + 1] \times 10^{-3} N \cdot m$ are taken from [36].

4.1. Simulation Conditions. The attitude values at $t = 0$ are given by $q_0(0) = 0.8834$, $q(0) = [0.03, -0.02, -0.03]^T$, and $\omega(0) = [0, 0, 0]^T$. For simulation, the initial values of indicator function and failure parameter estimates are chosen as: $\chi_{1i}(0) = 1$, $i = 1, 2, 3, 4$, $\chi_{2i}(0) = 0$, $\chi_{3i}(0) = 0$, $i = 1, 2, 3$; $\theta_{1(i)}(0) = [0, 0]^T$, and $\theta_{4(i)}(0) = [0, 0]^T$. Basis functions of failure model (10) and disturbance model (4) are $\varpi_1(t) = \varpi_4(t) = [1, \sin(0.25t)]^T \in R^2$ and $\varpi_{d1} = \varpi_{d2} = \varpi_{d3} = [1, \sin(0.01t), \cos(0.01t)]^T \in R^3$.

The design parameters are chosen as $\gamma_{1i} = 1$, $\gamma_{2i} = 1$, $\gamma_{3i} = 1$, $c_{0i} = c_0 = 1$, $\gamma_i = 1$, $R_i = 2$, $\varepsilon_i = 4$, $i = 1, 2, 3$,

$$
\begin{aligned}
K &= \begin{bmatrix} 12.2 & 3.9 \\ 8.5 & 2.7 \\ 9.1 & 2.3 \end{bmatrix}, \\
\Gamma_{di} &= \begin{bmatrix} 3.3 & 0 & 3.3 \\ 0 & 3.3 & 3.3 \\ 3.3 & 3.3 & 3.3 \end{bmatrix}, \\
\Gamma_{1i} &= \begin{bmatrix} 16.3 & 0 & 0 \\ 0 & 16.3 & 0 \\ 0 & 0 & 16.3 \end{bmatrix}, \\
\Gamma_{4i} &= \begin{bmatrix} 31.4 & 0 & 0 \\ 0 & 31.4 & 0 \\ 0 & 0 & 31.4 \end{bmatrix}, \\
P_{c1} &= \begin{bmatrix} 3.53 & 6.32 \\ 1.05 & 4.39 \end{bmatrix}, \\
P_{c2} &= \begin{bmatrix} 3.53 & 10.51 \\ 1.05 & 6.58 \end{bmatrix}, \\
P_{c3} &= \begin{bmatrix} 3.53 & 4.23 \\ 1.05 & 3.79 \end{bmatrix}.
\end{aligned} \tag{101}
$$

A second-order reference model $W_{mi}(s) = 1/(s^2 + 2s + 1)$ and the reference input signal $r_i(t) = 0$, $i = 1, 2, 3$, are chosen to generate the given command $y_m(t)$ to be tracked by system output $y(t)$.

In the numerical simulation, for comparison, three cases are conducted: (1) attitude tracking control using our proposed modified MRAC based adaptive failure compensation controller (68) (denoted as "MMRAC based FTC"); (2) attitude tracking control using the standard MRAC-based adaptive failure compensation controller (denoted as "SMRAC based FTC") without transient performance compensator; and (3) attitude tracking control using the direct adaptive failure compensation controller (denoted as "DAC-based FTC") in [35]. The attitude tracking responses are analyzed to study the performances of the controllers.

4.2. Simulation Results. To demonstrate the superior performance of the proposed control scheme, two actuator failure conditions are simulated: Case 1—intermittent fault occurring in actuator u_1—and Case 2—Alternate faults occurring in actuators u_1 and u_4.

Case 1. Intermittent fault occurring in actuator u_1. In this case, the following failure conditions are considered as follows:

(i) When $0 \le t < 100s$, all the reaction wheels function healthily, $u_i(t) = v_i(t)$, $i = 1, 2, 3, 4$

(ii) When $100s \le t < 200s$, actuator u_1 failed, $u_1(t) = 2\,Nm$ and $u_i(t) = v_i(t)$, $i = 2, 3, 4$

(iii) When $t \ge 200s$, actuator u_1 returns to normal, $u_i(t) = v_i(t)$, $i = 1, 2, 3, 4$

(iv) When $t \ge 300s$, actuator u_1 is out of control, $u_1(t) = 0.75 \sin(0.25t)Nm$, $u_i(t) = v_i(t)$, $i = 2, 3, 4$

Figure 2(a) shows the simulated results obtained by including the faulty actuators for three controllers, namely the designed MMRAC based fault tolerant controller marked with solid line, the SMRAC-based fault-tolerant controller marked with dashed line, and the DAC-based fault-tolerant controller marked with dotted line. All the three fault-tolerant controllers can compensate for both the constraint and time varying faults, although the system performance degrades to some degree, the overshoot a setting time increase significantly once the failure is introduced. However, the system ultimately regulates the attitude to zero asymptotically; that is, the attitude stabilization maneuver is still performed successfully due to the fault-tolerant performance of the three controllers to uncertain actuator failures. It can be found from Figure 2(c) at the moments when actuator u_1 failed at $t = 100s$ and $t = 300s$ (shown in Figure 2(b), which is corresponding with the simulation conditions), the overshoot of the system implemented by our designed MMRAC-based fault-tolerant controller are smaller than the SMRAC- and DAC-based fault-tolerant controller even before the actuators have failed, and this is because the effect caused by parameter estimation errors of both failure and disturbances on the transient performance has been reduced by the H_∞ compensator. These simulations demonstrate the theoretical result that the desired performance of the system can be achieved by the proposed fault tolerant control even if the faults are unknown in advance.

Case 2. Alternate Faults Occurring in Actuator u_1 and u_4. In this case, the following failure conditions are considered as follows:

(i) When $0 \le t < 100s$, all the reaction wheels function healthily, $u_i(t) = v_i(t)$, $i = 1, 2, 3, 4$

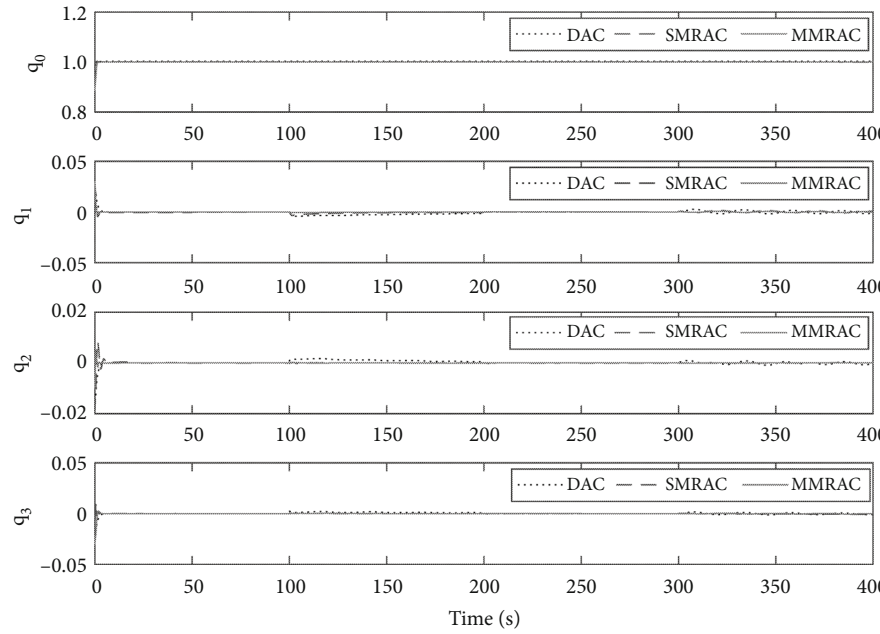

(a) Response of system output

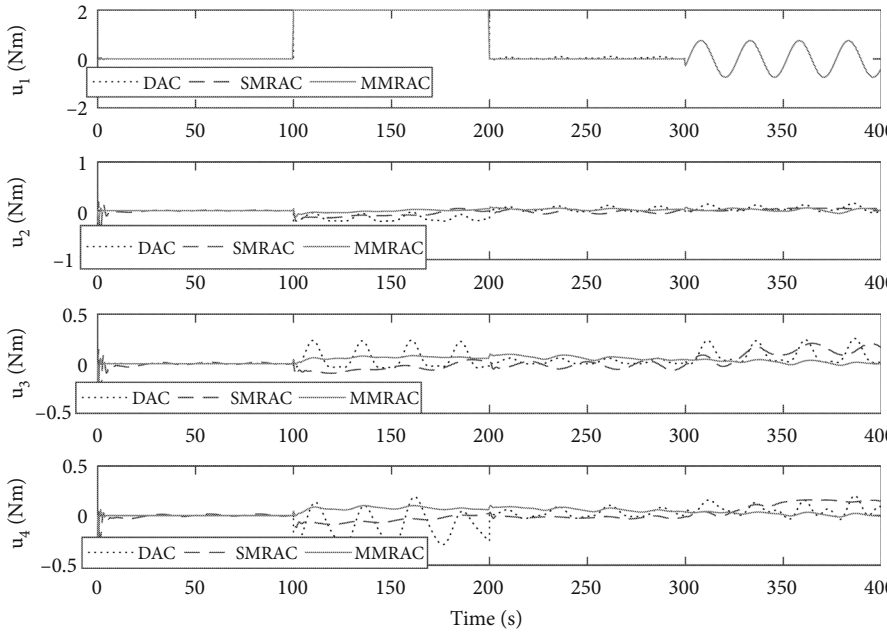

(b) Control input signals for different fault scenarios

Figure 2: Continued.

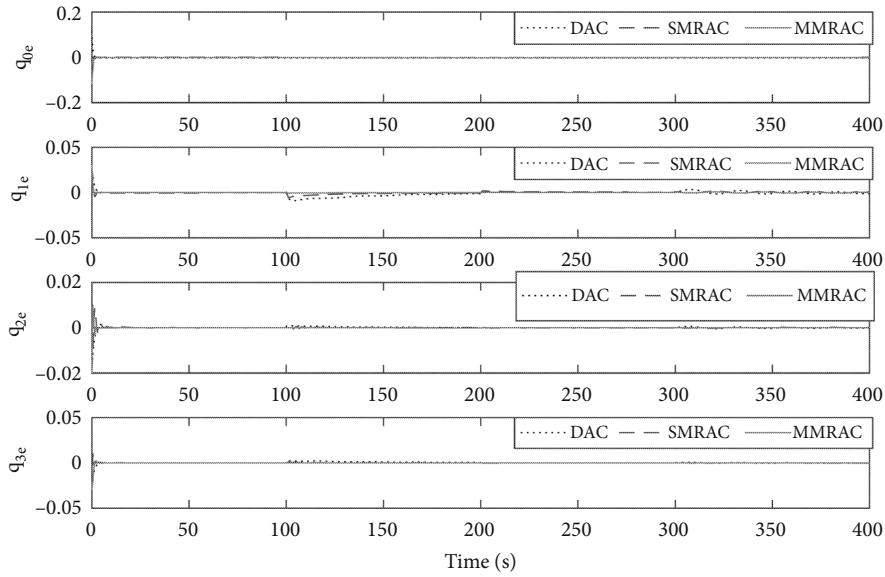

(c) Responses of tracking errors

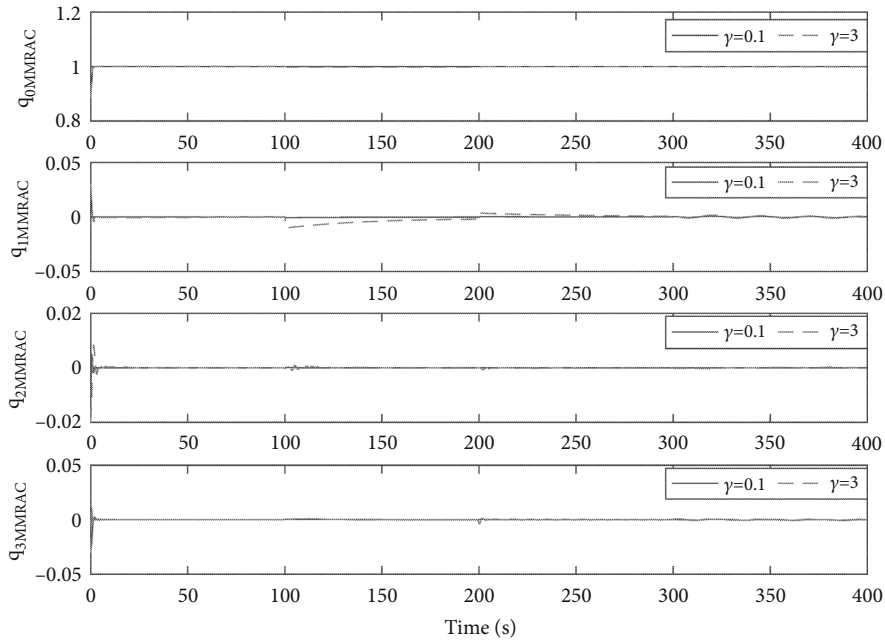

(d) System outputs for different γ in the MMAC design

Figure 2: Attitude tracking control using MMRAC-, SMRAC-, and DAC-based fault-tolerant control schemes for Case 1.

(ii) When $100s \le t < 200s$, actuator u_1 failed, $u_1(t) = 3.5Nm$ and $u_i(t) = v_i(t), i = 2, 3, 4$

(iii) When $t \ge 200s$, actuator u_1 returns to normal, $u_i(t) = v_i(t), i = 2, 3, 4$

(iv) When $t \ge 300s$, actuator u_4 is out of control, $u_4(t) = 1.75 \sin(0.25t)\text{Nm}, u_i(t) = v_i(t), i = 1, 2, 3$

This example represents the severe case in which both two actuators experience failure at the moments of $t = 100s$ and $t = 300s$, respectively. Actually, the failure conditions in Case 2 can be regarded as a mixed pattern of intermittent failure and permanent failure. As shown in Figure 3(b), when u_1 is stuck at the instant $t = 100s$ and becomes normal at $t = 200s$, that is an intermittent failure occurred in actuator u_1, which is activated and inactivated by itself. The system produces an erroneous result when such fault is active during the period of $100s \le t < 200s$ and produces a correct result when it is inactive for $t \ge 200s$. At $t = 300s$, actuator u_4 undergoes time-varying failure and never come back as normal. Figure 3(a) shows the results using the three different control laws based on the same simulation conditions. Clearly, compared with attitude tracking response for Case 1, the attitude control performance deteriorates severely due to the multiple uncertainties of actuator failure, with severe overshoots in the attitude orientation, although the

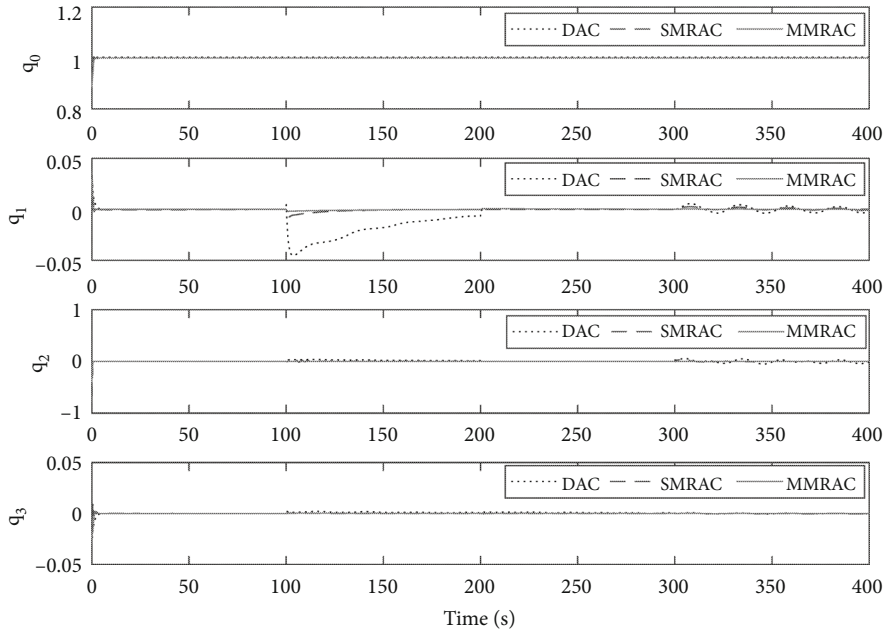

(a) Response of system output

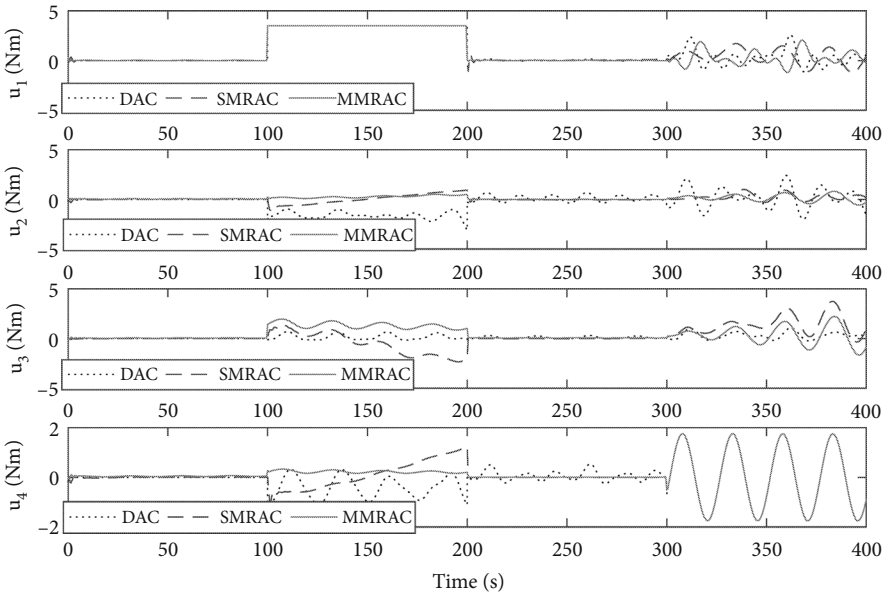

(b) Control input signals for different fault scenarios

Figure 3: Continued.

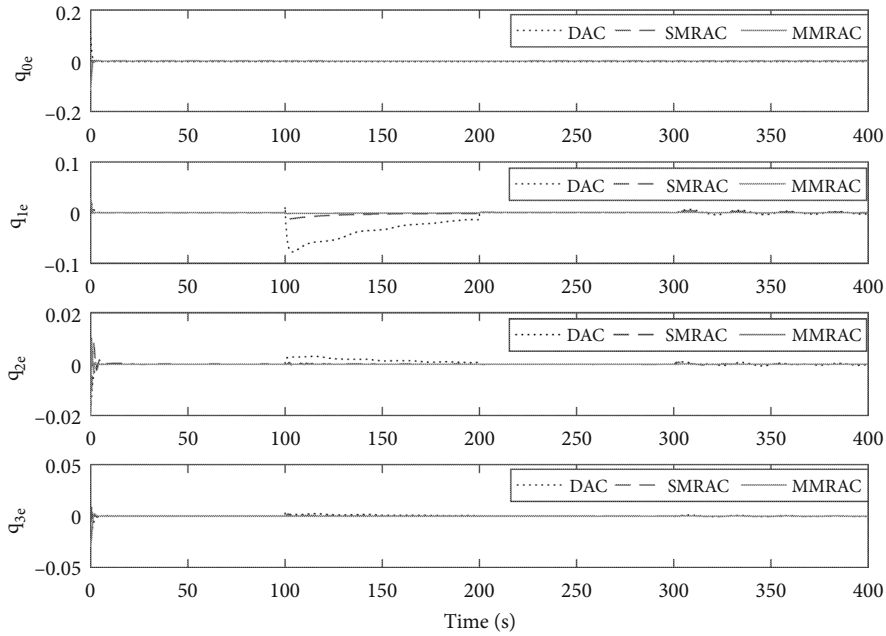

(c) Responses of tracking errors

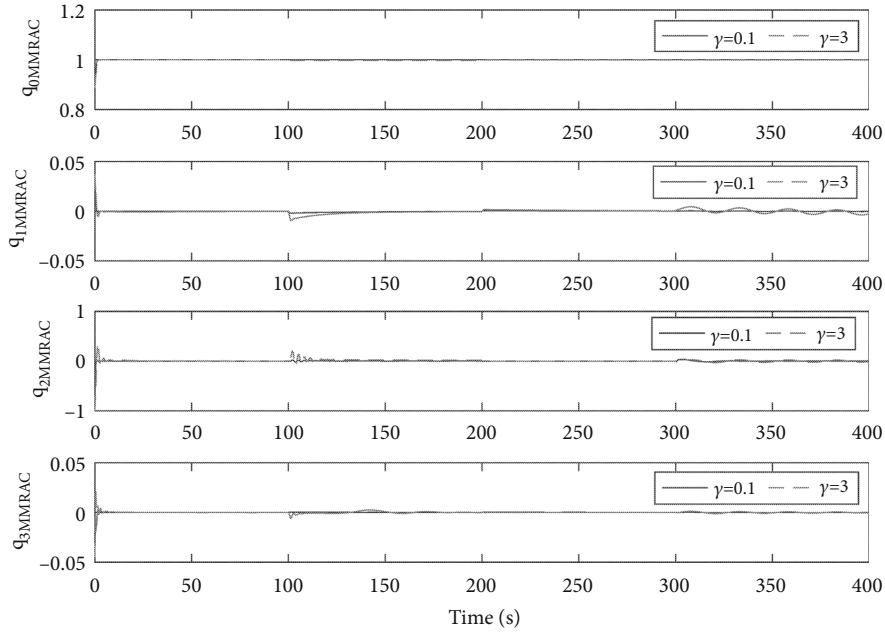

(d) System outputs for different γ in the MMAC design

Figure 3: Attitude tracking control using MMRAC-, SMRAC-, and DAC-based fault-tolerant control schemes for Case 2.

objective of asymptotic attitude tracking can be achieved finally, as clearly indicated from the output tracking errors present in Figure 3(c).

In summary, for both the normal, intermittent failure and permanent failure cases, the proposed controller significantly improves the normal control performance of the closed-loop attitude system compared to the SMRAC- and DAC-based fault-tolerant control approaches. For the cases with actuator faults, the proposed method gives better transient performance than those controllers without including the transient performance compensator. As the faults become more severe, the proposed controller still guarantees system stability and asymptotic output tracking of a given command.

Furthermore, comparing the modified control scheme with different γ_i $(i = 1, 2)$, it can be found from Figures 2(d) and 3(d) that with smaller $\gamma_1 = 0.1$, the compensator takes more effects on transient oscillations inhibition with a smaller following error of trajectory than that with $\gamma_2 = 3$, which keeps an agreement with the performance analysis by the criterion of L_1 bound or mean squared value.

5. Conclusions

With multiple uncertain actuator faults, the control system of rigid spacecraft attitude is optimized by designing an improved adaptive FTC method in this study. And the major conclusions are as follows. (1) A model reference adaptive control algorithm combing with feedback linearization technology is adopted to propose a basic control law for achieving the desired closed-loop system performance. Then, as an additional item of robust adaptive control, an H_∞ compensator is introduced to optimize the transient performance. (2) Based on the modified basic control design, multiple targeted adaptive failure compensators are designed to handle the corresponding failure patterns. Multiple controllers are fused into a comprehensive controller by using a weighted algorithm, thus multiple uncertain actuator faults are solved. (3) Under different fault conditions with and without additional transient performance improvers, contrastive simulation analysis of output tracking control is adopted to proof the significance of the designed theoretical method. (4) The fault compensation control for spacecraft whose parameters are known, is researched in this paper. The way to overcoming the fault compensation difficulty on the spacecraft with unknown system parameters can be found by the further extended method which is described in this research.

Data Availability

The data (system parameters and simulation parameters) used to support the findings of this study are included within the article.

Conflicts of Interest

The authors declare that they have no conflicts of interest.

Acknowledgments

This work was supported by the National Natural Science Foundation of China under grant 61903165 and Postgraduate Research & Practice Innovation Program of Jiangsu Province under grant XSJCX20_21.

References

[1] Y. M. Zhang and J. Jiang, "Bibliographical review on reconfigurable fault-tolerant control systems," *Annual Reviews in Control*, vol. 32, no. 2, pp. 229–252, 2008.

[2] C. Sun and Y. Lin, "Adaptive output feedback fault tolerant control for uncertain nonlinear systems based on actuator switching," *Journal of the Franklin Institute*, vol. 358, no. 11, pp. 5722–5749, 2021.

[3] Y. Fadili and I. Boumhidi, "Fault tolerant control for wind turbine system based on model reference adaptive control and particle swarm optimization algorithm," *Journal of Circuits, Systems and Computers*, vol. 29, no. 3, pp. 2050037–2050037.34, 2020.

[4] J. A. Brizuela Mendoza, F. Sorcia-Vzquez, J. Y. Rumbo Morales, and R. E. Lozoya Ponce, "Active fault tolerant control based on eigenstructure assignment applied to a 3-DOF helicopter," *Asian Journal of Control*, vol. 23, no. 2, pp. 673–684, 2021.

[5] J. H. Wang, J. Tavoosi, A. Mohammadzadeh et al., "Non-singleton type-3 fuzzy approach for flowmeter fault detection: experimental study in a gas industry," *Sensors*, vol. 21, no. 21, p. 7419, 2021.

[6] H. Y. Yang, Y. C. Jiang, and S. Yin, "Adaptive fuzzy fault-tolerant control for Markov jump systems with additive and multiplicative actuator faults," *IEEE Transactions on Fuzzy Systems*, vol. 29, no. 4, pp. 772–785, 2021.

[7] P. Li, P. Huang, C. Y. He, and X. Q. Liu, "Finite-time dynamic surface fault-tolerant control for hypersonic vehicle with mismatched disturbances," *International Journal of Control Automation and Systems*, vol. 19, no. 7, pp. 2309–2322, 2021.

[8] M. N. Hasan, M. Haris, and S. Y. Qin, "Fault-tolerant spacecraft attitude control: a critical assessment," *Progress in Aerospace Sciences*, vol. 130, article 100806, 2022.

[9] S. Yin, B. Xiao, S. X. Ding, and D. H. Zhou, "A review on recent development of spacecraft attitude fault tolerant control system," *IEEE Transactions on Industrial Electronics*, vol. 63, no. 5, pp. 3311–3320, 2016.

[10] T. Cao, H. J. Gong, P. Cheng, and Y. X. Xue, "A novel learning observer-based fault-tolerant attitude control for rigid spacecraft," *Aerospace Science and Technology*, vol. 128, article 107751, 2022.

[11] F. Q. Di, A. J. Li, Y. Guo, C. Q. Wang, and L. H. Wang, "Attitude tracking control for fractionated spacecraft with actuator failures under adaptive event-triggered strategy," *Advances in Space Research*, vol. 70, no. 5, pp. 1209–1221, 2022.

[12] X. Wu, S. B. Luo, C. S. Wei, and Y. X. Liao, "Observer-based fault-tolerant attitude tracking control for rigid spacecraft with actuator saturation and faults," *Acta Astronautica*, vol. 178, pp. 824–834, 2021.

[13] D. Zhao, H. Yang, B. Jiang, and Y. L. Wen, "Attitude stabilization of a flexible spacecraft under actuator complete failure," *Acta Astronautica*, vol. 123, pp. 129–136, 2016.

[14] M. N. Hasan, M. Haris, and S. Y. Qin, "Flexible spacecraft's active fault-tolerant and anti-unwinding attitude control with vibration suppression," *Aerospace Science and Technology*, vol. 122, article 107397, 2022.

[15] M. M. Tavakoli and N. Assadian, "Actuator failure-tolerant control of an all-thruster satellite in coupled translational and rotational motion using neural networks," *International Journal of Adaptive Control and Signal Processing*, vol. 32, no. 12, pp. 1748–1763, 2018.

[16] S. Boulouma, S. Labiod, and H. Boubertakh, "Direct adaptive control of a flexible spacecraft with disturbances and uncertain actuator failures," *Mechanical Systems & Signal Processing*, vol. 110, pp. 73–89, 2018.

[17] M. Pouzesha and S. Mobayen, "Event-triggered fractional-order sliding mode control technique for stabilization of disturbed quadrotor unmanned aerial vehicles," *Aerospace Science and Technology*, vol. 121, article 107337, 2022.

[18] B. Xiao, Q. Hu, D. Wang, and E. K. Poh, "Attitude tracking control of rigid spacecraft with actuator misalignment and fault," *IEEE Transactions on Control Systems Technology*, vol. 21, no. 6, pp. 2360–2366, 2013.

[19] J. F. Quindlen, G. Chowdhary, and J. P. How, "Hybrid model reference adaptive control for unmatched uncertainties," in *Proceedings of the American Control Conference*, pp. 1125–1130, Chicago, IL, USA, July 2015.

[20] V. Ghaffffari and S. Mobayen, "Robust $H\infty$ integral controller design for regulation problem of uncertain nonlinear systems with non-zero set-point," *Communications in Nonlinear Science and Numerical Simulation*, vol. 107, article 106158, 2022.

[21] G. Chowdhary, T. Yucelen, M. Mhlegg, and E. N. Johnson, "Concurrent learning adaptive control of linear systems with exponentially convergent bounds," *International Journal of Adaptive Control and Signal Processing*, vol. 27, no. 4, pp. 280–301, 2013.

[22] Y. Pan and H. Yu, "Composite learning from adaptive dynamic surface control," *IEEE Transactions on Automatic Control*, vol. 61, no. 9, pp. 2603–2609, 2016.

[23] O. Mofifid, S. Mobayen, C. W. Zhang, and B. Esakki, "Desired tracking of delayed quadrotor UAV under model uncertainty and wind disturbance using adaptive super-twisting terminal sliding mode control," *ISA Transactions*, vol. 123, pp. 455–471, 2022.

[24] A. M. Khanasadurai, V. Krishnasamy, and R. T. Karunakaran, "Improved transient performance of a fuzzy modified model reference adaptive controller for an interacting coupled tank system using real-coded genetic algorithm," *International Journal of Chemical Engineering*, vol. 2014, Article ID 351973, 9 pages, 2014.

[25] S. B. Prusty, U. C. Pati, and K. K. Mahapatra, "A novel fuzzy based adaptive control of the four tank system," in *IEEE Conference on Computer, Communication, Control and Information Technology*, pp. 1–6, Hooghly, India, 2015.

[26] R. Ortega, D. N. Gerasimov, N. E. Barabanov, and V. O. Nikiforov, "Adaptive control of linear multivariable systems using dynamic regressor extension and mixing estimators: removing the high-frequency gain assumptions," *Automatica*, vol. 110, article 108589, 2019.

[27] R. B. Anderson, J. A. Marshall, and A. L'Afflitto, "Novel model reference adaptive control laws for improved transient dynamics and guaranteed saturation constraints," *Journal of the Franklin Institute*, vol. 358, no. 12, pp. 6281–6308, 2021.

[28] K. Wang, T. Meng, W. J. Wang, R. T. Song, and Z. H. Jin, "Finite-time extended state observer based prescribed performance fault tolerance control for spacecraft proximity operations," *Advances in Space Research*, vol. 70, no. 5, pp. 1270–1284, 2022.

[29] S. Gao, Y. Jing, G. M. Dimirovski, and Y. Zheng, "Adaptive fuzzy fault-tolerant control for the attitude tracking of spacecraft within finite time," *Acta Astronautica*, vol. 189, pp. 166–180, 2021.

[30] Y. X. Ji, L. Chen, D. X. Zhang, and X. W. Shao, "Neural network-based nonsingular fixed-time pose tracking control for spacecraft with actuator faults," *Advances in Space Research*, vol. 69, no. 6, pp. 2555–2573, 2022.

[31] X. D. Shao, Q. L. Hu, Y. Shi, and B. Y. Jiang, "Fault-tolerant prescribed performance attitude tracking control for spacecraft under input saturation," *IEEE Transactions on Control Systems Technology*, vol. 28, no. 2, pp. 574–582, 2020.

[32] X. W. Huang and G. R. Duan, "Fault-tolerant attitude tracking control of combined spacecraft with reaction wheels under prescribed performance," *ISA Transactions*, vol. 98, pp. 161–172, 2020.

[33] B. Guo and Y. Chen, "Adaptive fast sliding mode fault tolerant control integrated with disturbance observer for spacecraft attitude stabilization system," *ISA Transactions*, vol. 94, pp. 1–9, 2019.

[34] J. Sun, "A modified model reference adaptive control scheme for improved transient performance," *IEEE Transactions on Automatic Control*, vol. 38, no. 8, pp. 1255–1259, 1993.

[35] X. L. Yao, G. Tao, Y. J. Ma, and R. Y. Qi, "Adaptive actuator failure compensation design for spacecraft attitude control," *IEEE Transactions on Aerospace and Electronic Systems*, vol. 52, no. 3, pp. 1021–1034, 2016.

[36] Y. J. Ma, B. Jiang, and G. Tao, "Adaptive actuator failure identification for microsatellites under closed-loop control," *IEEE Transactions on Control Systems Technology*, vol. 23, no. 3, pp. 910–923, 2015.

Hindawi
International Journal of Aerospace Engineering
Volume 2022, Article ID 6447812, 15 pages
https://doi.org/10.1155/2022/6447812

Research Article

Fixed-Time Fault-Tolerant Tracking Control of Fixed-Wing UAVs with Actuator Fault and Unmatched Disturbances

Zhonghua Wu and Shuaipeng Zheng

School of Electrical Engineering and Automation, Henan Polytechnic University, Jiaozuo 454000, China

Correspondence should be addressed to Zhonghua Wu; wuzhonghua@hpu.edu.cn

Received 14 April 2022; Accepted 6 September 2022; Published 21 November 2022

Academic Editor: Hao Chen

This paper presents a dynamic surface fixed-time fault-tolerant control strategy for the longitudinal dynamic model of fixed-wing unmanned aerial vehicles (UAVs). Firstly, a novel disturbance observer is constructed to precisely estimate the lumped disturbance. Secondly, without fractional power terms in the designed fixed-time fault-tolerant controller, the potential singular value problem is tactfully avoided, which often exists in the stability analysis of the traditional fixed-time controller design. Thirdly, a novel fixed-time filter is proposed to overcome the phenomenon of "differential explosion" in the backstepping control scheme. Lyapunov stability analysis guarantees that the tracking errors can converge to the neighborhood of the origin in the fixed time. The simulation results verify the effectiveness of the proposed control scheme.

1. Introduction

Fixed-wing UAVs have played an essential role in high-risk and complex missions due to their flexibility and maneuverability [1]. The complex flight conditions make the UAVs subject to actuator fault during operation, which may degrade the stability and robustness of flight control systems, and even lead to a catastrophic accident, thus requiring to explore the fault-tolerant control (FTC) of UAVs. Many researchers have concentrated on addressing the control problem of fixed-wing UAVs subject to actuator fault, thereby publishing numerous results regarding passive or active FTC. Active FTC identifies faults through fault detection and diagnosis block in real time, while passive FTC uses a single fixed controller through the robust control strategy [2–5].

An adaptive control approach consisting of a radial base function neural network (RBFNN) was proposed for coaxial octorotor UAV subject to actuator faults [6]. By introducing a prescribed performance function on the synchronized tracking errors, the decentralized finite-time adaptive fault-tolerant synchronization tracking control scheme is proposed for multi-UAVs in the presence of actuator faults [7]. A distributed adaptive FTC scheme is proposed in virtual of a distributed sliding mode estimator and disturbance observers [8]. In the presence of actuator fault, the distributed fault-tolerant output regulation for heterogeneous linear multiagent systems is proposed using the distributed fixed-time observer and adaptive fault-tolerant controller [9]. A constrained control scheme based on model reference adaptive control is investigated for the longitudinal motion of a commercial aircraft with actuator faults and saturation nonlinearities [10]. By using the extended Kalman filter (EKF) to update the weighting parameters of the neural network (NN), a new online detection strategy is developed to detect faults in sensors and actuators of UAVs [11].

The external disturbance may degrade the flight performance of fixed-wing UAVs directly. Therefore, it is essential to construct a disturbance observer against its adverse effect. A disturbance observer combined with a time delay estimation is designed to weaken the influence caused by the unknown dynamic parameters in the actuator of the rehabilitation robot [12]. A novel fixed-time extended state observer is presented to estimate the state errors and the total disturbances in the presence of nonlinear couplings, uncertain parameters, and external disturbances [13]. A

disturbance observer is incorporated into the control structure to efficiently estimate the lumped disturbances, including modeling inaccuracies and external perturbations [14]. A fixed-time adaptive fast super-twisting disturbance observer is built to estimate the external disturbance, in which two tunable gains are adjusted in real time by an adaptive law [15]. The disturbance observers, as mentioned above, need to know the upper bound of the external disturbance, which may hinder its practical engineering applications.

Backstepping control schemes have been widely used in the control system design of fixed-wing UAVs. However, the repeated derivation of the virtual control law in the backstepping designs will largely increase the computational complexity, called the "differential explosion" phenomenon. By introducing a first-order filter to estimate the derivative of the virtual control laws, the dynamic surface control (DSC) scheme is first proposed in [16]. An observer-based fuzzy neural dynamic surface control is presented for a flexible-joint manipulator system with input saturation and unknown disturbance [17]. Moreover, a composite learning fixed-time DSC scheme is proposed for nonlinear strict feedback systems with parameter uncertainties [18]. A constrained adaptive DSC approach is presented for uncertain nonlinear systems subject to full-state constraints [19].

Unlike the traditional finite-time control schemes, the upper bound of convergence time is irrelevant to the initial conditions in the fixed-time control scheme, leading to its extensive applications in UAVs. By introducing a continuously differentiable switching function, an adaptive fixed-time control strategy is proposed for autonomous ship landing operations of UAVs [20]. Moreover, a fixed-time controller combined with the obstacle Lyapunov function is designed for a class of surface ship systems with output constraints [21]. Motivated by the practical requirements of high precision and faster convergence rate for an automatic carrier landing, a fixed-time nonlinear flight controller is presented [22]. Anti-saturation coordinated controller is designed [23], which can guarantee the safe distance constraint of each spacecraft in the process of completing the configuration reconstruction task in a specified time. Using a distributed fixed-time observer to estimate the states of the virtual leader, a fixed-time attitude coordinated control is investigated for multispacecraft systems with unknown external disturbance [24]. However, those mentioned above backstepping fixed-time controllers contain fractional power terms, which may encounter the singular problem caused by the repeated derivation of the virtual control law.

Inspired by recent results [25–27], a fixed-time fault-tolerant controller without fractional power terms is proposed for fixed-wing UAVs subject to actuator fault and external disturbances. The main contributions of this work are threefold:

(1) Different from the conventional fixed-time algorithm, a simple fixed-time fault-tolerant controller scheme without fractional power terms is proposed, which overcomes the potential singularity problem often encountered in fixed-time backstepping designs

(2) Unlike the traditional DSC schemes, this paper proposes a simple and smooth fixed-time filter in the control design, reducing the complexity of the control system and ensuring dynamic surface filter error to satisfy fixed-time convergence

(3) A new type of disturbance observer, with an adaptive term to estimate the upper bound of the lumped disturbance, is proposed, thus leading to an accurate estimation of the lumped disturbance

The layout of this paper is organized as follows. The problem formulation and preliminaries are introduced in Section 2. The construction of the new type of disturbance observer is described in Section 3. The fixed-time fault-tolerant controller and a new fixed-time dynamic surface filter are presented in Section 4. In Section 5, the numerical simulation indicates the effectiveness of the proposed control scheme, followed by the conclusions in Section 6.

2. Problem Formulation and Preliminaries

2.1. Model Description. The nonlinear longitudinal dynamic model of fixed-wing UAV is given as follows:

$$\begin{aligned} \dot{\gamma} &= \frac{L + T\sin\alpha}{m\mathrm{V}} - \frac{g}{V}\cos\gamma + \Delta_\gamma, \\ \dot{\alpha} &= q - \dot{\gamma} + \Delta_\alpha, \\ \dot{q} &= \frac{M}{I_{yy}} + \Delta_q, \end{aligned} \tag{1}$$

where γ, α and q are the flight-path angle, angle of attack, and pitch rate, respectively. m represents the mass of the UAV. g is the gravity acceleration, I_{yy} denotes the moment of inertia, $\Delta_\alpha, \Delta_\gamma, \Delta_q$ represent unknown external disturbances, and $T = T_{\max}\delta_T$ is the engine thrust.

The aerodynamic force and moment of the UAV are expressed as

$$\begin{aligned} L &= 0.5\rho V^2 \mathrm{S}C_L, \\ M &= 0.5\rho V^2 \mathrm{S}\mathrm{c}C_m, \end{aligned} \tag{2}$$

where ρ denotes the air density and S represents the wing platform area. C_L and C_m are the aerodynamic coefficients for drag force and pitch moment, respectively. The aerodynamic force and moment coefficients can be expressed as

$$\begin{aligned} C_L &= C_{L\alpha}\alpha + C_{L0}, \\ C_m &= C_{m\alpha}\alpha + C_{m0} + \frac{cq}{2V}C_{mq} + C_{m\delta_e}\delta_e, \end{aligned} \tag{3}$$

where $C_{L\alpha}, C_{L0}, C_{m\alpha}, C_{m0}, C_{mq}, C_{m\delta_e}$ represent the aerodynamic coefficients. δ_e is the actual elevator deflection.

2.2. Actuator Faults Model. To account for the actuator faults, the actual elevator deflection δ_e can be modeled as

$$\delta_e = p_1\delta_{e0} + b_{f1}, \tag{4}$$

where δ_{e0} denotes the designed elevator deflection and p_1 is the remaining control effectiveness factor with $0 < p_1 \le 1$. b_{f1} is the fault-bias factor.

2.3. System Transformation and Preparation. By substituting (2)–(4) into (1) and defining the state vector $[x_1 \quad x_2 \quad x_3]^T = [\gamma \quad \alpha \quad q]^T$, $u_0 = \delta_{e0}$, the longitudinal dynamics can be rewritten as

$$\begin{aligned} \dot{x}_1 &= f_1 + g_1x_2 + d_1, \\ \dot{x}_2 &= f_2 + g_2x_3 + d_2, \\ \dot{x}_3 &= f_3 + g_3u_0 + d_3, \end{aligned} \tag{5}$$

where

$$\begin{aligned} f_1 &= \frac{0.5\rho V^2 \mathrm{SC}_{L0}}{m\mathrm{V}} - \frac{g}{V}\cos\gamma, f_2 = -\dot{\gamma}, g_2 = 1, \\ g_1 &= \frac{0.5\rho V^2 \mathrm{SC}_{L\alpha} + T}{m\mathrm{V}}, g_3 = \frac{0.5\rho V^2 \mathrm{Sc}C_{m\delta_e}}{I_{\mathrm{yy}}}, \\ f_3 &= \frac{0.5\rho V^2 \mathrm{Sc}\left(C_{m\alpha}\alpha + C_{m0} + (\mathrm{cq}/2V)C_{m\mathrm{q}}\right)}{I_{\mathrm{yy}}}, \\ d_1 &= \Delta_\gamma, d_2 = \Delta_\alpha, d_3 = \Delta_q + g_3(p_1 - 1)\delta_{e0} + g_3b_{f1}. \end{aligned} \tag{6}$$

2.3.1. Control Objective. The control objective is to design a fixed-time fault-tolerant control scheme for the longitudinal dynamic model of fixed-wing UAVs subject to actuator fault and external disturbances, such that all the signals in the closed-loop system are bounded, and the reference signal tracking error converges to a small neighborhood of the origin in a fixed time.

Assumption 1. All states of the system (1) are measurable. Meanwhile, the reference trajectory γ_d is smoothly bounded and known.

Assumption 2. There exist unknown positive constants p_i such that $|d_i| \le p_i$ with $i = 1, 2, 3$.

Lemma 3. *[28] For a common dynamical system, $\dot{x}(t) = f(t, x)$ with $x(0) = 0$ and the origin be an equilibrium point, where $x \in R^n$ and $f : R_+ \times R^n \longrightarrow R^n$. Defining a Lyapunov candidate, $V(x) \ge 0$. If we can get that*

$$\dot{V}(x) \le -\mu_1 V(x)^\alpha - \mu_2 V(x)^\beta + C, \tag{7}$$

where μ_1, μ_2, α, and β are positive real numbers with $\alpha \in (0, 1)$, $\beta \in (1, \infty)$, then the origin $x = 0$ of the system is practical fixed-time stable, and the settling time function T_s can be estimated by

$$T_s \le \frac{1}{\mu_1(1-\alpha)} + \frac{1}{\mu_2(\beta-1)}. \tag{8}$$

Lemma 4. *[29] For any constant $\varepsilon > 0$ and any variable $x \in R$, the following inequality holds*

$$|x| - \frac{x^2}{\sqrt{x^2 + \varepsilon^2}} \le \varepsilon. \tag{9}$$

Lemma 5. *[26] For any positive real numbers $x_1, x_2, \cdots, x_n$ and $\alpha \in (0, 1)$, one has*

$$\left(\sum_{i=1}^{n} x_i\right)^\alpha \le \sum_{i=1}^{n} x_i^\alpha. \tag{10}$$

Lemma 6. *[30] If $x_i \ge 0$, $i = 1, \cdots, n$, then, the following inequality holds*

$$\left(\sum_{i=1}^{n} x_i\right)^2 \le n\sum_{i=1}^{n} x_i^2. \tag{11}$$

Lemma 7. *[21] For $x, y \in R$, Young's inequality holds*

$$xy \le \frac{\kappa^p}{p}|x|^p + \frac{1}{q\kappa^q}|y|^q, \tag{12}$$

where $\kappa > 0$, $p > 1$, $q > 1$, and $(p-1)(q-1) = 1$.

Lemma 8. *[19] For any constant $\delta > 0$ and any variable $x \in R$, the following inequality holds*

$$|x| - x\tanh\left(\frac{x}{\delta}\right) \le k\delta, \tag{13}$$

where k is a positive constant satisfying $k = e^{-(k+1)}$.

3. Disturbance Observer Design

In this section, a new type disturbance observer is proposed to eliminate the influence of the lumped disturbances.

3.1. Disturbance Observer Design. The disturbance observer is given as follows

$$\widehat{d}_i = \lambda_{i1}\pi_i + \lambda_{i2}\frac{\pi_i}{\sqrt{\pi^2 + (\varepsilon_i/\lambda_{i2})^2}} + \lambda_{i3}\pi_i^3 + \widehat{p}_i\tanh\left(\frac{\widehat{p}_i\pi_i}{\delta_i}\right), \tag{14}$$

where $\widehat{d}_i$ is the estimation of d_i and $\lambda_{i1}, \lambda_{i2}, \lambda_{i3}, \delta_i, \varepsilon_i$ are positive constants, $i = 1, 2, 3$. $\widehat{p}_i$ denotes the estimated value of the upper bound of the external unmatched disturbance signal. π_i is the auxiliary state of the disturbance observer,

which is governed by

$$\begin{aligned} \pi_i &= x_i - s_i, \\ \dot{s}_i &= \lambda_{i1}\pi_i + \lambda_{i2}\frac{\pi_i}{\sqrt{\pi^2 + (\varepsilon_i/\lambda_{i2})^2}} + \lambda_{i3}\pi_i^3 \\ &\quad + \widehat{p}_i \tanh\left(\frac{\widehat{p}_i\pi_i}{\delta_i}\right) + g_i x_{i+1} + f_i. \end{aligned} \tag{15}$$

$\widehat{p}_i$ can be calculated as

$$\dot{\widehat{p}}_i = |\pi_i| - \frac{\sigma_{1i}}{n_i}\widehat{p}_i - \frac{\sigma_{2i}}{n_i^2}\widehat{p}_i^3, \tag{16}$$

where $\sigma_{1i}, \sigma_{2i}, n_i$ are positive constants, $\tilde{p}_i = p_i - \widehat{p}_i$.

Defining the disturbance observer estimation error, $\tilde{d}_i = d_i - \widehat{d}_i$. Then, the derivative of π_i with respect to time can be written as

$$\dot{\pi}_i = d_i - \dot{\widehat{d}}_i = \dot{\tilde{d}}_i. \tag{17}$$

Remark 9. The disturbance observer design presented in [31] requires the upper bound of the external unmatched disturbance in advance, while the proposed disturbance observer releases this restrictive condition. Instead of using the sign function in the disturbance observer design [31], an adaptive term $\widehat{p}_i \tanh(\widehat{p}_i\pi_i/\delta_i)$ is introducing in the proposed novel disturbance observer, which successfully eliminates the chattering phenomenon.

3.2. Stability Analysis

Theorem 10. *Consider system (5), and assume that Assumptions 1 and 2 hold. If the disturbance observer is designed as (14) and there exist positive constants $\lambda_{i1}, \lambda_{i2}, \lambda_{i3}, \delta_i, \varepsilon_i, \sigma_{1i}, \sigma_{2i}, n_i$ for $i = 1, 2, 3$, then the estimated error $\tilde{p}_i$ and auxiliary state π_i converge to sets $\Omega_{\tilde{p}_i} = \{\tilde{p}_i \le \sqrt{2\sqrt{M/\mu_2}}\}, \Omega_{\pi_i} = \{\pi_i \le \sqrt{2\sqrt{M/\mu_2}}\}$ in a fixed time $T_d \le 2/\mu_1 + 1/\mu_2$, respectively.*

Proof. Consider the Lyapunov function candidate as

$$V_d = \sum_{i=1}^{3}\left(\frac{1}{2}\pi_i^2 + \frac{1}{2}\tilde{p}_i^2\right). \tag{18}$$

Then, it can be found that

$$\begin{aligned} \dot{V}_d &= \sum_{i=1}^{3}\pi_i\dot{\pi}_i + \tilde{p}_i\dot{\tilde{p}}_i, \\ &= \sum_{i=1}^{3}\left[\pi_i d_i - \lambda_{i1}\pi_i^2 - \lambda_{i2}\frac{\pi_i^2}{\sqrt{\pi^2 + (\varepsilon_i/\lambda_{i2})^2}} - \lambda_{i3}\pi_i^4\right. \\ &\quad - \widehat{p}_i\pi_i \tanh\left(\frac{\widehat{p}_i\pi_i}{\delta_i}\right) + \widehat{p}_i|\pi_i| - p_i|\pi_i| \\ &\quad \left. + \frac{\sigma_{1i}}{n_i}\tilde{p}_i\widehat{p}_i + \frac{\sigma_{2i}}{n_i^2}\tilde{p}_i\widehat{p}_i^3\right]. \end{aligned} \tag{19}$$

According to Lemma 4, we have

$$-\lambda_{i2}\frac{\pi_i^2}{\sqrt{\pi^2 + (\varepsilon_i/\lambda_{i2})^2}} \le -\lambda_{i2}|\pi_i| + \varepsilon_i. \tag{20}$$

Relying on Lemma 7, one gets

$$\pi_i d_i \le \lambda_{i1}\pi_i^2 + \frac{1}{4\lambda_{i1}}d_i^2. \tag{21}$$

From Lemma 8, we get

$$\widehat{p}_i|\pi_i| - \widehat{p}_i\pi_i \tanh\left(\frac{\widehat{p}_i\pi_i}{\delta_i}\right) \le |\widehat{p}_i\pi_i| - \widehat{p}_i\pi_i \tanh\left(\frac{\widehat{p}_i\pi_i}{\delta_i}\right) \le k\delta_i. \tag{22}$$

With regard to the terms $(\sigma_{1i}/n_i)\tilde{p}_i\widehat{p}_i$ and $(\sigma_{2i}/n_i^2)\tilde{p}_i\widehat{p}_i^3$ in (19), one can find that

$$\begin{aligned} \frac{\sigma_{1i}}{n_i}\tilde{p}_i\widehat{p}_i &= \frac{\sigma_{1i}}{n_i}\left(\tilde{p}_i p_i - \tilde{p}_i^2\right) + \frac{\sigma_{1i}\gamma_i}{\sqrt{2n_i}}\tilde{p}_i - \frac{\sigma_{1i}\gamma_i}{\sqrt{2n_i}}\tilde{p}_i \\ &\le \frac{\sigma_{1i}}{n_i}\left(\frac{1}{2}\tilde{p}_i^2 + \frac{1}{2}p_i^2 - \tilde{p}_i^2\right) + \frac{\sigma_{1i}}{2n_i}\tilde{p}_i^2 + \frac{\sigma_{1i}\gamma_i^2}{4} - \frac{\sigma_{1i}\gamma_i}{\sqrt{2n_i}}\tilde{p}_i, \end{aligned} \tag{23}$$

$$\begin{aligned} \frac{\sigma_{2i}}{n_i^2}\tilde{p}_i\widehat{p}_i^3 &= \frac{\sigma_{2i}}{n_i^2}\left(-\tilde{p}_i^4 - 3\tilde{p}_i^2 p_i^2 + \tilde{p}_i p_i^3 + 3p_i\tilde{p}_i^3\right) \\ &\le \frac{\sigma_{2i}}{n_i^2}\left(-\tilde{p}_i^4 - 3\tilde{p}_i^2 p_i^2 + \frac{3\theta_i^{4/3}}{4}\left|p_i^3\right|^{4/3}\right. \\ &\quad \left. + \frac{1}{4\theta_i^4}\tilde{p}_i^4 + 3p_i^2\tilde{p}_i^2 + \frac{3}{4}\tilde{p}_i^4\right), \end{aligned} \tag{24}$$

where $\gamma_i\theta_i$ are two positive constants.

□

Substituting (20), (21), (22), (23), and (24) into the derivative of V_d results in

$$\dot{V}_d \le \sum_{i=1}^{3}\left[-\sqrt{2}\lambda_{i2}\left(\frac{1}{2}\pi_i^2\right)^{1/2} - 4\lambda_{i3}\left(\frac{1}{2}\pi_i^2\right)^2 - \frac{\sigma_{2i}\left(\theta_i^4-1\right)}{\theta_i^4 n_i^2}\left(\frac{1}{2}\tilde{p}_i^2\right)^2 - \frac{\sigma_{1i}\gamma_i}{\sqrt{n_i}}\left(\frac{1}{2}\tilde{p}_i^2\right)^{1/2}\right] + M, \tag{25}$$

where $M = \sum_{i=1}^{3}[\varepsilon_i + k\delta_i + (3\sigma_{2i}\theta_i^{4/3}/4n_i^2)|p_i^3|^{4/3} + (\sigma_{1i}\gamma_i^2/4) + ((\sigma_{1i}/2n_i) + (1/4\lambda_{i1}))p_i^2]$.

Then, one has

$$\dot{V}_d \le -\mu_1 V_d^{1/2} - \mu_2 V_d^2 + M \le 0. \tag{26}$$

According to the above analysis, if $V_d \ge \sqrt{M/\mu_2}$, then $\dot{V}_d \le -\mu_1 {V_d}^{1/2} \le 0$, we can have that V_d will converge to the set $\{V_d : V_d \le \sqrt{M/\mu_2}\}$ in a fixed-time $T_d \le 2/\mu_1 + 1/\mu_2$, and thus, estimated error $\tilde{p}_i$ and auxiliary states π_i are uniformly ultimately bounded in a fixed time $T_d \le 2/\mu_1 + 1/\mu_2$.

4. Controller Design

In this section, a fixed-time fault-tolerant controller without fractional power terms scheme is proposed to eliminate the singular value problem for a fixed-wing UAV against actuator fault. To prevent the phenomenon of "differential explosion," a new fixed-time dynamic surface filter is added in the backstepping design.

4.1. Fixed-Time Controller and Filter Design. The tracking errors are defined as

$$\begin{aligned} z_1 &= x_1 - x_{1c}, \\ z_2 &= x_2 - x_{2c}, \\ z_3 &= x_3 - x_{3c}, \end{aligned} \tag{27}$$

where z_i is the tracking error, and x_{ic} is the fixed-time filter output signal, $i = 1, 2, 3$, $\gamma_d = x_{1c}$.

The filter errors are defined as

$$\begin{aligned} y_2 &= x_{2c} - x_{2d}, \\ y_3 &= x_{3c} - x_{3d}, \end{aligned} \tag{28}$$

where x_{id} is the virtual control signal and y_i is the error of x_{ic}, x_{id} with $y_i(0) = 0$, $i = 2, 3$.

Step 1. According to (27) and (28), we have

$$\dot{z}_1 = g_1(z_2 + y_2 + x_{2d}) + f_1 + d_1 - \dot{x}_{1c}. \tag{29}$$

The virtual control signal is designed as

$$x_{2d} = \frac{1}{g_1}\left[-f_1 - \hat{d}_1 - k_{11}\frac{z_1}{\sqrt{z_1^2 + (\varepsilon_{z1}/k_{11})^2}} - k_{12}z_1^3 - \left(\frac{k_{13}}{2} + \frac{g_1^2}{2k_{f23}}\right)z_1 + \dot{x}_{1c}\right], \tag{30}$$

where $k_{11}, k_{12}, k_{13}, k_{f23}, \varepsilon_{z1}$ are positive constants.

Remark 11. Different from the conventional fixed-time algorithm with fractional power terms presented in [22], the proposed fixed-time controllers do not contain fractional power terms, which overcome the potential singularity problem often caused by the repeated derivation of the virtual control law in fixed-time backstepping designs.

The Lyapunov function candidate is considered to be

$$V_1 = \frac{1}{2}z_1^2. \tag{31}$$

The time derivative of V_1 can be represented as

$$\dot{V}_1 = z_1\tilde{d}_1 - k_{11}\frac{z_1^2}{\sqrt{z_1^2 + (\varepsilon_{z1}/k_{11})^2}} - k_{12}z_1^4 - \left(\frac{k_{13}}{2} + \frac{g_1^2}{2k_{f23}}\right)z_1^2 + z_1z_2g_1 + z_1g_1y_2. \tag{32}$$

By applying Young's inequality and Lemma 4, one has

$$\begin{aligned} z_1\tilde{d}_1 &\le \frac{k_{13}z_1^2}{2} + \frac{1}{2k_{13}}\tilde{d}_1^2, \\ -k_{11}\frac{z_1^2}{\sqrt{z_1^2 + (\varepsilon_{z1}/k_{11})^2}} &\le -k_{11}|z_1| + \varepsilon_{z1}, \\ z_1g_1y_2 &\le \frac{g_1^2}{2k_{f23}}z_1^2 + \frac{k_{f23}}{2}y_2^2. \end{aligned} \tag{33}$$

Then, one has

$$\dot{V}_1 \le \frac{1}{2k_{13}}\tilde{d}_1^2 - k_{11}|z_1| + \varepsilon_{z1} - k_{12}z_1^4 + z_1z_2g_1 + \frac{k_{f23}}{2}y_2^2. \tag{34}$$

Step 2. Using (27) and (28), we have

$$\dot{z}_2 = g_2(z_3 + y_3 + x_{3d}) + f_2 + d_2 - \dot{x}_{2c}. \tag{35}$$

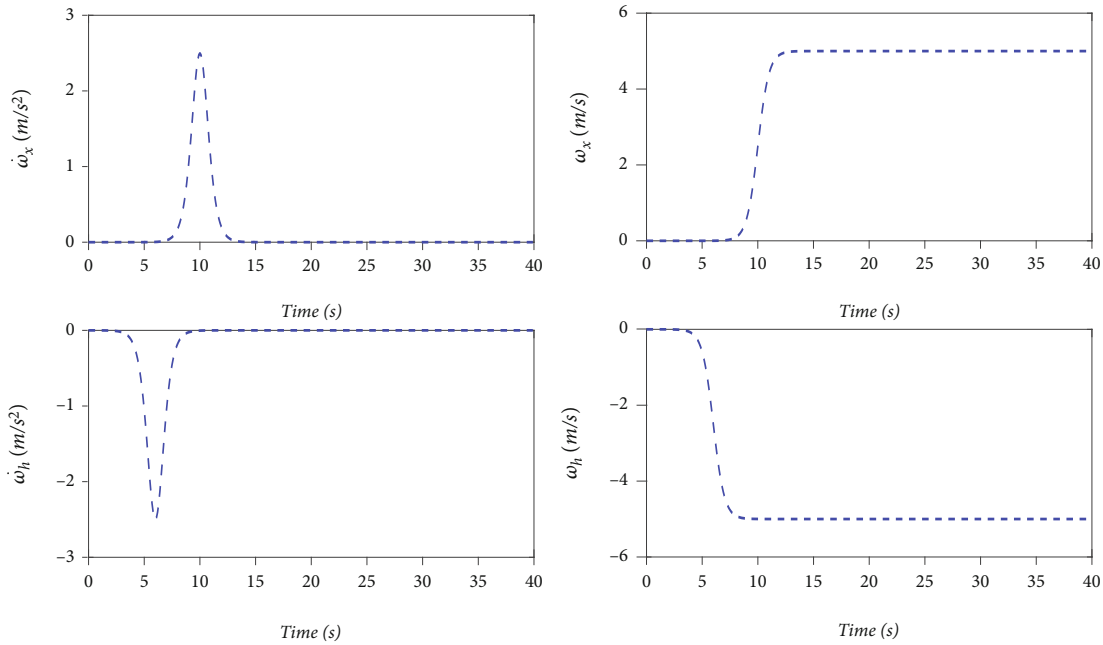

Figure 1: The curves of wind disturbance.

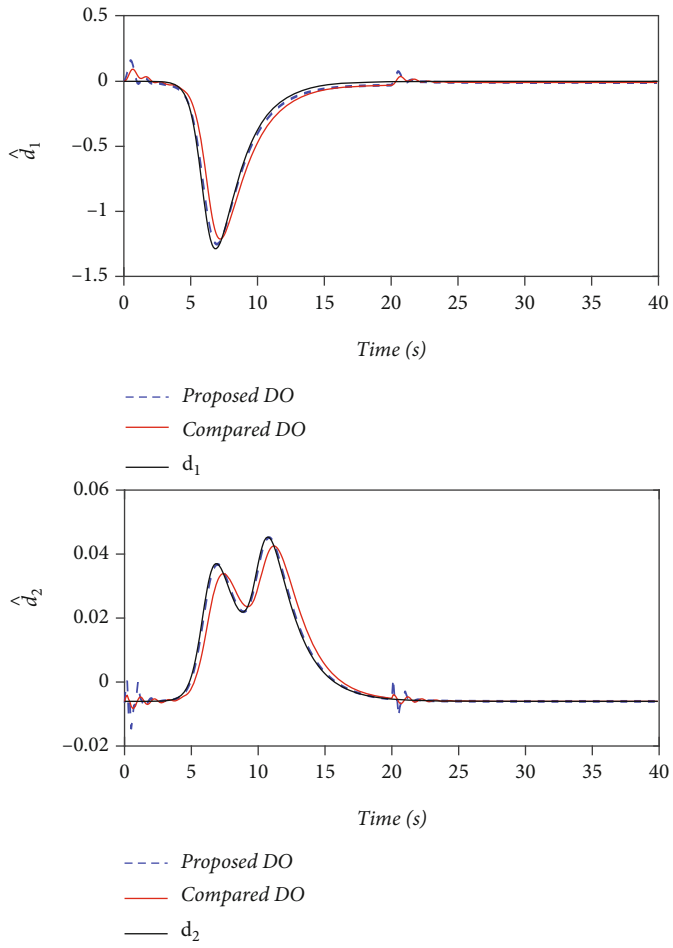

Figure 2: Estimation of d_1 and d_2.

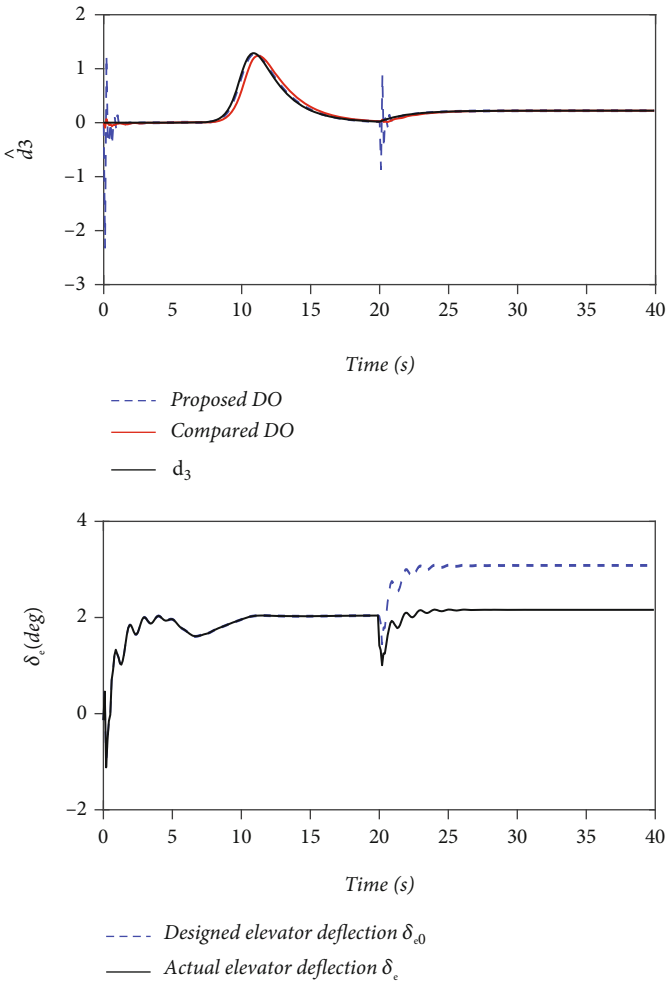

Figure 3: Estimation of d_3 and control input.

The virtual control signal is designed as

$$x_{3d} = \frac{1}{g_2}\left[-f_2 - \hat{d}_2 - k_{21}\frac{z_2}{\sqrt{z_2^2 + (\varepsilon_{z2}/k_{21})^2}} - k_{22}z_2^3 - \left(\frac{k_{23}}{2} + \frac{g_2^2}{2k_{f33}}\right)z_2 + \dot{x}_{2c} - g_1 z_1\right], \tag{36}$$

where $k_{21}, k_{22}, k_{23}, k_{f33}, \varepsilon_{z2}$ are positive constants.

The fixed-time filter is designed as

$$\dot{x}_{2c} = -k_{f21}\frac{y_2}{\sqrt{y_2^2 + (\varepsilon_{y2}/k_{f21})^2}} - k_{f22}y_2^3 - k_{f23}y_2, \tag{37}$$

where $k_{f21}, k_{f22}, k_{f23}, \varepsilon_{y2}$ are positive constants.

The Lyapunov function candidate is considered as

$$V_2 = \frac{1}{2}z_2^2 + \frac{1}{2}y_2^2. \tag{38}$$

The time derivative of V_2 can be represented as

$$\begin{aligned}\dot{V}_2 = {} & z_2\tilde{d}_2 - k_{21}\frac{z_2^2}{\sqrt{z_2^2 + (\varepsilon_{z2}/k_{21})^2}} - k_{22}z_2^4 \\ & - \left(\frac{k_{23}}{2} + \frac{g_2^2}{2k_{f33}}\right)z_2^2 - z_1 z_2 g_1 + z_2 z_3 g_2 \\ & + z_2 g_2 y_3 - k_{f21}\frac{y_2^2}{\sqrt{y_2^2 + (\varepsilon_{y2}/k_{f21})^2}} \\ & - k_{f22}y_2^4 - k_{f23}y_2^2 - \dot{x}_{2d}y_2.\end{aligned} \tag{39}$$

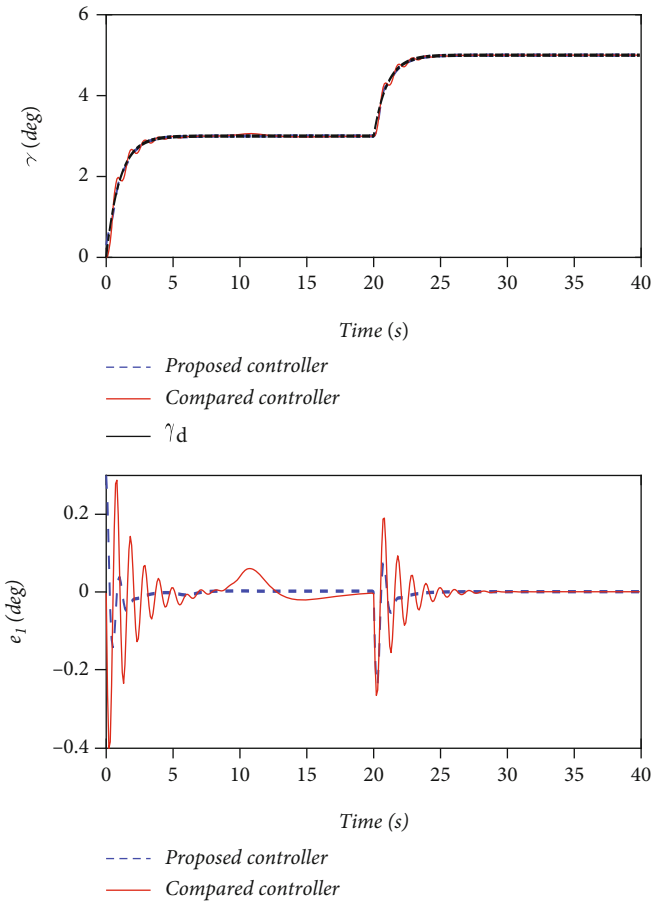

Figure 4: Tracking error e_1 and the trajectory of γ.

By applying Young's inequality and Lemma 4, we have

$$\begin{aligned} z_2\tilde{d}_2 &\le \frac{k_{23}}{2}z_2^2 + \frac{1}{2k_{23}}\tilde{d}_2^2, -k_{21}\frac{z_2^2}{\sqrt{z_2^2 + (\varepsilon_{z2}/k_{21})^2}} \\ &\le -k_{21}|z_2| + \varepsilon_{z2}, -k_{f21}\frac{y_2^2}{\sqrt{y_2^2 + (\varepsilon_{y2}/k_{f21})^2}} \\ &\le -k_{f21}|y_2| + \varepsilon_{y2}, \\ z_2 g_2 y_3 &\le \frac{g_2^2}{2k_{f33}}z_2^2 + \frac{k_{f33}}{2}y_3^2. \end{aligned} \tag{40}$$

Then, one has

$$\begin{aligned} \dot{V}_2 \le{}& \frac{1}{2k_{23}}\tilde{d}_2^2 - k_{21}|z_2| + \varepsilon_{z2} - k_{22}z_2^4 - z_1 z_2 g_1 \\ &+ z_2 z_3 g_2 - k_{f21}|y_2| + \varepsilon_{y2} - k_{f22}y_2^4 - k_{f23}y_2^2 \\ &+ \frac{k_{f33}}{2}y_3^2 - \dot{x}_{2d}y_2. \end{aligned} \tag{41}$$

Step 3. According to (27) and (28), we have

$$\dot{z}_3 = g_3 u_0 + f_3 + d_3 - \dot{x}_{3c}. \tag{42}$$

The virtual control signal is designed as

$$u_0 = \frac{1}{g_3}\left[-f_3 - \hat{d}_3 - k_{31}\frac{z_3}{\sqrt{z_3^2 + (\varepsilon_{z3}/k_{31})^2}} - k_{32}z_3^3 - k_{33}z_3 + \dot{x}_{3c} - g_2 z_2\right], \tag{43}$$

where $k_{31}, k_{32}, k_{33}, \varepsilon_{z3}$ are positive constants.

The fixed-time filter is designed as

$$\dot{x}_{3c} = -k_{f31}\frac{y_3}{\sqrt{y_3^2 + (\varepsilon_{y3}/k_{f31})^2}} - k_{f32}y_3^3 - k_{f33}y_3, \tag{44}$$

where $k_{f31}, k_{f32}, k_{f33}, \varepsilon_{y3}$ are positive constants.

Consider the following Lyapunov function candidate

$$V_3 = \frac{1}{2}z_3^2 + \frac{1}{2}y_3^2. \tag{45}$$

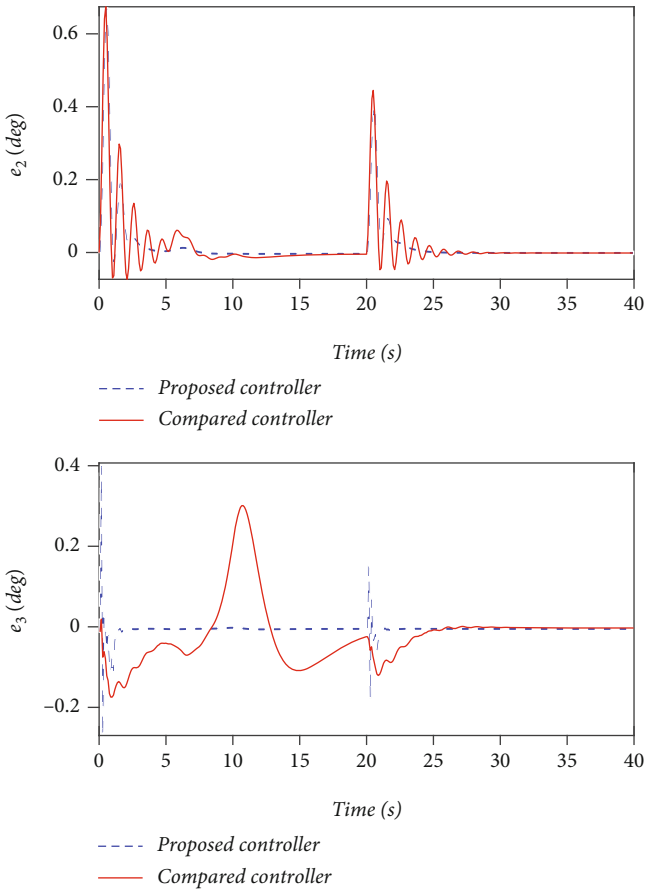

FIGURE 5: Tracking errors e_2 and e_3.

The time derivative of V_3 can be represented as

$$\begin{aligned}\dot{V}_3 = {} & z_3\tilde{d}_3 - k_{31}\frac{z_3^2}{\sqrt{z_3^2 + (\varepsilon_{z3}/k_{31})^2}} - k_{32}z_3^4 - k_{33}z_3^2 \\ & - z_2z_3g_2 - k_{f31}\frac{y_3^2}{\sqrt{y_3^2 + (\varepsilon_{y3}/k_{f31})^2}} - k_{f32}y_3^4 \\ & - k_{f33}y_3^2 - \dot{x}_{3d}y_3.\end{aligned} \tag{46}$$

Similar to the analysis of (33), (40), one has

$$\begin{aligned}\dot{V}_3 \le {} & \frac{1}{4k_{33}}\tilde{d}_3^2 - k_{31}|z_3| + \varepsilon_{z3} - k_{32}z_3^4 - z_2z_3g_2 \\ & - k_{f31}|y_3| + \varepsilon_{y3} - k_{f32}y_3^4 - k_{f33}y_3^2 - \dot{x}_{3d}y_3.\end{aligned} \tag{47}$$

4.2. Stability Analysis

Theorem 12. *Consider system (5), and assume that Assumptions 1 and 2 hold. The disturbance observer is designed as (14). The fixed-time controller is built as (30), (36), and (43), and dynamic filter is constructed as (37) and (44). For a given constant $P_1 > 0$, if $V(0) \le P_1$ and there exist the following positive constants $k_{i1}, k_{i2}, k_{i3}, \varepsilon_{zi}, \sigma_{1i}, \sigma_{2i}, n_i, \lambda_{i1}, \lambda_{i2}, \lambda_{i3}, \delta_i, \varepsilon_i, \theta_i, \gamma_i$ for $i = 1, 2, 3$ and $k_{fi1}, k_{fi2}, k_{fi3}, \varepsilon_{yi}$ for $i = 2, 3$, then, reference signal tracking errors z_i and fixed-time filter errors y_i converge to the neighborhood near the origin $\Omega_{z_i} = \{z_i \le \sqrt{2\sqrt{C/\mu_4}}\}, \Omega_{y_i} = \{y_i \le \sqrt{2\sqrt{C/\mu_4}}\}$ in a fixed time $T_s \le 2/\mu_3 + 1/\mu_4$.*

Remark 13. By differentiating x_{2d}, x_{3d}, one can obtain

$$\begin{aligned}\dot{x}_{2d} = {} & -\frac{\partial x_{2d}}{\partial f_1}\dot{f}_1 - \frac{\partial x_{2d}}{\partial \hat{d}_1}\dot{\hat{d}}_1 - \frac{\partial x_{2d}}{\partial z_1}\dot{z}_1 - \frac{\partial x_{2d}}{\partial y_2}\dot{y}_2 \\ & + \frac{\partial x_{2d}}{\partial g_1}\dot{g}_1 + \frac{\partial x_{2d}}{\partial \dot{x}_{1c}}\ddot{x}_{1c}, \\ \dot{x}_{3d} = {} & -\frac{\partial x_{3d}}{\partial f_2}\dot{f}_2 - \frac{\partial x_{3d}}{\partial \hat{d}_2}\dot{\hat{d}}_2 - \frac{\partial x_{3d}}{\partial z_2}\dot{z}_2 - \frac{\partial x_{2d}}{\partial z_1}\dot{z}_1 \\ & - \frac{\partial x_{3d}}{\partial y_3}\dot{y}_3 + \frac{\partial x_{2d}}{\partial g_1}\dot{g}_1 + \frac{\partial x_{2d}}{\partial g_2}\dot{g}_2 + \frac{\partial x_{3d}}{\partial \dot{x}_{2c}}\ddot{x}_{2c}.\end{aligned} \tag{48}$$

Because each partial of $\dot{x}_{2d}$ and $\dot{x}_{3d}$ is a continuous on a compact set $\Omega_V \times \Omega_{V_d}$, it has

$$-\dot{x}_{\mathrm{id}}y_i \le |\dot{x}_{\mathrm{id}}y_i| \le \frac{k_{\mathrm{fi}3}y_i^2}{2} + \frac{\bar{M}_{\mathrm{id}}^2}{2k_{\mathrm{fi}3}}, \tag{49}$$

2, 3.

Proof. The Lyapunov function candidate is considered to be

$$V = \sum_{i=1}^{3} V_i. \tag{50}$$

□

The time derivative of V can be represented as

$$\begin{aligned}\dot{V} = {} & \sum_{i=1}^{3} z_i\dot{z}_i + \sum_{i=2}^{3} y_i\dot{y}_i \\ \le {} & \sum_{i=1}^{3}\left(-\sqrt{2}k_{i1}\left(\frac{1}{2}z_i^2\right)^{1/2} - 4k_{i2}\left(\frac{1}{2}z_i^2\right)^2\right) \\ & + \sum_{i=2}^{3}\left(-\sqrt{2}k_{fi1}\left(\frac{1}{2}y_i^2\right)^{1/2} - 4k_{fi2}\left(\frac{1}{2}y_i^2\right)^2\right) + C\end{aligned} \tag{51}$$

where $C = \sum_{i=1}^{3}((1/2k_{i3})\tilde{d}_i^2 - (1/4k_{33})\tilde{d}_3^2 + \varepsilon_{\mathrm{zi}}) + \sum_{i=2}^{3}(\varepsilon_{yi} + (\bar{M}_{\mathrm{id}}^2/2k_{\mathrm{fi}3}))$.

Equation (51) can be further transformed as

$$\dot{V} \le -\mu_3V^{1/2} - \mu_4V^2 + C, \tag{52}$$

where μ_3 and μ_4 can be expressed as $\mu_3 = \min\{\sqrt{2}k_{11}, \sqrt{2}k_{i1}, \sqrt{2}k_{fi1}\}, \mu_4 = \min\{4k_{12}, 4k_{i2}, 4k_{fi2}\}, i = 2, 3$.

Note that, from (52), if $V \ge \sqrt{C/\mu_4}$, then $\dot{V} \le -\mu_3V^{1/2} \le 0$, which validates the boundedness of V. The boundedness of V means the boundedness of z_i for $i = 1, 2, 3$ and y_i for $i = 2, 3$.

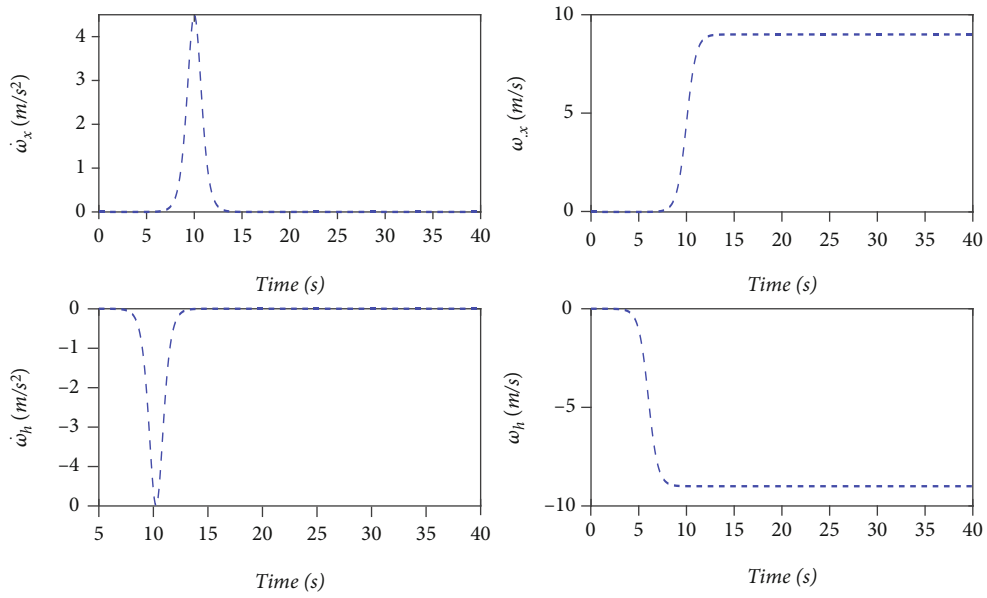

Figure 6: The curves of wind disturbance.

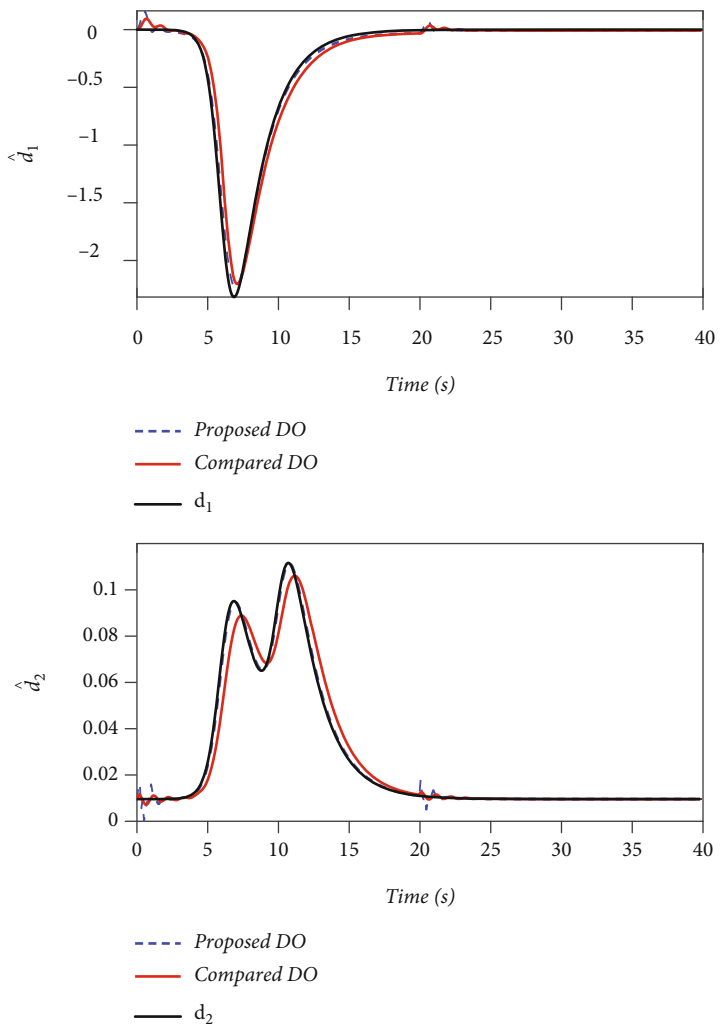

Figure 7: Estimation of d_1 and d_2.

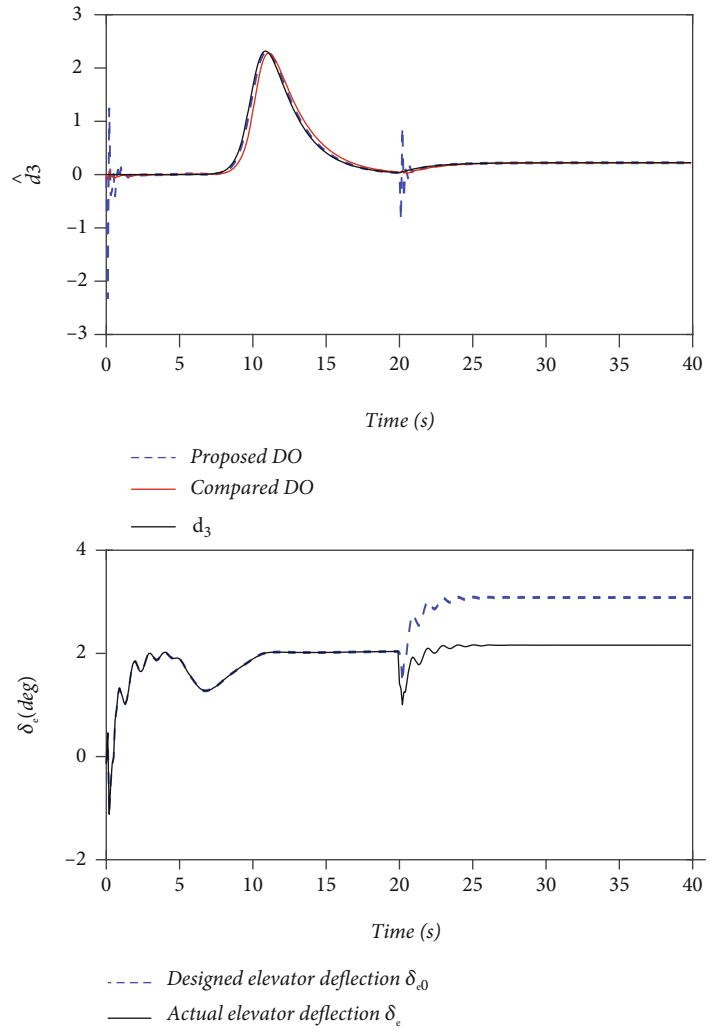

FIGURE 8: Estimation of d_3 and control input.

Naturally, it can be shown that the derivative of fixed-time filter output signal $\dot{x}_{ic}$ is bounded because of the boundedness of y_i. Then, we can get that the virtual control signal x_{id} is bounded because y_i, z_1, and $\dot{x}_{ic}$ are both bounded.

According to above analysis, one can get that V will converge to the set $\{V : V \le \sqrt{C/\mu_4}\}$ in fixed-time $T_s \le 2/\mu_3 + 1/\mu_4$. Moreover, we have that the tracking errors z_i and the filter errors $y_i i = 1, 2, 3$ will converge to the sets

$$\Omega_{z_i} = \left\{ z_i \le \sqrt{2\sqrt{\frac{C}{\mu_4}}} \right\},$$
$$\Omega_{y_i} = \left\{ y_i \le \sqrt{2\sqrt{\frac{C}{\mu_4}}} \right\}. \tag{53}$$

5. Numerical Simulations

In this section, comparative method [21] is used to verify the effectiveness of the proposed composite control scheme. The detailed parameters of the longitudinal model can refer to [27].

The controller parameters are designed as

$$\begin{aligned}
&k_{11} = k_{21} = k_{31} = 0.1, k_{12} = k_{22} = k_{32} = 0.1, \varepsilon_{z1} \\
&\quad = \varepsilon_{z2} = \varepsilon_{z3} = 0.01, k_{13} = 0.2, k_{23} = 0.7, k_{33} = 0.4, \\
&k_{f21} = 10, k_{f22} = 1, k_{f23} = 10, k_{f31} = 1, k_{f32} \\
&\quad = 0.001, k_{f33} = 10, \varepsilon_{y2} = 0.1, \varepsilon_{y3} = 0.0001, \theta_1 \\
&\quad = \theta_2 = \theta_3 = 1.1, \\
&\lambda_{11} = 10, \lambda_{12} = 0.5, \lambda_{13} = 0.5, \lambda_{21} = 10, \lambda_{22} \\
&\quad = 0.5, \lambda_{23} = 0.5, \lambda_{31} = 10, \lambda_{32} = 0.5, \gamma_1 \\
&\quad = \gamma_2 = \gamma_3 = 0.1, \\
&\lambda_{33} = 0.5, \varepsilon_1 = \varepsilon_2 = \varepsilon_3 = 0.5, \delta_1 = \delta_2 = \delta_3 \\
&\quad = 0.5, \frac{\sigma_{11}}{n_1} = \frac{\sigma_{12}}{n_2} = \frac{\sigma_{13}}{n_3} = 10, \frac{\sigma_{21}}{n_1^2} \\
&\quad = \frac{\sigma_{22}}{n_2^2} = \frac{\sigma_{23}}{n_3^2} = 0.01.
\end{aligned} \tag{54}$$

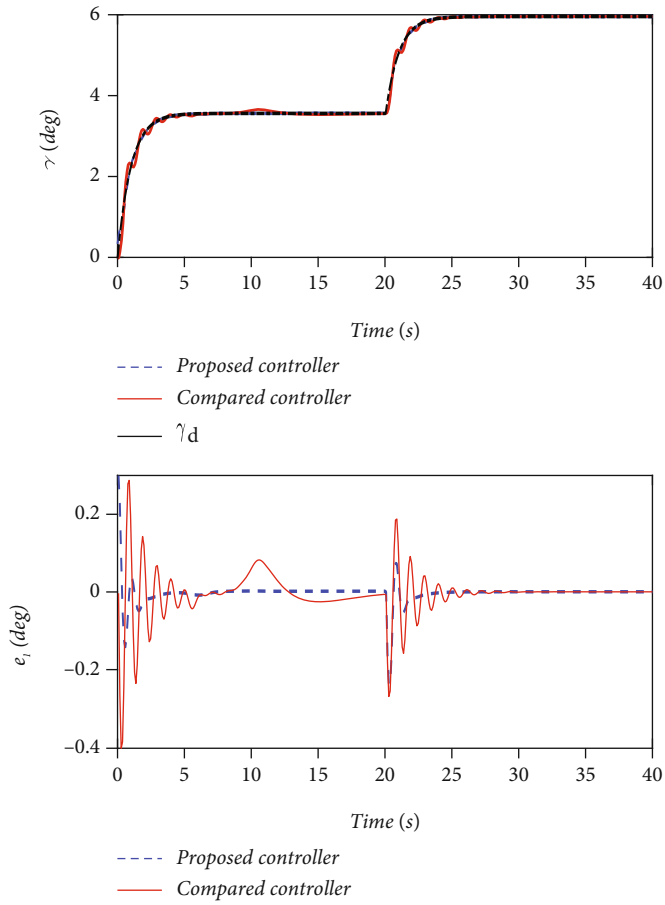

Figure 9: Tracking error e_1 and trajectories of γ.

The reference signal x_d is generated through the following filter:

$$\gamma_d(s) = \frac{5}{s+5}\gamma_d(s). \tag{55}$$

The initial state of the system is that $x_1(0) = 0, x_2(0) = 0, x_3(0) = 0$ and the disturbance signal including wind disturbance [32] is defined as

$$\Delta_\gamma = \dot{\omega}_h, \Delta_\alpha = \left(\frac{\dot{\omega}_h}{30}\right) - \left(\frac{\dot{\omega}_x}{30}\right), \Delta_q = \dot{\omega}_x, \tag{56}$$

where ω_x, ω_h are wind components.

The reference signal and actuator fault model are designed as

$$y_d = \begin{cases} 3, t < 20 \\ 5, t \geq 20 \end{cases}, \begin{cases} p_1 = 1, b_{f1} = 0, t < 20 \\ p_1 = 0.7, b_{f1} = 0.07, t \geq 20 \end{cases}. \tag{57}$$

Case 14. Against actuator fault and slight external disturbances.

In this simulation, external wind disturbances are considered to verify the robustness of the proposed composite control scheme. Figure 1 gives the wind disturbances. Figure 2 shows the estimated lumped disturbances. One can find that the compared DO and the proposed DO are both able to estimate lumped disturbances including actuator fault and external unmatched disturbances. However, the compared DO exhibits a larger disturbance estimation error. Curves of elevator deflection are shown as Figure 3. Figures 4 and 5 illustrate the tracking errors of flight-path angle, angle of attack, and pitch rate. It can be found that flight-path angle, angle of attack, and pitch rate react reasonably. The proposed controller exhibits smaller tracking errors than the compared method, when the actuator is fault at $t = 20s$.

Case 15. Against actuator fault and severe external disturbances.

In this simulation, severe wind disturbances are imposed on the UAV. The other conditions are kept as Case 14. Figure 6 gives the curves of the wind disturbances. Figures 7 and 8 illustrate the lumped disturbances estimation. Figures 9 and 10 describe the tracking errors. It can be seen that the disturbance estimation errors of the proposed DO are much smaller than the compared method. It is validated that the proposed controller operates well even though there exist the reinforced wind disturbance and actuator fault.

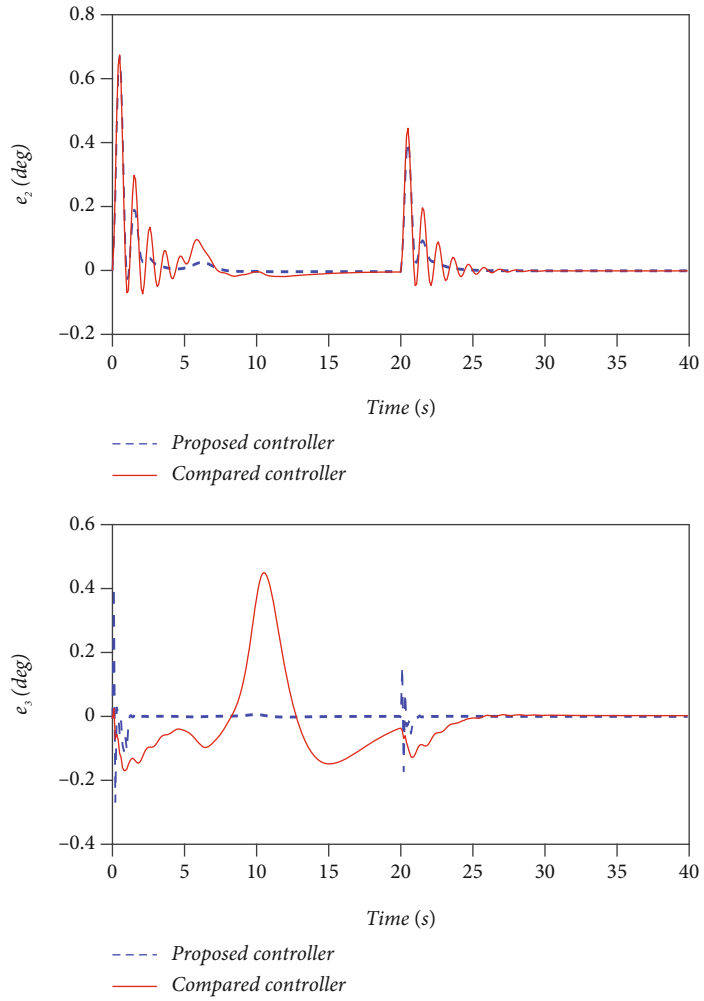

FIGURE 10: Tracking errors e_2 and e_3.

6. Conclusions

In this paper, the fixed-time fault-tolerant tracking control problem for the fixed-wing UAVs subject to external disturbances and actuator fault has been addressed. To estimate the lumped disturbance with unknown upper bound precisely, a new disturbance observer has been proposed. A new fixed-time fault-tolerant controller without fractional power terms has been proposed in this paper, which overcomes the potential singularity problem often encountered in fixed-time backstepping design procedures. Moreover, a new fixed-time dynamic surface filter has been added in the controller design to prevent the phenomenon of "differential explosion." Lyapunov stability analysis has proven the stability of the proposed control scheme. The simulation results verify the effectiveness of the proposed method.

Data Availability

The data used to support the findings of this study are included within the article.

Conflicts of Interest

The authors declare that they have no known competing financial interests or personal relationships that could have appeared to influence the work reported in this paper.

Acknowledgments

This work is supported by the National Natural Science Foundation of China (Grant no. 61903126), Key R&D and Promotion Projects in Henan Province (Grant no. 212102210197, 202102210130), the Key Scientific Research Project of Colleges and Universities in Henan Province (Grant no. 20A590001), the Outstanding Youth Fund of Henan Polytechnic University (Grant no. 722515/003/034), Outstanding Youth Fund of Henan Polytechnic University (Grant no. J2022-7), and the Doctoral Innovation Fund of Henan Polytechnic University (Grant no. 760807/028).

References

[1] Y. Xu, S. Tong, and Y. Li, "Adaptive fuzzy fault-tolerant output feedback control of uncertain nonlinear systems with actuator

faults based on dynamic surface technique," *Journal of the Franklin Institute*, vol. 350, no. 7, pp. 1768–1786, 2013.

[2] S. Gao, H. Dong, B. Ning, and X. Yao, "Single-parameter-learning-based fuzzy fault-tolerant output feedback dynamic surface control of constrained-input nonlinear systems," *Information Sciences*, vol. 385-386, pp. 378–394, 2017.

[3] H. Khebbache, S. Labiod, and M. Tadjine, "Adaptive sensor fault-tolerant control for a class of multi-input multi-output nonlinear systems: adaptive first-order filter-based dynamic surface control approach," *ISA Transactions*, vol. 80, pp. 89–98, 2018.

[4] H. Khebbache, M. Tadjine, and S. Labiod, "Adaptive sensor-fault tolerant control for a class of MIMO uncertain nonlinear systems: adaptive nonlinear filter-based dynamic surface control," *Journal of the Franklin Institute*, vol. 353, no. 6, pp. 1313–1338, 2016.

[5] Q. Lei, J. Yu, and Q. G. Wang, "Discrete-time command filtered adaptive fuzzy fault-tolerant control for induction motors with unknown load disturbances," *Journal of the Franklin Institute*, vol. 358, no. 5, pp. 2765–2779, 2021.

[6] S. Zeghlache, H. Mekki, A. Bouguerra, and A. Djerioui, "Actuator fault tolerant control using adaptive RBFNN fuzzy sliding mode controller for coaxial octorotor UAV," *ISA Transactions*, vol. 80, pp. 267–278, 2018.

[7] Z. Yu, Y. Zhang, Z. Liu, Y. Qu, C.-Y. Su, and B. Jiang, "Decentralized finite-time adaptive fault-tolerant synchronization tracking control for multiple UAVs with prescribed performance," *Journal of the Franklin Institute*, vol. 357, no. 16, pp. 11830–11862, 2020.

[8] Z. Yu, Y. Zhang, B. Jiang et al., "Distributed adaptive fault-tolerant close formation flight control of multiple trailing fixed-wing UAVs," *ISA Transactions*, vol. 106, pp. 181–199, 2020.

[9] Y. Cai, H. Zhang, J. Zhang, S. Sun, and Q. He, "Distributed fault-tolerant output regulation for heterogeneous linear multi- agent systems under actuator faults," *Journal of the Franklin Institute*, vol. 358, no. 7, pp. 3303–3331, 2021.

[10] Y. Liu, X. Dong, Z. Ren, and J. Cooper, "Fault-tolerant control for commercial aircraft with actuator faults and constraints," *Journal of the Franklin Institute*, vol. 356, no. 7, pp. 3849–3868, 2019.

[11] A. Abbaspour, P. Aboutalebi, K. K. Yen, and A. Sargolzaei, "Neural adaptive observer-based sensor and actuator fault detection in nonlinear systems: application in UAV," *ISA Transactions*, vol. 67, pp. 317–329, 2017.

[12] B. Brahmi, M. Driscoll, I. K. El Bojairami, M. Saad, and A. Brahmi, "Novel adaptive impedance control for exoskeleton robot for rehabilitation using a nonlinear time-delay disturbance observer," *ISA Transactions*, vol. 108, pp. 381–392, 2021.

[13] L. Zhang, C. Wei, R. Wu, and N. Cui, "Fixed-time extended state observer based non-singular fast terminal sliding mode control for a VTVL reusable launch vehicle," *Aerospace Science and Technology*, vol. 82-83, pp. 70–79, 2018.

[14] Y. Huang, M. Zhu, Z. Zheng, and M. Feroskhan, "Fixed-time autonomous shipboard landing control of a helicopter with external disturbances," *Aerospace Science and Technology*, vol. 84, pp. 18–30, 2019.

[15] L. Cui, X. Hou, Z. Zuo, and H. Yang, "An adaptive fast super-twisting disturbance observer-based dual closed-loop attitude control with fixed-time convergence for UAV," *Journal of the Franklin Institute*, vol. 359, no. 6, pp. 2514–2540, 2022.

[16] D. Swaroop, J. K. Hedrick, P. P. Yip, and J. C. Gerdes, "Dynamic surface control for a class of nonlinear systems," *IEEE Transactions on Automatic Control*, vol. 45, no. 10, pp. 1893–1899, 2000.

[17] Y. Hu, S. Dian, R. Guo, S. Li, and T. Zhao, "Observer-based dynamic surface control for flexible-joint manipulator system with input saturation and unknown disturbance using type-2 fuzzy neural network," *Neurocomputing*, vol. 436, pp. 162–173, 2021.

[18] X. Wu, W. Zheng, X. Zhou, and S. Shao, "Adaptive dynamic surface and sliding mode tracking control for uncertain QUAV with time-varying load and appointed-time prescribed performance," *Journal of the Franklin Institute*, vol. 358, no. 8, pp. 4178–4208, 2021.

[19] X. Yang, Y. Ge, W. Deng, and J. Yao, "Adaptive dynamic surface tracking control for uncertain full-state constrained nonlinear systems with disturbance compensation," *Journal of the Franklin Institute*, vol. 359, no. 6, pp. 2424–2444, 2022.

[20] K. Xia and H. Son, "Adaptive fixed-time control of autonomous VTOL UAVs for ship landing operations," *Journal of the Franklin Institute*, vol. 357, no. 10, pp. 6175–6196, 2020.

[21] Z. Zhang and Y. Wu, "Further results on fixed-time stabilization and tracking control of a marine surface ship subjected to output constraints," *Ieee Transactions on Systems Man Cybernetics-Systems*, vol. 51, no. 9, pp. 5300–5310, 2021.

[22] Z. Guan, H. Liu, Z. Zheng, M. Lungu, and Y. Ma, "Fixed-time control for automatic carrier landing with disturbance," *Aerospace Science and Technology*, vol. 108, article 106403, 2021.

[23] M. Zhuang, L. Tan, K. Li, and S. Song, "Fixed-time formation control for spacecraft with prescribed performance guarantee under input saturation," *Aerospace Science and Technology*, vol. 119, article 107176, 2021.

[24] Y. Tian, C. Du, P. Lu, Q. Jiang, and H. Liu, "Nonsingular fixed-time attitude coordinated tracking control for multiple rigid spacecraft," *ISA Transactions*, 2022.

[25] X. Jin, "Adaptive fixed-time control for MIMO nonlinear systems with asymmetric output constraints using universal barrier functions," *IEEE Transactions on Automatic Control*, vol. 64, no. 7, pp. 3046–3053, 2018.

[26] J. Tan, Y. Dong, P. Shao, and G. Qu, "Anti-saturation adaptive fault-tolerant control with fixed-time prescribed performance for UAV under AOA asymmetric constraint," *Aerospace Science and Technology*, vol. 120, article 107264, 2022.

[27] Z. Wu, J. Ni, W. Qian, X. Bu, and B. Liu, "Composite prescribed performance control of small unmanned aerial vehicles using modified nonlinear disturbance observer," *ISA Transactions*, vol. 116, pp. 30–45, 2021.

[28] H. Li, C.-L. Liu, Y. Zhang, and Y.-Y. Chen, "Adaptive neural networks-based fixed-time fault-tolerant consensus tracking for uncertain multiple Euler-Lagrange systems," *ISA Transactions*, 2021.

[29] S. Q. Liu and J. F. Whidborne, "Observer-based incremental backstepping sliding-mode fault-tolerant control for blended-wing-body aircrafts," *Neurocomputing*, vol. 464, pp. 546–561, 2021.

[30] L. Wei, M. Chen, and T. Li, "Disturbance-observer-based formation-containment control for UAVs via distributed adaptive event -triggered mechanisms," *Journal of the Franklin Institute*, vol. 358, no. 10, pp. 5305–5333, 2021.

[31] Z. Gao and G. Guo, "Fixed-time sliding mode formation control of AUVs based on a disturbance observer," *IEEE/CAA Journal of Automatica Sinica*, vol. 7, no. 2, pp. 539–545, 2020.

[32] C. Liu and W.-H. Chen, "Disturbance rejection flight control for small fixed-wing unmanned aerial vehicles," *Journal of Guidance, Control, and Dynamics*, vol. 39, no. 12, pp. 2810–2819, 2016.

Hindawi
International Journal of Aerospace Engineering
Volume 2022, Article ID 8385913, 18 pages
https://doi.org/10.1155/2022/8385913

Research Article

Decentralized Adaptive Fault-Tolerant Cooperative Control for Multiple UAVs with Input Saturation and State Constraints

Minrui Fu,[1] **Yiwei Xu**,[1] **Ziquan Yu**,[1] **and Youmin Zhang**[2]

[1]*College of Automation Engineering, Nanjing University of Aeronautics and Astronautics, Nanjing 211106, China*
[2]*Department of Mechanical, Industrial and Aerospace Engineering, Concordia University, Montreal, Quebec, Canada H3G 1M8*

Correspondence should be addressed to Youmin Zhang; ymzhang@encs.concordia.ca

Received 1 April 2022; Revised 26 July 2022; Accepted 29 July 2022; Published 5 October 2022

Academic Editor: Shaoming He

This paper proposes a fault-tolerant cooperative control (FTCC) scheme for multiple UAVs in a distributed communication network against input saturation, full-state constraints, actuator faults, and unknown dynamics. Firstly, by considering physical limitations, an auxiliary control signal is designed to simplify the analysis process. Secondly, to avoid the difficulty in the backstepping design caused by full-state constraints, virtual control signals are constructed to transform constrained variables, while the dynamic surface control is adopted to avoid the phenomenon of "differential explosion." Thirdly, a disturbance observer (DO) is designed to estimate the unknown uncertainty caused by parameter uncertainty and actuator fault. Moreover, a recurrent wavelet fuzzy neural network (RWFNN) is used to compensate for the estimation errors of DO. Finally, it is proved that all states are uniformly ultimately bounded (UUB) by Lyapunov and invariant set theory. The effectiveness of the proposed scheme is further demonstrated by the simulation results.

1. Introduction

In recent years, the development of unmanned aerial vehicle (UAV) technology has led to wide applications. However, single UAV provides limited capabilities, which may not be applicable to some highly complex tasks. Inspired by multiagent technology, researchers begin to investigate the application technology of multiple UAVs (multi-UAVs). Compared with a single UAV, multi-UAVs have more benefits in terms of forest fire monitoring, area detection, and disaster assistance. Unlike a single UAV, the cooperative control of multi-UAVs need the information from neighboring UAVs, which significantly increasing the control design challenge.

As the basis of multi-UAVs control, the cooperative control design is an important task. In the past few years, numerous research results of cooperative control have been reported. In [1], a cooperative control strategy for motion control of multiple unmanned vehicles was proposed, which can keep the formation during the motion. In [2], a novel distributed intermittent control framework for containment control of multiagent system was proposed, which can reduce the communication burden via a directed graph. In [3], the obstacle avoidance problem of multi-UAVs in multiple obstacle environment was studied. In [4], a robust adaptive control strategy for cooperative control of UAVs under the decentralized communication network was proposed against uncertainty. In [5], the authors investigated the cooperative transport control problem using multirotor UAVs. In [6], a system analysis method was proposed for the tracking control problem of multi-UAVs. The distributed framework was used to describe the dynamic model of UAV, and the information of nodes and networks were considered in the distributed control design. [7] studied the output feedback formation control of multi-UAVs without velocity and angular velocity sensors, which were obtained via the state observer. However, the above researches only focused on the distributed control of the first-order or second-order systems, and there exist few research on the cooperative control of fixed-wing UAVs with high-order nonlinear characteristics.

In addition, the number of components in the multi-UAV system is more than that of a single UAV. Therefore,

the probability of multi-UAVs suffering from the actuator, sensor, or component faults is higher than that of a single UAV. At present, many research results show that the incidence of actuator fault in flight is the highest. Therefore, many scholars mainly focus on actuator faults [8, 9]. The probability of actuator fault occurred in the multi-UAVs will also increase due to the fact that the number of actuators is significantly increased. When an actuator fault of a UAV in the communication network occurs and is not handled in time, it will reduce the stability and threaten the safety of all UAVs [10], making the investigation on fault-tolerant cooperative control (FTCC) a necessary task. In [11], based on the design of inner-outer-loop control and back-stepping control, an FTCC strategy was designed for multi-UAVs against permanent faults. In [12], Yu et al. further studied the FTCC design method of multi-UAVs by using a similar control framework of reference generator technology. It should be emphasized that the results [11, 12] are about the FTCC scheme of multi-UAVs under the master-slave framework, which cannot be directly applied to the distributed cooperative control design. Considering the diversity of research on cooperative control of multi-UAVs in the communication network, the FTCC scheme for multi-UAVs under distributed communication network needs to be further investigated.

Moreover, the actual multi-UAV system often encounters some problems such as input saturation, inaccurate aerodynamic parameters, and external interference, which lead to system instability or performance degradation [13–16]. Recently, many results have been reported to solve the problem of input saturation. In [17], a piecewise auxiliary system was introduced to deal with the asymmetric input constraints for a class of uncertain multi-input and multi-output nonlinear systems. Then, the auxiliary system was further used to deal with the force and moment constraints on ship [18]. In [19], another auxiliary signal was constructed using the error between the desired control input and the saturation control input. In [20], to solve the disadvantages of conventional methods based on the hyperbolic tangent function, an nth-order auxiliary dynamic system was skillfully constructed to avoid the effect of input saturation.

It should be emphasized that although numerous studies have been reported on the above literature, few results have studied the input saturation, inaccurate aerodynamic parameters, and external interference encountered by multi-UAVs in distributed communication networks at the same time. However, such factors are inevitable in the formation flight of multi-UAVs. If these factors are not solved in time, it may lead to the instability of the networked UAV system.

Furthermore, due to physical limitations, UAV states should be constrained. However, control strategies developed recently for multi-UAVs in the distributed communication network rarely consider these constraints on the states. Based on the above discussion, this paper proposes a distributed FTCC scheme for multi-UAVs under the distributed communication network with input saturation, state constraints, actuator faults, and unknown dynamics. In this work, to avoid the difficulty in designing the control policy due to the input saturation, an auxiliary control signal is designed to transform the restricted input. To handle the full-state constraint problem, virtual control signals are defined to replace the constraints, which can simplify the back-stepping design. For the unknown nonlinear dynamics caused by actuator faults and other unknown uncertainties, disturbance observer (DO) is designed for providing the estimation, while a recurrent wavelet fuzzy neural network (RWFNN) is adopted to further compensate the estimation error. In the RWFNN, the online adaptive learning strategy of parameters is designed based on the Lyapunov theory. Compared with other existing works, the main contributions of this paper are as follows:

(1) In [21–23], actuator faults, input saturation, output constraints, and external disturbances were considered, while the state constraints were not taken into account. To obtain satisfactory control performance against such factors, the FTCC scheme is designed in this paper by simultaneously considering the state constraints, actuator faults, and external disturbances.

(2) Compared with [24–27], which assessed uncertainty dynamics by designing a DO without compensation of the DO estimation error, this work further adopts an RWFNN to offset the estimation error, in which the parameters are updated by the proposed online learning strategy.

The organization of this paper is arranged as follows. Section 2 describes the preliminaries and problem statement. The design process of the FTCC scheme and the stability analysis are given in Section 3. Section 4 shows the simulation results and analysis. Finally, the conclusion is drawn in Section 5.

2. Preliminaries and Problem Statement

2.1. System Dynamics. In this paper, the cooperative control of N UAVs is investigated. The set of UAVs is denoted as $\Omega = \{1, 2, \cdots, N\}$, and the position dynamics of the ith UAV is described as

$$\begin{cases} \dot{x}_i = V_i \cos\gamma_i \cos\chi_i, \\ \dot{y}_i = V_i \cos\gamma_i \sin\chi_i, \\ \dot{z}_i = V_i \sin\gamma_i, \end{cases} \tag{1}$$

where $i \in \Omega$, x_i, y_i, and z_i are the positions. V_i, γ_i, and χ_i are velocity, flight path angle, and heading angle, respectively.

The aerodynamic force equations are given by

$$\begin{cases} \dot{V}_i = \dfrac{1}{m_i}(-D_i + T_i \cos\alpha_i \cos\beta_i) - g \sin\gamma_i, \\ \dot{\chi}_i = \dfrac{1}{m_i V_i \cos\gamma_i}((L_i \sin\mu_i + Y_i \cos\mu_i) + T_i(\sin\alpha_i \sin\mu_i - \cos\alpha_i \sin\beta_i \cos\mu_i)), \\ \dot{\gamma}_i = \dfrac{1}{m_i V_i}(L_i \cos\mu_i - Y_i \sin\mu_i) - \dfrac{g\cos\gamma_i}{V_i} + \dfrac{T_i}{m_i V_i}(\cos\alpha_i \sin\beta_i \sin\mu_i + \sin\alpha_i \cos\mu_i), \end{cases} \tag{2}$$

where $i \in \Omega$, m_i and g are the mass of the ith UAV and

gravitational coefficient, respectively; T_i, D_i, L_i, Y_i are the thrust, drag, lift, and lateral forces, respectively, and μ_i, α_i, and β_i are the bank angle, angle of attack, and sideslip angle, respectively.

The attitude kinematic model is expressed as

$$\begin{cases} \dot{\alpha}_i = q_i - \tan\beta_i(p_i\cos\alpha_i + r_i\sin\alpha_i), \\ \dot{\beta}_i = p_i\sin\alpha_i - r_i\cos\alpha_i + \dot{\chi}_i\cos\gamma_i\cdot\cos\mu_i - \dot{\gamma}_i\sin\mu_i, \\ \dot{\mu}_i = p_i\cos\alpha_i + \dfrac{r_i\sin\alpha_i}{\cos\beta_i} + \dot{\gamma}_i\cdot\cos\mu_i\tanh\beta_i + \dot{\chi}_i(\sin\gamma_i + \cos\gamma_i\sin\mu_i\tan\beta_i), \end{cases} \tag{3}$$

where $i \in \Omega$. p_i, q_i, and r_i are the angular rates.

The angular rate model is given as

$$\begin{cases} \dot{p}_i = (c_{i1}r_i + c_{i2}p_i)q_i + c_{i3}\mathscr{L}_i + c_{i4}\mathscr{N}_i, \\ \dot{q}_i = c_{i5}p_ir_i - c_{i6}\left(p_i^2 - r_i^2\right) + c_{i7}\mathscr{M}_i, \\ \dot{r}_i = (c_{i8}p_i - c_{i2}r_i)q_i + c_{i4}\mathscr{L}_i + c_{i9}\mathscr{N}_i, \end{cases} \tag{4}$$

where $i \in \Omega$. $\mathscr{L}_i$, $\mathscr{M}_i$, and $\mathscr{N}_i$ are roll, pitch, and yaw moments, respectively.

The forces T_i, D_i, L_i, and Y_i and the aerodynamic moments $\mathscr{L}_i$, $\mathscr{M}_i$, and $\mathscr{N}_i$ are expressed as

$$\begin{cases} T_i = T_{i\,\max}\delta_{T_i}, D_i = Q_is_iC_{iD}, \\ L_i = Q_is_iC_{iL}, Y_i = Q_is_iC_{iY}, \\ \mathscr{L}_i = Q_is_ib_iC_{i\mathscr{L}}, \mathscr{M}_i = Q_is_ic_iC_{i.\mathscr{M}}, \\ \mathscr{N}_i = Q_is_ib_iC_{i.\mathscr{N}}, \end{cases} \tag{5}$$

where $Q_i = \rho V_i^2/2$ is the dynamic pressure and s_i, b_i, and c_i represent the wing area, wing span, and mean aerodynamic chord, respectively. $T_{i\,\max}$ and δ_{T_i} are the maximum thrust and instantaneous thrust throttle setting, respectively. C_{iL}, C_{iD}, C_{iY}, $C_{i\mathscr{L}}$, $C_{i.\mathscr{M}}$, and $C_{i.\mathscr{N}}$ are given by

$$\begin{cases} C_{iL} = C_{iL0} + C_{iL\alpha}\alpha_i, \\ C_{iD} = C_{iD0} + C_{iD\alpha}\alpha_i + C_{iD\alpha^2}\alpha_i^2, \\ C_{iY} = C_{iY0} + C_{iY\beta}\beta_i, \end{cases} \tag{6}$$

$$\begin{cases} C_{i\mathscr{L}} = C_{i\mathscr{L}0} + C_{i\mathscr{L}\beta}\beta_i + C_{i\mathscr{L}\delta_a}\delta_{ia} + C_{i\mathscr{L}\delta_r}\delta_{ir} + \dfrac{C_{i\mathscr{L}p}b_ip_i + C_{i\mathscr{L}r}b_ir_i}{2V_i}, \\ C_{i.\mathscr{M}} = C_{i.\mathscr{M}0} + C_{i.\mathscr{M}\alpha}\alpha_i + C_{i.\mathscr{M}\delta_e}\delta_{ie} + \dfrac{C_{i.\mathscr{M}q}c_iq_i}{2V_i}, \\ C_{i.\mathscr{N}} = C_{i.\mathscr{N}0} + C_{i.\mathscr{N}\beta}\beta_i + C_{i.\mathscr{N}\delta_{ia}}\delta_{ia} + C_{i.\mathscr{N}\delta_r}\delta_{ir} + \dfrac{C_{i.\mathscr{N}p}b_ip_i}{2V_i} + \dfrac{C_{i.\mathscr{N}r}b_ir_i}{2V_i}, \end{cases} \tag{7}$$

where δ_{ia}, δ_{ie}, and δ_{ir} are aileron, elevator, and rudder deflections, respectively. C_{iL0}, $C_{iL\alpha}$, C_{iD0}, $C_{iD\alpha}$, $C_{iD\alpha^2}$, C_{iY0}, $C_{iY\beta}$, $C_{i\mathscr{L}0}$, $C_{i\mathscr{L}\beta}$, $C_{i\mathscr{L}\delta_a}$, $C_{i\mathscr{L}\delta_r}$, $C_{i\mathscr{L}p}$, $C_{i\mathscr{L}r}$, $C_{i.\mathscr{M}0}$, $C_{i.\mathscr{M}\alpha}$, $C_{i.\mathscr{M}\delta_e}$, $C_{i.\mathscr{M}q}$, $C_{i.\mathscr{N}0}$, $C_{i.\mathscr{N}\beta}$, $C_{i.\mathscr{N}\delta_a}$, $C_{i.\mathscr{N}\delta_r}$, $C_{i.\mathscr{N}p}$, and $C_{i.\mathscr{N}r}$ are aerodynamic derivatives. The definition of the inertial terms $c_{ij}(j = 1, 2, \cdots, 9)$ in (4) can be found in [28].

2.2. Control-Oriented Model. By defining $\mathbf{X}_{i1} = [\mu_i, \alpha_i, \beta_i]^T$, $\mathbf{X}_{i2} = [p_i, q_i, r_i]^T$, and $\mathbf{U}_i = [\delta_{1a}, \delta_{1e}, \delta_{1r}]^T$ and substituting (5), (6), and (7) into (1), (2), (3), and (4), then it follows that

$$\dot{\mathbf{X}}_{i1} = \mathbf{F}_{i1} + \mathbf{G}_{i1}\mathbf{X}_{i2} \tag{8}$$

$$\dot{\mathbf{X}}_{i2} = \mathbf{F}_{i2} + \mathbf{G}_{i2}\mathbf{U}_i \tag{9}$$

where $\mathbf{F}_{i1}$, $\mathbf{G}_{i1}$, $\mathbf{F}_{i2}$, and $\mathbf{G}_{i2}$ are given by

$$\mathbf{F}_{i1} = \begin{bmatrix} 0 & \sin\gamma_i + \cos\gamma_i\sin\mu_i\tan\beta_i & \cos\mu_i\tan\beta_i \\ 0 & -\dfrac{\cos\gamma_i\sin\mu_i}{\cos\beta_i} & -\dfrac{\cos\mu_i}{\cos\beta_i} \\ 0 & \cos\gamma_i\cos\mu_i & -\sin\mu_i \end{bmatrix} \begin{bmatrix} \dfrac{-D_i + T_i\cos\alpha_i\cos\beta_i}{m_i} - g\sin\gamma_i \\ \dfrac{1}{m_iV_i\cos\gamma_i}[L_i\sin\mu_i + Y_i\cos\mu_i + \\ T_i(\sin\alpha_i\sin\mu_i - \cos\alpha_i\sin\beta_i\cos\mu_i)] \\ -\dfrac{g\cos\gamma_i}{V_i} + \dfrac{1}{m_iV_i}[L_i\cos\mu_i - Y_i\sin\mu_i \\ +T_i(\cos\alpha_i\sin\beta_i\sin\mu_i + \sin\alpha_i\cos\mu_i)] \end{bmatrix},$$

$$\mathbf{G}_{i1} = \begin{bmatrix} \dfrac{\cos\alpha_i}{\cos\beta_i} & 0 & \dfrac{\sin\alpha_i}{\cos\beta_i} \\ -\cos\alpha_i\tan\beta_i & 1 & -\sin\alpha_i\tan\beta_i \\ \sin\alpha_i & 0 & -\cos\alpha_i \end{bmatrix},$$

$$\mathbf{F}_{i2} = [F_{i21}, F_{i22}, F_{i23}]^{\mathrm{T}}$$

$$\begin{cases} F_{i21} = c_{i1}q_ir_i + c_{i2}p_iq_i + c_{i3}\bar{q}_is_ib_i\left(C_{i\mathscr{L}0} + C_{i\mathscr{L}\beta_i} + \dfrac{C_{i\mathscr{L}p}b_ip_i}{2V_i} + \dfrac{C_{i\mathscr{L}r}b_ir_i}{2V_i}\right) \\ F_{i22} = c_{i5}p_ir_i - c_{i6}\left(p_i^2 - r_i^2\right) + c_{i7}\bar{q}_is_ic_i\left(C_{i.\mathscr{M}0} + C_{i.\mathscr{M}\alpha}\alpha_i + \dfrac{C_{i.\mathscr{M}q}c_iq_i}{2V_i}\right) \\ F_{i23} = c_{i8}p_iq_i - c_{i2}q_ir_i + c_{i4}\bar{q}_is_ib_i\left(C_{i\mathscr{L}0} + C_{i\mathscr{L}\beta}\cdot\beta_i + \dfrac{C_{i\mathscr{L}p}b_ip_i}{2V_i} + \dfrac{C_{i\mathscr{L}r}b_ir_i}{2V_i}\right) + c_{i9}\bar{q}_is_ib_i\cdot\left(C_{i.\mathscr{N}0} + C_{i.\mathscr{N}\beta_i} + \dfrac{C_{i.\mathscr{N}p}b_ip_i}{2V_i} + \dfrac{C_{i.\mathscr{N}r}b_ir_i}{2V_i}\right) \end{cases}$$

$$\begin{cases} \mathbf{G}_{i2} = \begin{bmatrix} a_{11} & 0 & a_{13} \\ 0 & a_{22} & 0 \\ a_{31} & 0 & a_{33} \end{bmatrix}, \\ a_{11} = c_{i3}\bar{q}_i s_i b_i C_{i\mathscr{L}\delta_a} + c_{i4}\bar{q}_i s_i b_i C_{i\mathscr{N}\delta_a}, \\ a_{13} = c_{i3}\bar{q}_i s_i b_i C_{i\mathscr{L}\delta_r} + c_{i4}\bar{q}_i s_i b_i C_{i\mathscr{N}\delta_r}, \\ a_{22} = c_{i7}\bar{q}_i s_i c_i C_{i\mathscr{M}\delta_e}, \\ a_{31} = c_{i4}\bar{q}_i s_i b_i C_{i\mathscr{L}\delta_a} + c_{i9}\bar{q}_i s_i b_i C_{i\mathscr{N}\delta_a}, \\ a_{33} = c_{i4}\bar{q}_i s_i b_i C_{i\mathscr{L}\delta_r} + c_{i9}\bar{q}_i s_i b_i C_{i\mathscr{N}\delta_r}. \end{cases} \tag{10}$$

It can be seen that $\mathbf{F}_{i2}$ and $\mathbf{G}_{i2}$ have many aerodynamic parameters. However, it is difficult to obtain accurate aerodynamic parameters of UAVs in practical engineering applications. To facilitate the design of the controller, $\mathbf{F}_{i2}$ and $\mathbf{G}_{i2}$ can be decomposed into known items $\mathbf{F}_{i20}$, $\mathbf{G}_{i20}$ and unknown items $\Delta\mathbf{F}_{i2}$, $\Delta\mathbf{G}_{i2}$, respectively.

Then, the attitude model can be described as

$$\dot{\mathbf{X}}_{i1} = \mathbf{F}_{i1} + \mathbf{G}_{i1}\mathbf{X}_{i2}, \tag{11}$$

$$\dot{\mathbf{X}}_{i2} = \mathbf{F}_{i20} + \Delta\mathbf{F}_{i2} + (\mathbf{G}_{i20} + \Delta\mathbf{G}_{i2})\mathbf{U}_i, \tag{12}$$

where $\Delta\mathbf{F}_{i2}$, and $\Delta\mathbf{G}_{i2}$ are unknown nonlinear functions caused by the uncertain parameters, while $\mathbf{F}_{i1}$, $\mathbf{G}_{i1}$, $\mathbf{F}_{i20}$, and $\mathbf{G}_{i20}$ are known functions.

Remark 1. Due to the physical constraints, the sideslip angle $\beta_i \neq \pm\pi/2$, and $\det(\boldsymbol{G}_{i1}) = -\sec\beta_i$, so $\boldsymbol{G}_{i1}$ is invertible. In addition, $\boldsymbol{G}_{i2}$ is related to aerodynamic parameters so that it is invertible in the flight envelope.

2.3. Actuator Fault and Input Saturation. In this paper, the actuator fault is considered, which includes gain and bias failures. Therefore, the fault model can be expressed as [29]

$$\mathbf{U}_i = \boldsymbol{\rho}_i\mathbf{U}_{i0} + \mathbf{U}_{\mathrm{if}}, \tag{13}$$

where $i \in \Omega$, $\mathbf{U}_{i0} = [u_{i01}, u_{i02}, u_{i03}]^T$ represents the designed control signal, and $\mathbf{U}_i = [\delta_{ia}, \delta_{ie}, \delta_{ir}]^T$ is the actual control signal. $\boldsymbol{\rho}_i = \mathrm{diag}\{\rho_{i1}, \rho_{i2}, \rho_{i3}\}$ with $0 < \rho_{i1}, \rho_{i2}, \rho_{i3} \leq 1$ represents the gain fault matrix, and $\mathbf{U}_{\mathrm{if}} \in \mathbb{R}^3$ represents bias fault vector.

In the practical application, the output of the actuator is limited. In order to avoid the incredible phenomenon caused by actuator saturation, the designed control signal $\mathbf{U}_{i0}$ needs to satisfy the following constraint:

$$u_{i0\tau\ \min} \leq u_{i0\tau} \leq u_{i0\tau\ \max}, \quad \tau = \{1, 2, 3\}, \tag{14}$$

where $\tau = \{1, 2, 3\}$, $u_{i0\tau\ \max}$ is a positive constant and $u_{i0\tau\ \min}$ is a negative constant, which is the maximum and minimum allowable values for the actuator, respectively.

To solve input saturation problem, an auxiliary signal $\mathbf{v}_i = [v_{i1}, v_{i2}, v_{i3}]^T$ is used to get control signal $\mathbf{U}_{i0}(\mathbf{v}_i)$, and $\mathbf{U}_{i0}(v_i) = [u_{i01}(v_{i1}), u_{i02}(v_{i2}), u_{i03}(v_{i3})]^{\mathrm{T}}$, which is expressed as

$$u_{i0\tau}(v_{i\tau}) = \begin{cases} u_{i0\tau\ \max}\tanh\left(\dfrac{v_{i\tau}}{u_{i0\tau\ \max}}\right), v_{i\tau} \geq 0, \\ u_{i0\tau\ \min}\tanh\left(\dfrac{v_{i\tau}}{u_{i0\tau\ \min}}\right), v_{i\tau} < 0. \end{cases} \tag{15}$$

By substituting (13) and (15) into (12), then the attitude model can be expressed as

$$\dot{\mathbf{X}}_{i1} = \mathbf{F}_{i1} + \mathbf{G}_{i1}\mathbf{X}_{i2}, \tag{16}$$

$$\dot{\mathbf{X}}_{i2} = \mathbf{F}_{i20} + \mathbf{G}_{i20}\mathbf{U}_{i0}(\mathbf{v}_i) + \mathbf{D}_i, \tag{17}$$

where $\mathbf{D}_i = \Delta\mathbf{F}_{i2} + \mathbf{G}_{i20}((\rho_i - \mathbf{I}_3)\mathbf{U}_{i0} + \mathbf{U}_{\mathrm{if}}) + \Delta\mathbf{G}_{i2}\mathbf{U}_i$ is an unknown nonlinear function. Due to $\mathbf{D}_i$ being related to auxiliary control signal $\mathbf{v}_i$, designing the observer of unknown function $\mathbf{D}_i$ for generating the control signal $\mathbf{v}_i$ will cause the problem of "algebraic ring," which is solved by introducing the following first-order filter:

$$\dot{\boldsymbol{v}}_i = -\boldsymbol{\Lambda}\boldsymbol{v}_i + \boldsymbol{\xi}, \tag{18}$$

where $\boldsymbol{\Lambda}$ is a diagnonal matrix with positive eigenvalue and $\boldsymbol{\xi}$ is an auxiliary control signal.

Remark 2. As shown in (13), the fault that occurs in the actuator will diminish its ability to provide control input. For example, the range of motion of the rudder surface can reach $-25 \sim 25$ deg in the normal state, while it may deteriorate into $-20 \sim 20$ deg after the fault occurs. It seems in the fault conditions the actuator is more likely to occur saturation, i.e., cannot reach to the expected control value. In this paper, the upper and lower boundaries of the control input are fixed to the values in the normal state of the actuator, and a hyperbolic function is used to prevent actuator saturation as shown in (15). Meanwhile, using virtual control signal $\mathbf{v}_i$ and $\boldsymbol{\xi}$ to generate the expected control signal $\mathbf{U}_{i0}$ and using RWFNN to evaluate uncertainty item $\mathbf{D}_i$ which contains the actuator bias section, even though the fault could occur, the system can still keep stable.

2.4. State Constraints. The states $\mathbf{X}_{i1} = [\mu_i, \alpha_i, \beta_i]^{\mathrm{T}}$ and $\mathbf{X}_{i2} = [p, q, r]^{\mathrm{T}}$ generally have constraints in the practical application. In this paper, such a problem has been concerned. Due to the fact that states $\mathbf{X}_{i1}$ and $\mathbf{X}_{i2}$ have limits, inspired by works [30, 31], a transformation is used to convert the restricted states $\mathbf{X}_{i1}$ and $\mathbf{X}_{i2}$ to unrestricted states $\mathbf{Z}_{i1}$ and $\mathbf{Z}_{i2}$:

$$Z_{i1\tau} = \ln\frac{X_{i1\tau} - \underline{X}_{i1\tau}}{\overline{X}_{i1\tau} - X_{i1\tau}}, \tag{19}$$

$$Z_{i2\tau} = \ln \frac{X_{i2\tau} - \underline{X}_{i2\tau}}{\bar{X}_{i2\tau} - X_{i2\tau}}, \tag{20}$$

where $\tau = 1, 2, 3$. $X_{i1\tau}$, $X_{i2\tau}$, $Z_{i1\tau}$ and $Z_{i2\tau}$ represent the τth element of $\mathbf{X}_{i1}$, $\mathbf{X}_{i2}$, $\mathbf{Z}_{i1}$, and $\mathbf{Z}_{i2}$, respectively. $\bar{X}_{i1\tau}$ and $\bar{X}_{i2\tau}$ represent maximum allowable range of the τth element of $\mathbf{X}_{i1}$ and $\mathbf{X}_{i2}$, respectively, while the $\underline{X}_{i1\tau}$ and $\underline{X}_{i2\tau}$ represent minimum allowable range of the τth element of $\mathbf{X}_{i1}$ and $\mathbf{X}_{i2}$, respectively.

Remark 3. Since (19) and (20) are bijective, $\mathbf{X}_{i1}$ and $\mathbf{X}_{i2}$ will always stay in their own limits if $\mathbf{Z}_{i1}$ and $\mathbf{Z}_{i2}$ are bounded on $\forall t \geq 0$.

2.5. Basic Graph Theory. In this paper, an undirected graph $\mathcal{G} = \{\mathcal{V}, \mathcal{C}, \mathcal{A}\}$ is used to describe the formation flight of N UAVs. The set of UAVs is described by $\mathcal{V} = \{v_1, v_2, \cdots, v_N\}$, $\mathcal{C} \subseteq \mathcal{V} \times \mathcal{V}$ represents the communication links between UAVs, and $\mathcal{A} \in R^{N\times N}$ is the adjacency matrix. If the link between the ith UAV and jth UAV exists, $a_{ij} = a_{ji} = 1$, which are the elements of $\mathcal{A}$. A path from the ith UAV to the kth UAV can be a sequence $v_i \longrightarrow v_j \longrightarrow v_k$, where $(v_i, v_j), (v_j, v_k) \in \mathcal{C}$. If there exists a path between any two UAVs, then $\mathcal{G}$ is a connected graph. A set is defined as $N_i = \{j : (v_i, v_j) \in \mathcal{C}, i \neq j\}$, and the degree matrix is defined as $\mathcal{D} = \text{diag}\{d_i\} \in \mathbb{R}^{N\times N}$, where $d_i = \sum_{j\in N_i} a_{ij}$. The Laplacian matrix $\mathcal{L} \in \mathbb{R}^{N\times N}$ is denoted as

$$\mathcal{L} = \mathcal{D} - \mathcal{A}. \tag{21}$$

Assumption 4. The undirected graph $\mathcal{G}$ containing N UAVs is connected.

Lemma 5. *Under Assumption 4, $\mathcal{L}$ and $\mathcal{L} + \text{diag}(\Omega)$ are symmetric and positive definite [32].*

2.6. Control Objective. In this paper, the control objective is to design an FTCC scheme for N UAVs, such that the attitude tracking error of each UAVs can be finally uniformly bounded, while the attitude $\mathbf{X}_{i1}$ and $\mathbf{X}_{i2}$ of all UAVs are always in limits, even when a portion of UAVs is subjected to actuator saturation and actuator faults.

3. Fault-Tolerant Cooperative Controller Design and Stability Analysis

In this section, the process of designing the FTCC scheme for N UAVs will be described. A main method adopted in the design is transforming the individual tracking error of each UAV to the synchronization tracking error.

3.1. Fault-Tolerant Cooperative Controller Design. Define the independent tracking error of ith UAV as $\tilde{\mathbf{Z}}_{i1} = \mathbf{Z}_{i1} - \mathbf{Z}_{i1d}$, then the cooperative tracking error of ith UAV is defined as

$$\mathbf{E}_{i1} = \lambda_1 \tilde{\mathbf{Z}}_{i1} + \lambda_2 \sum_{j\in N_i} a_{ij}\left(\tilde{\mathbf{Z}}_{i1} - \tilde{\mathbf{Z}}_{j1}\right), \tag{22}$$

where $\mathbf{E}_{i1} = [E_{i11}, E_{i12}, E_{i13}]^T$, λ_1 and λ_2 are positive parameters, which are used to regulate the cooperative tracking performance.

Using the Kronecker product "$\otimes$", and define $\mathbf{E}_1 = [\mathbf{E}_{11}^T, \mathbf{E}_{21}^T, \cdots, \mathbf{E}_{N1}^T]^T$, $\tilde{\mathbf{Z}}_1 = [\tilde{\mathbf{Z}}_{11}^T, \tilde{\mathbf{Z}}_{21}^T, \cdots, \tilde{\mathbf{Z}}_{N1}^T]^T$, then the cooperative tracking error of all UAVs can be expressed as

$$\mathbf{E}_1 = [(\lambda_1 \mathbf{I}_N + \lambda_2 \mathcal{L}) \otimes \mathbf{I}_3]\tilde{\mathbf{Z}}_1. \tag{23}$$

By recalling Lemma 5, it yields $\|\tilde{\mathbf{Z}}_1\| = \|[(\lambda_1 + \lambda_2\mathcal{L})^{-1} \otimes \mathbf{I}_3]\mathbf{E}_1\| \leq 1/(\sigma_{\min}(\lambda_1 + \lambda_2\mathcal{L}))\|\mathbf{E}_1\|$, where $\sigma_{\min}(\cdot)$ represents the minimum singular value of matrix "$\cdot$." Therefore, $\tilde{\mathbf{Z}}_1 \longrightarrow 0$ if $\mathbf{E}_1 \longrightarrow 0$.

Using (22), the synchronization error of each UAV $\mathbf{E}_{i1}$ can be expressed as

$$\mathbf{E}_{i1} = \left(\lambda_1 + \lambda_2 \sum_{j\in N_i}^{j\neq i} a_{ij}\right)\tilde{\mathbf{Z}}_{i1} - \lambda_2 \sum_{j\in N_i}^{j\neq i} a_{ij}\tilde{\mathbf{Z}}_{j1}. \tag{24}$$

Differentiating (24) yields

$$\begin{aligned}\dot{\mathbf{E}}_{i1} &= A_i\left(\mathbf{g}_{i1}(\mathbf{X}_{i1})\dot{\mathbf{X}}_{i1} - \mathbf{g}_{i1}(\mathbf{X}_{i1d})\dot{\mathbf{X}}_{i1d}\right) - \lambda_2 \sum_{j\in N_i}^{j\neq i} a_{ij}\dot{\tilde{\mathbf{Z}}}_{j1} \\ &= A_i\left(\mathbf{g}_{i1}(\mathbf{X}_{i1})\dot{\mathbf{X}}_{i1} - \mathbf{g}_{i1}(\mathbf{X}_{i1d})\dot{\mathbf{X}}_{i1d}\right) \\ &\quad - \lambda_2 \sum_{j\in N_i}^{j\neq i} a_{ij}\left(\mathbf{g}_{i1}\left(\mathbf{X}_{j1}\right)\dot{\mathbf{X}}_{j1} - \mathbf{g}_{i1}\left(\mathbf{X}_{j1d}\right)\dot{\mathbf{X}}_{j1d}\right),\end{aligned} \tag{25}$$

where $A_i = \lambda_1 + \lambda_2 \sum_{j\in N_i}^{j\neq i} a_{ij}$, $\mathbf{g}_{i1}(\mathbf{x})$ is $\mathbb{R}^3 \longrightarrow \mathbb{R}^{3\times 3}$, $\mathbf{x} = [x_1, x_2, x_3]^{\mathrm{T}}$, which is expressed as

$$\begin{cases} \mathbf{g}_{i1}(\mathbf{x}) = \text{diag}\{g_{i1\tau}(x_\tau)\}, \quad \tau = \{1, 2, 3\}, \\ g_{i1\tau}(x_\tau) = \dfrac{\bar{X}_{i1\tau} - \underline{X}_{i1\tau}}{(x_\tau - \underline{X}_{i1\tau})(\bar{X}_{i1\tau} - x_\tau)}. \end{cases} \tag{26}$$

Substituting (11) into (25) yields

$$\dot{\mathbf{E}}_{i1} = A_i\mathbf{g}_{i1}(\mathbf{X}_{i1})(\mathbf{F}_{i1} + \mathbf{G}_{i1}\mathbf{X}_{i2}) - A_i\mathbf{g}_{i1}(\mathbf{X}_{i1d})\dot{\mathbf{X}}_{i1d} - \lambda_2 \sum_{j\in N_i}^{j\neq i} a_{ij}\dot{\tilde{\mathbf{Z}}}_{j1}. \tag{27}$$

Based on the back-stepping control architecture, (27) can be expressed as

$$\begin{aligned}\dot{\mathbf{E}}_{i1} &= A_i\mathbf{g}_{i1}(\mathbf{X}_{i1})\mathbf{F}_{i1} - A_i\mathbf{g}_{i1}(\mathbf{X}_{i1d})\dot{\mathbf{X}}_{i1d} - \lambda_2 \sum_{j\in N_i}^{j\neq i} a_{ij}\dot{\tilde{\mathbf{Z}}}_{j1} \\ &\quad + A_i\mathbf{g}_{i1}(\mathbf{X}_{i1})\mathbf{G}_{i1} \cdot (\mathbf{X}_{i2} - \mathbf{Z}_{i2} + \mathbf{E}_{i2} + \mathbf{Z}_{i2d}),\end{aligned} \tag{28}$$

where $\mathbf{E}_{i2} = \mathbf{Z}_{i2} - \mathbf{Z}_{i2d}$ and $\mathbf{Z}_{i2d}$ is a virtual control signal.

By using a low-pass filter, one has

$$\dot{\mathbf{Z}}_{i2d} = -k_{\epsilon_1}\left(\mathbf{Z}_{i2d} - \bar{\mathbf{Z}}_{i2d}\right), \tag{29}$$

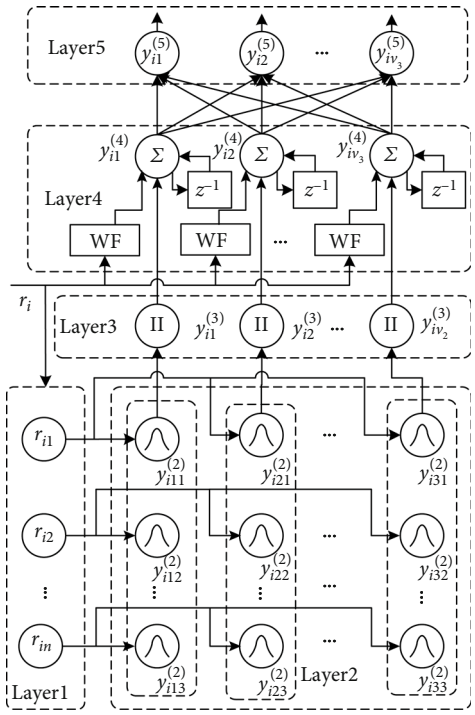

Figure 1: The structure of the RWFNN for each UAV.

where k_{ϵ_1} is a positive constant and $\bar{\mathbf{Z}}_{i2d}$ is an auxiliary signal, designed as

$$\bar{\mathbf{Z}}_{i2d} = (\mathbf{A}_i\mathbf{g}_{i1}(\mathbf{X}_{i1})\mathbf{G}_{i1})^{-1}\left(\lambda_2 \sum_{j\in N_i}^{j\neq i} a_{ij}\dot{\bar{\mathbf{Z}}}_{j1} - \mathbf{A}_i\mathbf{g}_{i1}(\mathbf{X}_{i1})(\mathbf{F}_{i1} + \mathbf{G}_{i1}(\mathbf{X}_{i2} - \mathbf{Z}_{i2})) + \mathbf{A}_i\mathbf{g}_{i1}(\mathbf{X}_{i1d})\dot{\mathbf{X}}_{i1d} - \mathbf{K}_{i1}\mathbf{E}_{i1}\right), \tag{30}$$

where $\mathbf{K}_{i1}$ is a positive diagonal matrix.

Defining the filtering error as $\boldsymbol{\epsilon}_{i1} = \mathbf{Z}_{i2d} - \bar{\mathbf{Z}}_{i2d}$, one can obtain

$$\dot{\boldsymbol{\epsilon}}_{i1} = -k_{\epsilon_{i1}}\boldsymbol{\epsilon}_{i1} - \dot{\bar{\mathbf{Z}}}_{i2d}. \tag{31}$$

By substituting (30) into (28), one can obtain

$$\begin{aligned}\mathbf{E}_{i1}^T\dot{\mathbf{E}}_{i1} \le{}& -\mathbf{E}_{i1}^{\mathrm{T}}\mathbf{K}_{i1}\mathbf{E}_{i1} + \mathbf{E}_{i1}^{\mathrm{T}}A_i\mathbf{g}_{i1}(\mathbf{X}_{i1})\mathbf{G}_{i1}\cdot\mathbf{E}_{i2} \\ &+ \frac{1}{2h_{i1}}\left\|\mathbf{E}_{i1}^{\mathrm{T}}A_i\mathbf{g}_{i1}(\mathbf{X}_{i1})\mathbf{G}_{i1}\right\|^2 + \frac{h_{i1}}{2}\|\boldsymbol{\epsilon}_{i1}\|^2,\end{aligned} \tag{32}$$

where h_{i1} is a positive constant and $\|\cdot\|$ represents 2-norm of vector.

To estimate the unknown function $\mathbf{D}_i$ of each UAV, the following DO is designed for the ith UAV:

$$\hat{\mathbf{D}}_i = k_2\left(\mathbf{X}_{i2} - \hat{\mathbf{X}}_{i2}\right) + k_1k_2\int\left(\mathbf{X}_{i2} - \hat{\mathbf{X}}_{i2}\right)\mathrm{d}t, \tag{33}$$

$$\dot{\hat{\mathbf{X}}}_{i2} = \mathbf{F}_{i20} + \mathbf{G}_{i20}\mathbf{U}_{i0}(\mathbf{v}_i) + \hat{\mathbf{D}}_i + k_1\left(\mathbf{X}_{i2} - \hat{\mathbf{X}}_{i2}\right), \tag{34}$$

where k_1 and k_2 are positive parameters, $\hat{\mathbf{D}}_i$ is the estimate of $\mathbf{D}_i$.

Define $\mathbf{e}_{X_{i2}} = \mathbf{X}_{i2} - \hat{\mathbf{X}}_{i2}$ and $\tilde{\mathbf{D}}_i = \mathbf{D}_i - \hat{\mathbf{D}}_i$, one can obtain

$$\dot{\mathbf{e}}_{X_{i2}} + k_1\mathbf{e}_{X_{i2}} = \tilde{\mathbf{D}}_i. \tag{35}$$

Taking the derivative of (35) and using (33) give

$$\dot{\tilde{\mathbf{D}}}_i + k_2\tilde{\mathbf{D}}_i = \dot{\mathbf{D}}. \tag{36}$$

From (36), it can be known that the estimation error $\tilde{\mathbf{D}}_i$ will not converge to zero since $\dot{\mathbf{D}} \neq 0$. In order to estimate the unknown function $\mathbf{D}_i$ more accurate, a five-layer RWFNN is used to estimate the error $\tilde{\mathbf{D}}_i$ of the DO with defining $\boldsymbol{\Delta}_i = \tilde{\mathbf{D}}_i$.

The RWFNN structure is illustrated in Figure 1, including five layers (input layer, membership layer, rule layer, composite layer, and output layer) [33]. The components of the RWFNN are introduced as follows:

Layer 1–Input Layer: Input layer is the first layer, where $\mathbf{r}_i = [r_{i1}, r_{i2}, \cdots, r_{iv_1}]^T$ is the input features of RWFNN. The output of layer 1 is expressed as

$$y_{ij}^{(1)} = r_{ij}, \tag{37}$$

where $j \in \{1, 2, \cdots, v_1\}$, v_1 is the dimension of input features, and $y_{ij}^{(1)}$ represents the output of jth neuron of Layer 1.

Layer 2–Membership Layer: Layer 2 has v_1 rows and v_2 columns, and its output can be described as

$$y_{ijk}^{(2)} = e^{-\left(y_{ij}^{(1)} - c_{ijk}\right)^2/\sigma_{ijk}^2}, \tag{38}$$

where $j \in \{1, 2, \cdots, v_1\}$, $k \in \{1, 2, \cdots, v_2\}$. v_2 is a positive constant, depending on the number of neurons. $y_{ijk}^{(2)}$ denotes the neuron of layer 2 in row j, column k.

Layer 3–Rule Layer: Layer 3 has v_2 neurons, and the output of layer 3 is described as

$$y_{ik}^{(3)} = \prod_{j=1}^{v_1} y_{ijk}^{(2)}, \tag{39}$$

where $k \in \{1, 2, \cdots, v_2\}$, and $y_{ik}^{(3)}$ denotes the kth neuron of Layer 3.

Layer 4–Composite Layer: Layer 4 also has v_2 neurons, and the input of Layer 4 consists the output of the wavelet layer, recurrent layer, and Layer 2, where the output of wavelet layer is described as

$$\begin{aligned}\psi_{ik} &= \sum_{j=1}^{v_1} w_{ijk}^F\phi_{ijk}(r_{ij}), \\ \phi_{ijk}(r_{ij}) &= \frac{1}{\sqrt{b_{ijk}}}\left[1 - \frac{\left(r_{ij} - a_{ijk}\right)^2}{b_{ijk}^2}\right]e^{-\left(r_{ij} - a_{ijk}\right)^2/2b_{ijk}^2},\end{aligned} \tag{40}$$

where $j \in \{1, 2, \cdots, v_1\}$, $k \in \{1, 2, \cdots, v_2\}$, ϕ_{ijk} is the output of

the jth neuron of Layer 1 to kth neuron of wavelet layer. ψ_{ik} represents the output of kth neuron of wavelet. w_{ijk}^F, a_{ijk}, and b_{ijk} represent the connecting weight, translation, and dilation variables, respectively.

The output of Layer 4 is expressed as

$$y_{ik}^{(4)} = y_{ik}^{(3)} \psi_{ik} w_{ik}^r y_{ik}^{(4)}(t-1), \tag{41}$$

where $y_{ik}^{(4)}$ is the output of kth neuron of Layer 4. w_{ik}^r and $y_{ik}^{(4)}(t-1)$ represent the recurrent weight and the output at the previous time step of the kth neuron, respectively.

Layer 5–Output Layer: Layer 5 has v_3 neurons, which determines the dimension of the final output. Each neuron's output of this layer is given by

$$y_{il}^{(5)} = \sum_{k=1}^{v_2} w_{ikl}^{(5)} y_{ik}^{(4)}, \tag{42}$$

where $l \in \{1, 2, \cdots, v_3\}$, $w_{ikl}^{(5)}$ is the connecting weight, and $y_{il}^{(5)}$ denotes the lth neuron of Layer 5.

Using (42), one can express $\mathbf{y}_i^{(5)}$ in the following vector form:

$$\mathbf{y}_i^{(5)} = \boldsymbol{\omega}_i^{(5)} \mathbf{y}_i^{(4)} \left(\boldsymbol{\omega}_i^r, \boldsymbol{\omega}_i^F, \mathbf{c}_i, \boldsymbol{\sigma}_i\right), \tag{43}$$

$y_{i1}^{(4)}, \cdots, dy_{ik}^{(4)}, \cdots, d_{iv_2}^{(4)}{}^{\mathrm{T}}] \in \mathbb{R}^{v_2 \times 1}$. $\boldsymbol{\omega}_i^{(5)} \in \mathbb{R}^{v_3 \times v_2}$, $\boldsymbol{\omega}_i^r \in \mathbb{R}^{v_2 \times 1}$, $\boldsymbol{\omega}_i^F \in \mathbb{R}^{v_1 v_2 \times 1}$, $\mathbf{c}_i \in \mathbb{R}^{v_1 v_2 \times 1}$, and $\boldsymbol{\sigma}_i \in \mathbb{R}^{v_1 v_2 \times 1}$, which are expressed as

$$\begin{aligned}
\boldsymbol{\omega}_i^{(5)} &= \left[\boldsymbol{\omega}_{i1}^5, \boldsymbol{\omega}_{i2}^{(5)}, \cdots, \boldsymbol{\omega}_{il}^{(5)}, \cdots, \boldsymbol{\omega}_{iv_3}^{(5)}\right]^T, \\
\boldsymbol{\omega}_{il}^{(5)} &= \left[\omega_{i1l}^{(5)}, \omega_{i2l}^{(5)}, \cdots, \omega_{ikl}^{(5)}, \cdots, \omega_{iv_2 l}^{(5)}\right]^T, \\
\boldsymbol{\omega}_i^r &= \left[\omega_{i1}^r, \omega_{i2}^r, \cdots, \omega_{ik}^r, \cdots, \omega_{iv_2}^r\right]^T, \\
\boldsymbol{\omega}_i^F &= \left[\boldsymbol{\omega}_{i1}^F, \boldsymbol{\omega}_{i2}^F, \cdots, \boldsymbol{\omega}_{ik}^F, \cdots, \boldsymbol{\omega}_{iv_2}^F\right]^T, \\
\boldsymbol{\omega}_{ik}^F &= \left[\omega_{i1k}^F, \omega_{i2k}^F, \cdots, \omega_{ijk}^F, \cdots, \omega_{iv_1 k}^F\right], \\
\mathbf{c}_i &= \left[\mathbf{c}_{i1}, \mathbf{c}_{i2}, \cdots, \mathbf{c}_{ik}, \cdots, \mathbf{c}_{iv_2}\right]^T, \\
\mathbf{c}_{ik} &= \left[c_{i1k}, c_{i2k}, \cdots, c_{ijk}, \cdots, c_{iv_1 k}\right], \\
\boldsymbol{\sigma}_i &= \left[\boldsymbol{\sigma}_{i1}, \boldsymbol{\sigma}_{i2}, \cdots, \boldsymbol{\sigma}_{ik}, \cdots, \boldsymbol{\sigma}_{iv_2}\right]^T, \\
\boldsymbol{\sigma}_{ik} &= \left[\sigma_{i1k}, \sigma_{i2k}, \cdots, \sigma_{ijk}, \cdots, \sigma_{iv_1 k}\right].
\end{aligned} \tag{44}$$

In this paper, v_3 is set as 3 due to the fact that the estimated variable $\boldsymbol{\Delta}_i$ is three-dimensional. Therefore, there exist optimal values $\boldsymbol{\omega}_i^{(5)*}$, $\boldsymbol{\omega}_i^{r*}$, $\boldsymbol{\omega}_i^{F*}$, $\mathbf{c}_i^*$, and $\boldsymbol{\sigma}_i^*$, such that

$$\boldsymbol{\Delta}_i = \mathbf{y}_i^{(5)*} + \varepsilon_{i1} = \boldsymbol{\omega}_i^{(5)*} \mathbf{y}_i^{(4)*} \left(\boldsymbol{\omega}_i^{r*}, \boldsymbol{\omega}_i^{F*}, \mathbf{c}_i^*, \boldsymbol{\sigma}_i^*\right) + \varepsilon_{i1}, \tag{45}$$

where ε_{i1} is the approximation error.

To design the adaptive law of weights for estimating the unknown item, it is needed to obtain the gradient of $\mathbf{y}_i^{(5)}$ of its variables firstly.

Differentiating both sides of $\mathbf{y}_i^{(5)}$, one can obtain

$$d\mathbf{y}_i^{(5)} = d\boldsymbol{\omega}_i^{(5)} \cdot \mathbf{y}_i^{(4)} + \boldsymbol{\omega}_i^{(5)} d\mathbf{y}_i^{(4)}, \tag{46}$$

To yield $d\mathbf{y}_i^{(4)}$, by the same way, differentiating both sides of $y_{ik}^{(4)}$, then

$$dy_{ik}^{(4)} = dy_{ik}^{(3)}(\mathbf{c}_{ik}, \boldsymbol{\sigma}_{ik}) + d\psi_{ik}\left(\boldsymbol{\omega}_{ik}^F\right) + d\left(\omega_{ik}^r y_{ik}^{(4)}(t-1)\right). \tag{47}$$

For term $dy_{ik}^{(3)}$, one can obtain it by combining (37), (38), and (39), that is

$$\begin{aligned}
dy_{ik}^{(3)} &= \sum_{j=1}^{v_1} \left(dc_{ijk} \cdot \frac{2\left(y_{ij}^{(1)} - c_{ijk}\right)}{\sigma_{ijk}^2} \prod_{j=1}^{v_1} y_{ijk}^{(2)} \right) \\
&\quad + \sum_{j=1}^{v_1} \left(d\sigma_{ijk} \cdot \frac{2\left(y_{ij}^{(1)} - c_{ijk}\right)^2}{\sigma_{ijk}^3} \prod_{j=1}^{v_1} y_{ijk}^{(2)} \right) \\
&= 2\left(\mathbf{y}_i^{(1)\mathrm{T}} - \mathbf{c}_{ik}\right) \diamond (\boldsymbol{\sigma}_{ik})^2 \cdot \prod_{j=1}^{v_1} y_{ijk}^{(2)} . d\mathbf{c}_{ik}^T \\
&\quad + 2\left(\mathbf{y}_i^{(1)\mathrm{T}} - \mathbf{c}_{ik}\right)^2 \diamond (\boldsymbol{\sigma}_{ik})^3 . \prod_{j=1}^{v_1} y_{ijk}^{(2)} \cdot d\boldsymbol{\sigma}_{ik}^T,
\end{aligned} \tag{48}$$

where "$\diamond$" represents dot division between matrices, and "$(*)^n$" represent the aligned "$*$" itself does n times dot product. And the $\mathbf{c}_{ik}$ and $\boldsymbol{\sigma}_{ik}$ have been defined in (44).

For the term $d\psi_{ik}$ and $d(\omega_{ik}^r y_{ik}^{(4)}(t-1))$, there exists

$$\begin{aligned}
d\boldsymbol{\psi}_{ik} &= d\left(\sum_{j=1}^{v_1} \omega_{ijk}^F \phi_{ijk}\left(r_{ij}\right)\right) \\
&= \sum_{j=1}^{v_1} \left(\phi_{ijk}\left(r_{ij}\right) \cdot d\omega_{ijk}^F\right) = \boldsymbol{\phi}_{ik} \cdot d\boldsymbol{\omega}_{ik}^{F\mathrm{T}},
\end{aligned} \tag{49a}$$

$$d\left(\omega_{ik}^r y_{ik}^{(4)}(t-1)\right) = y_{ik}^{(4)}\Big|_{t-1} \cdot d\omega_{ik}^r. \tag{49b}$$

Then, by combining (50), (48), and (49), $dy_{ik}^{(4)}$ can be expressed as

$$dy_{ik}^{(4)} = \boldsymbol{\Gamma}_{ik}^c d\mathbf{c}_{ik}^T + \boldsymbol{\Gamma}_{ik}^\sigma d\boldsymbol{\sigma}_{ik}^T + \boldsymbol{\Gamma}_{ik}^F d\boldsymbol{\omega}_{ik}^{F\mathrm{T}} + \Gamma_{ik}^r d\omega_{ik}^r, \tag{50}$$

where

$$\begin{cases} \boldsymbol{\Gamma}_{ik}^{c} = 2\left(\mathbf{y}_i^{(1)T} - \mathbf{c}_{ik}\right) \diamond (\boldsymbol{\sigma}_{ik})^2 \cdot \prod_{j=1}^{v_1} y_{ijk}^{(2)}, \\ \boldsymbol{\Gamma}_{ik}^{\sigma} = 2\left(\mathbf{y}_i^{(1)T} - \mathbf{c}_{ik}\right)^2 \diamond (\boldsymbol{\sigma}_{ik})^3 \cdot \prod_{j=1}^{v_1} y_{ijk}^{(2)}, \\ \boldsymbol{\Gamma}_{ik}^{F} = \phi_{ik}, \\ \Gamma_{ik}^{r} = y_{ik}^{(4)}\Big|_{t-1}. \end{cases} \tag{51}$$

Using (50) and (51), one can further write $d\mathbf{y}_i^{(4)}$ as

$$d\mathbf{y}_i^{(4)} = \boldsymbol{\Gamma}_i^{c} d\mathbf{c}_i + \boldsymbol{\Gamma}_i^{\sigma} d\boldsymbol{\sigma}_i + \boldsymbol{\Gamma}_i^{F} d\boldsymbol{\omega}_i^{F} + \boldsymbol{\Gamma}_i^{r} d\boldsymbol{\omega}_i^{r}, \tag{52}$$

where

$$\begin{aligned} \boldsymbol{\Gamma}_i^{c} &= \begin{bmatrix} \boldsymbol{\Gamma}_{i1}^{c} & \mathbf{0} & \cdots & \cdots & \cdots & \mathbf{0} \\ \mathbf{0} & \boldsymbol{\Gamma}_{i2}^{c} & \cdots & \cdots & \cdots & \mathbf{0} \\ \vdots & \vdots & \ddots & \vdots & \vdots & \vdots \\ \mathbf{0} & \cdots & \cdots & \boldsymbol{\Gamma}_{ik}^{c} & \cdots & \mathbf{0} \\ \vdots & \vdots & \vdots & \vdots & \ddots & \vdots \\ \mathbf{0} & \cdots & \cdots & \cdots & \cdots & \boldsymbol{\Gamma}_{iv_2}^{c} \end{bmatrix}, \\ \boldsymbol{\Gamma}_i^{\sigma} &= \begin{bmatrix} \boldsymbol{\Gamma}_{i1}^{\sigma} & \mathbf{0} & \cdots & \cdots & \cdots & \mathbf{0} \\ \mathbf{0} & \boldsymbol{\Gamma}_{i2}^{\sigma} & \cdots & \cdots & \cdots & \mathbf{0} \\ \vdots & \vdots & \ddots & \vdots & \vdots & \vdots \\ \mathbf{0} & \cdots & \cdots & \boldsymbol{\Gamma}_{ik}^{\sigma} & \cdots & \mathbf{0} \\ \vdots & \vdots & \vdots & \vdots & \ddots & \vdots \\ \mathbf{0} & \cdots & \cdots & \cdots & \cdots & \boldsymbol{\Gamma}_{iv_2}^{\sigma} \end{bmatrix}, \\ \boldsymbol{\Gamma}_i^{F} &= \begin{bmatrix} \boldsymbol{\Gamma}_{i1}^{F} & \mathbf{0} & \cdots & \cdots & \cdots & \mathbf{0} \\ \mathbf{0} & \boldsymbol{\Gamma}_{i2}^{F} & \cdots & \cdots & \cdots & \mathbf{0} \\ \vdots & \vdots & \ddots & \vdots & \vdots & \vdots \\ \mathbf{0} & \cdots & \cdots & \boldsymbol{\Gamma}_{ik}^{F} & \cdots & \mathbf{0} \\ \vdots & \vdots & \vdots & \vdots & \ddots & \vdots \\ \mathbf{0} & \cdots & \cdots & \cdots & \cdots & \boldsymbol{\Gamma}_{iv_2}^{F} \end{bmatrix}, \\ \boldsymbol{\Gamma}_i^{r} &= \begin{bmatrix} \Gamma_{i1}^{r} & 0 & \cdots & \cdots & \cdots & 0 \\ 0 & \Gamma_{i2}^{r} & \cdots & \cdots & \cdots & 0 \\ \vdots & \vdots & \ddots & \vdots & \vdots & \vdots \\ 0 & \cdots & \cdots & \Gamma_{ik}^{r} & \cdots & 0 \\ \vdots & \vdots & \vdots & \vdots & \ddots & \vdots \\ 0 & \cdots & \cdots & \cdots & \cdots & \Gamma_{iv_2}^{r} \end{bmatrix}. \end{aligned} \tag{53}$$

Moreover, using the property of Kronecker product, the term $d\boldsymbol{\omega}_i^{(5)} \cdot \mathbf{y}_i^{(4)}$ in (58) can be transformed to the following column vector form:

$$d\boldsymbol{\omega}_i^{(5)} \cdot \mathbf{y}_i^{(4)} = \left(\mathbf{I}_n \otimes \mathbf{y}_i^{(4)}\right) \cdot d\left(\mathrm{vec}\left(\boldsymbol{\omega}_i^{(5)T}\right)\right), \tag{54}$$

where "$\otimes$" represents Kronecker product, and "vec$(*)$" represents the operation that converts the aligned "$*$" to a column vector, that means

$$\mathrm{vec}\left(\boldsymbol{\omega}_i^{(5)\mathrm{T}}\right) = \left[\omega_{i1}^{(5)\mathrm{T}}, \cdots, \omega_{\mathrm{il}}^{(5)\mathrm{T}}, \cdots, \omega_{iv_3}^{(5)T}\right]^T. \tag{55}$$

To simplify the representation, using $\vec{\boldsymbol{\omega}}_i^{(5)}$ to represent $\mathrm{vec}(\boldsymbol{\omega}_i^{(5)T})$. Employing (58), (52), and (54) yeilds the following total differential equation:

$$\begin{aligned} d\mathbf{y}_i^{(5)} = \boldsymbol{\Gamma}_i^{5} d\vec{\boldsymbol{\omega}}_i^{(5)} + \boldsymbol{\omega}_i^{(5)} \boldsymbol{\Gamma}_i^{c} d\mathbf{c}_i + \boldsymbol{\omega}_i^{(5)} \boldsymbol{\Gamma}_i^{\sigma} d\boldsymbol{\sigma}_i \\ + \boldsymbol{\omega}_i^{(5)} \boldsymbol{\Gamma}_i^{F} d\boldsymbol{\omega}_i^{F} + \boldsymbol{\omega}_i^{(5)} \boldsymbol{\Gamma}_i^{r} d\boldsymbol{\omega}_i^{r}, \end{aligned} \tag{56}$$

where

$$\boldsymbol{\Gamma}_i^{5} = \mathbf{I}_n \otimes \mathbf{y}_i^{(4)}. \tag{57}$$

On the other hand, the total derivative of $d\mathbf{y}_i^{(5)}$ can be expressed as the following total differential form:

$$\begin{aligned} d\mathbf{y}_i^{(5)} = \left(\frac{\partial \mathbf{y}_i^{(5)}}{\partial \vec{\boldsymbol{\omega}}_i^{(5)}}\right)^T d\vec{\boldsymbol{\omega}}_i^{(5)} + \left(\frac{\partial \mathbf{y}_i^{(5)}}{\partial \mathbf{c}_i}\right)^{\mathrm{T}} d\mathbf{c}_i + \left(\frac{\partial \mathbf{y}_i^{(5)}}{\partial \boldsymbol{\sigma}_i}\right)^{\mathrm{T}} d\boldsymbol{\sigma}_i \\ + \left(\frac{\partial \mathbf{y}_i^{(5)}}{\partial \boldsymbol{\omega}_i^{F}}\right)^{\mathrm{T}} d\boldsymbol{\omega}_i^{F} + \left(\frac{\partial \mathbf{y}_i^{(5)}}{\partial \boldsymbol{\omega}_i^{r}}\right)^{\mathrm{T}} d\boldsymbol{\omega}_i^{r}. \end{aligned} \tag{58}$$

Hence, one can derive that

$$\begin{cases} \left(\dfrac{\partial \mathbf{y}_i^{(5)}}{\partial \vec{\boldsymbol{\omega}}_i^{(5)}}\right)^T = \boldsymbol{\Gamma}_i^{5}, \left(\dfrac{\partial \mathbf{y}_i^{(5)}}{\partial \mathbf{c}_i}\right)^T = \boldsymbol{\omega}_i^{(5)} \boldsymbol{\Gamma}_i^{c} \\ \left(\dfrac{\partial \mathbf{y}_i^{(5)}}{\partial \boldsymbol{\sigma}_i}\right)^T = \boldsymbol{\omega}_i^{(5)} \boldsymbol{\Gamma}_i^{\sigma}, \left(\dfrac{\partial \mathbf{y}_i^{(5)}}{\partial \boldsymbol{\omega}_i^{F}}\right)^T = \boldsymbol{\omega}_i^{(5)} \boldsymbol{\Gamma}_i^{F}, \\ \left(\dfrac{\partial \mathbf{y}_i^{(5)}}{\partial \boldsymbol{\omega}_i^{r}}\right)^T = \boldsymbol{\omega}_i^{(5)} \boldsymbol{\Gamma}_i^{r}. \end{cases} \tag{59}$$

Taking into account (58) and (59) and using the Taylor expansion, $\mathbf{y}_i^{(5)}$ can be expressed as

$$\begin{aligned} \mathbf{y}_i^{(5)} = \mathbf{y}_i^{(5)*} + \boldsymbol{\Gamma}_i^{5}\left(\vec{\boldsymbol{\omega}}_i^{(5)} - \vec{\boldsymbol{\omega}}_i^{(5)*}\right) + \boldsymbol{\omega}_i^{(5)} \boldsymbol{\Gamma}_i^{c}(\mathbf{c}_i - \mathbf{c}_i^{*}) + \boldsymbol{\omega}_i^{(5)} \boldsymbol{\Gamma}_i^{\sigma}(\boldsymbol{\sigma}_i - \boldsymbol{\sigma}_i^{*}) \\ + \boldsymbol{\omega}_i^{(5)} \boldsymbol{\Gamma}_i^{F}\left(\boldsymbol{\omega}_i^{F} - \boldsymbol{\omega}_i^{F*}\right) + \boldsymbol{\omega}_i^{(5)} \boldsymbol{\Gamma}_i^{r}(\boldsymbol{\omega}_i^{r} - \boldsymbol{\omega}_i^{r*}) + \varepsilon_{i2}. \end{aligned} \tag{60}$$

Using $\widehat{\boldsymbol{\Delta}}_i$ to estimate the unknown item $\boldsymbol{\Delta}_i$, and it is expressed as

$$\widehat{\boldsymbol{\Delta}}_i = \mathbf{y}_i^{(5)} + \operatorname{diag}\left(\operatorname{sign}\left(\mathbf{E}_{i2}^T \mathbf{g}_{i2}(\mathbf{X}_{i2})\right)\right)\widehat{\mathbf{H}}_i \triangleq \mathbf{y}_i^{(5)} + \boldsymbol{\Gamma}_i^H \widehat{\mathbf{H}}_i, \quad (61)$$

where $\boldsymbol{\Gamma}_i^H = \operatorname{diag}(\operatorname{sign}(\mathbf{E}_{i2}^{\mathrm{T}} \mathbf{g}_{i2}(\mathbf{X}_{i2})))$ and $\widehat{\mathbf{H}}_i$ is an estimated value and will be introduced later.

Defining $\tilde{\boldsymbol{\Delta}}_i = \widehat{\boldsymbol{\Delta}}_i - \boldsymbol{\Delta}_i$, $\tilde{\vec{\boldsymbol{\omega}}}_i^{(5)} = \vec{\boldsymbol{\omega}}_i^{(5)} - \vec{\boldsymbol{\omega}}_i^{(5)*}$, $\tilde{\mathbf{c}}_i = \mathbf{c}_i - \mathbf{c}_i^*$, $\tilde{\boldsymbol{\sigma}}_i = \boldsymbol{\sigma}_i - \boldsymbol{\sigma}_i^*$, $\tilde{\boldsymbol{\omega}}_i^F = \boldsymbol{\omega}_i^F - \boldsymbol{\omega}_i^{F*}$, and $\tilde{\boldsymbol{\omega}}_i^r = \boldsymbol{\omega}_i^r - \boldsymbol{\omega}_i^{r*}$ and combining (45), (60), and (61), it yeilds

$$\begin{aligned}\tilde{\boldsymbol{\Delta}}_i = {} & \boldsymbol{\Gamma}_i^5 \tilde{\vec{\boldsymbol{\omega}}}_i^{(5)} + \boldsymbol{\omega}_i^{(5)} \boldsymbol{\Gamma}_i^c \tilde{\mathbf{c}}_i + \boldsymbol{\omega}_i^{(5)} \boldsymbol{\Gamma}_i^\sigma \tilde{\boldsymbol{\sigma}}_i + \boldsymbol{\omega}_i^{(5)} \boldsymbol{\Gamma}_i^F \tilde{\boldsymbol{\omega}}_i^F \\ & + \boldsymbol{\omega}_i^{(5)} \boldsymbol{\Gamma}_i^r \tilde{\boldsymbol{\omega}}_i^r + \boldsymbol{\varepsilon}_{i2} - \boldsymbol{\varepsilon}_{i1} + \boldsymbol{\Gamma}_i^H \widehat{\mathbf{H}}_i.\end{aligned} \quad (62)$$

Taking the derivative of $\mathbf{E}_{i2}$ and using (17) and (20), one can obtain

$$\dot{\mathbf{E}}_{i2} = \dot{\mathbf{Z}}_{i2} - \dot{\mathbf{Z}}_{i2d} = \mathbf{g}_{i2}(\mathbf{X}_{i2})(\mathbf{F}_{i20} + \mathbf{G}_{i20}\mathbf{U}_{i0}(\mathbf{v}_i) + \mathbf{D}_i) - \dot{\mathbf{Z}}_{i2d}, \quad (63)$$

where $\mathbf{g}_{i2}(\mathbf{x})$ and $\mathbf{x} = [x_1, x_2, x_3]^{\mathrm{T}}$ are

$$\begin{cases} \boldsymbol{g}_{i2}(\boldsymbol{x}) = \operatorname{diag}\{g_{i2\tau}(x_\tau)\}, \tau = \{1, 2, 3\}, \\ g_{i2\tau}(x_\tau) = \dfrac{\bar{X}_{i2\tau} - \underline{X}_{i2\tau}}{(x_\tau - \underline{X}_{i2\tau})(\bar{X}_{i2\tau} - x_\tau)}. \end{cases} \quad (64)$$

By using the back-stepping method and defining $\mathbf{v}_{id}$ as a virtual control signal, then $\dot{\mathbf{E}}_{i2}$ can be expressed as

$$\begin{aligned}\dot{\mathbf{E}}_{i2} = {} & \mathbf{g}_{i2}(\mathbf{X}_{i2})(\mathbf{F}_{i20} + \mathbf{G}_{i20}\mathbf{v}_{id} + \mathbf{G}_{i20}(\mathbf{U}_{i0} - \mathbf{v}_i) \\ & + \mathbf{G}_{i20}\mathbf{E}_{i3} + \mathbf{D}_i) - \dot{\mathbf{Z}}_{i2d},\end{aligned} \quad (65)$$

where $\mathbf{E}_{i3} = \mathbf{v}_i - \mathbf{v}_{id}$. In order to reduce computational burden of taking time derivative for virtual control signal $\mathbf{v}_{id}$, a filter is used to obtain $\mathbf{v}_{id}$, which is given by

$$\dot{\mathbf{v}}_{id} = -k_{\epsilon_2}(\mathbf{v}_{id} - \bar{\mathbf{v}}_{id}), \quad (66)$$

where k_{ϵ_2} is a positive constant, and $\bar{\mathbf{v}}_{id}$ is an auxiliary signal, designed as

$$\begin{aligned}\bar{\mathbf{v}}_{id} = {} & (\mathbf{g}_{i2}(\mathbf{X}_{i2})\mathbf{G}_{i20})^{-1}\Big[-\mathbf{g}_{i2}(\mathbf{X}_{i2})\Big(\mathbf{F}_{i20} + \mathbf{G}_{i20}(\mathbf{U}_{i0}(\mathbf{v}_i) - \mathbf{v}_i) + \widehat{\mathbf{D}}_i + \widehat{\boldsymbol{\Delta}}_i + \widehat{\mathbf{H}}_i\Big) \\ & + \dot{\mathbf{Z}}_{i2d} - \mathbf{K}_{i2}\mathbf{E}_{i2} - A_i\mathbf{g}_{i1}(\mathbf{X}_{i1}) \cdot \mathbf{G}_{i1}\mathbf{E}_{i1}\Big],\end{aligned} \quad (67)$$

where $\mathbf{K}_{i2}$ is a positive diagonal matrix.

Define the filter error as $\boldsymbol{\epsilon}_{i2} = \mathbf{v}_{id} - \bar{\mathbf{v}}_{id}$, then one can obtain from (66) that

$$\dot{\boldsymbol{\epsilon}}_{i2} = -k_{\boldsymbol{\epsilon}_{i2}}\boldsymbol{\epsilon}_{i2} - \dot{\bar{\mathbf{v}}}_{id}. \quad (68)$$

Substituting (65) with (67) and (62), with considering $|\boldsymbol{\varepsilon}_{i1} - \boldsymbol{\varepsilon}_{i2}| \le \mathbf{H}_i$ in which $|*|$ represents the absolute value of the matrix "$*$", while defining $\widehat{\mathbf{H}}_i$ as the estimation of $\mathbf{H}_i$ and $\tilde{\mathbf{H}}_i = \mathbf{H} - \widehat{\mathbf{H}}_i$ as the estimation error, one can obtain

$$\begin{aligned}\boldsymbol{E}_{i2}^{\mathrm{T}}\dot{\boldsymbol{E}}_{i2} \le {} & -\boldsymbol{E}_{i2}^{\mathrm{T}}\boldsymbol{K}_{i2}\boldsymbol{E}_{i2} - \boldsymbol{E}_{i2}^{\mathrm{T}}\boldsymbol{A}_i\boldsymbol{g}_{i1}(\boldsymbol{X}_{i1})\boldsymbol{G}_{i1}\boldsymbol{E}_{i1} + \boldsymbol{E}_{i2}^{\mathrm{T}}\boldsymbol{g}_{i2}(\boldsymbol{X}_{i2}) \\ & \cdot \Big[\boldsymbol{G}_{i20}\boldsymbol{E}_{i3} + \boldsymbol{G}_{i20}\boldsymbol{\epsilon}_{i2} - \boldsymbol{\Gamma}_i^5 \cdot \dot{\tilde{\vec{\boldsymbol{\omega}}}}_i^{(5)} - \boldsymbol{\omega}_i^{(5)}\boldsymbol{\Gamma}_i^c\tilde{\mathbf{c}}_i - \boldsymbol{\omega}_i^{(5)}\boldsymbol{\Gamma}_i^\sigma\tilde{\boldsymbol{\sigma}}_i - \boldsymbol{\omega}_i^{(5)}\boldsymbol{\Gamma}_i^F\tilde{\boldsymbol{\omega}}_i^F - \boldsymbol{\omega}_i^{(5)}\boldsymbol{\Gamma}_i^r\tilde{\boldsymbol{\omega}}_i^r\Big] \\ & + \left|\boldsymbol{E}_{i2}^{\mathrm{T}}\boldsymbol{g}_{i2}(\boldsymbol{X}_{i2})\right|\tilde{\boldsymbol{H}}_i.\end{aligned} \quad (69)$$

Taking the time derivative of $\mathbf{E}_{i3}$ and using (18), one can obtain

$$\dot{\mathbf{E}}_{i3} = -\boldsymbol{\Lambda}\mathbf{v}_i + \boldsymbol{\xi} - \dot{\mathbf{v}}_{id}. \quad (70)$$

Design the auxiliary control signal $\boldsymbol{\xi}$ as

$$\boldsymbol{\xi} = \begin{cases} \boldsymbol{\Lambda}\boldsymbol{v}_i + \dot{\boldsymbol{v}}_{id} - \boldsymbol{K}_{i3}\boldsymbol{E}_{i3} - \boldsymbol{g}_{i2}(\boldsymbol{X}_{i2})\boldsymbol{G}_{i20}\boldsymbol{E}_{i2} - \dfrac{1}{\|\boldsymbol{E}_{i3}\|^2}\left(\dfrac{h_{i1}}{2}\|\boldsymbol{\epsilon}_{i1}\|^2 + \dfrac{h_{i2}}{2}\|\boldsymbol{\epsilon}_{i2}\|^2\right)\boldsymbol{E}_{i3}, \\ (\|\boldsymbol{E}_{i3}\|^2 > \mu_{ib}), \\ \boldsymbol{\Lambda}\boldsymbol{v}_i + \dot{\boldsymbol{v}}_{id} - \boldsymbol{K}_{i3}\boldsymbol{E}_{i3} - \boldsymbol{g}_{i2}(\boldsymbol{X}_{i2})\boldsymbol{G}_{i20}\boldsymbol{E}_{i2} - \dfrac{1}{\mu_{ib}}\left(\dfrac{h_{i1}}{2}\|\boldsymbol{\epsilon}_{i1}\|^2 + \dfrac{h_{i2}}{2}\|\boldsymbol{\epsilon}_{i2}\|^2\right)\boldsymbol{E}_{i3}, \\ (\|\boldsymbol{E}_{i3}\|^2 \le \mu_{ib}), \end{cases} \quad (71)$$

where $\mathbf{K}_{i3}$ is a positive diagonal matrix, and h_{i1} and h_{i2} are positive constants.

By combining (70) and (71), one has

$$\mathbf{E}_{i3}^T\dot{\mathbf{E}}_{i3} \le -\mathbf{E}_{i3}^T\mathbf{K}_{i3}\mathbf{E}_{i3} - \mathbf{E}_{i3}^T\mathbf{g}_{i2}(\mathbf{X}_{i2})\mathbf{G}_{i20}\mathbf{E}_{i2}. \quad (72)$$

Finally, the adaptive laws of RWFNN for the ith UAV are developed as

$$\begin{cases} \dot{\vec{\boldsymbol{\omega}}}_i^{(5)} = \eta_{i1}^{-1}\left[-\gamma_{i1}\vec{\boldsymbol{\omega}}_i^{(5)} + \left(\boldsymbol{E}_{i2}^{\mathrm{T}}\boldsymbol{g}_{i2}(\boldsymbol{X}_{i2})\boldsymbol{\Gamma}_i^5\right)^T\right], \\ \dot{\mathbf{c}}_i = \eta_{i2}^{-1}\left[-\gamma_{i2}\mathbf{c}_i + \left(\boldsymbol{E}_{i2}^{\mathrm{T}}\mathbf{g}_{i2}(\boldsymbol{X}_{i2})\boldsymbol{\omega}_i^{(5)}\boldsymbol{\Gamma}_i^c\right)^T\right], \\ \dot{\boldsymbol{\sigma}}_i = \eta_{i3}^{-1}\left[-\gamma_{i3}\boldsymbol{\sigma}_i + \left(\boldsymbol{E}_{i2}^{\mathrm{T}}\boldsymbol{g}_{i2}(\boldsymbol{X}_{i2})\boldsymbol{\omega}_i^{(5)}\boldsymbol{\Gamma}_i^\sigma\right)^T\right], \\ \dot{\boldsymbol{\omega}}_i^F = \eta_{i4}^{-1}\left[-\gamma_{i4}\boldsymbol{\omega}_i^F + \left(\boldsymbol{E}_{i2}^{\mathrm{T}}\boldsymbol{g}_{i2}(\boldsymbol{X}_{i2})\boldsymbol{\omega}_i^{(5)}\boldsymbol{\Gamma}_i^F\right)^T\right], \\ \dot{\boldsymbol{\omega}}_i^r = \eta_{i5}^{-1}\left[-\gamma_{i5}\boldsymbol{\omega}_i^r + \left(\boldsymbol{E}_{i2}^{\mathrm{T}}\boldsymbol{g}_{i2}(\boldsymbol{X}_{i2})\boldsymbol{\omega}_i^{(5)}\boldsymbol{\Gamma}_i^r\right)^T\right], \\ \dot{\widehat{\boldsymbol{H}}}_i = \eta_{i6}^{-1}\left[-\gamma_{i6}\widehat{\boldsymbol{H}}_i + \left|\boldsymbol{E}_{i2}^{\mathrm{T}}\boldsymbol{g}_{i2}(\boldsymbol{X}_{i2})\right|^T\right], \end{cases} \quad (73)$$

where $\gamma_{i1} \sim \gamma_{i5}$ are discontinuous switching constants to prevent the weights to infinity and γ_{i6} is a positive constant,

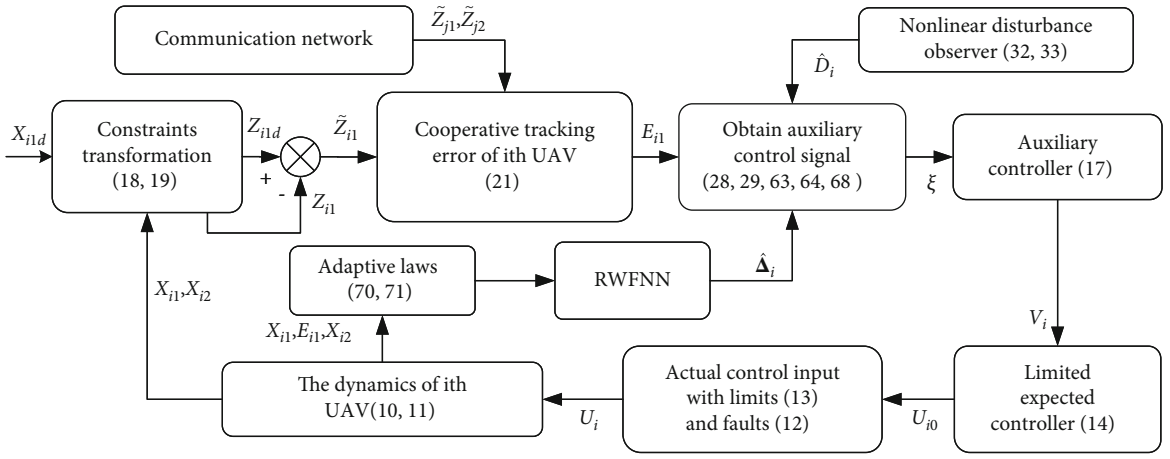

Figure 2: The proposed control scheme for the ith UAV.

where the switching constants are designed as

$$\gamma_{i1} = \begin{cases} 0 & \text{if } \left\|\vec{\boldsymbol{\omega}}_i^{(5)}\right\|^2 \le \bar{\omega}^{(5)}, \\ \bar{\gamma}_{i1} & \text{if } \left\|\vec{\boldsymbol{\omega}}_i^{(5)}\right\|^2 > \bar{\omega}^{(5)}, \end{cases} \tag{74a}$$

$$\gamma_{i2} = \begin{cases} 0 & \text{if } \|\boldsymbol{c}_i\|^2 \le \bar{c}, \\ \bar{\gamma}_{i2} & \text{if } \|\boldsymbol{c}_i\|^2 > \bar{c}, \end{cases} \tag{74b}$$

$$\gamma_{i3} = \begin{cases} 0 & \text{if } \|\boldsymbol{\sigma}_i\|^2 \le \bar{\sigma}, \\ \bar{\gamma}_{i3} & \text{if } \|\boldsymbol{\sigma}_i\|^2 > \bar{\sigma}, \end{cases} \tag{74c}$$

$$\gamma_{i4} = \begin{cases} 0 & \text{if } \left\|\boldsymbol{\omega}_i^F\right\|^2 \le \bar{\omega}_i^F, \\ \bar{\gamma}_{i4} & \text{if } \left\|\boldsymbol{\omega}_i^F\right\|^2 > \bar{\omega}_i^F, \end{cases} \tag{74d}$$

$$\gamma_{i5} = \begin{cases} 0 & \text{if } \|\boldsymbol{\omega}_i^r\|^2 \le \bar{\omega}_i^r, \\ \bar{\gamma}_{i5} & \text{if } \|\boldsymbol{\omega}_i^r\|^2 > \bar{\omega}_i^r, \end{cases} \tag{74e}$$

where $\bar{\omega}^{(5)}$, $\bar{c}$, $\bar{\sigma}$, $\bar{\omega}_i^F$, and $\bar{\omega}_i^r$ are positive constants, which represent the boundness of weight $\vec{\boldsymbol{\omega}}_i^{(5)}, \mathbf{c}_i, \boldsymbol{\sigma}_i, \boldsymbol{\omega}_i^F, \boldsymbol{\omega}_i^r$, respectively.

To this end, the proposed FTCC scheme is shown in Figure 2 to better illustrate the design principle and functional components in the control system.

Remark 6. Many papers choose multiplication on input and recurrence data as an operation on the neuron of the composite layer in RWFNN. However, it is sometimes problematic. For example, when inputs from layer 3 are minuscule, the outputs of the composite neuron will also become exceedingly small under multiplication. Under the limitation of computational precision, the outputs are equal to zero. Since the outputs will loop to the next multiplication, the outputs will always be zero, which causes neuron inactivation. Therefore, this paper uses the addition operation as an alternative, and the back-propagation gradient is deduced in detail using vectorized expressions, i.e., (46)–(59).

3.2. Stability Analysis

Theorem 7. *Consider the N UAVs (1)–(4) under the distributed communication network against the actuator faults (13), states constraints, and input saturation (15), if the control laws are chosen as (30), (67), and (71), the disturbance observers are developed as (33), and (34), and the adaptive laws are constructed as (73), (74a); then, all the states in the system are ultimately uniformly bounded and strictly confined within the limits.*

Proof. Choose a Lyapunov function as

$$\begin{aligned} V = \frac{1}{2}\sum_{i=1}^{N}\Big[& \boldsymbol{E}_{i1}^{\mathrm{T}}\boldsymbol{E}_{i1}^{\mathrm{T}} + \boldsymbol{E}_{i2}^{\mathrm{T}}\boldsymbol{E}_{i2}^{\mathrm{T}} + \boldsymbol{E}_{i3}^{\mathrm{T}}\boldsymbol{E}_{i3}^{\mathrm{T}} + \eta_{i1}\cdot\tilde{\vec{\boldsymbol{\omega}}}_i^{(5)\mathrm{T}}\tilde{\vec{\boldsymbol{\omega}}}_i^{(5)} \\ & + \eta_{i2}\tilde{\mathbf{c}}_i^{\mathrm{T}}\tilde{\mathbf{c}}_i + \eta_{i3}\tilde{\boldsymbol{\sigma}}_i^{\mathrm{T}}\boldsymbol{\sigma}_i + \eta_{i4}\cdot\tilde{\boldsymbol{\omega}}_i^{F\mathrm{T}}\tilde{\boldsymbol{\omega}}_i^F + \eta_{i5}\tilde{\boldsymbol{\omega}}_i^{r\mathrm{T}}\tilde{\boldsymbol{\omega}}_i^r \\ & + \eta_{i6}\tilde{\boldsymbol{H}}_i^{\mathrm{T}}\tilde{\boldsymbol{H}}_i + \boldsymbol{\epsilon}_{i1}^{\mathrm{T}}\cdot\boldsymbol{\epsilon}_{i1} + \boldsymbol{\epsilon}_{i2}^{\mathrm{T}}\boldsymbol{\epsilon}_{i2}\Big]. \end{aligned} \tag{75}$$

By taking the time derivative of V, combining (32), (69), (72), (31), and (68) and using Young inequality, one has

$$\begin{aligned} \dot{V} \le & \sum_{i=1}^{N}\left(-\mathbf{E}_{i1}^{\mathrm{T}}\mathbf{K}_{i1}\mathbf{E}_{i1} - \mathbf{E}_{i2}^{\mathrm{T}}\mathbf{K}_{i2}\mathbf{E}_{i2} - \mathbf{E}_{i3}^{\mathrm{T}}\mathbf{K}_{i3}\cdot\mathbf{E}_{i3}\right) \\ & + \sum_{i=1}^{N}\Bigg[\frac{1}{2h_{i1}}\left\|\mathbf{E}_{i1}^{\mathrm{T}}\mathbf{A}_i\mathbf{g}_{i1}(\mathbf{X}_{i1})\mathbf{G}_{i1}\right\|^2 + \frac{h_{i1}}{2}\|\boldsymbol{\epsilon}_{i1}\|^2 \\ & + \frac{1}{2h_{i2}}\left\|\mathbf{E}_{i1}^{\mathrm{T}}\mathbf{g}_{i2}(\mathbf{X}_{i2})\mathbf{G}_{i20}\right\|^2 + \frac{h_{i2}}{2}\|\boldsymbol{\epsilon}_{i2}\|^2 \\ & - \gamma_{i1}\tilde{\vec{\boldsymbol{\omega}}}_i^{(5)\mathrm{T}}\vec{\boldsymbol{\omega}}_i - \gamma_{i2}\tilde{\mathbf{c}}_i^{\mathrm{T}}\mathbf{c}_i - \gamma_{i3}\cdot\tilde{\boldsymbol{\sigma}}_i^{\mathrm{T}}\boldsymbol{\sigma}_i - \gamma_{i4}\tilde{\boldsymbol{\omega}}_i^{F\mathrm{T}}\boldsymbol{\omega}_i^F \\ & - \gamma_{i5}\tilde{\boldsymbol{\omega}}_i^{r\mathrm{T}}\boldsymbol{\omega}_i^r - \gamma_{i6}\tilde{\mathbf{H}}_i^{\mathrm{T}}\widehat{\mathbf{H}}_i - \left(k_{\epsilon_{i1}} - \frac{1}{2}\right)\|\boldsymbol{\epsilon}_{i1}\|^2 \\ & - \left(k_{\epsilon_{i2}} - \frac{1}{2}\right)\|\boldsymbol{\epsilon}_{i2}\|^2 + \frac{1}{2}\left\|\dot{\bar{\mathbf{Z}}}_{i2d}\right\|^2 + \frac{1}{2}\left\|\dot{\bar{\mathbf{v}}}_{i2}\right\|^2\Bigg]. \end{aligned} \tag{76}$$

Under the condition of (74a), the term $\gamma_{i1}\overset{\sim}{\vec{\omega}}_i^{(5)\mathrm{T}}\vec{\omega}_i$ has the following property:

$$-\gamma_{i1}\overset{\sim}{\vec{\omega}}_i^{(5)\mathrm{T}}\vec{\omega}_i^{(5)} \le \bar{\gamma}_{i1}\left(\bar{\omega}^{(5)} + 2\left\|\vec{\omega}^{(5)*}\right\|^2 - \frac{1}{2}\left\|\overset{\sim}{\vec{\omega}}_i^{(5)}\right\|^2\right). \quad (77)$$

The reason is as follows:

When $\bar{\omega}^{(5)} \ge \|\vec{\omega}_i^{(5)}\|^2$, $\gamma_{i1} = 0$, then

$$\begin{aligned}
-\gamma_{i1}\overset{\sim}{\vec{\omega}}_i^{(5)\mathrm{T}}\vec{\omega}_i^{(5)} = 0 &\le \bar{\gamma}_{i1}\left(\bar{\omega}^{(5)} - \left\|\vec{\omega}_i^{(5)}\right\|^2\right) \\
&= \bar{\gamma}_{i1}\left(\bar{\omega}^{(5)} - \left\|\vec{\omega}_i^{(5)*} + \overset{\sim}{\vec{\omega}}_i^{(5)*}\right\|^2\right) \\
&\le \bar{\gamma}_{i1}\left(\bar{\omega}^{(5)} - \left\|\left|\vec{\omega}_i^{(5)*}\right| - \left|\overset{\sim}{\vec{\omega}}_i^{(5)*}\right|\right\|^2\right) \\
&\le \bar{\gamma}_{i1}\left(\bar{\omega}^{(5)} + 2\left|\vec{\omega}_i^{(5)*}\right|^{\mathrm{T}}\left|\overset{\sim}{\vec{\omega}}_i^{(5)*}\right| - \left\|\overset{\sim}{\vec{\omega}}_i^{(5)*}\right\|^2\right) \\
&\le \bar{\gamma}_{i1}\left(\bar{\omega}^{(5)} + 2\left\|\vec{\omega}_i^{(5)*}\right\|^2 - \frac{1}{2}\left\|\overset{\sim}{\vec{\omega}}_i^{(5)*}\right\|^2\right).
\end{aligned} \quad (78)$$

On the other hand, when $\bar{\omega}^{(5)} < \|\vec{\omega}_i^{(5)}\|^2$, $\gamma_{i1} = \bar{\gamma}_{i1}$, then,

$$\begin{aligned}
-\gamma_{i1}\overset{\sim}{\vec{\omega}}_i^{(5)\mathrm{T}}\vec{\omega}_i^{(5)} &= -\bar{\gamma}_{i1}\overset{\sim}{\vec{\omega}}_i^{(5)\mathrm{T}}\left(\vec{\omega}_i^{(5)*} + \overset{\sim}{\vec{\omega}}_i^{(5)}\right) \\
&\le -\frac{1}{2}\bar{\gamma}_{i1}\left(\left\|\overset{\sim}{\vec{\omega}}_i^{(5)\mathrm{T}}\right\|^2 - \left\|\vec{\omega}_i^{(5)*}\right\|^2\right).
\end{aligned} \quad (79)$$

Hence, by combining (78) and (79), one can obtain (77). By the same way, one can conclude that

$$\begin{cases}
-\gamma_{i2}\tilde{\mathbf{c}}_i^T\mathbf{c}_i \le \bar{\gamma}_{i2}\left(\bar{c} + 2\|\boldsymbol{c}^*\|^2 - \frac{1}{2}\|\tilde{\boldsymbol{c}}_i\|^2\right), \\
-\gamma_{i3}\tilde{\boldsymbol{\sigma}}_i^T\boldsymbol{\sigma}_i \le \bar{\gamma}_{i3}\left(\bar{\sigma} + 2\|\boldsymbol{\sigma}^*\|^2 - \frac{1}{2}\|\tilde{\boldsymbol{\sigma}}_i\|^2\right), \\
-\gamma_{i4}\tilde{\boldsymbol{\omega}}_i^{F\mathrm{T}}\boldsymbol{\omega}_i^F \le \bar{\gamma}_{i4}\left(\bar{\omega}^F + 2\left\|\boldsymbol{\omega}^{F*}\right\|^2 - \frac{1}{2}\left\|\tilde{\boldsymbol{\omega}}_i^F\right\|^2\right), \\
-\gamma_{i5}\tilde{\boldsymbol{\omega}}_i^{rT}\boldsymbol{\omega}_i^r \le \bar{\gamma}_{i5}\left(\bar{\omega}^r + 2\|\boldsymbol{\omega}^{r*}\|^2 - \frac{1}{2}\|\tilde{\boldsymbol{\omega}}_i^r\|^2\right).
\end{cases} \quad (80)$$

Furthermore, the term $\gamma_{i6}\tilde{\mathbf{H}}_i^T\hat{\mathbf{H}}_i$ in (76) satisfies that

$$-\gamma_{i6}\tilde{\mathbf{H}}_i^{\mathrm{T}}\hat{\mathbf{H}}_i \le -\frac{1}{2}\gamma_{i6}\left(\left\|\tilde{\mathbf{H}}_i\right\|^2 - \|\mathbf{H}_i\|^2\right). \quad (81)$$

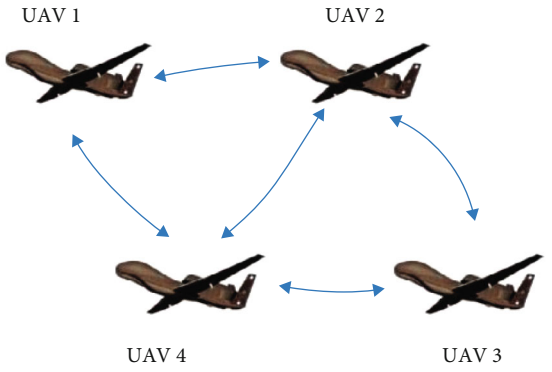

Figure 3: Communication topology.

Table 1: Initial attitudes of all UAVs.

	$\mu_i(0)$ (rad)	$\alpha_i(0)$ (rad)	$\beta_i(0)$ (rad)
UAV 1	0.01	0.01	0.01
UAV 2	-0.015	-0.015	-0.015
UAV 3	0.02	0.02	0.02
UAV 4	-0.025	-0.025	-0.025

Substituting (76) with (77), (80), and (81) then yeilds

$$\begin{aligned}
\dot{V} \le \sum_{i=1}^{N}\Bigg[&-\mathbf{E}_{i1}^{\mathrm{T}}\left(\mathbf{K}_{i1} - \frac{1}{2h_{i1}}\|A_i\mathbf{g}_{i1}(\mathbf{X}_{i1})\mathbf{G}_{i1}\|^2\right)\cdot\mathbf{E}_{i1} - \mathbf{E}_{i2}^{\mathrm{T}} \\
&\cdot\left(\mathbf{K}_{i2} - \frac{1}{2h_{i2}}\|\mathbf{g}_{i2}(\mathbf{X}_{i2})\mathbf{G}_{i20}\|^2\right)\mathbf{E}_{i2} - \mathbf{E}_{i3}^{\mathrm{T}}\mathbf{K}_{i3}\mathbf{E}_{i3}\Bigg] \\
&+ \sum_{i=1}^{N}\Bigg[-\frac{1}{2}\bar{\gamma}_{i1}\left\|\overset{\sim}{\vec{\omega}}_i^{(5)}\right\|^2 - \frac{1}{2}\bar{\gamma}_{i2}\cdot\|\tilde{\mathbf{c}}_i\|^2 - \frac{1}{2}\bar{\gamma}_{i3}\|\tilde{\boldsymbol{\sigma}}_i\|^2 \\
&- \frac{1}{2}\bar{\gamma}_{i4}\left\|\tilde{\boldsymbol{\omega}}_i^F\right\|^2 - \frac{1}{2}\bar{\gamma}_{i5}\cdot\|\tilde{\boldsymbol{\omega}}_i^r\|^2 - \frac{1}{2}\gamma_{i6}\left\|\tilde{\mathbf{H}}_i\right\|^2 \\
&- \left(k_{\epsilon_{i1}} - \frac{1+h_{i1}}{2}\right)\cdot\|\boldsymbol{\epsilon}_{i1}\|^2 - \left(k_{\boldsymbol{\epsilon}_{i2}} - \frac{1+h_{i2}}{2}\right)\|\boldsymbol{\epsilon}_{i2}\|^2\Bigg] + \delta,
\end{aligned} \quad (82)$$

where δ is

$$\begin{aligned}
\delta = \sum_{i=1}^{N}\Bigg[&\frac{1}{2}\left\|\dot{\bar{\mathbf{Z}}}_{i2d}\right\|^2 + \frac{1}{2}\left\|\dot{\bar{\mathbf{v}}}_{i2}\right\|^2 + \bar{\gamma}_{i1}\left(\bar{\omega}^{(5)} + 2\left\|\vec{\omega}^{(5)*}\right\|^2\right) \\
&+ \bar{\gamma}_{i2}\left(\bar{c} + 2\|\mathbf{c}^*\|^2\right) + \bar{\gamma}_{i3}\left(\bar{\sigma} + 2\|\boldsymbol{\sigma}^*\|^2\right) \\
&+ \bar{\gamma}_{i4}\left(\bar{\omega}^F + 2\left\|\boldsymbol{\omega}^{F*}\right\|^2\right) + \bar{\gamma}_{i5}\left(\bar{\omega}^r + 2\|\boldsymbol{\omega}^{r*}\|^2\right) + \frac{1}{2}\gamma_{i6}\|\mathbf{H}_i\|^2\Bigg].
\end{aligned} \quad (83)$$

By choosing the parameters $\mathbf{K}_{i1}$ and $\mathbf{K}_{i2}$ as

$$\begin{cases}
\mathbf{K}_{i1} = \mathbf{K}_{i10} + \frac{1}{2h_{i1}}\|A_i\mathbf{g}_{i1}(\mathbf{X}_{i1})\mathbf{G}_{i1}\|^2 \\
\mathbf{K}_{i2} = \mathbf{K}_{i20} + \frac{1}{2h_{i2}}\|\mathbf{g}_{i2}(\mathbf{X}_{i2})\mathbf{G}_{i20}\|^2
\end{cases}, \quad (84)$$

respectively, where $\mathbf{K}_{i10}$ and $\mathbf{K}_{i20}$ are positive diagonal

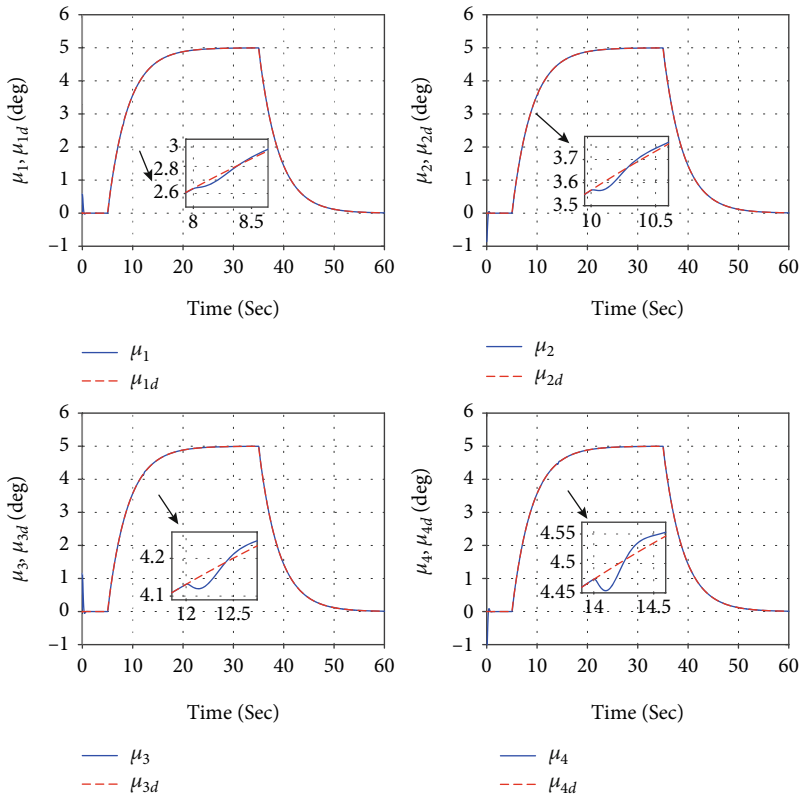

Figure 4: Bank angles μ_i and references μ_{id} of all UAVs ($i = 1, 2, 3, 4$).

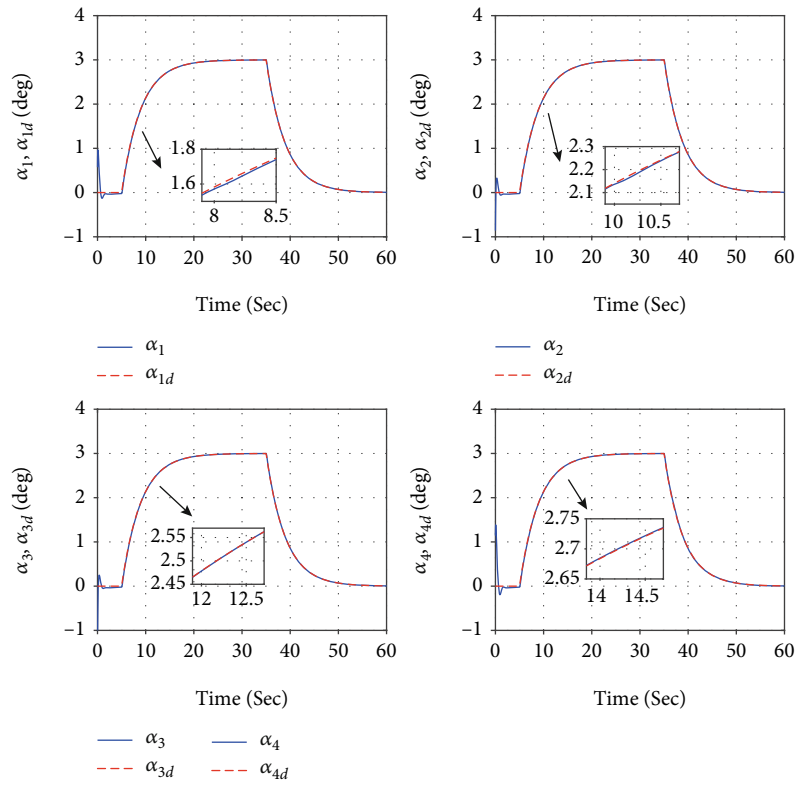

Figure 5: Attack angles α_i and references α_{id} of all UAVs ($i = 1, 2, 3, 4$).

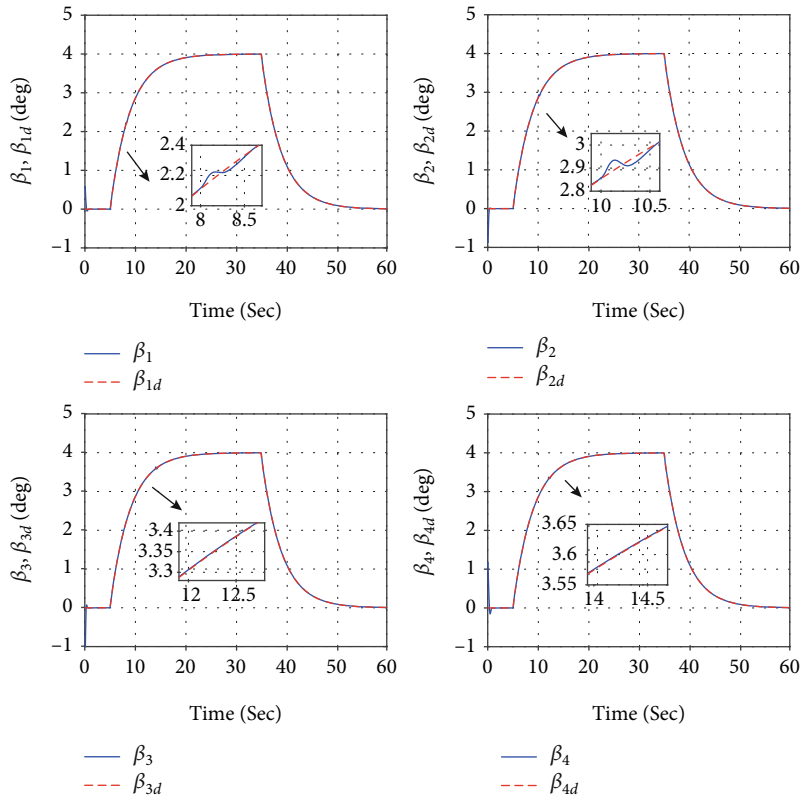

FIGURE 6: Sideslip angles β_i and references β_{id} of all UAVs ($i = 1, 2, 3, 4$).

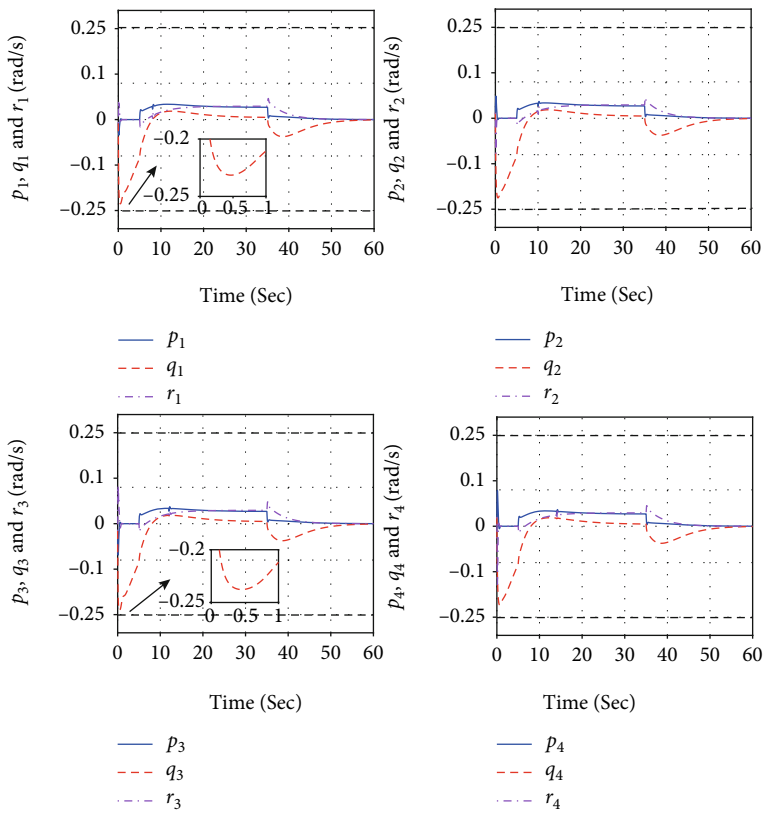

FIGURE 7: The time responses of p_i, q_i, and r_i with the developed control scheme ($i = 1, 2, 3, 4$).

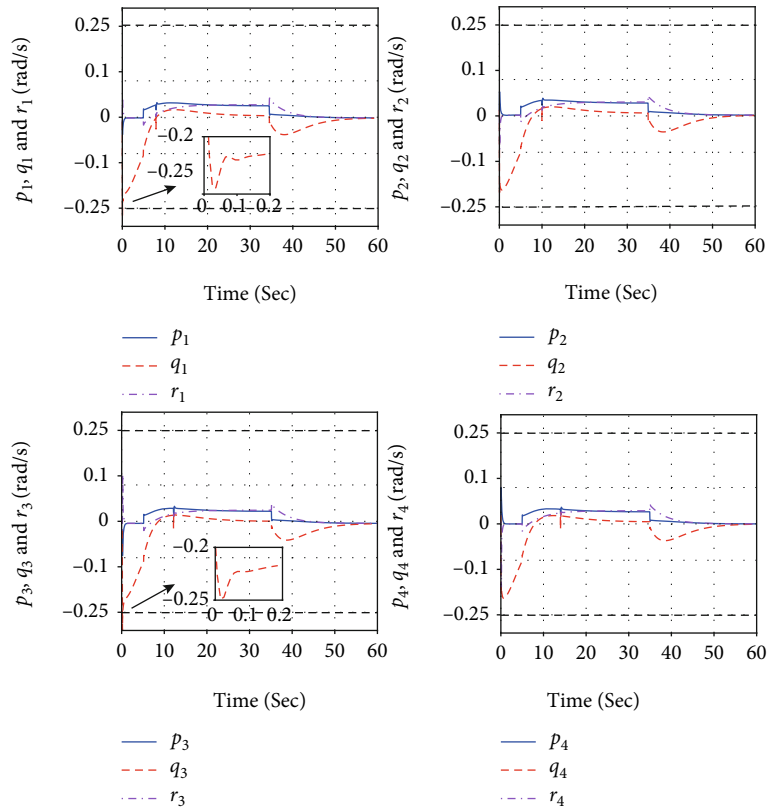

Figure 8: The time responses of p_i, q_i, and r_i without the constraint mechanism ($i = 1, 2, 3, 4$).

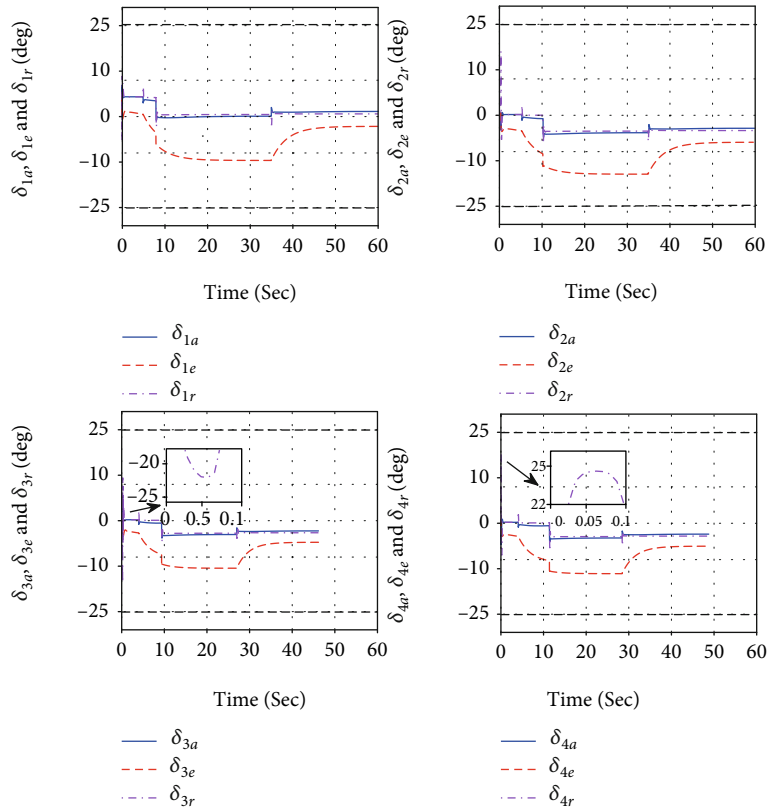

Figure 9: Control input signals δ_{ia}, δ_{ie}, and δ_{ir} of each UAVs ($i = 1, 2, 3, 4$).

matrices, (82) can be expressed as

$$\dot{V} \le -cV + \delta, \tag{85}$$

where c is

$$\begin{aligned} c = \min\{&\lambda_{\min}(2\mathbf{K}_{i10}), \lambda_{\min}(2\mathbf{K}_{i20}), \lambda_{\min}(2\mathbf{K}_{i30}), \\ &\eta_{i1}^{-1}\bar{\gamma}_{i1}, \eta_{i2}^{-1}\bar{\gamma}_{i2}, \eta_{i3}^{-1}\bar{\gamma}_{i3}, \eta_{i4}^{-1}\bar{\gamma}_{i4}, \eta_{i5}^{-1}\bar{\gamma}_{i5}, \eta_{i6}^{-1}\bar{\gamma}_{i6}, 2k_{\epsilon_{i1}} \\ &- 1 - h_{i1}, 2k_{\epsilon_{i2}} - 1 - h_{i2}\}. \end{aligned} \tag{86}$$

The expressions $\dot{\bar{\mathbf{Z}}}_{i2d}$ and $\dot{\bar{\mathbf{v}}}_{id}$ can be respectively obtained from (30) and (67), given by

$$\begin{aligned} \dot{\bar{\mathbf{Z}}}_{i2d} = &\frac{\partial \bar{\mathbf{Z}}_{i2d}}{\partial \mathbf{X}_{i1}}\dot{\mathbf{X}}_{i1} + \frac{\partial \bar{\mathbf{Z}}_{i2d}}{\partial \mathbf{E}_{i1}}\dot{\mathbf{E}}_{i1} + \frac{\partial \bar{\mathbf{Z}}_{i2d}}{\partial \mathbf{X}_{i1d}}\dot{\mathbf{X}}_{i1d} + \frac{\partial \bar{\mathbf{Z}}_{i2d}}{\partial \dot{\mathbf{X}}_{i1d}}\ddot{\mathbf{X}}_{i1d} \\ &+ \sum_{j\in N_i}^{j\neq i} a_{ij}\frac{\partial \bar{\mathbf{Z}}_{i2d}}{\partial \mathbf{Z}_{j1}}\dot{\mathbf{Z}}_{j1} + \frac{\partial \bar{\mathbf{Z}}_{i2d}}{\partial \mathbf{X}_{i2}}\dot{\mathbf{X}}_{i2} + \frac{\partial \bar{\mathbf{Z}}_{i2d}}{\partial \mathbf{Z}_{i2}}\dot{\mathbf{Z}}_{i2}, \\ \dot{\bar{\mathbf{v}}}_{id} = &\frac{\partial \bar{\mathbf{v}}_{id}}{\partial \mathbf{X}_{i1}}\dot{\mathbf{X}}_{i1} + \frac{\partial \bar{\mathbf{v}}_{id}}{\partial \mathbf{X}_{i2}}\dot{\mathbf{X}}_{i2} + \frac{\partial \bar{\mathbf{v}}_{id}}{\partial \mathbf{v}_i}\dot{\mathbf{v}}_i + \frac{\partial \bar{\mathbf{v}}_{id}}{\partial \hat{\mathbf{D}}_i}\dot{\hat{\mathbf{D}}}_i + \frac{\partial \bar{\mathbf{v}}_{id}}{\partial \hat{\Delta}_i}\dot{\hat{\Delta}}_i \\ &+ \frac{\partial \bar{\mathbf{v}}_{id}}{\partial \hat{\mathbf{H}}_i}\dot{\hat{\mathbf{H}}}_i + \frac{\partial \bar{\mathbf{v}}_{id}}{\partial \dot{\mathbf{Z}}_{i2d}}\ddot{\mathbf{Z}}_{i2d} + \frac{\partial \bar{\mathbf{v}}_{id}}{\partial \mathbf{E}_{i1}}\dot{\mathbf{E}}_{i1} + \frac{\partial \bar{\mathbf{v}}_{id}}{\partial \mathbf{E}_{i2}}\dot{\mathbf{E}}_{i2}. \end{aligned} \tag{87}$$

Define the following two vectors $\mathbf{X}_d$ and $\mathbf{E}_d$

$$\begin{cases} \mathbf{X}_d = \mathrm{col}\{\mathbf{X}_{1d}, \cdots, \mathbf{X}_{id}, \cdots, \mathbf{X}_{Nd}\}, \\ \mathbf{X}_{id} = \mathrm{col}\{\mathbf{X}_{i1d}, \dot{\mathbf{X}}_{i1d}, \ddot{\mathbf{X}}_{i1d}\}, \\ \mathbf{E}_d = \mathrm{col}\{\mathbf{E}_{1d}, \cdots, \mathbf{E}_{id}, \cdots, \mathbf{E}_{Nd}\}, \\ \mathbf{E}_i = \mathrm{col}\{\mathbf{E}_{i1}, \mathbf{E}_{i2}, \mathbf{E}_{i3}\}. \end{cases} \tag{88}$$

For any constants $\bar{B}_{X_d} > 0$, $\bar{B}_E > 0$, the sets $\mathscr{X} \coloneqq \{\mathbf{X}_d : \|\mathbf{X}_d\|^2 \le \bar{B}_{X_d}\}$ and $\mathscr{E} \coloneqq \{\mathbf{E}_d : \|\mathbf{E}_d\|^2 \le \bar{B}_E\}$ are compact ones. Then, $\mathscr{P} \coloneqq \mathscr{X} \times \mathscr{E}$ is also compact. Due to the fact that $\dot{\bar{\mathbf{Z}}}_{i2d}$ and $\dot{\bar{\mathbf{v}}}_{id}$ both are continuous function, considering the continuous property, there exists a constant $\delta_M > 0$ when $\forall (\mathbf{X}_d, \mathbf{E}_d) \in \mathscr{P}$ such that

$$\left\|\dot{\bar{\mathbf{Z}}}_{i2d}\right\|^2 + \left\|\dot{\bar{\mathbf{v}}}_{id}\right\|^2 \le \delta_M. \tag{89}$$

Therefore, there exists a constant $\bar{\delta} > 0$ satisfying

$$\delta \le \bar{\delta}, \forall (\mathbf{X}_d, \mathbf{E}_d) \in \mathscr{P}. \tag{90}$$

For any constant $\bar{B}_E$, there exists several parameters and initial condition satisfying

$$V(0) \le \bar{\delta}/c < 2\bar{\delta}/c \le \bar{B}_E, \tag{91}$$

such that

$$V(t) \le \frac{\bar{\delta}}{c}, \forall t \ge 0, \tag{92}$$

and $\mathscr{E}$ is an invariant set.

The above result (92) can be approved by contradiction. Since the reference input $\mathbf{X}_d$ must be bounded, that leads to $\mathbf{X}_d \in \mathscr{X}$ on $\forall t \ge 0$. Assuming $\exists t_1$, $V(t_1) > \bar{\delta}/c$, due to V is a continuous function, considering the continuous property, there exists a moment t_0 such that $V(t_0) = \bar{\delta}/c$, $V(t_{0+}) > \bar{\delta}/c$. Noticing $\|\mathbf{E}_d\|^2 \le 2V$ in (75), there exists $\|\mathbf{E}_d(t_0)\|^2 \le 2\bar{\delta}/c$. Considering (91) yields $(\mathbf{X}_d(t_0), \mathbf{E}_d(t_0)) \in \mathscr{P}$, so $\delta(t_0) \le \bar{\delta}$. Moreover, by taking account of (85), one can derive $\dot{V}(t_0) \le -cV(t_0) + \delta(t_0) = -\bar{\delta} + \delta(t_0) \le 0$. Hence, that causes $V(t_{0+}) \le V(t_0)$, which leads contradiction. This completes the proof of (91). Furthermore, considering $\|\mathbf{E}_d\|^2 \le 2V$ and (92), (91), one can derive $\mathscr{E}$ is an invariant set.

Therefore, all the signals in the system are uniformly bounded, and the states $\mathbf{X}_{i1}$, $\mathbf{X}_{i2}$ are always within their constraints. □

4. Simulation Results and Analysis

To illustrate the effectiveness and the superiority of the proposed FTCC scheme in this paper, using MATLAB/Simulink to simulate four UAVs whose communication topology is shown in Figure 3.

Figure 3 shows the communication network, and the parameters of UAVs are referred to [28]. The element a_{ij} of the adjacency matrix $\mathscr{A}$ is defined as 1 if the link between ith UAV and jth UAV existed; otherwise, $a_{ij} = 0$. The initial attitudes of all UAVs are presented in Table 1, and the initial angular rates are defined opposite as values of attitudes. The initial values of V_i, χ_i, and γ_i of all UAVs are set as 30 m/s, 0.01 rad and 0.01 rad, respectively.

Assuming the safe range of the attitudes μ_i, α_i, and β_i of all UAVs are $-8 \sim 8$ deg, and the corresponding angular velocity p_i, q_i, r_i are $-0.25 \sim 0.25$ rad/s. In addition, the maximum operation range of control surfaces δ_{ia}, δ_{ie}, and δ_{ir} are $-25 \sim 25$ deg.

Therefore, for any ith UAV, the upper bound $\bar{\mathbf{X}}_{i1}$ and the lower bound $\underline{\mathbf{X}}_{i1}$ of states $\mathbf{X}_{i1}$ are defined as $[8, 8, 8]^T$ deg and $-[8, 8, 8]^T$ deg, respectively. Similarly, the upper bound $\bar{\mathbf{X}}_{i2}$ and the lower bound $\underline{\mathbf{X}}_{i2}$ of states $\mathbf{X}_{i2}$ are $[0.25, 0.25, 0.25]^T$ rad/s and $-[0.25, 0.25, 0.25]^T$ rad/s, respectively. The upper bound $u_{i0\tau\ \max}$ and the lower bound $u_{i0\tau\ \min}$ are -25 deg and 25 deg, respectively.

The main control parameters are chosen as $\mathbf{K}_{i10} = \mathrm{diag}\{5, 5, 5\}$, $\mathbf{K}_{i20} = \mathrm{diag}\{20, 20, 20\}$, $\mathbf{K}_{i3} = \mathrm{diag}\{30, 30, 30\}$, $\eta_{i1} = \eta_{i2} = \eta_{i3} = \eta_{i4} = \eta_{i5} = 1.5$, $\eta_{i6} = 1.8$, $k_{\epsilon_{i1}} = k_{\epsilon_{i2}} = 100$, $h_{i1} = h_{i2} = 20$, and $\mu_{ib} = 0.001$.

To verify the effectiveness of the proposed FTCC scheme under actuator fault, the following fault signals are chosen:

$$\begin{cases} \boldsymbol{\rho}_1 = \boldsymbol{\rho}_2 = \boldsymbol{\rho}_3 = \boldsymbol{\rho}_4 = 1, \\ \mathbf{U}_{1f} = \mathbf{U}_{2f} = \mathbf{U}_{3f} = \mathbf{U}_{4f} = 0^\circ \end{cases} (t < 8)$$

$$\begin{cases} \boldsymbol{\rho}_1 = \text{diag}\,\{0.7,0.9,0.8\}, \\ \boldsymbol{\rho}_2 = \boldsymbol{\rho}_3 = \boldsymbol{\rho}_4 = 0, \\ \mathbf{U}_{1f} = [3^\circ, 2^\circ, 4^\circ]^T, \\ \mathbf{U}_{2f} = \mathbf{U}_{3f} = \mathbf{U}_{4f} = 0^\circ, \end{cases} (8 \le t < 10),$$

$$\begin{cases} \boldsymbol{\rho}_1 = \boldsymbol{\rho}_2\ \text{diag}\,\{0.7,0.9,0.8\}, \\ \boldsymbol{\rho}_3 = \boldsymbol{\rho}_4 = 0, \\ \mathbf{U}_{1f} = \mathbf{U}_{2f} = [3^\circ, 2^\circ, 4^\circ]^{\mathrm{T}}, \\ \mathbf{U}_{3f} = \mathbf{U}_{4f} = \mathbf{U}_{4f} = \mathbf{0}^\circ, \end{cases} (10 \le t < 12), \quad (93)$$

$$\begin{cases} \boldsymbol{\rho}_1 = \boldsymbol{\rho}_2 = \boldsymbol{\rho}_3 = \text{diag}\,\{0.7,0.9,0.8\}, \\ \boldsymbol{\rho}_4 = 0, \\ \mathbf{U}_{1f} = \mathbf{U}_{2f} = \mathbf{U}_{3f} = [3^\circ, 2^\circ, 4^\circ]^T, \\ \mathbf{U}_{4f} = 0^\circ, \end{cases} (12 \le t < 14),$$

$$\begin{cases} \boldsymbol{\rho}_1 = \boldsymbol{\rho}_2 = \boldsymbol{\rho}_3 = \boldsymbol{\rho}_4 = \text{diag}\,\{0.7,0.9,0.8\}, \\ \mathbf{U}_{1f} = \mathbf{U}_{2f} = \mathbf{U}_{3f} = \mathbf{U}_{4f} = [3^\circ, 2^\circ, 4^\circ]^T. \end{cases} (t \ge 14).$$

Remark 8. The reason of choosing the main control parameter briefly describes as follows. The parameter $\boldsymbol{K}_{i10}$ decides the closed-loop dynamics of $\dot{\boldsymbol{E}}_{i1}$, which can be approximated as $\dot{\boldsymbol{E}}_{i1} \approx -\boldsymbol{K}_{i1}\boldsymbol{E}_{i1} + \boldsymbol{E}_{i1}^T A_i g_{i1}(\boldsymbol{X}_{i1})\boldsymbol{G}_{i1}\boldsymbol{E}_{i2} + h_{i1}/2 \cdot \|\boldsymbol{\epsilon}_{i1}\|^2$ according to (32) and (84), and the term $\boldsymbol{E}_{i1}^T A_i g_{i1}(\boldsymbol{X}_{i1})\boldsymbol{G}_{i1}\boldsymbol{E}_{i2} + h_{i1}/2 \cdot \|\boldsymbol{\epsilon}_{i1}\|^2$will rapidly reduce due to the response of inner-loop dynamics $\boldsymbol{E}_{i2}$and $\boldsymbol{\epsilon}_{i1}$ are converge rapidly, then, it can be further represented as $\dot{\boldsymbol{E}}_{i1} \approx -\boldsymbol{K}_{i10}\boldsymbol{E}_{i1}$, so that the settling time of the dynamic $\boldsymbol{E}_{i1}$ approximately equal to $3/\lambda_{\min}(\boldsymbol{K}_{i10})$. There exists a tradeoff – a larger value $\boldsymbol{K}_{i10}$ helps to reduce the settling time while it needs larger change of the state $\boldsymbol{X}_{i2}$, which may cause saturation, so $\boldsymbol{K}_{i10}$ is taken as diag $\{5, 5, 5\}$. Similarly, parameters $\boldsymbol{K}_{i20}$ and $\boldsymbol{K}_{i3}$ decide the convergence rate of the inner-loop control errors $\boldsymbol{E}_{\mathrm{i2}}$ and $\boldsymbol{E}_{\mathrm{i3}}$, respectively, and their values normally take several times as the $\boldsymbol{K}_{\mathrm{i10}}$ to get faster response. Moreover, for parameters $\eta_{\mathrm{i1}} \sim \eta_{\mathrm{i6}}$, their inverses serve as learning rates of neural network, which usually take as a value among 1 ~ 1000 for fixed rate learning algorithms. In addition, parameters $k_{\epsilon_{\mathrm{i1}}}$ and $k_{\epsilon_{\mathrm{i2}}}$ are adjustment factors of dynamic surface filter, which are usually taken as a large value. Finally, for μ_{ib}, it can adjust the astringency of the error $\boldsymbol{E}_{\mathrm{i3}}$, which is the smaller the better, but the too small value will tend to cause virtual control signal "explosion".

The response of bank angle μ_i, angle of attack α_i, and sideslip angle β_i of each UAV are shown in Figures 4–6, respectively. It can be seen that all UAVs can track their references μ_{id}, α_{id}, and β_{id}. Although the fault occurs to UAV 1, UAV 2, UAV 3, and UAV 4 at 8 s, 10 s, 12 s, and 14 s, respectively, all UAVs can quickly track individual references again.

The response of state $\mathbf{X}_{i2}$ is shown in Figure 7. It can be seen that the states p_i, q_i, and r_i of all UAVs never exceed its upper or lower bound. Meanwhile, if the state constraints are not considered in the FTCC scheme, the states q_1 and q_3 will exceed the lower bound, which is shown in Figure 8. In addition, the control input signals δ_{ia}, δ_{ie}, and δ_{ir} are presented in Figure 9. Since the actuator constraint scheme (15) is adopted, the input signals never exceed their upper and lower bounds.

5. Conclusion and Future Work

This paper has explored an FTCC scheme for multi-UAVs under the distributed communication network, in which the issues including input saturation, state constraints, actuator faults, and unknown disturbances have all been taken into account.

It can be noted that the proposed FTCC scheme only considers fixed and undirected communication network. In addition, communication delay and communication interferences are not considered, and finite-time convergence technology has not been considered in the FTCC scheme, so the control performance cannot be achieved in finite time. Moreover, compared to the Euler attitude angles, the airflow attitude angles are necessary and easy to combine with the UAV's outer loop for position control, hence in this paper, it is directly used in the attitude control. However, using the airflow attitude angles for feedback control is less reliable than the former. Furthermore, sensor fault may occur at the same time, which perhaps outweigh the risk of actuator fault, so it deserves more attention and investigation. Finally, state measurements have been directly used in the control law without considering noise filtering, so that the performance may be degraded when sensor measurements have severe noises. Taking into account the noise filtering algorithms and sensor faults simultaneously will significantly increases the difficulty of proving the closed-loop system stability, which makes the issue challenging.

Therefore, in future work, the essence of communication delays, finite-time convergence technology, the reliability of using airflow attitude angle, sensor fault, and noise filtering will be taken into account on the basis of existing research. Besides, based on the simulation results from MATLAB/Simulink, the hardware-in-the-loop verification scheme will be adopted to further verify the proposed control scheme towards more practical applications.

Data Availability

No data were used to support this study.

Conflicts of Interest

The authors declare that they have no conflicts of interest.

Acknowledgments

This work was supported in part by National Natural Science Foundation of China (Nos. 61833013 and 62003162), Natural Science Foundation of Jiangsu Province of China (No. BK20200416), China Postdoctoral Science Foundation (Nos. 2020TQ0151 and 2020M681590), Aeronautical Science Foundation of China (No. 20200007018001), Science and Technology on Space Intelligent Control Laboratory (No. HTKJ2022KL502015), and Natural Sciences and Engineering Research Council of Canada.

References

[1] I. Bayezit and B. Fidan, "Distributed cohesive motion control of flight vehicle formations," *IEEE Transactions on Industrial Electronics*, vol. 60, no. 12, pp. 5763–5772, 2013.

[2] Y. Yang, H. Modares, K. G. Vamvoudakis, Y. Yin, and D. C. Wunsch, "Dynamic intermittent feedback design for H_∞ containment control on a directed graph," *IEEE Transactions on Cybernetics*, vol. 50, no. 8, pp. 3752–3765, 2019.

[3] A. Hegde and D. Ghose, "Multi-UAV collaborative transportation of payloads with obstacle avoidance," *IEEE Control Systems Letters*, vol. 6, pp. 926–931, 2022.

[4] X. Xiang, C. Liu, H. Su, and Q. Zhang, "On decentralized adaptive full-order sliding mode control of multiple UAVs," *ISA Transactions*, vol. 71, Part 2, pp. 196–205, 2017.

[5] K. Umemoto, T. Endo, and F. Matsuno, "Dynamic cooperative transportation control using friction forces of N multi-rotor unmanned aerial vehicles," *Journal of Intelligent & Robotic Systems*, vol. 100, no. 3-4, pp. 1085–1095, 2020.

[6] G. P. Kladis, P. P. Menon, and C. Edwards, "Fuzzy distributed cooperative tracking for a swarm of unmanned aerial vehicles with heterogeneous goals," *International Journal of Systems Science*, vol. 47, no. 16, pp. 3803–3811, 2016.

[7] L. He, X. Sun, and Y. Lin, "Distributed output-feedback formation tracking control for unmanned aerial vehicles," *International Journal of Systems Science*, vol. 47, no. 16, pp. 3919–3928, 2016.

[8] S. Park, J. Bae, Y. Kim, and S. Kim, "Fault tolerant flight control system for the tilt-rotor UAV," *Journal of the Franklin Institute*, vol. 350, no. 9, pp. 2535–2559, 2013.

[9] J. He, R. Qi, B. Jiang, and J. Qian, "Adaptive output feedback fault-tolerant control design for hypersonic flight vehicles," *Journal of the Franklin Institute*, vol. 352, no. 5, pp. 1811–1835, 2015.

[10] Z. Yu, Y. Zhang, B. Jiang, F. Jun, and Y. Jin, "A review on fault-tolerant cooperative control of multiple unmanned aerial vehicles," *Chinese Journal of Aeronautics*, vol. 35, no. 1, pp. 1–18, 2022.

[11] X. Qing, H. Yang, B. Jiang, D. Zhou, and Y. Zhang, "Fault tolerant formations control of UAVs subject to permanent and intermittent faults," *Journal of Intelligent & Robotic Systems*, vol. 73, no. 1-4, pp. 589–602, 2014.

[12] X. Yu, Z. Liu, and Y. Zhang, "Fault-tolerant formation control of multiple UAVs in the presence of actuator faults," *International Journal of Robust and Nonlinear Control*, vol. 26, no. 12, pp. 2668–2685, 2016.

[13] J. R. Azinheira and A. Moutinho, "Hover control of an UAV with backstepping design including input saturations," *IEEE Transactions on Control Systems Technology*, vol. 16, no. 3, pp. 517–526, 2008.

[14] S. Zhu and D. Wang, "Adversarial ground target tracking using UAVs with input constraints," *Journal of Intelligent & Robotic Systems*, vol. 65, no. 1-4, pp. 521–532, 2012.

[15] Y. Zhang, Y. Yang, Y. Zhao, and G. Wen, "Distributed finite-time tracking control for nonlinear multi-agent systems subject to external disturbances," *International Journal of Control*, vol. 86, no. 1, pp. 29–40, 2013.

[16] Z. Ding, "Consensus disturbance rejection with disturbance observers," *IEEE Transactions on Industrial Electronics*, vol. 62, no. 9, pp. 5829–5837, 2015.

[17] M. Chen, S. S. Ge, and B. Ren, "Adaptive tracking control of uncertain MIMO nonlinear systems with input constraints," *Automatica*, vol. 47, no. 3, pp. 452–465, 2011.

[18] J. Du, X. Hu, M. Krstić, and Y. Sun, "Robust dynamic positioning of ships with disturbances under input saturation," *Automatica*, vol. 73, pp. 207–214, 2016.

[19] B. Xu, "Disturbance observer-based dynamic surface control of transport aircraft with continuous heavy cargo airdrop," *IEEE Transactions on Systems, Man, and Cybernetics: Systems*, vol. 47, no. 1, pp. 161–170, 2017.

[20] Y. Yang, L. Tang, W. Zou, and D.-W. Ding, "Robust adaptive control of uncertain nonlinear systems with unmodeled dynamics using command filter," *International Journal of Robust and Nonlinear Control*, vol. 31, no. 16, pp. 7764–7784, 2021.

[21] Z. Yu, Y. Zhang, B. Jiang et al., "Composite adaptive disturbance observer-based decentralized fractional-order fault-tolerant control of networked UAVs," *IEEE Transactions on Systems, Man, and Cybernetics: Systems*, vol. 52, no. 2, pp. 799–813, 2022.

[22] Y. Yang and C. Z. Xu, "Adaptive fuzzy leader-follower synchronization of constrained heterogeneous multiagent systems," *IEEE Transactions on Fuzzy Systems*, vol. 30, no. 1, pp. 205–219, 2022.

[23] K. Zhao, L. Chen, and C. L. P. Chen, "Event-based adaptive neural control of nonlinear systems with deferred constraint," *IEEE Transactions on Systems, Man, and Cybernetics: Systems*, no. article 3143359, pp. 1–10, 2022.

[24] H. Bang, J. Kim, and Y. Jung, "Spacecraft attitude control compensating internal payload motion using disturbance observer technique," *International Journal of Aeronautical and Space Sciences*, vol. 20, no. 2, pp. 459–466, 2019.

[25] W. Qi, G. Zong, and S. F. Su, "Fault detection for semi-Markov switching systems in the presence of positivity constraints," *IEEE Transactions on Cybernetics*, 2021.

[26] W. Qi, G. Zong, and W. X. Zheng, "Adaptive event-triggered SMC for stochastic switching systems with semi-Markov process and application to boost converter circuit model," *IEEE Transactions on Circuits and Systems I: Regular Papers*, vol. 68, no. 2, pp. 786–796, 2021.

[27] H. He, W. Qi, Z. Liu, and M. Wang, "Adaptive attack-resilient control for Markov jump system with additive attacks," *Nonlinear Dynamics*, vol. 103, no. 2, pp. 1585–1598, 2021.

[28] Z. Yu, Y. Zhang, Z. Liu, Y. Qu, and C. Y. Su, "Distributed adaptive fractional-order fault-tolerant cooperative control of networked unmanned aerial vehicles via fuzzy neural networks," *IET Control Theory & Applications*, vol. 13, no. 17, pp. 2917–2929, 2019.

[29] J. D. Boskovic, S. E. Bergstrom, and R. K. Mehra, "Robust integrated flight control design under failures, damage, and state-dependent disturbances," *Journal of Guidance, Control, and Dynamics*, vol. 28, no. 5, pp. 902–917, 2005.

[30] K. Zhao, L. Chen, W. Meng, and L. Zhao, "Unified mapping function-based neuroadaptive control of constrained uncertain robotic systems," *Cybernetics*, vol. PP, pp. 1–10, 2022.

[31] K. Zhao, Y. Song, C. L. W. Meng, C. L. P. Chen, and L. Chen, "Low-cost approximation-based adaptive tracking control of output-constrained nonlinear systems," *IEEE Transactions on Neural Networks and Learning Systems*, vol. 32, no. 11, pp. 4890–4900, 2021.

[32] Z. Qu, "Matrix theory for cooperative systems," *Cooperative Control of Dynamical Systems: Applications to Autonomous Vehicles*, pp. 153–193, 2009.

[33] Z. Yu, Y. Zhang, B. Jiang et al., "Fractional-order adaptive fault-tolerant synchronization tracking control of networked fixed-wing UAVs against actuator-sensor faults via intelligent learning mechanism," *IEEE Transactions on Neural Networks and Learning Systems*, vol. 32, no. 12, pp. 5539–5553, 2021.

Hindawi
International Journal of Aerospace Engineering
Volume 2022, Article ID 9104823, 11 pages
https://doi.org/10.1155/2022/9104823

Research Article

Fault-Tolerant Guidance of Rocket Vertical Landing Phase Based on MPC Framework

Jingqi Li,[1] **Yaosong Long**,[2] **Mao Su**,[3] **Lei Liu**,[1] **Bo Wang**,[1] **and Zhongtao Cheng**[1]

[1]*National Key Laboratory of Science and Technology on Multispectral Information Processing, School of Artificial Intelligence and Automation, Huazhong University of Science and Technology, Wuhan 430074, China*
[2]*School of Aerospace Engineering, Huazhong University of Science and Technology, Wuhan 430074, China*
[3]*Designing Institute of Hubei Space Technology Academy, Wuhan 430074, China*

Correspondence should be addressed to Zhongtao Cheng; ztcheng@hust.edu.cn

Received 30 March 2022; Revised 21 June 2022; Accepted 6 July 2022; Published 12 August 2022

Academic Editor: Lingxia Mu

For the vertical landing process of reusable rockets, the landing accuracy is likely to be affected by disturbances and faults during flight. In this paper, a fault-tolerant guidance method based on the MPC framework is put forward. First, we propose a piecewise guidance algorithm that combines a trajectory optimization algorithm based on convex optimization with the MPC framework. With the fast trajectory optimization algorithm and the MPC framework that recursively introduces the real-time state, this algorithm forms a robust closed loop. Then, we design an integrated guidance, navigation, and control (GNC) system to enhance the fault tolerance and robustness of the guidance method. Simulation experiments verify that this method is fault-tolerant to various fault conditions including navigation system failures, control system failures, drag coefficient deviations, and atmospheric density deviations. This guidance method is robust enough to overcome disturbances and faults, and it has great potential for online use.

1. Introduction

Launching a rocket is a high-cost and high-risk investment, and there is growing concern about how to make it economical. Building reusable rockets is an effective way to reduce costs and create business value. At present, many countries have invested plenty of research in rocket recovery technology. Two US companies, Blue Origin and SpaceX, have successfully conducted rocket recovery experiments, proving the feasibility of vertical landing technology. The rocket recovery mission is generally divided into four flight phases: the attitude adjustment phase, the power deceleration phase, the aerodynamic deceleration phase, and the vertical landing phase [1], so as to ensure that the rocket lands vertically and softly at the predetermined location. The recovery process is confronted with difficulties including large spans of airspace and velocity domain, large changes in the flight environment, complex flight constraints, and strong disturbances and uncertainties, any of which may lead to errors. The accumulated errors generated by preceding phases must be eliminated in the vertical landing phase which is the last phase of the recovery mission [2]. The time is short but the precision is high. Therefore, extremely high requirements are placed on the guidance speed and accuracy of this phase. Research on fast and accurate guidance method of rocket vertical landing phase is the basis for successfully recovering a rocket.

The study of the landing problem began with the Apollo project. Due to the limited computing ability, researchers could only apply analytical guidance law in that era [3]. Unlike the lunar landing mission, more complex path constraints and rigorous terminal conditions must be considered for rocket vertical landing problems. However, the derivation of the analytical method is cumbersome, making it unsuitable for most complex nonlinear problems [4]. Thanks to the research on numerical methods by

mathematicians and the development of computers' computing ability [2], the trajectory optimization of rocket vertical landing problems mainly relies on numerical algorithms these days.

The vertical landing problem can be expressed as an optimal control problem with the objective of minimum fuel consumption, subject to the constraints of dynamic equations and the constraints on state and control variables. It can be transformed into a nonlinear programming problem (NLP) through time discretization. Early studies found that the pseudospectral methods had high accuracy in solving NLP. In recent years, these methods have been widely used for trajectory optimization problems. Chen and Xia [5] used a pseudospectral method to analyze the ascent trajectory characteristics of a solid rocket-powered launch vehicle. Mu et al. [6] planned the Mars landing trajectory by the Gauss pseudospectral method. However, the real-time performance and convergence of these methods cannot meet the requirements of online guidance [2]. Subsequent studies have shown that convex optimization is more advantageous for online trajectory optimization. As long as the problem is transformed into a convex optimization form, it can theoretically be solved in polynomial time by the interior point method [7]. Convex optimization was first applied to Mars landing [8, 9]. In order to convert the landing problem into a convex problem, Açıkmeşe et al. [10] proposed a lossless convexification method to deal with thrust constraints and proved that the lossless convexification problem is equivalent to the original problem, which greatly promoted the development of convex optimization methods in the field of trajectory optimization. However, not all constraints can be convexified by lossless convexification. A more general approach is successive convexification, which linearizes the original nonconvex problem into a series of convex subproblems and then iteratively finds the optimal solution of the subproblems. In 2013, Lu and Liu [11] proposed successive convexification for convexifing dynamic equations and other nonconvex constraints when they studied the rendezvous problem. They later used this method to solve the hypersonic vehicle reentry problem [12] and the rocket landing problem [13]. The advantages of convex optimization including computational efficiency and insensitivity to initial guesses make it an efficient method for solving trajectory optimization problems. It is widely used in the aerospace field, such as low-thrust transfers [14], rendezvous problem [15], re-entry problem [12], and the vertical landing problem studied in this paper.

There are two commonly used coordinate systems for modeling rocket vertical landing problems, the velocity coordinate system [16–20] and the landing point coordinate system [21–25]. In this paper, the three-degree-of-freedom dynamics of the rocket are derived based on the landing point coordinate system. Since Szmuk et al. [21] applied successive convex optimization to solve the rocket vertical landing problem in 2016, research on trajectory optimization of landing problems has become more and more abundant and mature. The current research focus is to improve the convergence performance and solution efficiency of successive convex optimization, so that the approach can meet the needs of online guidance. In Ref. [24], a convex feasible set (CFS) method is proposed to convexify the angle of attack constraint which is a nonconvex-nonconcave inequality. Ref. [25] presents a two-stage successive convexification method. Simulation experiments show that the performance of the two-stage method is more stable and efficient than the single-stage method. Ref. [26] compares the computational performance and solution accuracy of six discretization methods. In Ref. [18], an online update strategy for trust regions is proposed to speed up the convergence of successive convex optimization.

However, the rocket will be affected by wind interference and environmental uncertainties after entering the atmosphere, and modules such as the navigation system and the control system may malfunction during the landing process. Trajectory optimization alone cannot overcome these disturbances and faults. Therefore, it is necessary to design an online fault-tolerant guidance method to ensure landing accuracy. A fault-tolerant control method has been proposed to deal with parametric uncertainties and unknown actuator failures [27]. But there is a lack of research on guidance methods for vertical landing problems at present. In Ref. [22], a receding horizon guidance method based on convex optimization is proposed. Ref. [28] and Ref. [29] both propose to construct a guidance, navigation, and control (GNC) system for closed-loop guidance, but they do not give a specific algorithm.

In recent years, some researchers put forward a guidance method based on trajectory optimization and model predictive control (MPC) framework. MPC is a control strategy that recursively solves an optimal control problem with updated system states at each sampling time. Ref. [30] presents the MPC algorithm for the optimal guidance and reconfiguration of swarms of spacecraft. In Ref. [31], MPC is used for asteroid landing. Ref. [32] reviews applications of MPC in the aerospace guidance field. For the online guidance problem of the rocket vertical landing phase, a successive convexification + MPC guidance algorithm is proposed by Ref. [33]. Ref. [19] embeds a pseudospectral-improved successive convexification (PISC) algorithm in the MPC framework to construct a parallel feasibility-guaranteed guidance algorithm. Ref. [34] designs an antidelay model predictive control (AD-MPC) scheme for carrier landing. Ref. [35] implements a successive convexification MPC-based guidance algorithm to solve the six-degree-of-freedom powered descent guidance problem.

In this paper, we propose a piecewise guidance algorithm that embeds a convex optimization-based trajectory optimization algorithm in the MPC framework. An integrated GNC system is then designed to further improve the fault tolerance and robustness of the entire system. The rest of this paper is organized as follows. In Section 2, a mathematical description of the rocket vertical landing problem is given. Section 3 elaborates the online trajectory optimization algorithm based on convex optimization, including convexification and discretization methods for transforming the original problem into a second-order cone programming (SOCP) problem. In Section 4, the trajectory optimization algorithm is embedded in the MPC framework, and a

piecewise guidance method is proposed to cope with the bang-bang characteristic of the control. Section 5 designs an integrated GNC system. In Section 6, simulation experiments are carried out to verify the reliability, accuracy, robustness, and fault tolerance of the guidance method. Section 7 concludes the whole work.

2. Problem Formulation

In this section, we use the inertial reference frame to formulate the fuel-optimal rocket vertical landing problem as a standard optimal control problem.

2.1. Dynamics and Constraints. The rocket's flight time during the vertical landing phase is so short that the Earth's surface can be assumed to be a horizontal plane. Based on this assumption, we build an inertial reference frame with the origin O located at the predetermined landing point as shown in Figure 1. The OX axis is perpendicular to the plane, and the upward direction is positive. The OY axis is parallel to the plane, and the direction pointing to the rocket's launch point is positive. The OZ axis and the other two axes form a right-handed Cartesian coordinate system.

In this reference frame, the rocket's three-degree-of-freedom dynamics are

$$\begin{cases} \dot{\boldsymbol{r}}(t) = \boldsymbol{v}(t), \\ \dot{\boldsymbol{v}}(t) = \dfrac{\boldsymbol{T}(t) + \boldsymbol{D}(t)}{m(t)} + \boldsymbol{g}, \\ \dot{m}(t) = -\dfrac{\|\boldsymbol{T}(t)\|}{I_{sp} g_0}, \end{cases} \tag{1}$$

where $\boldsymbol{r}(t)$, $\boldsymbol{v}(t)$, and $m(t)$ represent the position vector, velocity vector, and mass of the rocket, respectively. $\boldsymbol{T}(t)$ is the thrust vector of the rocket engine. $\|\cdot\|$ represents the 2-norm of the vector.

During the landing phase, the constraints on thrust magnitude and direction are expressed as

$$T_{\min} \le \|\boldsymbol{T}(t)\| \le T_{\max}, \tag{2}$$

$$\|\boldsymbol{T}(t)\| \cos \eta_{\max} \le \mathbf{e}_x \boldsymbol{T}(t), \tag{3}$$

where $T_{\min}$ and $T_{\max}$ represent the minimum and maximum thrust magnitude that the engine can provide, respectively. $\eta_{\max}$ is the maximum allowable value of the angle between the thrust direction and the OX direction. $\boldsymbol{D}(t)$ is the aerodynamic drag calculated by the following formula:

$$\boldsymbol{D}(t) = -\frac{1}{2} \rho S_D C_D \|\boldsymbol{v}(t)\| \boldsymbol{v}(t), \tag{4}$$

where ρ is the air density, S_D is the drag reference area, and C_D is the drag coefficient.

To prevent the rocket from colliding with the ground or being interfered with by the ground protrusion during flight, a glide-slope constraint is imposed to restrict the path of the rocket to lie within an upward-facing cone:

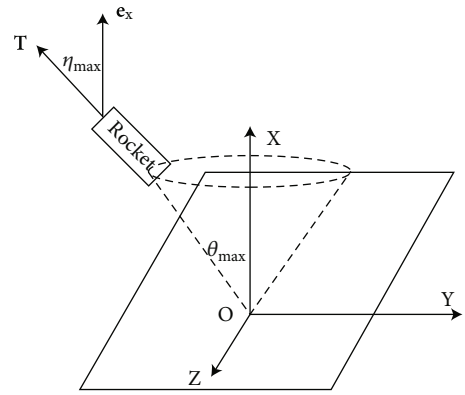

Figure 1: Inertial reference frame.

$$\|\boldsymbol{r}(t)\| \cos \theta_{\max} \le \boldsymbol{e}_x \boldsymbol{r}(t), \tag{5}$$

where $\mathbf{e}_x$ represents the unit vector in the OX direction. $\theta_{\max}$ is the maximum allowable half-cone angle.

We also need to consider boundary conditions. The rocket's initial position vector, velocity vector, and mass are specified as fixed parameters. Its final position and velocity vectors are fixed, too. The thrust vector at the terminal time must be in the OX direction. The fuel remaining of the rocket must be nonnegative, which means that the landing mass of the rocket must be greater than the dry mass which is denoted as m_{dry}. The boundary conditions are summarized as

$$\boldsymbol{r}(0) = \boldsymbol{r}_0, \boldsymbol{v}(0) = \boldsymbol{v}_0, m(0) = m_0, \tag{6}$$

$$\boldsymbol{r}(t_f) = 0, \boldsymbol{v}(t_f) = 0, \boldsymbol{T}(t_f) = \|\boldsymbol{T}(t_f)\| e_x, m(t_f) \ge m_{\text{dry}}. \tag{7}$$

2.2. Performance Index. The performance index of the fuel-optimal rocket vertical landing problem is selected as minimizing the fuel consumption, which is equivalent to maximizing the terminal mass of the rocket. Therefore, the objective function is expressed as

$$J = -m(t_f). \tag{8}$$

To sum up, with thrust vector $\boldsymbol{T}$ as the control variable and $[\boldsymbol{r}^T, \boldsymbol{v}^T, m]^T$ as the state variables, the rocket vertical landing problem can be formulated as an optimal control problem with free terminal time:

$$\begin{aligned} &\text{Problem0} : \min_{\boldsymbol{T}} J = -m(t_f), \\ &\text{subject to } (1)(2)(3)(5)(6)(7). \end{aligned} \tag{9}$$

3. Trajectory Optimization Algorithm Based on Convex Optimization

In this section, we will elaborate on the trajectory optimization algorithm based on convex optimization and embedded in the subsequent guidance system. This includes the use of convexification and discretization methods to convert Problem0 into a convex problem, as well as iteratively solving the converted problem afterward.

3.1. Convexification. The thrust magnitude constraint in Problem0 is nonconvex. Its nonconvex feasible region can be relaxed through lossless convexification to form a high-dimensional convex feasible region, transforming the nonconvex constraint into a relaxed convex constraint. Using the above method, we introduce a slack variable Γ to transform Eq. (2) into

$$\|\boldsymbol{T}(t)\| \le \Gamma(t), \tag{10}$$

$$T_{\min} \le \Gamma(t) \le T_{\max}. \tag{11}$$

By replacing the nonconvex constraint (Eq. (2)) in Problem0 with the convex constraints (Eqs. (10) and (11)), the nonconvex problem is converted into a relaxed problem. Studies have shown that the optimal solution to the relaxed problem is also the optimal solution to Problem0 [8–10]. Taking $\boldsymbol{T}$ and Γ as control variables, that is, the control variables are redefined as $\boldsymbol{u} = [\Gamma, \boldsymbol{T}^T]^T$. The dynamics are transformed into

$$\boldsymbol{f}(\boldsymbol{x}, \boldsymbol{u}) = \begin{bmatrix} \dot{\boldsymbol{r}}(t) = \boldsymbol{v}(t) \\ \dot{\boldsymbol{v}}(t) = \dfrac{\boldsymbol{T}(t) + \boldsymbol{D}(t)}{m(t)} + \boldsymbol{g} \\ \dot{m}(t) = \dfrac{-\Gamma}{(I_{sp} g_0)} \end{bmatrix}. \tag{12}$$

The nonlinearity of Eq. (12) is caused by the free terminal time, aerodynamic drag $\boldsymbol{D}(t)$, and the denominator $m(t)$. It can be linearized through successive convexification. In this paper, the terminal time is added to the optimization variables, which will be optimized together with the state and control variables in the subsequent optimization process. t_f in Eq. (12) is a hidden variable. Define $\tau \triangleq t/t_f$. Apply the chain rule to make t_f explicit:

$$\frac{d\boldsymbol{x}}{dt} = \frac{d\boldsymbol{x}}{d\tau}\frac{d\tau}{dt}. \tag{13}$$

Eq. (12) is transformed into

$$\frac{d\boldsymbol{x}}{d\tau} = \boldsymbol{f}(\boldsymbol{x}, \boldsymbol{u}) t_f. \tag{14}$$

We adopt successive convexification to iteratively solve Eq. (14). The first-order Taylor expansion is performed at the kth iteration to transform Eq. (14) into

$$\begin{aligned} \frac{d\boldsymbol{x}}{d\tau} = {} & \boldsymbol{f}\left(\boldsymbol{x}^k, \boldsymbol{u}^k\right) t_f^k + \boldsymbol{A}\left(\boldsymbol{x}^k, \boldsymbol{u}^k\right)\left(\boldsymbol{x} - \boldsymbol{x}^k\right) t_f^k \\ & + \boldsymbol{B}\left(\boldsymbol{x}^k, \boldsymbol{u}^k\right)\left(\boldsymbol{u} - \boldsymbol{u}^k\right) t_f^k + \boldsymbol{f}\left(\boldsymbol{x}^k, \boldsymbol{u}^k\right)\left(t_f - t_f^k\right), \end{aligned} \tag{15}$$

where $\boldsymbol{A}(\boldsymbol{x}^k, \boldsymbol{u}^k)$ and $\boldsymbol{B}(\boldsymbol{x}^k, \boldsymbol{u}^k)$ are the gradients of $\boldsymbol{f}(\boldsymbol{x}, \boldsymbol{u})$ with respect to the state variables $\boldsymbol{x} = [\boldsymbol{r}^T, \boldsymbol{v}^T, m]^T$ and control variables $\boldsymbol{u} = [\Gamma, \boldsymbol{T}^T]^T$, respectively.

3.2. Discretization. The problem is still infinite-dimensional after convexification and needs to be discretized into a finite-dimensional problem. We adopt the trapezoidal discretization to discretize the problem. This requires the time of flight to be evenly divided into N discrete intervals, i.e., $N + 1$ discrete points (the value of N in each guidance cycle will be discussed later). The subscript $i (i = 1, \cdots, N + 1)$ represents the ith discrete point of the state or control variable, then, Eq. (15) is discretized as

$$\begin{aligned} \boldsymbol{x}_{i+1} = {} & \boldsymbol{x}_i + \frac{1}{2N}\left(\boldsymbol{A}_i^k\left(\boldsymbol{x}_i - \boldsymbol{x}_i^k\right) t_f^k + \boldsymbol{B}_i^k\left(\boldsymbol{u}_i - \boldsymbol{u}_i^k\right) t_f^k + \boldsymbol{f}_i^k t_f\right) \\ & + \frac{1}{2N}\left(\boldsymbol{A}_{i+1}^k\left(\boldsymbol{x}_{i+1} - \boldsymbol{x}_{i+1}^k\right) t_f^k + \boldsymbol{B}_{i+1}^k\left(\boldsymbol{u}_{i+1} - \boldsymbol{u}_{i+1}^k\right) t_f^k + \boldsymbol{f}_{i+1}^k t_f\right), \end{aligned} \tag{16}$$

where $\boldsymbol{A}_i^k = \boldsymbol{A}(\boldsymbol{x}_i^k, \boldsymbol{u}_i^k)$, $\boldsymbol{B}_i^k = \boldsymbol{B}(\boldsymbol{x}_i^k, \boldsymbol{u}_i^k)$, and $\boldsymbol{f}_i^k = \boldsymbol{f}(\boldsymbol{x}_i^k, \boldsymbol{u}_i^k)$.

After discretization, constraints (3), (5), (6), (7), (10), and (11) are transformed into

$$\|\boldsymbol{T}_i\| \cos \eta_{\max} \le \boldsymbol{e}_x \boldsymbol{T}_i, \tag{17}$$

$$\|\boldsymbol{r}_i\| \cos \theta_{\max} \le \boldsymbol{e}_x \boldsymbol{r}_i, \tag{18}$$

$$\boldsymbol{r}_1 = \boldsymbol{r}_0, \boldsymbol{v}_1 = \boldsymbol{v}_0, m_1 = m_0, \tag{19}$$

$$\boldsymbol{r}_{N+1} = 0, \boldsymbol{v}_{N+1} = 0, \boldsymbol{T}_{N+1} = \|\boldsymbol{T}_{N+1}\| \boldsymbol{e}_x, m_{N+1} \ge m_{\text{dry}}, \tag{20}$$

$$\|\boldsymbol{T}_i\| \le \Gamma_i, \tag{21}$$

$$T_{\min} \le \Gamma_i \le T_{\max}. \tag{22}$$

3.3. Trajectory Optimization Algorithm. Define $H_i = I + t_f^k/(2N)\boldsymbol{A}_i^k$, $H_{i+1} = -I + t_f^k/(2N)\boldsymbol{A}_{i+1}^k$, $G_i = t_f^k/(2N)\boldsymbol{B}_i^k$, $G_{i+1} = t_f^k/(2N)\boldsymbol{B}_{i+1}^k$, $F_i = (\boldsymbol{f}_i^k + \boldsymbol{f}_{i+1}^k)/(2N)$, $C_i = \boldsymbol{A}_i^k \boldsymbol{x}_i^k t_f^k + \boldsymbol{B}_i^k \boldsymbol{u}_i^k t_f^k$. Equation (16) can be expressed as

$$H_i \boldsymbol{x}_i + H_{i+1} \boldsymbol{x}_{i+1} + G_i \boldsymbol{u}_i + G_{i+1} \boldsymbol{u}_{i+1} + F_i = \frac{1}{2N}(C_i + C_{i+1}). \tag{23}$$

The terminal time t_f is added to the control variables for optimization. Combine the discretized forms of state variables $\boldsymbol{x} = [\boldsymbol{r}^T, \boldsymbol{v}^T, m]^T$, control variables $\boldsymbol{u} = [\Gamma, \boldsymbol{T}^T]^T$ and t_f into a joint optimization variable Z, that is, define $Z = [\boldsymbol{x}_1^T, \cdots, \boldsymbol{x}_{N+1}^T, \boldsymbol{u}_1^T, \cdots, \boldsymbol{u}_{N+1}^T, t_f]^T$, then, Eq. (23) can be

transformed into the following matrix form:

$$MZ = C, \tag{24}$$

where

$$M = \begin{bmatrix} I & 0 & \cdots & 0 & 0 & 0 & 0 & \cdots & 0 & 0 & 0 \\ H_1 & H_2 & \cdots & 0 & 0 & G_1 & G_2 & \cdots & 0 & 0 & F_1 \\ \vdots & \vdots & \ddots & \vdots & \vdots & \vdots & \vdots & \ddots & \vdots & \vdots & \vdots \\ 0 & 0 & \cdots & H_N & H_{N+1} & 0 & 0 & \cdots & G_N & G_{N+1} & F_N \end{bmatrix},$$

$$C = 1/(2N) \begin{bmatrix} 2N\boldsymbol{x}_1 \\ C_1 + C_2 \\ \vdots \\ C_N + C_{N+1} \end{bmatrix}.$$

Problem0 is transformed into

$$\begin{aligned} &\text{Problem1} : \min_{\Gamma, \boldsymbol{T}, t_f} J = -m_{N+1}, \\ &\text{subject to } (24)\ (17)(18)(19)(20)(21)(22). \end{aligned} \tag{25}$$

Problem1 is an SOCP problem that can be solved iteratively using the interior-point algorithm. The solution steps are shown in Figure 2.

The convergence condition in Figure 2 is

$$\max_i \left| \boldsymbol{x}_i^{k+1} - \boldsymbol{x}_i^k \right| \le \varepsilon_{\boldsymbol{x}}, \quad \max_i \left| \boldsymbol{u}_i^{k+1} - \boldsymbol{u}_i^k \right| \le \varepsilon_u, \tag{26}$$

which means that if the difference between the values of the optimization variables of two consecutive iterations is within the specified tolerance range, the iteration should be stopped and the optimal solution is obtained.

4. Piecewise Guidance Algorithm Based on MPC Framework

In this section, on the basis of the trajectory optimization algorithm based on convex optimization detailed in the previous section, a piecewise guidance method combining the trajectory optimization algorithm with the MPC framework is proposed. At each sampling time, the real-time state of the rocket fed back by the navigation system is employed as the initial state to start the trajectory optimization algorithm. Then, the optimal values of a series of control variables from the current time to the landing point are obtained. But only the values in the current guidance cycle are applied to control the rocket until the next sampling time. Repeat these steps until the rocket lands at the predetermined point. Since the trajectory optimization algorithm needs to be provided with an initial guess, the optimization result obtained at the previous sampling time can be used as the initial trajectory at the current sampling time. The computational efficiency of the trajectory optimization algorithm based on convex optimization makes it possible for the guidance algorithm to form an effective closed loop. In addition, the practice of recursively introducing the real-time state of the rocket into the trajectory optimization ensures the stability, robustness, and fault tolerance of the closed-loop.

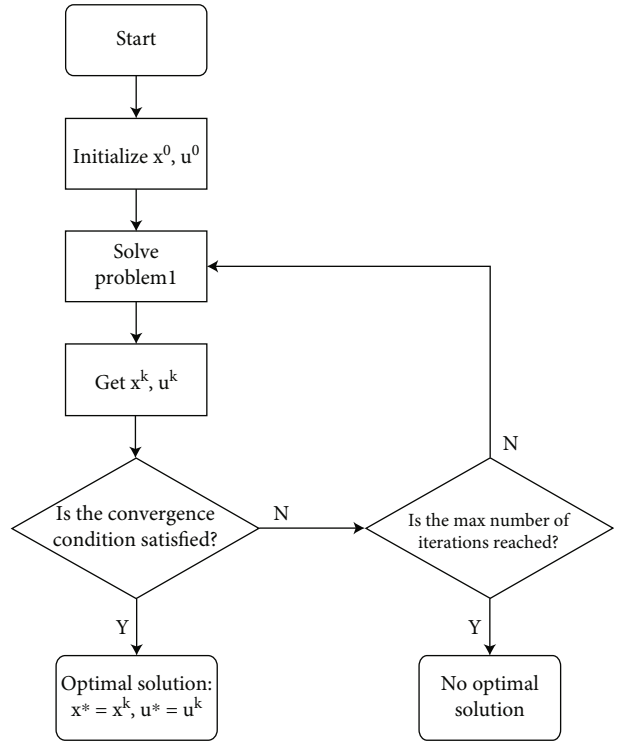

Figure 2: Solution steps for the trajectory optimization problem.

The piecewise method is to cope with the thrust magnitude's bang-bang characteristic. Bang-bang control means the control amount changes dramatically in a short period near the switching point. If the duration of each guidance cycle is too long and a fault occurs near the switching point, the trajectory will deviate from the optimal solution.

The piecewise guidance algorithm based on MPC framework is shown in algorithm 1, where t_i represents the sampling time of the ith trajectory optimization, $\mathscr{T}_i$ represents the terminal time obtained by the ith trajectory optimization, $\boldsymbol{T}$ represents the thrust series from the current time to the landing point, while $\boldsymbol{T}_i$ contains only the portion within the ith guidance cycle, Δt is the duration of each guidance cycle which is set initially, and Δt_i is the actual duration of the ith guidance cycle, $\Delta t_i = t_{i+1} - t_i$.

Over time, the time horizon of the optimization becomes shorter, and the number of discrete points for trajectory optimization within the guidance cycle should also be reduced accordingly. The number of discrete points taken by the ith trajectory optimization algorithm is determined by

$$N_i = \left\lceil N_{i-1} \frac{\mathscr{T}_{i-1} - t_i}{\mathscr{T}_{i-1} - t_{i-1}} \right\rceil, \tag{27}$$

where the ceiling function is defined as $\lceil x \rceil = \min \{n \in \mathbb{Z} | n \ge x\}$. $(\mathscr{T}_{i-1} - t_{i-1})$is the time horizon of the $(i-1)$th

Piecewise guidance algorithm based on MPC framework
Initialization: Save the initial trajectory to the database, set relevant parameters required by the trajectory optimization algorithm, and set the update index $i = 1$.
while$(\mathscr{T}_{i-1} - t_{i-1}) > 0$
  generate guidance commands according to the guidance cycle clock;
  sample the current state $\boldsymbol{x}(t_i)$(i.e. $\boldsymbol{r}(t_i), \boldsymbol{v}(t_i), m(t_i)$) of the rocket;
  employ the optimal trajectory $\boldsymbol{J}_{i-1}$ which was obtained in the previous guidance cycle as the initial guess. Start the trajectory optimization using the current state $\boldsymbol{x}(t_i)$. Obtain a new optimal trajectory $\boldsymbol{J}_i$ and an optimal thrust series $\boldsymbol{T}$. Save $\boldsymbol{J}_i$ to the database, implement $\boldsymbol{T}_i$, and set $i = i + 1$;
  if a fault occurs and t_i approaches the switching point
    shorten the duration of the guidance cycle: $\Delta t_i = \alpha \cdot \Delta t \ (0 < \alpha < 1)$;
  else
    $\Delta t_i = \Delta t$;
  end if
end while

Algorithm 1: Piecewise guidance algorithm based on MPC framework.

optimization, and $(\mathscr{T}_{i-1} - t_i)$ is the estimate of the time horizon of the ith optimization.

5. Integrated GNC System Design

In actual flight, a key technology to realize fault-tolerant guidance is designing a guidance, navigation, and control (GNC) system. The whole GNC system is closed-loop, where the navigation system consists of a variety of sensors for real-time measurement and evaluation of states including the rocket's position, velocity, and mass, the guidance system consists of the guidance algorithm proposed in the previous section to solve the landing trajectory, and the control system consists of the actuators to control the rocket to track the trajectory. The guidance system needs to provide the real-time state of the rocket to the guidance system before the trajectory optimization. And the control commands derived from the guidance algorithm need to be executed by the control system. Thanks to the division of labor and rapid cooperation of each system, the integrated GNC system has strong fault tolerance and robustness against various disturbances and faults including navigation system failures, control system failures, drag coefficient deviations, and atmospheric density deviations.

In this section, an integrated GNC system is built, as shown in Figure 3. In a guidance cycle, based on the current state $\boldsymbol{r}(t_i), \boldsymbol{v}(t_i), m(t_i)$ fed back by the navigation system, the guidance system adopts the trajectory optimization algorithm based on convex optimization to generate an optimal thrust series $\boldsymbol{T}$ (where $\boldsymbol{J}_{i-1}$ represents the initial guess which is the optimal trajectory of the last guidance). The control system outputs the thrust command $\boldsymbol{T}_i$ of the current guidance cycle and transmits it to the rocket, and the rocket system executes the command accordingly. In the simulation experiments, we use numerical integration to integrate the state of the rocket after one guidance cycle, which is used to simulate the real-time state of the rocket. Yet in actual flight, the state is measured by the navigation system and transmitted to the guidance system. Here comes the next guidance cycle, repeat the above until the rocket lands. The piecewise guidance algorithm proposed in the previous section and the integrated GNC system designed in this section ensure the fault tolerance of the guidance method.

6. Simulation Experiments

In this section, numerical simulations are provided to verify the reliability, accuracy, fault tolerance, and robustness of the proposed guidance method. All simulation experiments are carried out on MATLAB with the use of the modeling tool CVX [36, 37] to establish the guidance problem and the solver MOSEK [38] to solve it. We employ the fourth-order Runge-Kutta integration with a 0.01 s time step to obtain updated states at each sampling time. The parameters used in the simulations are shown in Table 1.

The number of discrete points for the first trajectory optimization is: $N = 40$. Assuming r_i^0, v_i^0, and m_i^0 vary linearly from the initial value to the terminal value, then, the initial guesses for all optimization parameters are

$$\begin{cases} \boldsymbol{r}_i^0 = \left(\boldsymbol{r}_f - \boldsymbol{r}_0\right)\dfrac{(i-1)}{N} + \boldsymbol{r}_0, \\ \boldsymbol{v}_i^0 = \left(\boldsymbol{v}_f - \boldsymbol{v}_0\right)\dfrac{(i-1)}{N} + \boldsymbol{v}_0, \\ m_i^0 = \left(m_{\text{dry}} - m_0\right)\dfrac{(i-1)}{N} + m_0, \\ \Gamma_i^0 = T_{\min}, \boldsymbol{T}_i^0 = \dfrac{-\Gamma_i^0 \boldsymbol{v}_i^0}{\left\|\boldsymbol{v}_i^0\right\|}, \\ t_f^0 = 40s. \end{cases} \tag{28}$$

The convergence condition is

$$\varepsilon_{\boldsymbol{r}} = 10^{-3}m, \varepsilon_{\boldsymbol{v}} = 10^{-3}m/s, \varepsilon_m = 10^{-3}kg, \varepsilon_\Gamma = 10^{-3}kN. \tag{29}$$

6.1. Reliability and Accuracy. In this subsection, we conduct the simulations in the absence of any faults and deviations. Figures 4 and 5 show the trajectories and control commands

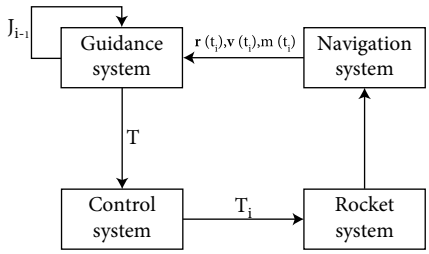

Figure 3: Integrated GNC system.

Table 1: Parameter values.

Parameter	Value	Units
$\boldsymbol{r}_0$	$[3500, 700, 0]^T$	m
$\boldsymbol{v}_0$	$[-200,-90, 0]^T$	m/s
m_0	27000	kg
m_{dry}	20000	kg
$T_{\min}$	100	kN
$T_{\max}$	300	kN
$\theta_{\max}$	80	°
$\eta_{\max}$	15	°
g_0	9.8	m/s2
I_{sp}	270	s
ρ	1.225	kg/m3
S_D	10	m2
C_D	2.2	—
Δt	1	s

of the rocket vertical landing phase obtained by the trajectory optimization algorithm and the guidance method presented in this paper, respectively. The red curves represent the results of the trajectory optimization algorithm, and the black is the guidance method. The differences between the results are small, demonstrating the reliability of the guidance method. We then perform numerical integration using the control commands to obtain the actual terminal states. Tables 2 and 3 show the terminal states and landing errors, respectively. It can be seen that the landing position and velocity errors of the guidance method are smaller than those of the trajectory optimization algorithm, which proves that the guidance method proposed in this paper has higher accuracy.

6.2. Fault Tolerance and Robustness. In this subsection, we assume three scenarios: faults occur in the navigation system, faults occur in the control system, and estimates of parameters (the drag coefficient and the atmospheric density) have deviations. Considering these scenarios, we apply the trajectory optimization algorithm and the guidance method proposed in this paper to conduct simulation experiments, respectively, and compare their results.

6.2.1. Faults Occur in the Navigation System. It is assumed that the navigation system has faults. Rather, the measurement of the real-time state of the rocket has the following errors:

$$\begin{cases} \|\boldsymbol{r}_{\text{measure}}\| = \|\boldsymbol{r}_{\text{true}}\| \pm \min\left(10, \|\boldsymbol{r}_{\text{true}}\| \times \varepsilon\%\right) \times \text{random}(0, 1), \\ \|\boldsymbol{v}_{\text{measure}}\| = \|\boldsymbol{v}_{\text{true}}\| \pm \min\left(1, \|\boldsymbol{v}_{\text{true}}\| \times \varepsilon\%\right) \times \text{random}(0, 1), \end{cases} \tag{30}$$

where 10 and 1 represent the absolute errors of the rocket's position and velocity, ε represents the maximum range of the relative error, $\text{random}(0, 1)$ represents a random number generated from [0,1], $\boldsymbol{r}_{\text{true}}, \boldsymbol{v}_{\text{true}}$ represents the actual state of the rocket, and $\boldsymbol{r}_{\text{measure}}, \boldsymbol{v}_{\text{measure}}$ represents the state measured by the navigation system and fed back to the guidance system. We take the value of ε as 5, 10, and 15 for experiments, and the landing errors under these fault conditions are shown in Table 4.

It can be seen from Table 4 that as the relative error of the measured state increases, the landing errors of the rocket also increase, but they remain within a small range. This experiment proves that the guidance method proposed in this paper is fault-tolerant and robust to navigation system faults.

6.2.2. Faults Occur in the Control System. It is assumed that the control system has two fault conditions: thrust cannot change continuously (that is, thrust is constant during each guidance cycle), and thrust magnitude has deviations. The trajectory optimization algorithm and the guidance method proposed in this paper are, respectively, applied to conduct simulations under the above two fault conditions, and their results are compared.

(1) Thrust Cannot Change Continuously. For trajectory optimization, we assume that thrust is constant per second, and for guidance, thrust is constant during each guidance cycle. The landing errors and landing masses are shown in Table 5.

(2) Thrust Magnitude Has Deviations. It is assumed that there are deviations within ±5% of the thrust magnitude. In the experiment, random deviations within ±5% are applied to the thrust magnitude obtained by the trajectory optimization algorithm and the guidance method. Then, the deviated thrust is used to control the rocket. The landing errors and landing masses are shown in Table 6.

It can be seen from Tables 5 and 6 that when the thrust cannot be continuously changed or the thrust magnitude has deviations, the landing position error and velocity error obtained by trajectory optimization are significantly larger than those obtained by guidance. The landing position errors of the guidance method under the two fault conditions remain at the same order of magnitude as that under the no-fault condition in Subsection 6.1, which demonstrates that the two fault conditions have little effect on the landing position. As for the landing velocity error, the guidance method can make it at the same order of magnitude as the no-fault condition when the thrust magnitude has deviations within ±5%. The error is one order of magnitude

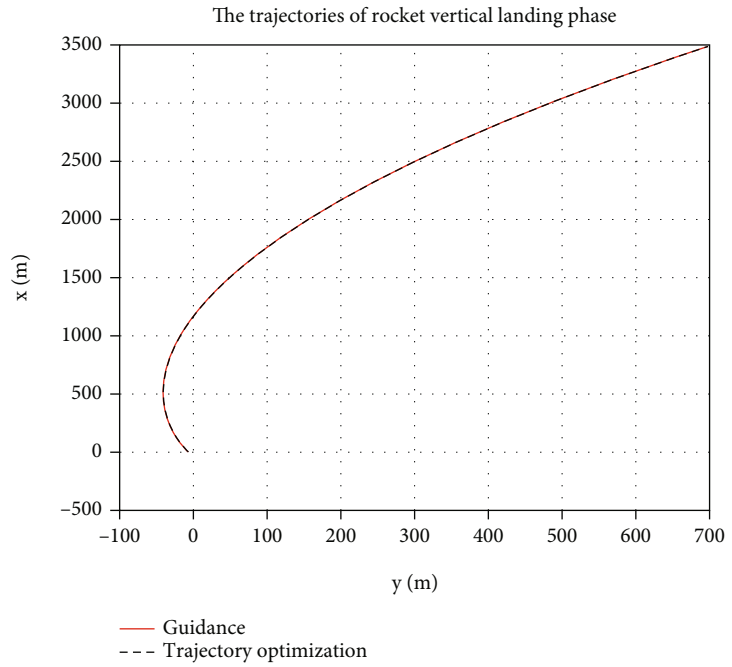

Figure 4: The trajectories of rocket vertical landing phase obtained by the guidance method and the trajectory optimization algorithm.

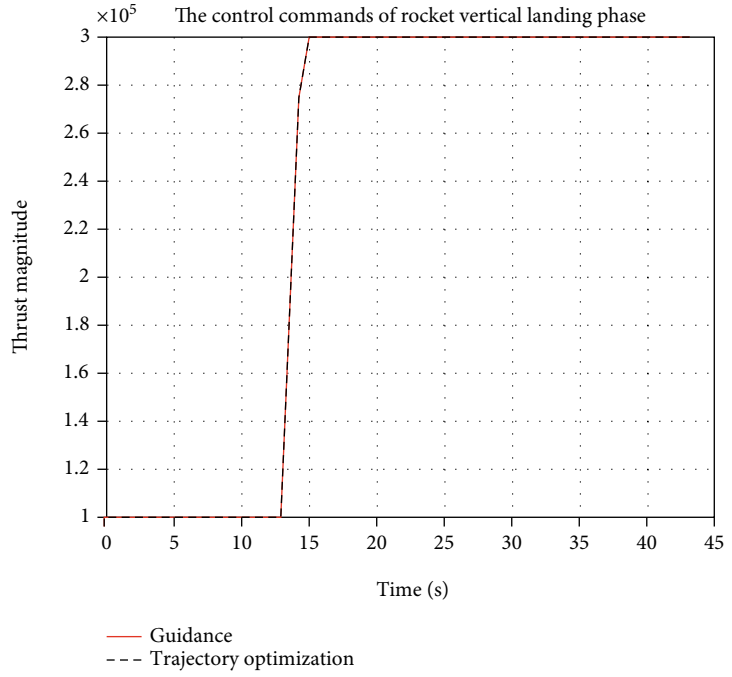

Figure 5: The control commands of rocket vertical landing phase obtained by the guidance method and the trajectory optimization algorithm.

Table 2: Terminal states.

	$t_f\,(s)$	$r_x(t_f)\,(m)$	$r_y(t_f)\,(m)$	$v_x(t_f)\,(m/s)$	$v_y(t_f)\,(m/s)$	$m(t_f)\,(kg)$
Trajectory optimization	43.18	-2.0085	-1.1821	-0.0646	-0.0332	23137.09
Guidance	43.18	-0.0276	-0.0241	-0.0210	-0.0043	23135.79

Table 3: Landing errors.

	Landing position error/m	Landing velocity error/(m/s)
Trajectory optimization	2.3305	0.0726
Guidance	0.0366	0.0214

Table 4: Landing errors and masses under the condition that the navigation system has faults.

	Landing position error/m	Landing velocity error/(m/s)	Landing mass/kg
$\varepsilon = 5$	2.4665	5.7779	23331.19
$\varepsilon = 10$	3.5750	5.8301	23329.48
$\varepsilon = 15$	4.0624	6.5514	23355.94

Table 5: Landing errors and masses under the condition that thrust cannot change continuously.

	Landing position error/m	Landing velocity error/(m/s)	Landing mass/kg
Trajectory optimization	407.6401	4.8062	23081.57
Guidance	0.0914	0.3145	23136.54

Table 6: Landing errors and masses under the condition that thrust magnitude has deviations.

	Landing position error/m	Landing velocity error/(m/s)	Landing mass/kg
Trajectory optimization	359.1367	6.3939	23137.13
Guidance	0.0185	0.0209	23133.57

Table 7: Landing errors and masses of the trajectory optimization algorithm.

Deviation	Landing position error/m	Landing velocity error/(m/s)	Landing mass/kg
$C_D + 15\%$	289.5933	4.9790	23135.95
$C_D - 15\%$	356.5689	6.2598	23135.95
$\rho + 15\%$	289.9584	4.9790	23135.95
$\rho - 15\%$	356.5689	6.2598	23135.95

Table 8: Landing errors and masses of the guidance method.

Deviation	Landing position error/m	Landing velocity error/(m/s)	Landing mass/kg
$C_D + 15\%$	0.0035	0.0239	23230.63
$C_D - 15\%$	4.1627	29.2456	23957.32
$\rho + 15\%$	0.0035	0.0239	23230.63
$\rho - 15\%$	4.1627	29.2456	23957.32

greater when the thrust cannot be continuously changed, but it still does not exceed 1 m/s. The simulation experiments demonstrate that the guidance method proposed in this paper is fault-tolerant and robust to control system faults.

6.2.3. Estimates of Parameters Have Deviations. It is assumed that the actual drag coefficient and atmospheric density differ by ±15% from the estimated values. We apply the trajectory optimization algorithm and the guidance method proposed in this paper to conduct simulation experiments using the estimated parameters. Then, we perform numerical integration using the actual parameters to obtain real terminal states. The landing errors and landing masses of the two algorithms under the fault condition are shown in Tables 7 and 8, respectively, (where $C_D + 15\%$ indicates that the actual drag coefficient has a value of $1.15 \times C_D$).

It can be seen from Tables 7 and 8 that the guidance method proposed in this paper can significantly improve the landing position accuracy in the case of the drag coefficient or the atmospheric density having deviations. When the actual values of the two parameters are larger than the estimated values, the accuracy of the landing velocity is also significantly improved. This experiment demonstrates the fault tolerance and robustness of the guidance method to the landing position in the presence of parameter deviations. However, when the actual values of the two parameters are smaller than the estimated values, the landing velocity errors obtained by the guidance method will become larger. We refer to the analysis of Ref. [19] and learn that when the actual values of the two parameters are decreased, part of the mechanical energy of the rocket cannot be dissipated as expected; and when the thrust magnitude saturates, there is no additional energy to compensate for the undissipated mechanical energy, leading to the error of the optimal trajectory becomes larger. Subsequent research on guidance methods should attempt to address this issue.

6.2.4. Combination of Various Faults. Finally, we consider navigation system failures, control system failures (thrust magnitude has deviations), drag coefficient deviations, and atmospheric density deviations at the same time and carry out Monte Carlo simulations (200 cases). For the navigation system and control system, the failures are added in the same way as the previous experiments. Drag coefficient deviations and atmospheric density deviations are considered to be normally distributed, and their means are set to zero. The 3σ values are, respectively, taken as $C_D \sim 15\%$, $\rho \sim 15\%$.

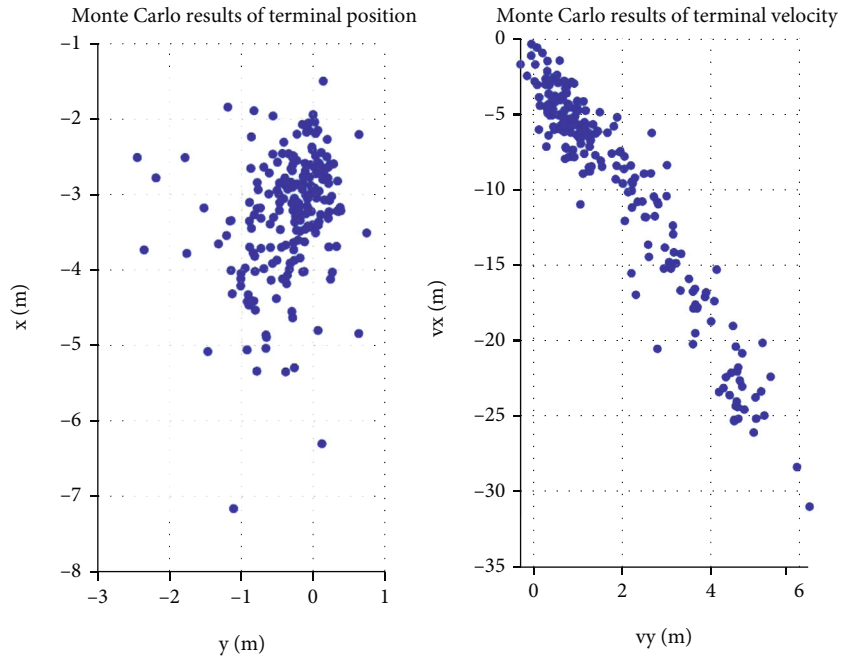

Figure 6: Monte Carlo results of terminal position and terminal velocity.

Results of terminal position and terminal velocity are shown in Figure 6. The maximum errors are (7.2551 m, 31.6108 m/s). This experiment proves that the guidance method can still keep the terminal states within acceptable limits under the combination of various faults.

7. Conclusions

In this paper, a fault-tolerant guidance method is proposed to realize online guidance of rocket vertical landing. The main contribution of this paper is that we propose a piecewise guidance algorithm. We first embed a trajectory optimization algorithm based on convex optimization in the MPC framework and then put forward a piecewise method to cope with the bang-bang characteristic of the thrust magnitude. An integrated GNC system is designed to enhance the fault-tolerance and robustness of the guidance method, which constitutes another contribution of this paper. Simulation experiments are conducted under conditions of no faults and deviations, navigation system failures, control system failures, drag coefficient deviations, and atmospheric density deviations, respectively, proving the reliability and fault-tolerance of the guidance method. The proposed method shows great potential for online use.

Data Availability

Data are available on request.

Conflicts of Interest

The authors declare that they have no conflicts of interest.

Acknowledgments

This study was cosupported in part by the National Natural Science Foundation of China (nos. 61903146 and 61873319).

References

[1] H. Zhao, H. Pan, C. Wang, X. Yi, and H. Hu, "Vertical landing guidance navigation and control of reusable launch vehicle," *Missiles and Space Vehicles*, vol. 1, pp. 76–81, 2021.

[2] Z. Song, C. Wang, S. Theil et al., "Survey of autonomous guidance methods for powered planetary landing," *Frontiers of Information Technology & Electronic Engineering*, vol. 21, no. 5, pp. 652–674, 2020.

[3] J. Meditch, "On the problem of optimal thrust programming for a lunar soft landing," *IEEE Transactions on Automatic Control*, vol. 9, no. 4, pp. 477–484, 1964.

[4] N. Cui, D. Guo, K. Li, and C. Z. Wei, "A survey of numerical methods for aircraft trajectory optimization," *Tactical Missile Technology*, vol. 5, pp. 37–51, 2020.

[5] S. Y. Chen and Q. L. Xia, "A multiconstrained ascent guidance method for solid rocket-powered launch vehicles," *International Journal of Aerospace Engineering*, vol. 2016, Article ID 6346742, 11 pages, 2016.

[6] L. Mu, J. Yu, Y. Zhang et al., "Landing trajectory generation using gauss pseudo-spectral method," in *2021 40th Chinese control conference (CCC)*, pp. 3751–3755, Shanghai, China, 2021.

[7] Z. Song and C. Wang, "Development of online trajectory planning technology for launch vehicle return and landing. astronautical systems," *Engineering Technology*, vol. 6, 2019.

[8] B. Acikmese and S. R. Ploen, "Convex programming approach to powered descent guidance for mars landing," *Journal of Guidance, Control, and Dynamics*, vol. 30, no. 5, pp. 1353–1366, 2007.

[9] L. Blackmore, B. Açikmeşe, and D. P. Scharf, "Minimum-landing-error powered-descent guidance for Mars landing using convex optimization," *Journal of Guidance, Control, and Dynamics*, vol. 33, no. 4, pp. 1161–1171, 2010.

[10] B. Açıkmeşe and L. Blackmore, "Lossless convexification of a class of optimal control problems with non- convex control constraints," *Automatica*, vol. 47, no. 2, pp. 341–347, 2011.

[11] X. Liu and P. Lu, "Robust trajectory optimization for highly constrained rendezvous and proximity operations," in *AIAA guidance Navigation, and Control (GNC) Conference*, p. 4720, Boston, MA, USA, 2013.

[12] X. Liu, Z. Shen, and P. Lu, "Entry trajectory optimization by second-order cone programming," *Journal of Guidance, Control, and Dynamics*, vol. 39, no. 2, pp. 227–241, 2016.

[13] X. Liu, "Fuel-optimal rocket landing with aerodynamic controls," *Journal of Guidance, Control, and Dynamics*, vol. 42, no. 1, pp. 65–77, 2019.

[14] Z. Wang and M. J. Grant, "Minimum-fuel low-thrust transfers for spacecraft: a convex approach," *IEEE Transactions on Aerospace and Electronic Systems*, vol. 54, no. 5, pp. 2274–2290, 2018.

[15] X. Lan, W. Xu, Z. Zhao, and G. Liu, "Autonomous control strategy of a swarm system under attack based on projected view and light transmittance," *IEEE/CAA Journal of Automatica Sinica*, vol. 8, no. 3, pp. 648–655, 2021.

[16] X. Liu, "Fuel-optimal rocket landing with aerodynamic controls," in *AIAA Guidance, Navigation, and Control Conference*, pp. 1732–1747, Grapevine, TX, USA, 2017.

[17] J. Zhao, Y. Huang, H. Li, and X. He, "Uncertainty optimization for return trajectory of vertical takeoff and vertical landing launch vehicle," *Acta Aeronautica et Astronautica Sinica*, , pp. 255–269, 2021.

[18] J. Wang, N. Cui, J. Guo, and D. Xu, "High precision rapid trajectory optimization algorithm for launch vehicle landing," *Control Theory & Applications*, vol. 35, no. 3, pp. 389–398, 2018.

[19] J. Wang, N. Cui, and C. Wei, "Optimal rocket landing guidance using convex optimization and model predictive control," *Journal of Guidance, Control, and Dynamics*, vol. 42, no. 5, pp. 1078–1092, 2019.

[20] Z. An, F. Xiong, and Z. Liang, "Landing-phase guidance of rocket using bias proportional guidance and convex optimization," *Acta Aeronautica et Astronautica Sinica*, vol. 41, no. 5, pp. 242–255, 2020.

[21] M. Szmuk, B. Acikmese, and A. W. Berning, "Successive convexification for fuel-optimal powered landing with aerodynamic drag and non-convex constraints," in *AIAA Guidance, Navigation, and Control Conference*, San Diego, California, USA, 2016.

[22] Z. Zhang, Y. Ma, G. Y. Geng, and M. L. Yu, "Convex optimization method used in the landing-phase on-line guidance of rocket vertical recovery," *Journal of Ballistics*, vol. 29, no. 1, 2017.

[23] N. Shao and X. Yan, "Multi-stage trajectory optimization for vertical pin-point landing of a reusable launch vehicle," *Journal of Astronautics*, vol. 35, 2019.

[24] L. Xie, H. Zhang, X. Zhou, and G. Tang, "A convex programming method for rocket powered landing with angle of attack constraint," *Access*, vol. 8, pp. 100485–100496, 2020.

[25] M. Yang and G. You, "A two-stage successive convexification method for the powered descent guidance problem," *Scientia Sinica Mathematica*, vol. 50, no. 9, pp. 234–247, 2020.

[26] D. Malyuta, T. Reynolds, M. Szmuk, M. Mesbahi, B. Acikmese, and J. M. Carson, "Discretization performance and accuracy analysis for the rocket powered descent guidance problem," in *AIAA Scitech 2019 Forum*, p. 925, San Diego, California, USA, 2019.

[27] S. Yuan, T. Liu, and Y. Huang, "Switched adaptive resilient control of missile autopilot systems," *IEEE Transactions on Aerospace and Electronic Systems*, vol. 57, no. 6, pp. 4227–4237, 2021.

[28] Y. Song, W. Zhang, X. Miao, Z. Zhang, and S. Gong, "Onboard guidance algorithm for the powered landing phase of a reusable rocket," *Journal of Tsinghua University (Science and Technology)*, vol. 61, no. 3, pp. 230–239, 2021.

[29] A. Botelho, M. Martinez, C. Recupero, A. Fabrizi, and G. de Zaiacomo, "Design of the landing guidance for the retropropulsive vertical landing of a reusable rocket stage," *CEAS Space Journal*, vol. 14, pp. 551–564, 2022.

[30] D. Morgan, S. J. Chung, and F. Y. Hadaegh, "Model predictive control of swarms of spacecraft using sequential convex programming," *Journal of Guidance, Control, and Dynamics*, vol. 37, no. 6, pp. 1725–1740, 2014.

[31] W. Dunham, C. Petersen, and I. Kolmanovsky, "Constrained control for soft landing on an asteroid with gravity model uncertainty," in *2016 American Control Conference (ACC)*, pp. 5842–5847, Boston, MA, USA, 2016.

[32] U. Eren, A. Prach, B. B. Koçer, S. V. Raković, E. Kayacan, and B. Açıkmeşe, "Model predictive control in aerospace systems: current state and opportunities," *Journal of Guidance, Control, and Dynamics*, vol. 40, no. 7, pp. 1541–1566, 2017.

[33] C. Wang and Z. Song, "Convex model predictive control for rocket vertical landing," in *2018 37th Chinese control conference (CCC)*, pp. 9837–9842, Wuhan, China, 2018.

[34] K. Cui, W. Han, Y. Liu, X. Wang, X. Su, and J. Liu, "Model predictive control for automatic carrier landing with time delay," *International Journal of Aerospace Engineering*, vol. 2021, Article ID 8613498, 19 pages, 2021.

[35] J. Guadagnini, M. Lavagna, and P. Rosa, "Model predictive control for reusable space launcher guidance improvement," *Acta Astronautica*, vol. 193, pp. 767–778, 2022.

[36] M. Grant and S. Boyd, "CVX: Matlab software for disciplined convex programming, version 2.0 beta," 2013, http://cvxr.com/cvx.

[37] M. Grant and S. Boyd, "Graph implementations for nonsmooth convex programs, Recent Advances in Learning and Control (a Tribute to M. Vidyasagar)," in *Lecture Notes in Control and Information Sciences*, V. Blondel, S. Boyd, and H. Kimura, Eds., pp. 95–110, Springer, 2008.

[38] E. D. Andersen, C. Roos, and T. Terlaky, "On implementing a primal-dual interior-point method for conic quadratic optimization," *Mathematical Programming*, vol. 95, no. 2, pp. 249–277, 2003.

Hindawi
International Journal of Aerospace Engineering
Volume 2022, Article ID 4481553, 14 pages
https://doi.org/10.1155/2022/4481553

Research Article

Reconfiguration Control Design of UAV against Actuator Faults Based on Control Allocation Method

Yuwei Cui, Aijun Li, Biao Duan, and Shabbir Wasif

School of Automation, Northwestern Polytechnical University, Xi'an Shaanxi 710072, China

Correspondence should be addressed to Yuwei Cui; cuiyuwei0505@mail.nwpu.edu.cn

Received 30 November 2021; Revised 5 April 2022; Accepted 11 May 2022; Published 28 May 2022

Academic Editor: Adel Ghenaiet

The paper concentrates on the problem of fault-tolerant control of UAV against actuator faults from the perspective of flight control system architecture. Using backstepping control method and inverse optimization theory, the design of backstepping optimal control law was constructed. Based on the fault monitoring mechanism of vehicle management computer in the distributed flight control and control allocation system, a fault-tolerant control design method was established in the case of multiple failure modes of the actuators, which compensates the influence caused by the failures. Finally, the effectiveness of the proposed strategy was verified by numerical simulation.

1. Introduction

In recent years, XQ-58A "Valkyrie" developed by the United States has started to verify its combat technology with manned fighters F-15X and F-35. While emphasizing joint operations, it also puts forward low-cost development requirements. This medium-size UAV with low-cost attritable aircraft technology (LCAAT) is more affordable than the X47B stealth UAV. In 2020, Russia demonstrated a high-speed, unmanned loyal wingman, named "Thunder". Similar to XQ-58A, it is capable of partnering with manned fighters and serving as a wingman in a front-line attack and detecting and destroying enemy and air defense targets, as discussed elsewhere [1–3].

With the worldwide research and development of all kinds of unmanned systems, the application of manned/unmanned aerial vehicles and unmanned swarm systems has been promoted. Unmanned systems are no longer synonymous with low cost and high risk but increasingly emphasize the following two aspects of technical requirements:

(i) Low cost and affordable economic cost

(ii) High fault tolerance and affordable security risks

For the fighter or large reconnaissance and combat UAVs, its cost can be increased. Therefore, the architecture of multiredundant hardware design is often used to improve the fault-tolerant ability of the entire aircraft system, especially for the flight control system with high safety and reliability. However, for consumable and low-cost unmanned systems such as loyal wingman, the architecture based on redundant hardware design brings high cost, large volume, large weight, and small load, which is often not acceptable. However, it is still expected to minimize the impact of failure, that is, to have higher fault tolerance.

There are many fault diagnosis and fault-tolerant control methods for sensors and actuators of flight control system. As early as 1990, as discussed by Professor Frank [4], international authority on fault diagnosis of control system divided fault diagnosis methods into three categories: analytical model-based methods, signal process-based methods, and knowledge-based methods, which have been accepted by many scholars [5, 6].

For the application of UAV flight control system, model-based fault detection, isolation, and adjustment methods can be used to reconstruct low redundancy/no redundancy signals for sensor faults, and the fault tolerance problem of

sensor signals can be solved by means of analytical redundancy, as discussed elsewhere [7–11].

But when the faults occur in the aircraft surface because of actuators, the detection and isolation method based on model cannot work, and it must be reconstructed through the control compensation of other surfaces to achieve fault tolerance. At present, many scholars have proposed adaptive control algorithms to solve various adaptive control problems in the case of surface failure, so as to achieve flight control, but the real-time performance of these algorithms is generally doubted, and a large number of algorithms need accurate mathematical models [12–15].

At present, the fault tolerant control towards actuator's faults is based on the results of fault detection [16]. Firstly, the faulty actuator should be isolated to avoid its fault spreading. Then, by adjusting the parameters of the controller or changing the structure of the controller, the stability and control performance of the system can be guaranteed. However, this method must be offline calculation of control law parameters required under various faults, and these parameters are stored in the flight control computer in advance. During the flight, according to the fault information obtained by fault detection, the matched control law parameters are selected to obtain the reconstructed flight control law. Since the parameters of the readjusted control law are designed off-line, the reconstructed flight control law can only tolerate the fault modes considered in advance, which limits the scalability of this method.

At the same time, we consider the possible failure modes of UAV actuators. At present, for small and medium-sized UAVs, electric actuators are basically used as the driving mechanism; and for large UAVs, with the continuous maturity of high-power electric actuators, the trend of replacing hydraulic actuators is also accelerating, due to the maintenance, pipeline, weight, leakage, and other problems caused by hydraulic actuators. Consider that there are two main failure modes of the electric actuators: nonoutput force and the output shaft stuck. From the perspective of surface control, the influence of the former is relatively small. And the most important thing is to realize fault detection, so that the fault can be found quickly. The second failure mode is trickier because it introduces additional unwanted moments that need to be balanced first in flight control.

In view of the multiple failure modes of UAV actuators, the strategy proposed in the paper adopts backstepping optimal control law and reconfiguration design based on a control allocation method to compensate the influence of faulty actuators, so as to achieve the goal of fault-tolerant control. The main contributions of the research are summarized as follows:

(1) Different from the adaptive control method, as referred to References [12–15], based on the optimal control law and the fault diagnosis result, control allocation methods carry out the mode switch. It does not need to carry out complex online calculation through the optimization algorithm, so it will not affect the real-time performance

(2) Compared with constructing off-line databases and adjusting the parameters or structure of controller, the reconfiguration control methods based on control allocation can compensate the influence of fault surfaces without adjusting the control law, thus extending its application scope

(3) More importantly, the paper presents a systematic solution, not just for the control algorithms. Through the modular control structure, the fault detection, control law, and control allocation algorithm are organically integrated, and a relatively comprehensive solution is proposed for the reconfiguration control against actuator faults

2. System Description and Preliminaries

A UAV adopts a conventional layout, and the independently controlled surfaces include the following: left fully moving elevator, right fully moving elevator, aileron, and V-shaped rudder. Because the left and right fully moving elevator can be controlled independently; that is to say, in addition to the pitching moment produced by the same deflection, the rolling moment can also be produced by the differential deflection, which provides additional control moment in the lateral direction. At the same time, the application of V-shaped rudder also provides a supplement for the generation of pitching moment. Therefore, the characteristics of multicontrol surfaces of the UAV provide conditions for the compensation control of actuators faults.

Firstly, the aircraft attitude dynamic equation in the body axial coordinate system is as follows:

$$\begin{bmatrix} \dot{\mu} \\ \dot{\alpha} \\ \dot{\beta} \end{bmatrix} = \begin{bmatrix} \dfrac{\cos\alpha}{\cos\beta} & 0 & \dfrac{\sin\alpha}{\cos\beta} \\ -\cos\alpha\tan\beta & 1 & -\sin\alpha\tan\beta \\ \sin\alpha & 0 & -\cos\alpha \end{bmatrix} \begin{bmatrix} p \\ q \\ r \end{bmatrix} + \begin{bmatrix} F_{\mu}(X) \\ F_{\alpha}(X) \\ F_{\beta}(X) \end{bmatrix}, \tag{1}$$

where α, β, and μ are, respectively, the angle of attack, sideslip angle, and roll angle and p, q, and r are, respectively, the pitch angle rate, yaw angle, rate and roll angle rate.

$$\begin{aligned} F_{\mu}(X) = {} & \frac{\sin\beta\cos\mu}{mV\cos\beta}\left(-D\sin\beta\sin\mu + L\cos\mu\right. \\ & \left. - Y\cos\beta\sin\mu - F_{\gamma t} - mg\cos\gamma\right) \\ & + \frac{\tan\gamma + \tan\beta\sin\mu}{mV}\left(D\sin\beta\cos\mu + L\sin\mu\right. \\ & \left. + Y\cos\beta\cos\mu + F_{\chi t}\right), \end{aligned}$$

$$\begin{aligned} F_{\alpha}(X) = {} & -\frac{\cos\mu}{mV\cos\beta}\left(-D\sin\beta\sin\mu + L\cos\mu\right. \\ & \left. - Y\cos\beta\sin\mu - F_{\gamma t} - mg\cos\gamma\right) + \frac{\sin\mu}{mV\cos\beta} \\ & \cdot \left(D\sin\beta\cos\mu + L\sin\mu + Y\cos\beta\cos\mu + F_{\chi t}\right), \end{aligned}$$

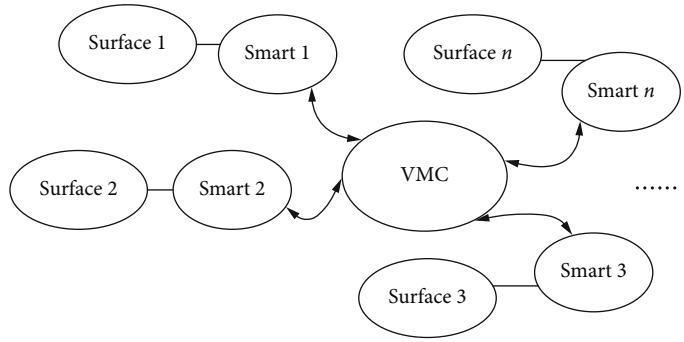

Figure 1: Distributed flight control system architecture.

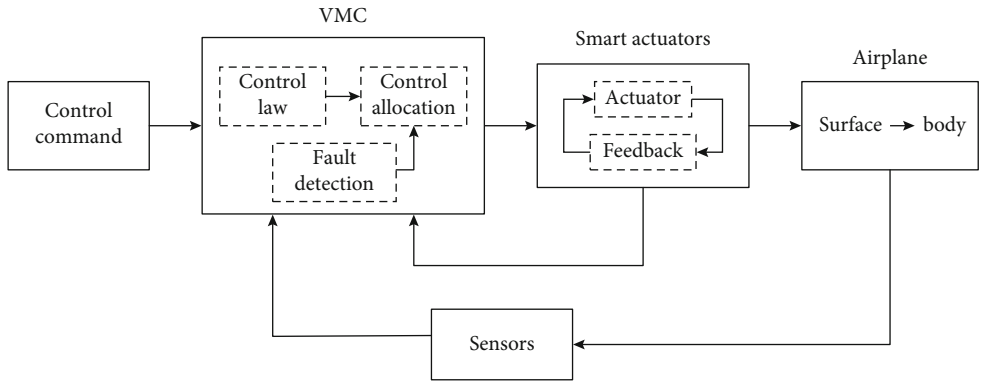

Figure 2: Reconfiguration control block diagram based on control allocation method.

$$F_\beta(X) = -\frac{\sin\mu}{mV}(-D\sin\beta\sin\mu + L\cos\mu - Y\cos\beta\sin\mu - F_{\gamma t} - mg\cos\gamma) + \frac{\cos\mu}{mV}(D\sin\beta\cos\mu + L\sin\mu + Y\cos\beta\cos\mu + F_{\chi t}),$$

$$F_{\chi t} = T\cdot dT\cdot(-\sin\mu\cos\alpha\sin\beta - \cos\mu\sin\alpha),$$

$$F_{\gamma t} = T\cdot dT\cdot(-\sin\mu\cos\alpha\sin\beta - \cos\mu\sin\alpha), \quad (2)$$

where m is mass, V is flight speed, γ is flight path angle, T is engine thrust, dT is thrust coefficient, and D, L, and Y are resistance force, lift force, and lateral force, respectively, as described below.

$$D = \bar{q}\cdot S\cdot c_d,$$
$$L = \bar{q}\cdot S\cdot c_l, \quad (3)$$
$$Y = \bar{q}\cdot S\cdot c_y,$$

where S is wing area, $\bar{q}$ is kinetic pressure, and c_d, c_l, and c_y are drag coefficient, lift coefficient, and lateral force coefficient, respectively.

Remark 1. The flight control system architecture of UAV can support the integrated design of actuator fault detection and flight control law. The following distributed system architecture in Figure 1 can be adopted [17–19]. The integrated VMC (vehicle management computer) realizes the fault detection of actuators, the calculation of flight control law, and the calculation of control allocation algorithm and finally forms the control instruction for each surface and transmits them to the SMART actuator located near the surface.

Remark 2. As shown in Figure 2, the integrated VMC will perform the fault detection, flight control law, and control allocation algorithm continually during the whole flight mission. The distributed system architecture, depending on the integrated design of VMC, can realize the reconfiguration control based on the control allocation method more conveniently, without affecting the servo control of the back-end actuator control loop in SMART. Meanwhile, it can be seen that after the introduction of control allocation module, the design of control law module in VMC does not need to be changed when some of actuators are faulty, which provides convenience for its application.

Remark 3. The fault detection toward actuators' fault modes needs to be added in the fault detection module of VMC. That is, the fault detection module can obtain all the data related to actuators fault modes, such as actuator position, motor HALL speed, and clutch drive current. Based on this, VMC can detect the failures of actuators. For example, when the motor HALL speed is high and the position of the actuator does not change, it can be considered that the actuator's output shaft is stuck at this time. When the clutch drive current is large, then the current control command of the motor

is cut off, and at this time, the actuator is in a state of non-output force. The paper does not make a comprehensive study of the specific fault detection strategy, only as the input conditions of the research.

3. Backstepping Optimal Controller Design

As we all know, the design of backstepping control law only considers the stability and convergence of the system and does not consider the optimal performance of the system [20, 21]. For the optimal control of the system, it is usually to find an admissible control with a given performance index, and the target functional takes the minimum value. This kind of problem ultimately comes down to the solution of Hamilton-Jacobi-Bellman partial differential equation. Compared with linear systems, the difficulty of nonlinear systems lies in that the HJB equation to be solved is often nonexistent or nonunique, which becomes the main obstacle to optimal control of nonlinear systems. This problem can be solved by introducing the inverse optimization into the design of uncertain nonlinear control systems through the robust control Lyapunov function [22]. The inverse optimization problem does not minimize the control law of a given target functional, but with the Lyapunov function for the robust stability of the system to make the controller is designed to minimize a backlog of objective functional, that is to say, first of all, get the control law, and then determine its optimal value function, so as to determine the optimal controller.

3.1. Derive the Control Law. For second order nonlinear systems,

$$\begin{aligned} \dot{x}_1 &= \phi(x_1) + x_2, \\ \dot{x}_2 &= u, \\ y &= x_1. \end{aligned} \tag{4}$$

(Step 1) For the subsystem x_1 in equation (4), virtual control law is designed with x_2 as the control input.

Choose the following form of control law:

$$x_2^{\text{des}} = -\psi(x_1). \tag{5}$$

Construct the following control Lyapunov function:

$$W(x_1) = \frac{1}{2}x_1^2. \tag{6}$$

Substituting into $x_2 = x_2^{\text{des}}$, its differential is $\dot{W} = (\phi(x_1) - \psi(x_1))x_1$.

When $(\phi(x_1) - \psi(x_1))x_1 < 0$ is satisfied, its negative definite can be guaranteed.

(Step 2) Introduce an error variable:

$$\bar{x}_2 = x_2 - x_2^{\text{des}} = x_2 + \psi(x_1). \tag{7}$$

So the system equation (4) is equal to

$$\begin{aligned} \dot{x}_1 &= \phi(x_1) - \psi(x_1) + \bar{x}_2, \\ \dot{\bar{x}}_2 &= u + \psi'(x_1)(\phi(x_1) - \psi(x_1) + \bar{x}_2). \end{aligned} \tag{8}$$

Construct the following control Lyapunov function:

$$V(x_1, \bar{x}_2) = F(x_1) + \frac{1}{2}\bar{x}_2^2, \tag{9}$$

where $F(x_1)$ is any effective control Lyapunov function of subsystem x_1, which means that when $x_2 = x_2^{des}$ is satisfied,

$$\dot{F}(x_1) = F'(x_1)(\phi(x_1) - \psi(x_1)) = -U(x_1), \tag{10}$$

where $U(x_1)$ is positive definite.

$$\begin{aligned} \dot{V} &= F'(x_1)[\phi(x_1) - \psi(x_1) + \bar{x}_2] + \bar{x}_2\left[u + \psi'(x_1)(\phi(x_1) - \psi(x_1) + \bar{x}_2)\right] \\ &= -U(x_1) + \bar{x}_2\left[F'(x_1) + u + \psi'(x_1)(\phi(x_1) - \psi(x_1)) + \psi'(x_1)\bar{x}_2\right). \end{aligned} \tag{11}$$

Choose $F'(x_1) = -\psi'(x_1)(\phi(x_1) - \psi(x_1))$, $F(0) = 0$; the item x_1 in the second items can be cancelled out.

Substituting $F'(x_1)$ into formula (10), the following formula can be obtained:

$$U(x_1) = \psi'(x_1)(\phi(x_1) - \psi(x_1))^2. \tag{12}$$

When $\psi'(x_1) > 0$ is satisfied, the positive definite is guaranteed.

And then, the Lyapunov function of the system is

$$\dot{V} = -U(x_1) + \bar{x}_2\left[u + \psi'(x_1)\bar{x}_2\right]. \tag{13}$$

In order to make $\dot{V}$ negative definite, the control law can be selected finally:

$$u = -k_2\bar{x}_2 = -k_2(x_2 + \psi(x_1)). \tag{14}$$

When $k_2 > \psi'(x_1)$ is satisfied, the negative definite of $\dot{V} = -U(x_1) - (k_2 - \psi'(x_1))\bar{x}_2^2$ is guaranteed.

3.2. Determine Its Optimal Value Function

Lemma 4 (see [23, 24]). *Consider the nonlinear system:*

$$\dot{x} = f(x) + g(x)u, \tag{15}$$

where $x \in R^n$ is the state variable and $u \in R^m$ is the control input.

And assume $g(x) \neq 0$. For a given feedback control $u(x)$, define the optimal value function:

$$J(x) = \int_0^\infty \left(Q(x) + u^T R(x) u\right) dt, \tag{16}$$

where $Q(x)$ is positive definite and $R(x)$ is symmetric positive definite.

The optimal value function $J(x)$ can be selected as the Lyapunov function $V(x)$. Then, the optimal control can be obtained:

$$u^*(x) = -\frac{1}{2} R^{-1}(x) \left(V_x(x) g(x)\right)^T. \tag{17}$$

Using Hamilton-Jacobi-Bellman equation

$$\min_u \left[Q(x) + u^T R(x) u + V_x(x)(f(x) + g(x)u)\right] = 0, \tag{18}$$

it can be obtained inversely:

$$\begin{aligned} R(x) &= -\frac{\left(V_x(x) g(x)\right)^T}{2u^*(x)}, \\ Q(x) &= -V_x(x) f(x) - \frac{1}{2} V_x(x) g(x) u^*(x). \end{aligned} \tag{19}$$

Based on Lemma 4, comparing the error system shown in equation (8) with the second order system shown in equation (4), the following can be obtained:

$$f(x) = \begin{pmatrix} \phi(x_1) - \psi(x_1) + \bar{x}_2 \\ \psi'(())(\phi(x_1) - \psi(x_1) + \bar{x}_2) \end{pmatrix}, g(x) = \begin{pmatrix} 0 \\ 1 \end{pmatrix}. \tag{20}$$

And

$$V_x = \left(F'(x_1)\bar{x}_2\right) = \left(-\psi'(x_1)(\phi(x_1) - \psi(x_1))\bar{x}_2\right). \tag{21}$$

Therefore, the optimal control performance parameters that can be achieved by the control law (17) are obtained by substituting formulas (20) and (21):

$$\begin{aligned} R(x) &= -\frac{\left(V_x(x) g(x)\right)^T}{2u(x)} = \frac{\bar{x}_2}{2k_2 \bar{x}_2} = \frac{1}{2k_2}, \\ Q(x) &= -V_x(x) f(x) - \frac{1}{2} V_x(x) g(x) u(x) \\ &= \psi'(x_1)(\phi(x_1) - \psi(x_1))^2 + \left(\frac{1}{2} k_2 - \psi'(x_1)\right) \bar{x}_2^2. \end{aligned} \tag{22}$$

If virtual control law $x_2^{des} = -\psi(x_1) = -k_1 x_1$ is selected, then, the linear control law of the system (4) is

$$u = -k_2(x_2 + k_1 x_1) \tag{23}$$

In order to $Q(x)$ be positive definite and the cost function to be a meaningful optimal performance, it must be guaranteed that

$$k_2 > 2k_1. \tag{24}$$

Therefore, combining (12), (14), and (23), we can get: when $0 < 2k_1 < k_2$ is satisfied; the origin of the system can be given global asymptotic stability.

And minimize the following optimal value function:

$$J = \int_0^\infty \left(\psi'(x_1)(\phi(x_1) - \psi(x_1))^2 + \left(\frac{1}{2}k - \psi'(x_1)\right)(x_2 + \psi(x_1))^2 + \frac{1}{2k} u^2\right) dt. \tag{25}$$

Similarly, if virtual control law $x_2^{des} = -\psi(x_1 - r) = -k_1 (x_1 - r)$ is selected, then, the linear control law of the system (4) is

$$\begin{aligned} u &= -k_2(\phi(r) + x_2 + k_1(x_1 - r)), \\ 0 &< 2k_1 < k_2. \end{aligned} \tag{26}$$

Defining $x - r = e$, the tracking problem of the system at $y = r$ can be transformed into the global asymptotic stability problem of the system at $x - r$, and the results of equations (23) and (24) above can be applied.

Then, the system obtains global asymptotic stability at $y = r$.

And minimize the following optimal value function:

$$\begin{aligned} J = \int_0^\infty \Bigg(& k_1 [\phi(x_1) - \phi(r) - k_1(x_1 - r)]^2 + \left(\frac{1}{2} k_2 - k_1\right) \\ & \cdot [x_2 + \phi(r) + k_1(x_1 - r)]^2 + \frac{1}{2k_2} u^2 \Bigg) dt. \end{aligned} \tag{27}$$

3.3. Design the Optimal Control Law. Considering the dynamics equation above, the following coordinate transformation is introduced:

$$\begin{bmatrix} p_d \\ q_d \\ r_d \end{bmatrix} = \begin{bmatrix} \cos\alpha \cos\beta & 0 & \sin\alpha \cos\beta \\ -\cos\alpha \sin\beta & \cos\beta & -\sin\alpha \sin\beta \\ -\sin\alpha & 0 & \cos\alpha \end{bmatrix} \begin{bmatrix} p \\ q \\ r \end{bmatrix}. \tag{28}$$

The corresponding dynamics equation becomes

$$\begin{bmatrix} \dot{\mu} \\ \dot{\alpha} \\ \dot{\beta} \end{bmatrix} = \begin{bmatrix} \frac{1}{\cos^2\beta} & 0 & 0 \\ 0 & \frac{1}{\cos\beta} & 0 \\ 0 & 0 & -1 \end{bmatrix} \begin{bmatrix} p_d \\ q_d \\ r_d \end{bmatrix} + \begin{bmatrix} F_\mu(X) \\ F_\alpha(X) \\ F_\beta(X) \end{bmatrix}. \tag{29}$$

Therefore, with the angular acceleration after coordinate transformation as the control input, a three-axis decoupled

second-order nonlinear system can be obtained, as shown below:

$$\begin{cases} \dot{\alpha} = \dfrac{1}{\cos\beta} \cdot q_d + F_\alpha(X), \\ \dot{q}_d = u_2, \end{cases} \tag{30}$$

$$\begin{cases} \dot{\beta} = -r_d + F_\beta(X), \\ \dot{r}_d = u_3, \end{cases} \tag{31}$$

$$\begin{cases} \dot{\mu} = \dfrac{1}{\cos^2\beta} \cdot p_d + F_\mu(X), \\ \dot{p}_d = u_1. \end{cases} \tag{32}$$

It can be found that the structures of equations (30), (31), (32), and (4) are exactly the same.

Comparing equations (4) and (30), the following can be found:

$$\begin{cases} x_1 = \alpha, \\ x_2 = \dfrac{1}{\cos\beta} \cdot q_d, \\ y = x_1, \end{cases} \quad \phi(x_1) = F_\alpha(X), \quad u = \frac{1}{\cos\beta} \cdot \dot{q}_d = \frac{1}{\cos\beta} \cdot u_2. \tag{33}$$

Therefore, it is easy to obtain the backstepping optimal controller to track control instructions $r = \alpha_{cmd}$:

$$u_2 = -k_q(q_d + \cos\beta F_\alpha(\alpha_{cmd}) + k_\alpha \cos\beta(\alpha - \alpha_{cmd})), \tag{34}$$

$$0 < 2k_\alpha < k_q. \tag{35}$$

At the same time, the following optimal value function can be minimized:

$$J = \int_0^\infty \left(k_\alpha[F_\alpha(\alpha) - F_\alpha(\alpha_{cmd}) - k_\alpha(\alpha\text{-}\alpha_{cmd})]^2 + \left(k_q - k_\alpha\right)\left[\frac{1}{\cos\beta} \cdot q_d + F_\alpha(\alpha_{cmd}) + k_\alpha(\alpha\text{-}\alpha_{cmd})\right]^2\right) dt. \tag{36}$$

Similarly, comparing equations (4) and (31), the following can be found:

$$\begin{cases} x_1 = \beta, \\ x_2 = -r_d, \\ y = x_1, \end{cases} \quad \phi(x_1) = F_\beta(X), \quad u = -\dot{r}_d = -u_3. \tag{37}$$

Therefore, it is easy to obtain the backstepping optimal controller to track control instructions $r = \beta_{cmd}$:

$$u_3 = k_r\left(-r_d + F_\beta(\beta_{cmd}) + k_\beta(\beta - \beta_{cmd})\right), \tag{38}$$

$$0 < 2k_\beta < k_r. \tag{39}$$

At the same time, the following optimal value function can be minimized:

$$J = \int_0^\infty \left(k_\beta\left[F_\beta(\beta) - F_\beta(()) - k_\beta(\beta - \beta_{cmd})\right]^2 + \left(k_r - k_\beta\right)\left[-r_d + F_\beta(\beta_{cmd}) + k_\beta(\beta - \beta_{cmd})\right]^2\right) dt. \tag{40}$$

Similarly, comparing equations (4) and (32), the following can be found:

$$\begin{cases} x_1 = \mu, \\ x_2 = \dfrac{1}{\cos^2\beta} \cdot p_d, \\ y = x_1, \end{cases} \quad \phi(x_1) = F_\mu(X), \quad u = \frac{1}{\cos^2\beta} \cdot \dot{p}_d = \frac{1}{\cos^2\beta} \cdot u_1. \tag{41}$$

Therefore, it is easy to obtain the backstepping optimal controller to track control instructions $r = \mu_{cmd}$:

$$u_1 = -k_p\left(p_d + \cos^2\beta F_\mu(\mu_{cmd}) + k_\mu \cos^2\beta(\mu - \mu_{cmd})\right), \tag{42}$$

$$0 < 2k_\mu < k_p. \tag{43}$$

At the same time, the following optimal value function can be minimized:

$$J = \int_0^\infty \left(k_\mu\left[F_\mu(\mu) - F_\mu(\mu_{cmd}) - k_\mu(\mu\text{-}\mu_{cmd})\right]^2 + \left(k_p - k_\mu\right)\left[\frac{1}{\cos^2\beta} \cdot p_d + F_\mu(\mu_{cmd}) + k_\mu(\mu\text{-}\mu_{cmd})\right]^2\right) dt. \tag{44}$$

Through formulas (34), (38), and (42), the angular acceleration $\omega_d'^{des} = [p'_{dcmd}\, q'_{dcmd}\, r'_{dcmd}]^T$ required to achieve attitude maneuver can be obtained. After integral operation and inverse coordinate transformation, the following formula can be obtained:

$$\omega^{des} = T_{bd}\left(\frac{1}{s}\omega_d'^{des}\right). \tag{45}$$

To this end, according to the expected flight attitude requirements, the angular velocity required to complete the maneuver can be obtained by using formula (45), and then,

through the following formula, it can be converted into the torque coefficient required by the maneuver, which is also the input of control allocation problem in the next section.

$$\begin{aligned} T &= IT_{bd}(\alpha, \beta)\dot{\omega}_d^{des} + \omega \times I\omega, \\ \nu &= (c_l c_m c_n)^T = \frac{1}{S\bar{q}} \text{ diag } (b, \bar{c}, b)^{-1} T, \end{aligned} \tag{46}$$

where T_{bd} is the coordinate transformation matrix converted to the body shafting, I is the rotational inertia matrix of the aircraft, b is the wingspan length, and $\bar{c}$ is the average aerodynamic chord length.

4. Fault Tolerant Control Design Based on Control Allocation

As mentioned above, as UAV plays an increasingly important role in the air combat system, the tasks it undertakes become more and more complex, and it needs to bear certain impact of faults. For the flight control system, the UAV has the characteristics of multicontrol surfaces, especially the introduction of multiredundant control surfaces, which provides a prerequisite for the reconfiguration control of UAV against actuator failures.

As shown in Figure 2, when the fault detection module in VMC finds that there is any fault mode toward actuators, the control allocation module in VMC will switch from the normal state to the specific fault state. Then, the fault tolerant control strategy based on the control allocation works, and the control instructions solved by the control allocation module will reflect the influence of the actuator fault mode.

4.1. Nonlinear Control Allocation Design Considerations. For the nonlinear system, assume its motion equation is

$$\dot{x} = f(x, g(x, u)), \tag{47}$$

where $f : R^n \times R^k \mapsto R^n$ and $g : R^n \times R^m \mapsto R^k$ are nonlinear and $k < m$.

It can be written as

$$\begin{aligned} \dot{x} &= f(x) + g_u(x, u), \\ g_u(x, u) &= B_v g(x, u), \end{aligned} \tag{48}$$

where $B_v \in R^{n \times k}$, f, and g have the same mapping form as above.

Introduce virtual controls:

$$\nu = g(x, u), \tag{49}$$

where $\nu \in R^k$; the state equation of the system can be rewritten as

$$\dot{x} = f(x) + B_v \nu = f(x) + B_v g(x, u). \tag{50}$$

Thus, nonlinear system (48) can be converted into equations (49) and (50), which can also use the standard form of the control allocation problem. It can be seen that with linear control allocation problem the difference is that mapping is a nonlinear form.

In the flight control system, the control allocation strategy is required to be solved in real time, but the nonlinear control allocation problem cannot be solved in real time. Therefore, one of the methods to solve this problem is to use the method of local approximation mapping, using linear mapping to approximate nonlinear mapping.

Through local Taylor form expansion, linearization at point u_0 can be obtained:

$$g(x, u) \approx g(x, u_0) + \frac{\partial g}{\partial u}(x, u_0) \cdot (u - u_0). \tag{51}$$

So introduce a linear mapping $B(x) = (\partial g / \partial u)(x, u_0)$; the nonlinear control allocation problem (49) can be converted to the linear control allocation problem:

$$\bar{\nu} = B(x)u, \tag{52}$$

$$\bar{\nu} = \nu - g(x, u_0) + B(x)u_0. \tag{53}$$

When a nonlinear control allocation problem is transformed into a linear problem, it can be solved in many ways. Optimization algorithms based on linear programming, with its lower operation cost and simplex method, have been widely studied in the process of solving control allocation problems [25, 26]. According to the authors' previous research results [27], the allocation algorithm based on linear programming is directly applied here.

Combined with formulas (52) and (53), the control allocation problem is described as follows.

For the known control efficiency matrix B and the given virtual control quantity $\nu(t)$, the feasible instruction $u(t)$ of the control surface is determined by considering the position limit and rate limit $\underline{u}(t) \le u(t) \le \bar{u}(t)$ of the control surfaces, so that $Bu(t) = \nu(t)$ is satisfied.

Thus, the linear programming problem can be solved with the following matrix:

$$\begin{aligned} A &= M \cdot B, b = -A \cdot u_{\min}, \\ Aeq &= [\,], beq = [\,], \\ f^T &= -\nu_d^T \cdot B, \\ lb &= 0 \; ub = u_{\max} - u_{\min}. \end{aligned} \tag{54}$$

The corresponding optimization objectives are

$$\max \left(\rho = \frac{\|B \cdot u\|}{\|\nu_d\|} \right) = \min \left(J = -\nu_d^T \cdot B \cdot u \right). \tag{55}$$

In the three-dimensional control allocation problem, the matrix M has only two rows, i.e.,

$$M = \begin{bmatrix} \nu_{d,2} & -\nu_{d,1} & 0 \\ \nu_{d,3} & 0 & -\nu_{d,1} \end{bmatrix} \tag{56}$$

and the coefficient matrix $A = M \cdot B$ of constraint conditions

also has only two rows, whose rank is 2. Therefore, the solution process is relatively simple.

The application of the method in the flight control system is toward to $v = (c_l\, c_m\, c_n)^T = (1/S\bar{q})\ \mathrm{diag}\,(b, \bar{c}, b)^{-1} T$, and the specific process can be summarized as the following steps:

(Step 1) According to the theory of nonlinear control allocation, the control efficiency matrix under nonlinear condition should be calculated from the expression of aerodynamic derivative $C_M = (C_l\, C_m\, C_n)^T$:

$$B(x) = \frac{\partial C_M}{\partial \delta}(\alpha, \beta, p, q, r, \delta_0). \tag{57}$$

δ_0 can be selected as the control input $u(t - T)$ of previous sampling time or a fixed point, such as $\delta_0 = 0$.

(Step 2) Then the virtual control input after Taylor linear expansion is calculated:

$$\bar{v} = v - C_M(\alpha, \beta, p, q, r, \delta_0) + B(x)\delta_0. \tag{58}$$

(Step 3) Using the control allocation method of formula (54) to solve the above formula, the solution of formula (58) can be obtained.

4.2. Fault Tolerant Control Design for Actuators. This section describes the fault-tolerant control scheme according to the control allocation design method described in Section 4.1 for the two possible fault modes of the electric actuators described in Figure 1. Fault mode 1 is nonoutput force of the actuator, and the other fault mode is output shaft stuck of the actuator.

The nonlinear system equations of an aircraft under normal conditions are described as follows:

$$\dot{x} = f(x) + B_v v = f(x) + B_v g(x, u), \tag{59}$$

where $g(x, u)$ represents the control efficiency of surfaces, which will change when the surfaces fails due to actuators. The following equation describes the nonlinear system equation of the aircraft in the case of failure:

$$\dot{x} = f(x) + B_v g_f(x, u_f), \tag{60}$$

where $g_f(x, u_f)$ represents the control efficiency matrix in the case of failure and $u_f \in R^n$ represents the control input. For different fault modes, equation (60) corresponds to different function forms.

According to the requirements of reconfiguration control, control allocation needs to achieve:

$$g(x, u) = g_f(x, u_f). \tag{61}$$

For the control allocation problem under normal conditions, the allocation objective is

$$v(t) = g(x, u). \tag{62}$$

The nonlinear control allocation problem (62) can be converted to the linear control allocation problem:

$$\bar{v} = v - g(x, u_0) + B(x)u_0 = B(x)u. \tag{63}$$

Similarly, for the control allocation problem under faulty conditions, the allocation objective is

$$v_f(t) = g_f(x, u_f). \tag{64}$$

After linearization,

$$g_f(x, u_f) \approx g_f(x, u_0) + \frac{\partial g_f}{\partial u}(x, u_0) \cdot (u_f - u_0). \tag{65}$$

The control efficiency matrix $B_f(x) = (\partial g_f/\partial u)(x, u_0)$ is introduced, and the linear control allocation problem similarly is as follows:

$$\bar{v}_f = v_f - g_f(x, u_0) + B_f(x)u_0 = B_f(x)u. \tag{66}$$

When the fault modes of the actuators occur, the change of aerodynamic coefficient, weight, and center of gravity of the aircraft can be ignored. On this premise, the change of control capability caused by the faulty actuators only comes from the change of control input.

Meanwhile, when the linearized equilibrium points are $u_0 = 0$, the following formula can be obtained:

$$g(x, u_0) = g_f(x, u_0), \tag{67}$$

$$B(x)u_0 = B_f(x)u_0. \tag{68}$$

Thus, compare formulas (64) and (67), and the requirements of reconfiguration control (61) can be converted into

$$\bar{v}(t) = \bar{v}_f(t). \tag{69}$$

4.2.1. Fault Mode 1: Output Shaft Stuck. The output shaft stuck of actuator refers to the fault mode in which the actuator is in a fixed position due to motor blocking or other mechanical reasons, which can be realized by the fault detection module of VMC. In this fault mode, the control surface connected to the actuator will also be stuck in a certain position. In this case, its deflection will not only fail to produce the desired control effect but also to produce unwanted additional forces and unwanted additional torques. Therefore,

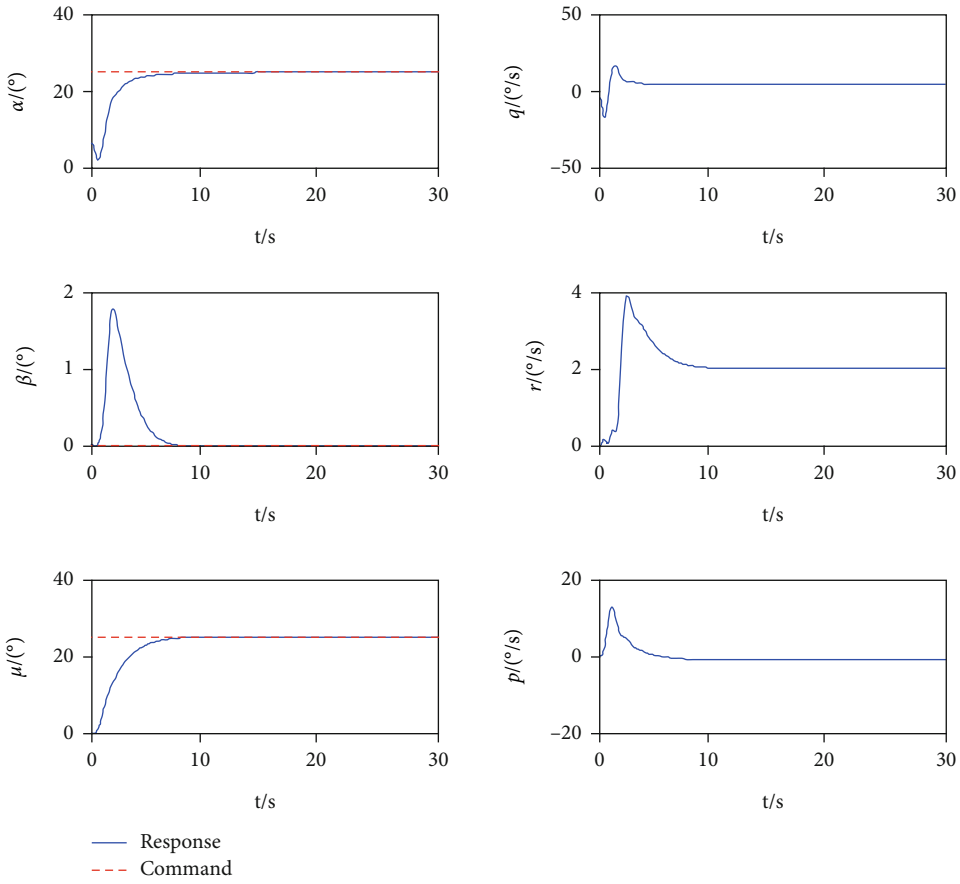

Figure 3: The state response of three-axis maneuver.

the influence of the stuck actuator must be offset in the control allocation.

When the shaft of actuator is stuck, the motion equation of the aircraft does not change, as shown in equation (60).

According to formula (66), the solution of control allocation for reconstruction control can be obtained:

$$\bar{v} = Bu = B_f u_f = B_f^* \cdot u_f^* + b_j \delta_f, \tag{70}$$

where assuming that the aircraft has m surfaces, $u_f^* = (\delta_1, \delta_2, \cdots \delta_j \cdots \delta_{m-1}) \in R^{m-1}$, B_f^* is the remaining control efficiency matrix after removing the stuck surface in B_f, b_j is the control efficiency coefficient of the stuck surface, and δ_f is the stuck position of the faulty surface.

After further derivation, the following can be obtained:

$$u_f^* = \left(B_f^*\right)^+ Bu - \left(B_f^*\right)^+ b_j \delta_f \tag{71}$$

Among them, the first item redistributes the torque required by the original surface to the remaining effective surfaces, and the second item is used to offset the additional influence caused by the stuck surface, so that the actual output of the stuck rudder surface is

$$u_f = \left(\delta_1, \delta_2, \cdots, \delta_{j-1}, \delta_f, \delta_{j+1}, \cdots, \delta_{m-1}\right). \tag{72}$$

4.2.2. Fault Mode 2: Nonoutput Force. Nonoutput force of actuator refers to the failure mode in which the clutch cuts off the current control output due to various reasons, and then, the actuator has no output force. It can be realized by the fault detection module of VMC. In this fault mode, the surface connected with the actuator will also be in a loosely floating state, that is, the control efficiency of the surface is zero. Then, it can be assumed that the loosely floating surface will not produce any aerodynamic and aerodynamic torque; that is, the effect of the control surface on the control input of the aircraft is zero.

Similar to fault mode 1, when the actuator has no output force, the state equation of the aircraft does not change. That is, only the control input of the loosely floating surface is zero, and the loss of control capability caused by the loss of control capability needs to be compensated by the remaining effective control surfaces.

Similarly, assuming u_f^* is the input of the remaining surface after removing the loosely-floating one, then,

$$\bar{v} = Bu = B_f u_f = B_f^* \cdot u_f^* + b_j \delta_f, \tag{73}$$

where, assuming that the aircraft has m surfaces, $u_f^* = (\delta_1, \delta_2, \cdots \delta_j \cdots \delta_{m-1}) \in R^{m-1}$, B_f^* is the remaining control efficiency matrix after removing the loosely floating surface in

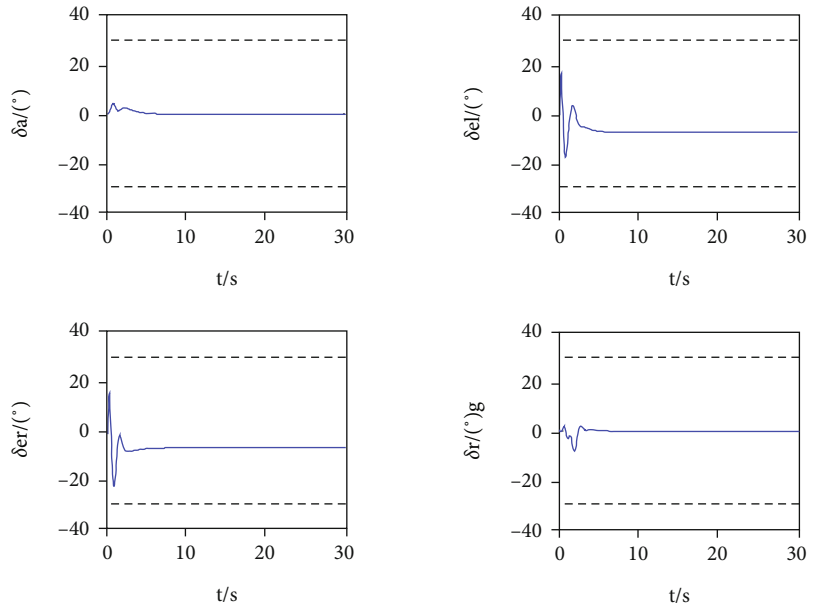

Figure 4: The deflection angle of surfaces. The forces and torques created by the four independent surfaces contribute to the aircraft's three-axis maneuver.

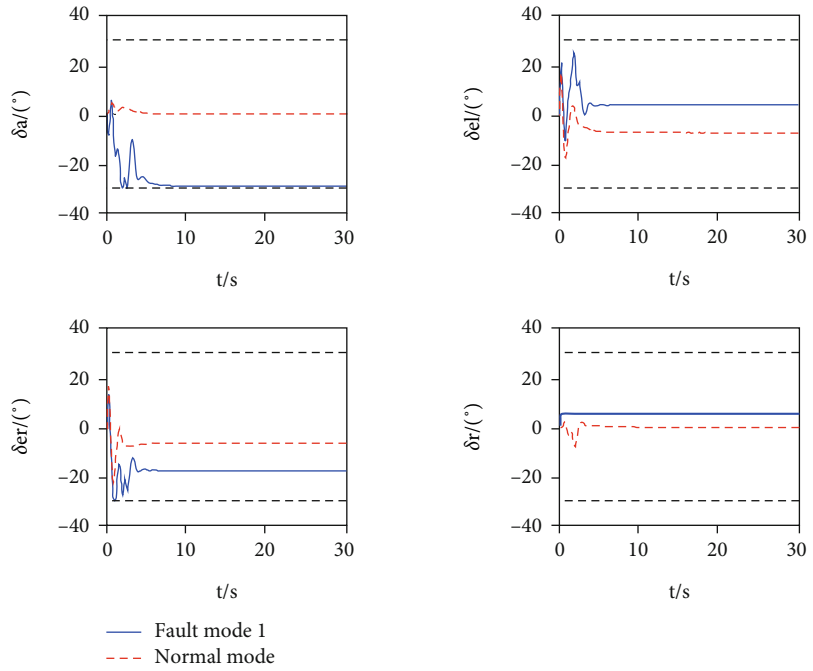

Figure 5: The deflection angle of surfaces against fault mode 1. The remaining surfaces compensate for the abnormal forces and torques caused by the stuck actuator attached to rudder.

B_f, b_j is the control efficiency coefficient of the loosely-floating surface, and $\delta_f = 0$.

Further derivation can be obtained:

$$u_f^* = \left(B_f^*\right)^+ Bu - \left(B_f^*\right)^+ b_j \delta_f. \tag{74}$$

Then, the actual output of the surfaces when the actuator has no output force can be obtained:

$$u_f = \left(\delta_1, \delta_2, \cdots \delta_{j-1}, 0, \delta_{j+1}, \cdots \delta_{m-1}\right). \tag{75}$$

5. Numerical Simulation

5.1. Control Objective. Based on the design of backstepping optimal controller in Section 3 and fault-tolerant control based on control allocation in Section 4, numerical simulations are conducted for the UAV.

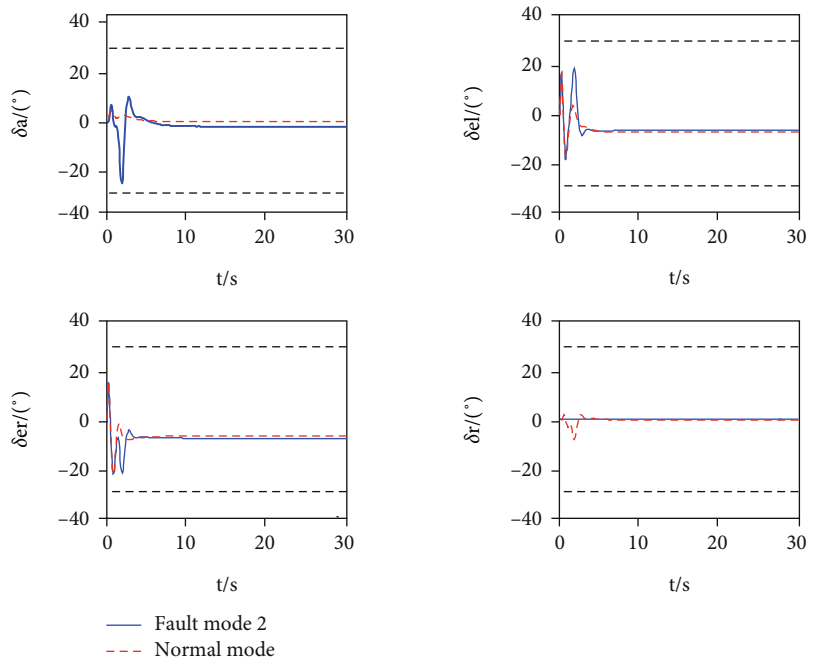

Figure 6: The deflection angle of surfaces against fault mode 2. The remaining surfaces also compensate for the loss forces and torques caused by the loosely floating actuator attached to rudder.

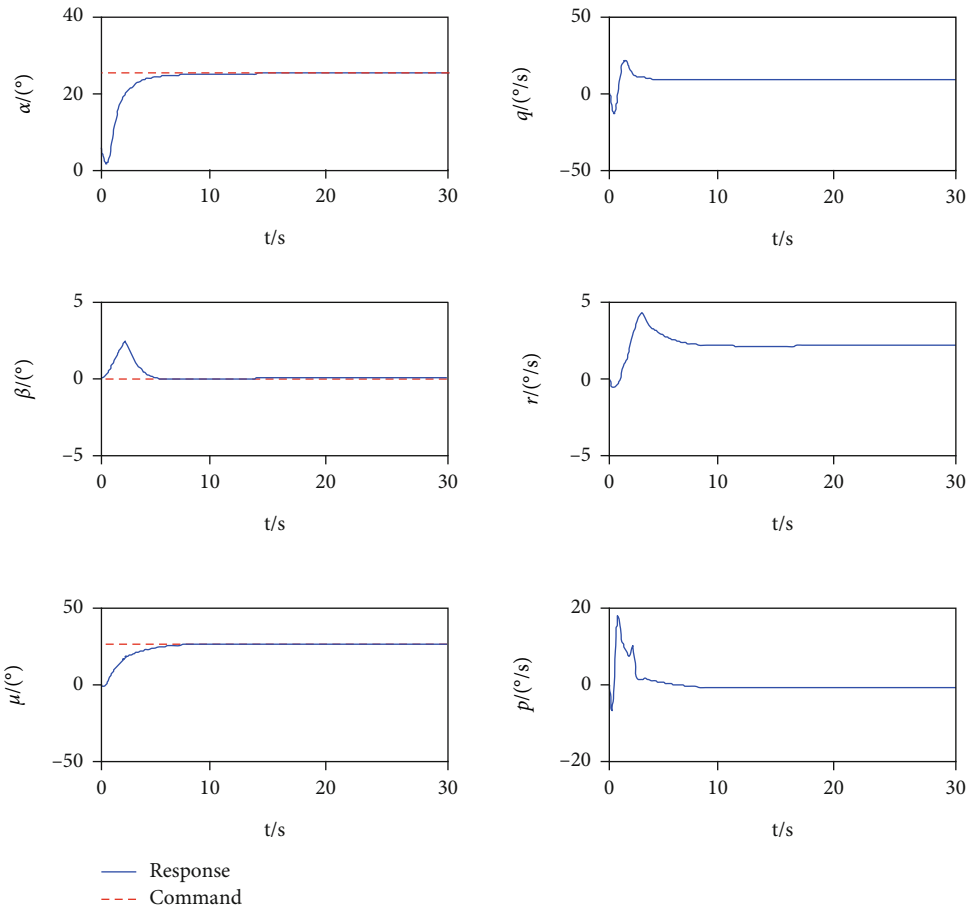

Figure 7: The state response of three-axis maneuver against fault mode 1.

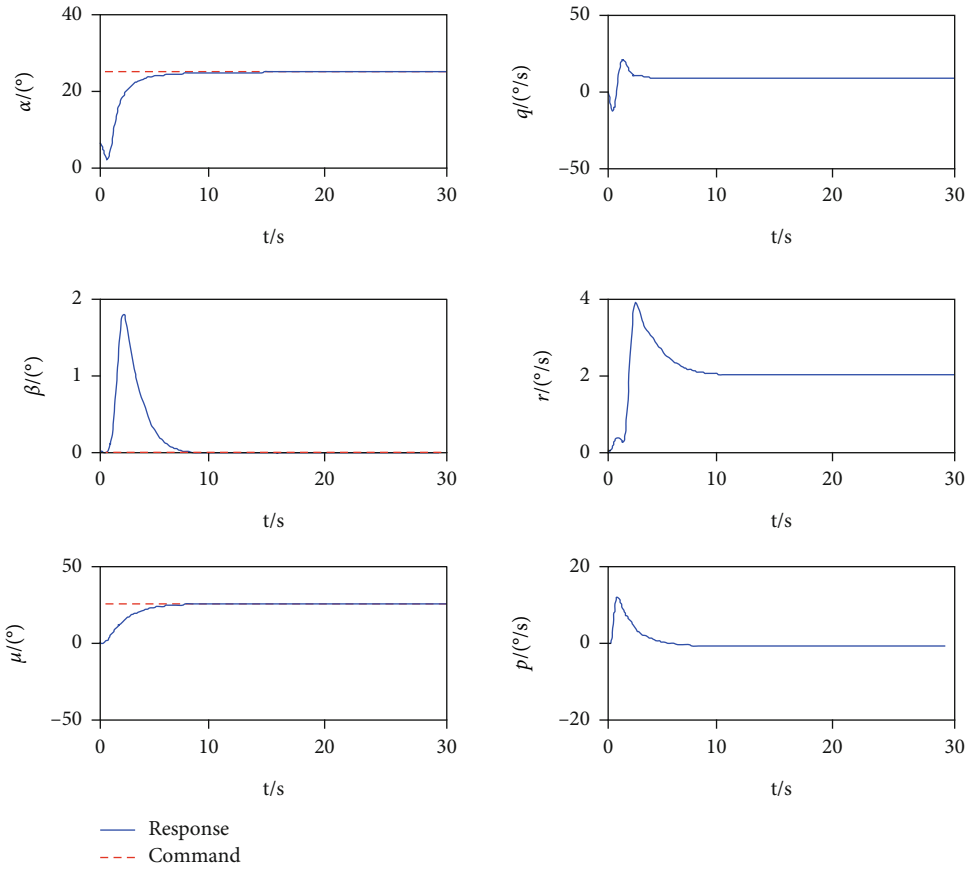

Figure 8: The state response of three-axis maneuver against fault mode 2.

In order to prove the correctness of the control law, the numerical simulation is carried out under the comparison of the two cases. The first set is three-axis maneuver without actuator failures, and the control objectives are $\alpha_{cmd} = 25^\circ$, $\beta_{cmd} = 0^\circ$, $\mu_{cmd} = 25^\circ$.

The fault tolerant control of three-axis maneuver under the condition of actuator faults is the second set. As above, the same simulated UAV object is used, and the initial trim conditions are the same. In the simulation, the parameters of backstepping optimal control law do not change, but the allocation algorithm switches from normal modes to the fault modes in control allocation. Also consider the three-axis maneuver; the control objectives are $\alpha_{cmd} = 25^\circ$, $\beta_{cmd} = 0^\circ$, $\mu_{cmd} = 25^\circ$.

Firstly, the deflection characteristics of the four surfaces of the UAV, namely, left elevator, right elevator, aileron, and rudder, are limited as follows:

$$U_{\max} = [30^\circ, 30^\circ, 30^\circ, 30^\circ],$$
$$U_{\min} = [-30^\circ, -30^\circ, -30^\circ, -30^\circ]. \quad (76)$$

It should be added here that the surface is stuck beyond the deflection limit due to mechanical reasons, and VMC cannot give the correct diagnosis through the fault detection module. The control allocation method may invalidate the input saturation strategy in these fault modes. And this failure condition is not covered in the paper because it cannot be correctly diagnosed.

Then, the initial trim conditions of the simulation are shown below: the trimming velocity is $V = 350$ft/s, the trimming angle of attack is $\alpha_0 = 6.76^\circ$, the remaining trimming flight statuses are $\beta_0 = \mu_0 = p_0 = q_0 = r_0 = 0$, and the trimming angles of deflection are, respectively $[\delta_{el}, \delta_{el}, \delta_a, \delta_r] = [-0.4449^\circ, -0.4449^\circ, -1.6193^\circ, 0.3226^\circ]$.

Finally, the parameters of the optimal controller described in Section 3 are $k_\alpha = 2.53$, $k_q = 5.76$, $k_\beta = 1.36$, $k_r = 5.14$, $k_\mu = 1.64$, and $k_p = 6.23$.

5.2. Simulation Result. It can be seen from the simulation results that the backstepping optimal controller can achieve a good control effect. In the control channels of the three axes, the controlled quantity can meet the requirements of the control instruction within 5 s, and the response has no overshoot and no steady-state error, refer to Figure 3. The black dotted lines in Figure 4 are the upper and lower limits of surface deflection. This proves that it is feasible and correct to design flight control system using backstepping optimal controller. At the same time, it also shows that the control allocation method can realize the correct distribution of control instructions on each controllable surface.

5.3. Simulation of Fault Mode 1. In the simulation, the electric actuator attached to the rudder is set to be stuck at 5°. Then, the rudder will also be stuck at 5°, and its deflection

will fail not only to produce the desired control effect but also to produce unwanted control effect.

5.4. Simulation of Fault Mode 2. In the simulation, the electric actuator attached to the rudder is set to nonoutput force. Then, the rudder will also be in a loosely floating state. Then, it can be assumed that the loosely floating rudder will not produce any aerodynamic and aerodynamic torque.

In Figures 5 and 6, the red curve is the deflection angle of surfaces without the actuator failure, and the blue curve is the deflection angle of surfaces in the corresponding fault mode, and the black dotted lines are the upper and lower limits of surface deflection. It can be seen that when actuator failures occur, the reconfiguration based on the control allocation method ensures remaining surfaces can compensate the influence caused by the faulty actuator. The angle of attack and the angle of roll track the control objectives quickly with stable performance; refer to Figures 7 and 8. Therefore, the design of control allocation completes the task of reconfiguration control well, obtains good control effect, and achieves the goal of fault-tolerant control.

6. Conclusion

The fault-tolerant control of UAV in the case of actuator failure in the flight control system is studied. Based on the backstepping control method derived from Lyapunov function, the nonlinear optimal control law was constructed by introducing inverse optimization strategy. And reconfiguration design based on control allocation is proposed. Through linearized nonlinear mapping, a fault-tolerant control scheme is designed for the actuators in two typical fault modes: stuck and nonoutput force. Through rigorous mathematical analysis and numerical simulation, the effectiveness of the control strategy is verified.

The integrated VMC in the FCS can realize online monitor of limited fault modes of actuators, which ensures the scheme proposed achieves better fault-tolerant control after the occurrence of known fault modes. However, mechanical transmission from the actuators to the surfaces, or the surfaces itself, cannot be directly dealt with by using the strategy proposed in the paper due to the lack of monitor results, such as the loss of part of the surface. It is worth further study.

Data Availability

No data were used to support to this study.

Conflicts of Interest

The authors declare that there are no conflicts of interest regarding publication of this article.

Acknowledgments

This work is cosupported by the Aeronautical Science Foundation of China (201958053003) and (20200007018001).

References

[1] H. Yin, J. Fan, T. Hou, D. Li, Y. Wang, and H. Chen, "Efficiency analysis of typical application based on manned/unmanned aerial vehicle cooperative combat," in *Proceedings of 2020 3rd International Conference on Unmanned Systems*, pp. 314–319, Harbin, China, 2020.

[2] L. Lei, "Development analysis of typical manned/unmanned aerial vehicle collaborative operations projects abroad," *Unmanned Systems Technology*, vol. 3, no. 4, pp. 83–90, 2020.

[3] L. Yue, H. Wei, and W. Yongqing, "Deep reinforcement learning with application to air confrontation intelligent decision-making of manned/unmanned aerial vehicle cooperative system," *IEEE Access*, vol. 8, pp. 67887–67898, 2020.

[4] P. M. Frank, "Fault diagnosis in dynamic systems using analytical and knowledge-based redundancy: a survey and some new results," *Automatica*, vol. 26, no. 3, pp. 459–474, 1990.

[5] Z. Zejun, Y. Hao, and J. Bin, "Fault tolerant consensus of multiple nonholonomic chained-form systems with actuator and communication faults," *International Journal of Robust and Nonlinear Control*, vol. 31, no. 18, pp. 9483–9500, 2021.

[6] M. Taimoor and L. Aijun, "Neural-sliding mode approach-based adaptive estimation, isolation and tolerance of aircraft sensor fault," *Aircraft Engineering and Aerospace Technology*, vol. 92, no. 2, pp. 237–255, 2019.

[7] J. Marzat, D. F. Piet-Lahanier, F. Damongeot, and E. Walter, "Model-based fault diagnosis for aerospace systems: a survey," *Proceedings of the Institution of Mechanical Engineers, Part G: Journal of Aerospace Engineering*, vol. 226, no. 10, pp. 1329–1360, 2012.

[8] J. Hu and X. Lingfei, "Multi-sensor fault diagnosis of aircraft engine based on Kalman Filter Group," *Proceedings of 2016 Chinese Intelligent Systems Conference*, vol. 404, pp. 363–379, 2016.

[9] Y. Gao, N. Wenhui, and F. Wan, "Deep belief net-based fault diagnosis of flight control system sensors," *Journal of Physics: Conference Series*, vol. 1631, no. 1, article 012186, 2020.

[10] I. Samy, I. Postlethwaite, and D.-W. Gu, "Survey and application of sensor fault detection and isolation schemes," *Control Engineering Practice*, vol. 19, no. 7, pp. 658–674, 2011.

[11] Y. Baojun and S. Zhaorui, "Reconfiguration of the angle of attack signal in disability of sensors," *Aeronautical Science & Technology*, vol. 29, no. 8, pp. 33–40, 2018.

[12] Y. Jun, N. Jing, and G. Guanbin, "Robust model reference adaptive control for transient performance enhancement," *International Journal of Robust and Nonlinear Control*, vol. 30, no. 15, pp. 6207–6228, 2020.

[13] R. B. Anderson, J. A. Marshall, A. L'Afflitto, and J. M. Dotterweich, "Model reference adaptive control of switched dynamical systems with applications to aerial robotics," *Journal of Intelligent and Robotic Systems*, vol. 100, no. 3-4, pp. 1265–1281, 2020.

[14] K. Prasanth, E. Ryan, and S. Koushil, "Geometric L1 adaptive attitude control for a quadrotor unmanned aerial vehicle," *Journal of Dynamic Systems, Measurement, and Control*, vol. 142, no. 3, article 031003, 2020.

[15] L. Yuqian, C. Jiaxing, and C. Chengyu, "Advanced autonomous underwater vehicles attitude control with L1 backstepping adaptive control strategy," *Sensors*, vol. 19, no. 22, article 4848, 2019.

[16] Z. Youmin and J. Jin, "Fault tolerant control system design with explicit consideration of performance degradation," *IEEE*

Transactions on Aerospace and Electronic Systems, vol. 39, no. 3, pp. 838–848, 2003.

[17] C. Yuwei, Z. Zhengyong, L. Zhengren, and L. Aijun, "A task scheduling method for network distributed flight control system," in *2019 Chinese Automation Congress, CAC*, pp. 480–483, Hangzhou, China, 2019.

[18] X. Wang, H. Fang, L. Dou, B. Xin, and J. Chen, "Integrated distributed formation flight control with aerodynamic constraints on attitude and control surfaces," *Nonlinear Dynamics*, vol. 91, no. 4, pp. 2331–2345, 2018.

[19] C. Yuwei and L. Aijun, "Research on the key technologies of network distributed flight control system," in *2020 Chinese Automation Congress, CAC*, pp. 6928–6931, Shanghai, China, 2020.

[20] S. Marc and P. Anthony, "Nonlinear adaptive flight control with a backstepping design approach," in *AIAA Guidance, Navigation, and Controsl Conference and Exhibit*, pp. 728–738, Boston, M A, U.S.A., 1998.

[21] H. Kaiyu, Y. Aaly, and C. Zian, "Fuzzy adaptive backstepping control of nonlinear uncertain systems with unmeasured states and input saturation," *IEEE Access*, vol. 8, pp. 228442–228453, 2020.

[22] J. Lofberg, "Backstepping with local LQ performance and global approximation of quadratic performance," in *Proceedings of the 2000 American Control Conference*, vol. 6, pp. 3898–3902, Chicago, IL, USA, 2000.

[23] S. Kang, J. Back, H. Shim, and J. H. Seo, "Locally optimal and robust backstepping design for C1 vector fields," in *International Conference on Control, Automation and Systems*, pp. 2212–2217, Seoul, Korea (South), 2007.

[24] K. Ezal, Z. Pan, and P. V. Kokotovic, "Locally optimal and robust backstepping design," *IEEE Transactions on Automatic Control*, vol. 45, no. 2, pp. 260–271, 2000.

[25] H. Xiuwei and D. Guangren, "Dynamic infinity-norm constrained control allocation for attitude tracking control of overactuated combined spacecraft," *IET Control Theory and Applications*, vol. 13, no. 11, pp. 1692–1703, 2019.

[26] Y. Wen, L. Chen, K. Liang, and D. Duan, "Nonlinear MPC for a sensorless multi-vectored propeller airship based on sliding mode observer with saturation," *Asian Journal of Control*, vol. 21, no. 1, pp. 248–263, 2019.

[27] Y. W. Cui, W. G. Zhang, G. W. Li, and J. P. Shi, "Research for multi-control-effector reconfigurable control based on linear programming," *Flight Dynamics*, vol. 29, no. 2, pp. 41–45, 2011.